SHL ITEM BARCODE
19 1774568 0

REFERENCE ONLY

UNIVERSITY OF LONDON THESIS

Degree MD Year 2008 Name of Author ALONZI, ROBERTO.

COPYRIGHT
This is a thesis accepted for a Higher Degree of the University of London. It is an unpublished typescript and the copyright is held by the author. All persons consulting the thesis must read and abide by the Copyright Declaration below.

COPYRIGHT DECLARATION
I recognise that the copyright of the above-described thesis rests with the author and that no quotation from it or information derived from it may be published without the prior written consent of the author.

LOAN
Theses may not be lent to individuals, but the University Library may lend a copy to approved libraries within the United Kingdom, for consultation solely on the premises of those libraries. Application should be made to: The Theses Section, University of London Library, Senate House, Malet Street, London WC1E 7HU.

REPRODUCTION
University of London theses may not be reproduced without explicit written permission from the University of London Library. Enquiries should be addressed to the Theses Section of the Library. Regulations concerning reproduction vary according to the date of acceptance of the thesis and are listed below as guidelines.

A. Before 1962. Permission granted only upon the prior written consent of the author. (The University Library will provide addresses where possible).

B. 1962 - 1974. In many cases the author has agreed to permit copying upon completion of a Copyright Declaration.

C. 1975 - 1988. Most theses may be copied upon completion of a Copyright Declaration.

D. 1989 onwards. Most theses may be copied.

☐ This copy has been deposited in the Library of ____________________

☑ This copy has been deposited in the University of London Library, Senate House, Malet Street, London WC1E 7HU.

EVALUATION OF THE OXYGENATION AND VASCULARITY OF PROSTATE CANCER USING MAGNETIC RESONANCE IMAGING

A thesis to be submitted to the University of London
for the degree of Doctor of Medicine

Roberto Alonzi

University College London

Marie Curie Research Wing
Mount Vernon Hospital
Rickmansworth Road
Middlesex
HA6 2RN
UK

ProQuest LLC
789 East Eisenhower Parkway
P.O. Box 1346
Ann Arbor, MI 48106-1346

Declaration

I declare that the work presented in this thesis is my own and has not been submitted for a degree or comparable award to this or any other university or institution.

Signed

Date 30/10/2008

Abstract

The outcome of radical treatment for prostate cancer is appreciably influenced by the presence of hypoxia. Oxygenation status may therefore be another underlying biological parameter, beyond the classic prognostic factors (age, clinical stage, Gleason score and prostate specific antigen), that predicts for treatment failure in this malignancy. Angiogenesis plays a pivotal role in the growth, invasion, metastasis and survival of prostate tumours. Measurements of angiogenesis have been linked with clinical and pathological stage, histological grade and the potential for metastasis formation. They also provide prognostic information and have been correlated with disease-specific survival and progression after treatment.

Magnetic resonance imaging techniques are capable of detecting the molecular, biochemical, physiological and metabolic changes that occur due to pathological processes within tissues. Experiments presented in this thesis have sought to evaluate the ability of Dynamic Contrast Enhanced MRI (DCE-MRI), Dynamic Susceptibility Contrast MRI (DSC-MRI), Intrinsic Susceptibility Weighted MRI (also known as Blood Oxygen Level Dependent (BOLD) MRI) and Diffusion Weighted Imaging (DWI) to characterise the oxygenation and vascular status of prostate tumours in animal models and in patients with prostate cancer.

This research has demonstrated the feasibility of hypoxia imaging in prostate cancer. Although MRI can not precisely map tissue pO_2, the combination of BOLD-MRI and dynamic susceptibility contrast MRI provides a valuable surrogate and predicts the pattern of hypoxia, as determined by pimonidazole immunohistochemistry, with reasonable accuracy. The research has also shown that prostate cancer responds to carbogen gas breathing and that androgen deprivation causes profound vascular collapse within one month of starting therapy. These findings should help in the rational design of future studies that aim to target tumour vasculature and combat tumour hypoxia in prostate cancer.

Acknowledgements

My Supervisors:

Professor Peter Hoskin for his inspiration and guidance, whose influence has and will continue to guide my career.

Dr Anwar Padhani for his energy, enthusiasm, scientific understanding and unwavering commitment.

Dr Ross Maxwell for his expertise, problem solving, patience but mostly for his scientific knowledge.

Completion of the work described in this thesis would not have been possible without the contribution of many people at Mount Vernon Hospital, the Paul Strickland Scanner Centre, the Gray Cancer Institute, the Royal Marsden Hospital, Watford General Hospital and the Lister Hospital. I am indebted to you all:

Prof. Michele Saunders
Mrs Frances Daley
Dr Rowena Smith
Dr Jayne Taylor
Mr James Stirling
Mr Ian Wilson
Dr Davina Honess
Dr Ros Locke
Dr Paul Barber
Dr James d'Arcy
Dr David Collins
Miss Jessica Milner
Miss Fiona Butler
Ms Jackie Anderson
Ms Sonia Noble
Dr Samita Agarwal
Ms Linda Fowler
Mr Manoah Pancharatnam
Prof. Thomas McNicholas
Mr Greg Boustead

To my family, May-ai and Leo, whose support means so much.

Table of Contents

Chapter 1

Chapter 2

Chapter 3

Chapter 4

Chapter 5

Chapter 6

Chapter 7

List of Tables

List of Figures

Publications arising from this research

Papers

Alonzi R, Hoskin P. Functional imaging in clinical oncology: magnetic resonance imaging- and computerised tomography-based techniques. *Clin Oncol (R Coll Radiol)*. 2006 Sep;**18(7)**:555-70.

Alonzi R, Padhani A. Dynamic Contrast Enhanced MRI in Prostate Cancer. *European Journal of Radiology*. 2007; **63**:335-350

Abstracts

R. Alonzi, A. R. Padhani, N. J. Taylor, J. J. Stirling, J. A. d'Arcy, D. J. Collins, M. I. Saunders and P. J. Hoskin The use of combined functional MRI to map tumour hypoxia in the human prostate gland. ISMRM 4-9 May 2008. Toronto (Canada).

R. Alonzi, N. J. Taylor, P. J. Hoskin, J. J. Stirling, J. A. d'Arcy, D. J. Collins, M. I. Saunders and A. R. Padhani. The reproducibility of quantitative and semi-quantitative dynamic and intrinsic susceptibility-weighted parameters in the human prostate. ISMRM 4-9 May 2008. Toronto (Canada).

R. Alonzi, R. Maxwell, J.I. Wilson, A. R. Padhani, M. I. Saunders and P. J. Hoskin Experiments to evaluate the validity of Blood Oxygen Level Dependent (BOLD) MRI and its response to hyperoxia, in two human prostate cancer xenografts. AACR 13-17 April 2008. San Diego, CA (USA).

R. Alonzi, P. J. Hoskin, N. J. Taylor, J. J. Stirling, B. Wilton, J. A. d'Arcy, D. J. Collins, M. I. Saunders and A. R. Padhani. The use of functional MRI to map tumor hypoxia in the human prostate gland. SCBT-MR 30 March – 2 April 2008. Charleston, SC (USA).

Alonzi R, Taylor NJ, Hoskin PJ, Stirling JJ, d'Arcy JA, Collins DJ, Saunders MI, Padhani AR. DCE and susceptibility-MRI investigations of prostate gland physiological changes with androgen deprivation. ISMRM 19-25 May 2007. Berlin (Germany).

Alonzi R, Padhani AR, Taylor NJ, Stirling JJ, Saunders MI, Hoskin PJ. Physiological changes within the prostate caused by androgen withdrawal. UKRO 18-21 Mar 2007. Edinburgh (UK).

Alonzi R, Padhani AR, Taylor NJ, Stirling JJ, Collins DJ, Saunders MI, Hoskin PJ. Functional MRI to investigate changes in oxygenation and vascularity of the prostate gland caused by androgen deprivation. ESTRO 8-12 Oct 2006. Leipzig (Germany).

Alonzi R, Hoskin PJ, Taylor NJ, Stirling JJ, Collins DJ, d'Arcy JA, Saunders MI, Padhani AR. Susceptibility and dynamic MRI investigations of the physiological changes to the prostate gland caused by androgen deprivation. ISMRM MR of Cancer Study Group Workshop: Frontiers in Metabolic, Molecular and Clinical Imaging.13-16 October 2006. Pocono Manor, PA, (USA).

Chapter 1

Introduction

Prostate Cancer and its Biology

1.1 Prostate Cancer – An Overview

1.1.1 Epidemiology

Carcinoma of the prostate is the commonest form of human cancer. Worldwide, more than 650,000 men are diagnosed every year, accounting for a tenth of all male malignancies. In the UK, it is the most common cancer in men, with a lifetime risk of being diagnosed with the disease of 1 in 13. Annually it is the cause of approximately 10,000 deaths [1-4]. Substantial increases in incidence have been reported in recent years [5], which have been closely linked to the emergent use of trans-urethral resection for urinary outflow symptoms during the 1980s and the subsequent introduction of PSA testing in the 1990s [6-8]. Prostate cancer risk is closely associated with age, 60% of cases occurring in men over the age of 70 years. In 2002 there were 31,923 new cases of prostate cancer diagnosed in the UK [2] and this figure will undoubtedly rise as the population at risk grows with the lengthening of life expectancy.

Despite this seemingly high burden of disease, only a third of all men diagnosed with prostate cancer actually die of their malignancy. The overall five-year survival rate for men diagnosed in England in 2000 – 2001 was 71%. For men that present with localised disease, 6 – 46% of patients will develop generalised disease without treatment, depending on age, stage, grade, PSA and ethnicity [9-18]. Untreated men diagnosed with early localised disease (T0 – T2), have only a 17% risk of developing metastases over the subsequent 20 years [16]. This risk increases substantially with T3 disease (34% at 10 years) and high grade cancer (74% at 10 years). These figures translate into a disease specific survival at 5 and 10 years of 70 – 98% and 50 – 92% respectively, if localised prostate cancer of any grade or stage is left untreated.

1.1.2 Predicting Outcome

The fact that so many men diagnosed with prostate cancer would have a normal life expectancy without treatment has lead to considerable efforts to predict which patients actually require therapy for localised disease. In the field of prostate cancer epidemiology, the definition of outcome can be a difficult concept. Most men are in their 60s and 70s at the time of diagnosis. In a disease with a natural history measured in decades, the general health of a study population will have a proportionally large influence on outcome compared to the small differences observed between treatment groups. For many men with localised disease, life expectancy will be unaffected by the success of their primary anti-cancer treatment. Therefore in order to measure treatment efficacy, surrogate measures are required. The relationship between the surrogate marker and the incidence of 'clinical events' determines whether that particular measure has prognostic value.

The most commonly used biomarker in prostate cancer is PSA and the associated outcome measure is biochemical (PSA) relapse-free-survival (RFS). Like all other 'relapse-free' or 'progression-free' estimates, PSA RFS is not a true measure of survival in that the end-point is not death. As a result it is subject to biases from the definition of relapse used and its method and frequency of measurement. In 1996 a consensus conference was convened to try to standardise the use of PSA as a biomarker for reporting outcomes in irradiated patients [19]. This ASTRO failure definition (three consecutive rises in PSA) provided a manner in which studies could be compared. However a number of features of the definition resulted in a discrepancy with the observed clinical outcome. Most notably these included a profound sensitivity to the length of follow up, a censoring artefact resulting from the fact that the date of relapse was backdated to a time midway between the PSA nadir and the third consecutive PSA rise and false positive results caused by benign fluctuations in PSA. A study by Thames *et al.* examined 102 different definitions of biochemical failure in 4839 men with localised prostate cancer to determine which predicted clinical failure most accurately [20]. Four definitions were found to be superior to the ASTRO definition. One of these has now been adopted as the new consensus definition and is now referred to as the RTOG-ASTRO Phoenix definition [21]. It is defined as a rise in PSA of 2ng/ml above the nadir level with the date of relapse being the date of the PSA test that satisfies this criterion. It must be noted that this is a consensus of expert opinion based on the best available data in 2006, as patterns of treatment change other definitions may become more appropriate measures of outcome.

Modification of the standard PSA test may provide more accurate prognostic information. The rate at which serum PSA levels change (PSA velocity) may be an important indicator of the presence of life-threatening disease. In a recently published study PSA velocity was determined in 980 men who were participants in the Baltimore

Longitudinal Study of Aging [22]. PSA velocity, measured 10-15 years before diagnosis, was associated with cancer-specific survival of 92% among men with PSA velocity of 0.35 ng/mL per year or less and 54% among men with PSA velocity above 0.35 ng/mL per year ($P < 0.001$). Furthermore, men with PSA velocity above 0.35 ng/mL per year had a higher relative risk of prostate cancer death than men with PSA velocity of 0.35 ng/mL per year or less (RR = 4.7, 95% CI = 1.3 to 16.5; P = 0.02).

The risk of relapse and death from localised prostate cancer depends on both clinical and biological factors. In localised disease the most powerful predictive factors for biochemical relapse are the pre-treatment serum PSA level, Gleason grade and TNM stage. Combination of these measures can be used to stratify patients. The 'Partin tables' were originally developed by urologists Alan Partin and Patrick Walsh based on accumulated data from 4,133 patients who had been surgically treated for prostate cancer [23]. They correlated PSA level, Gleason score, and estimated clinical stage with the definitive pathological stage. A probability was calculated for each of the following four: organ confined disease, extraprostatic extension, seminal vesicle invasion, and lymph node invasion. The primary value of the tables is for counselling patients regarding the probability of their tumour being a specific pathologic stage, rather than use as a strict decision-making tool. The nomograms help patients and their doctors make informed decisions based on the probability of a pathologic stage, the individual patient's risk tolerance, and the values they place on the various potential outcomes.

However, the Partin tables are calculated using clinical stage as assessed by digital rectal examination. Using modern imaging, highly accurate 'T' staging is now possible, with sensitivity and specificity of advanced MRI techniques frequently in excess of 90% [24-27]. As a result it is hard to justify a treatment decision based on a strategy that ignores some of the available information. Other normograms have been developed for the same purpose. A formula based only on PSA and grade, proposed by Roach *et al,* appears to be reasonably accurate at estimating the incidence of extracapsular extension in patients with low or intermediate risk disease [28]. The risk of biochemical failure following radiotherapy also correlated with the risk of extracapsular extension.

Numerous genetic and biological features have been shown to correlate with outcome following treatment for localised prostate cancer **(table 1.1)**. Currently none of these are used to direct the treatment decision. This is largely due to the fact that in general these predictive markers are not modality specific. They indicate that a relatively poor outcome is likely whichever treatment is chosen. With further validation, some of these indices may be useful, alone or in combination, to determine whether radical treatment

Table 1.1 Factors associated with poor outcome in localised prostate cancer – other than Stage, Gleason grade and PSA.

Category	Risk Factor	Risk
Demographic Factors	Age	Age > 65 increases likelihood of systemic relapse following local therapy
	Race	Risk of relapse higher in African Americans compared to white Americans
Histological Subtype	Periurethral Duct Carcinoma	Often anaplastic with frequent mitoses
	Transitional Cell Carcinoma	Approximately double rate of positive lymph-nodes
	Prostatic Duct Adenocarcinoma	35% 5-year survival (58% following radical RT)
	Sarcomatoid Carcinoma	Median survival < 2 years
Genetic Factors	Abnormal p53 protein expression	increased incidence of distant metastases, decreased RFS and decreased overall survival.
	Low p27 protein expression	Increased recurrence after radical prostatectomy
	p21 over-expression	Reduced 5-year survival
	DNA content	x 5 – 9 increased risk of relapse if tumour is not diploid
Morpholocical Factors	Multifocal disease	Approximately double recurrence rate
	Tumour Volume	Large volume predicts for LN and distant metastases
Microscopic Factors	Nuclear Morphometry	Low nuclear area and ellipsoid shape predict for poor prognosis
	Microvessel Density (MVD)	High MVD may predict for reduced disease specific survival
Cell Proliferation	Ki-67 labelling index	High index associated with a reduced 5-year PFS following surgery
	S-phase fraction (SPF)	High SPF associated with increased local progression and reduced time to metastases
Biological Factors	Hypoxia	Low prostate : muscle pO_2 ratio predicts for biochemical relapse
	E-Cadherin	Low levels correlate with recurrence after radical treatment
	Insulin-Like Growth Factor	High expression of binding protein predicts recurrence after prostatectomy
	Androgen Receptor Expression	higher AR expression results in poor overall survival in hormone-refractory prostate cancer
Surgery	Positive Surgical Margin	x 4 risk of biochemical relapse
Radiotherapy	Radiation Dose	Doses < 70 Gy associated with increased probability of biochemical recurrence

is appropriate at all. However, certain biological properties of tumours have specific relevance to radiotherapy in that they are known to alter radiation sensitivity. These include angiogenesis, hypoxia and proliferation. Identification of the level and distribution of these factors may guide treatment selection and facilitate specific targeting of radioresistant tumours.

1.1.3 Imaging Biomarkers

The interest in imaging biomarkers in oncology derives from the extensive use of imaging technologies in diagnosis and patient care. The fact that many of the cutting-edge imaging technologies work in vivo makes them especially suitable for observing the response in live patients. The generic term *biomarkers* applies to all detection methods used in the life sciences and may be defined as any detectable biologic parameter, whether biochemical, genetic, histologic, anatomic, physical, functional, or metabolic. By logical extension, imaging biomarkers are defined as any anatomic, physiologic, biochemical, or molecular parameter detectable with one or more imaging methods used to help establish the presence and/or severity of disease.

Recent advances in imaging offer exciting opportunities to develop and validate oncological biomarkers as valuable adjuncts to diagnosis, tests of treatment efficacy, and/or treatment monitoring. State-of-the-art structural, functional, and molecular imaging methods allow the tumours to be visualized noninvasively *in vivo* at submillimeter and subsecond spatial and temporal scales. However, the development and validation of imaging biomarkers present some special challenges, including the following: equipment evaluation, procedure standardization, data regarding reproducibility and replication, inter-observer variability, the production and measurement of reference standards, sensitivity to interventions or disease progression, inter-subject variance, choice of image reconstruction, automated versus observer-dependent image analysis and whether a reliable association can be demonstrated between the imaging biomarker and a clinical endpoint.

Every day, radiologists assess findings in imaging studies that gauge the effectiveness of medical treatments. These imaging biomarkers range from simple measurement of tumour mass to cutting-edge MR, PET or CT imaging sequences developed to enable evaluation of tumour biology. The clinical benefit of these techniques is obvious, however a broader and potentially more important use of these techniques is the systematic evaluation of the therapies themselves, where the imaging biomarkers become surrogate end points for clinical trials.

Key to the enormous potential of imaging biomarkers is the reality that many medical therapies alter the anatomic, physiologic, biochemical, or molecular parameters readily visualized with imaging techniques. Particularly with established modalities such as conventional radiography, CT or MR imaging, a large pool of existing imaging technologies may be brought to bear in a cost-effective manner to help assess the presence and severity of many diseases. Even imaging modalities that are not yet clinically approved and not generally applicable in patients may be used effectively in preclinical decision making, as is the case with a number of molecular imaging methods.

1.2 Prostate Cancer Angiogenesis

1.2.1 Overview

Angiogenesis involves a cascade of events in which mature, resting host endothelial cells are stimulated to proliferate, degrade their basement membranes and to form new blood vessels. The angiogenic process is a complex multistep sequence involving many growth factors (cytokines) and interactions between varieties of cell types. Angiogenesis is crucial for normal development and persists into adult life. Physiological processes such as wound healing and the regeneration of the endometrium during the normal menstrual cycle are dependent on new vessel growth. Pathological processes such as diabetic retinopathy and cancer are equally reliant on angiogenesis. The development of a new blood supply is an essential requirement for a tumour to grow larger than about 1mm^3 in size [29].

Angiogenesis plays a pivotal role in the growth, invasion, metastasis and survival of prostate cancer. Proliferation and apoptosis are intimately linked with prostate cancer angiogenesis [30]. Expression of angiogenic cytokines in prostate cancer can be induced as a response to hypoxic stress, by hormonal stimulation, but can also result from activation of oncogenes. Angiogenesis in prostate cancer is highly dependent on vascular endothelial growth factor (VEGF) [31]. It has been shown that VEGF is produced in abundance by the prostatic secretory epithelium of normal, hyperplastic, and tumour containing glands [32] **(figure 1.1)**. With respect to the vasculature, it is clear that VEGF is required for vascular homeostasis in benign prostatic hyperplasia (BPH) and maintains a high fraction of immature vessels (those without investing pericytes or smooth muscle cells) in prostate cancers.

Tumour cells promote angiogenesis by the upregulation of pro-angiogenic factors such as VEGF and its receptors as well as the downregulation of antiangiogenic factors such as thrombospondin-1 [33-37].

Figure 1.1 VEGF Immunostaining of malignant prostate tissue

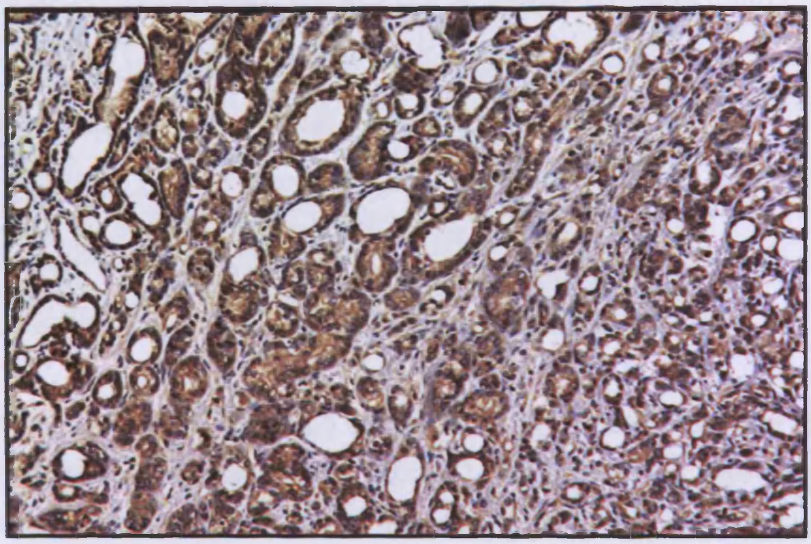

The upregulation of pro-angiogenic genes including VEGF, Angiopoietin-2, Nitric oxide synthase (NOS), Platelet derived growth factor (PDGF) and Basic and Acidic fibroblastic growth factor (bFGF and a FGF) is a feature of the tumour microenvironment [35, 38-44]. VEGF increases vessel permeability and induces endothelial cell migration and proliferation in conjunction with Ang-2 [45-48]. Endothelial spouts are then formed that develop into blind ending tubes, which anastomose together to form vascular loops [49].

Tumour vessels may lack protective mechanisms such as mural cells and a basement membrane. Even if mural cells are present, they may not be functionally normal: Morikawa et at observed abnormalities in pericyte shape and abnormal separations between alpha smooth muscle actin and CD31-positive cells on tumour vessels, indicating that pericytes were only loosely associated with endothelium [50] **(figure 1.2)**. Tumour vessels may not always have an intact endothelial cell lining. 'Mosaic' vessels have been observed that have focal regions where tumour cells appeared to be in contact with the vessel lumen [51, 52]. These features are likely to contribute to the increased vascular permeability of tumour vessels compared to those found in normal tissues.

Figure 1.2 Anti-smooth muscle actin stain of malignant prostate tissue

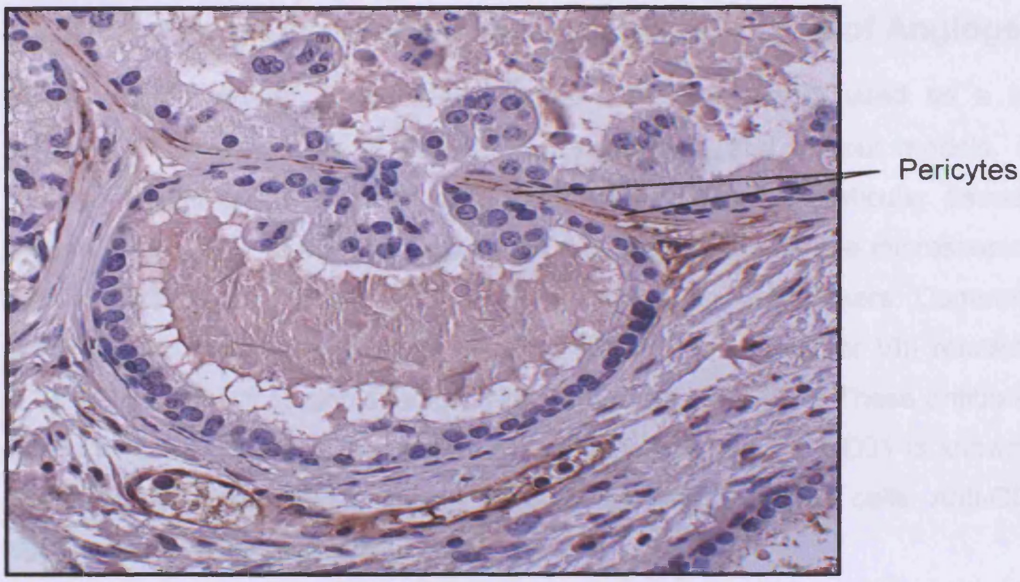

Increased microvessel density (MVD) counts are seen in BPH [53] and in high grade prostatic intraepithelial neoplasia [54]. Higher MVD counts are also associated with prostate cancer with Gleason scores greater than seven. Immuno-histochemical studies have found that MVD in prostate cancer and BPH are higher than in the peripheral zone [55] but there is an overlap in MVD counts between tumours and BPH.

MVD is a potential prognostic factor that has been correlated with clinical and pathological stage, metastasis and histological grade in prostate cancer. MVD has also been correlated with disease-specific survival and progression after treatment [56-58]. MVD has not however been shown to correlate consistently with outcome after radical prostatectomy [59].

There are a number of features of tumour vascularity that are characteristic of malignancy which are amenable to study by imaging techniques. These include: (1) Spatial heterogeneity and chaotic structure. (2) Poorly formed, fragile vessels with high permeability to macromolecules. (3) Arteriovenous shunting, high vascular tortuosity and vasodilatation. (4) Intermittent or unstable flow due to transient rises in already raised interstitial pressure. These and other microenvironment characteristics can be reflected by currently available, clinical imaging techniques such as dynamic contrast enhanced MRI, perfusion CT, diffusion MRI, proton MR spectroscopy and ultrasound.

1.2.2 The laboratory measurement of angiogenesis

1.2.2.1 The Immunohistochemical Quantification of Angiogenesis

Microvessel Density: Microvessel density (MVD) is widely used as a surrogate measure of angiogenesis in pathological specimens and tumour models. It simply involves counting the number of blood vessels within a particular tissue region. Immunohistochemical staining techniques are used to identify the microscopic vessels with several different vessel wall antigens being used as markers. Commonly used antibodies for assessing MVD in prostate cancer are anti-factor VIII related antigen (FVIIIAG or von Willebrand's factor), anti-CD34 and anti-CD31. These antibodies have different sensitivities and immunostaining characteristics. Anti-CD31 is known to stain plasma cells, macrophages and in some instances, carcinoma cells. Anti-CD34 also stains immature haematopoetic cells.

A study has evaluated these three endothelial markers of microvessels in benign and malignant prostatic tissue [60]. Fifteen benign hyperplastic prostate and 54 prostate cancer specimens were immunohistochemically stained for CD31, CD34 and vWF. The MVD obtained by each marker was quantified by a vessel count in standardized grids within the area of maximum angiogenesis. The data on MVD was interrelated and compared to tumor staging, grading and clinical follow-up. A significant correlation of the CD31/CD34/vWF-MVD data was observed in BPH tissue, but not in cancer. In prostate carcinoma, the most sensitive marker for newly derived blood vessels was CD34. While CD34-MVD demonstrated a significant association with tumour grading and PSA follow-up, CD31- or vWF-MVD did not. The group concluded that CD34 is the best marker for the immunohistochemical visualization of microvessels in benign and malignant human prostate tissue specimens.

Despite the fact that MVD counting is seemingly a simple technique, the area of tumour that is counted differs between researchers. Many count in areas seen to have high vascularity at low magnification, the so-called 'hotspot' method. Alternatively, some count in randomly selected areas or in specifically defined areas, such as the tumour edge. Methods of MVD measurement are varied and as yet no standardisation has been achieved. At a consensus meeting Vermeulen *et al.* have attempted to redress the problem by suggesting a standardised technique [61]. This involved counting vessels in the presumed highest angiogenic area. However, it is apparent that this has not been taken up as a standard method and will not work in some tumour types.

Chalkley Point Counting: This technique employs a 25-point eyepiece graticule, which is applied over a vascular 'hotspot' at x250 magnification [62]. The graticule is oriented so that maximum numbers of points are superimposed over areas of immunohistochemically-highlighted microvessels. The Chalkey count is the number of grid points that hit stained microvessels. It is therefore a relative area estimate rather than a true vessel count. One advantage of using this system is the reduction in bias produced by eliminating the uncertainly caused by distinguishing whether two adjacent stained areas represents one or two separate blood vessels.

Automated Analysis: Computerised analysis methods for immunohistochemical analysis are now increasingly used and are often reported in medical literature [63-67]. In general, these techniques employ standard immunohistochemical staining as described above. The histological slide is digitised and computer software differentiates the brown immunohistochemical stain from the background stain (usually blue haematoxylin). Results are displayed as the proportional area of brown stain as a percentage of the total area of the slide or region of interest. This gives a mean total vascular area rather than a true vessel count. Correlations between the two measures have been documented in prostate cancer **(appendix A)**.

1.2.2.2 Table 2: Examples of non-immunohistochemical angiogenesis models and assays

Model / Assay	Technique	Measurement
The dorsal skinfold window chamber model (rodents)	A flap of skin is dissected away from opposing surfaces of a dorsal skin flap leaving a fascial plane with associated vasculature. Tumour cells or small tumour pieces can be implanted into the window chamber	Allows for the direct examination of in vivo tumour angiogenesis and microcirculation
The cornea pocket assay	A cell line is evaluated by inserting the suspension into a micro pocket that has been surgically produced in the rabbit cornea Observations of the implants are performed with a slit lamp stereomicroscope.	Angiogenic activity is evaluated on the basis of the number and growth rate of newly formed capillaries.
The Matrigel plug assay	Matrigel is a matrix of a mouse basement membrane neoplasm known as Engelbreth-Holm-Swarm murine sarcoma	Matrigel containing test angiogenesis-inducing compounds or tumor cells can be injected subcutaneously in mice
Sponge assays	Subcutaneous implantation of various artificial sponges in animals can be used to study angiogenesis *in vivo*	Compounds to be evaluated are either injected directly into the sponges or incorporated into ELVAX or hydron pellets, which are placed in the center of the sponge
The chick chorioallantoic membrane (CAM) assay	The early chick embryo lacks a mature immune system. Tissue grafts are placed on the CAM through a window made in the eggshell	Compounds are either prepared in slow release polymer pellets, absorbed by gelatin sponges or air-dried on plastic discs and then implanted onto the CAM.

1.3 The Endocrine Regulation of Prostate Cancer

Androgens seem to regulate VEGF expression in prostate cancer cells and benign prostatic tissues [68]. VEGF expression in androgen-dependent cell lines is down regulated upon androgen withdrawal. Prostate tumours from these cell lines undergo vascular regression prior to tumour cell death [69]. Studies have demonstrated a link between androgen action and angiogenesis in androgen-responsive LNCaP [68], PC-82 and A2 [70] human prostate cancer xenografts. Androgen deprivation causes a reduction in tumour VEGF levels resulting in inhibition of angiogenesis and the collapse of tumour vasculature mediated by vascular endothelial cell apoptosis [69]. This results in tumour vessels adopting more normal vascular characteristics, including reduced diameter, tortuosity, vascular permeability and leukocyte adhesion.

Animal experiments have convincingly demonstrated that blood flow to the prostate gland is drastically reduced within a very short period of time following surgical castration in animal models [71, 72]. As measured in rat ventral prostate tissue, blood flow rates were reduced by 50% within 24 hours of castration. Neither a sham surgical castration procedure, nor immediate testosterone replacement following orchidectomy affected flow in this way. Prostatic capillaries degenerate during the early period after castration, whereas the larger vessels that survive become highly constricted [73]. This effect may be mediated by nitric oxide synthase (NOS) and cyclic GMP (cGMP). Acute prostatic vasoconstriction is likely to contribute significantly to a decrease in prostate blood flow following castration.

Clinical studies have provided evidence for a relationship between androgenic steroid stimulation and vascular activity in human prostate tissue using the 5-α reductase inhibitor Finasteride, which is widely used to treat the symptoms of benign prostatic hypertrophy. This suggests that hormonal therapy has the potential to alter the vascular system of the human prostate. Also, Immunohistochemical examination of prostate tissues obtained from patients treated with androgen-withdrawal for prostate cancer have noted a significant reduction of tissue microvascularity compared to hormone-naïve patients [74].

These results imply that blood flow regulation is a major mechanism through which androgen ablation affects the prostate gland. It explains the rapid changes in prostate volume and may be the primary factor influencing cell death. However, this dramatic reduction in blood flow potentially initiates tissue hypoxia, a consequence that has profound implications with regard to radioresistance.

Androgen deprivation has been the most common form of therapy for advanced prostate cancer since the 1940s following the demonstration, by Charles Huggins, that surgical castration could cause disease regression [75]. The advent of pharmacological methods for androgen ablation has led to the inclusion of hormonal therapies into radical treatment strategies for localised prostate cancer with the aim of increasing cure rates. There is still some uncertainty as to the optimal combination and schedule for endocrine therapies within the context of treatment for early prostate cancer, however a number of recent clinical studies have provided an evidence base for their use.

Neo-adjuvant hormonal therapy prior to radical prostatectomy does not improve overall survival, however it does reduce the rate of positive surgical margins and can significantly improve other pathological variables such as lymph node involvement and pathological staging [76-85]. Similarly, androgen deprivation following radical prostatectomy does not improve overall survival [86-88] although one study suggested an improvement in disease-specific survival at both five and ten years [87].

In combination with radiotherapy, androgen deprivation can be administered beforehand (neo-adjuvant) during (concomitant) or afterwards (adjuvant). Four randomised studies using neo-adjuvant and concomitant androgen deprivation have been published [89-92]. No overall survival benefits were observed in any of the reports, although sub-group analysis of one study suggested a possible advantage for the patients with Gleason grade 2-6 tumours [92]. The results from these four studies have been pooled in a meta-analysis [93]. The combined data confirms the lack of an overall survival benefit or any advantage in terms of disease specific survival. However, the meta-analysis did demonstrate a significant improvement in terms of both biochemical and clinical disease free survival (odds ratios of 1.93 and 1.86 respectively; $p < 0.00001$) in favour of neo-adjuvant androgen deprivation.

Four other trials have demonstrated the effectiveness of androgen deprivation in the adjuvant setting [86, 94-96]. The study by Bolla et al. was the only one of the four to demonstrate an overall survival advantage in its own right (78% versus 62% survival at 5 years in favour of three years of adjuvant goserelin, $p = 0.0002$). However meta-analysis of the 2844 patients included in these four studies demonstrates that overall survival, at both 5 years and 10 years, was significantly improved in the groups that received adjuvant hormones (odds ratio 1.29, $p = 0.007$ for 5 years and odds ratio 1.44, $p = 0.003$ for 10 years). A similar advantage was seen in terms of disease specific survival (odds ratio 2.10, $p < 0.00001$) and disease free survival (odds ratio 0.91, $p < 0.0001$) at five years.

Several other reports have assessed the use of neo-adjuvant, concomitant and adjuvant androgen deprivation together in combination with radiotherapy. The Radiation Therapy Oncology Group (RTOG) protocol 92-02 compared two months of neo-adjuvant and two months of concomitant hormonal therapy with or without the addition of two years of adjuvant androgen deprivation [97]. The patients that received the additional adjuvant therapy benefited from superior efficacy outcomes in terms of disease free survival, cause specific survival, biochemical failure, distant metastases and local progression. There was no benefit with respect to overall survival other than for a subgroup of patients with Gleason scores of eight to ten. Laverdière et al. reported a two-part study in which patients were initially randomised between external beam radiotherapy alone, three months of androgen ablation prior to radiation therapy and a third arm which received hormonal treatment for three months before radiotherapy continued until six months after radical treatment [91]. Initial analysis after two years of follow-up demonstrated that both arms that received androgen deprivation were superior to the group that were treated with radiotherapy alone. These two arms comprised the second part of the study, which contrary to RTOG 92-02, showed that there was no significant benefit from the addition of an adjuvant component to the pre-radiotherapy androgen deprivation.

The issue regarding the use of hormonal therapy in combination with permanent (low dose-rate) prostate brachytherapy is also the source of some uncertainty. Two large, non-randomised studies have reported conflicting results. A retrospective study of 938 consecutive patients from West Virginia, USA, demonstrated that after brachytherapy, androgen deprivation had no impact on overall or cause-specific survival for any risk group, although there was a suggestion of a beneficial effect on PSA progression free survival for high-risk patients [98]. In contrast, a much larger retrospective series from Arizona, USA, evaluated 2,378 consecutive patients, 464 of which had received pre-implant androgen deprivation for prostate downsizing [99]. The hormone treated group showed a 24% overall survival *detriment* at 10 years (44% versus 20%, $p = 0.02$), which was independent of stage, grade, PSA level and age.

Mechanistically, the sequencing of hormonal therapy and radiotherapy is of great importance. Androgen deprivation prior to or during radiation therapy has the potential to cause vascular, physiological, biochemical and genetic changes within a prostate tumour that may influence its radiobiology in terms of intrinsic radiosensitivity, initial clonogen number, potential clonogen doubling time, cell-loss factor and repopulation rate. In this scenario, hormonal therapy can be considered to be acting as a radio-modulator. By contrast, in the adjuvant setting androgen deprivation has no influence on tumour radiosensitivity and its actions can be regarded as additive rather than synergistic.

There is little doubt that much of the clinical benefit attributed to androgen deprivation results from its cytotoxicity and resulting reduction in tumour clonogen number. However, if this cytoreductive effect comes at the expense of an increased radio-resistance amongst the remaining tumour clonogens, then part or all of the beneficial effects of hormonal therapy may be lost, or even reversed, if the interaction between androgen deprivation and radiation is allowed to occur prior to or during radiotherapy.

It is relevant that only studies that have used androgen deprivation in the adjuvant setting have shown a survival benefit for combined modality treatment. Whereas the only study to demonstrate a detrimental effect caused by androgen deprivation, examined the use of neo-adjuvant hormones. No published study has ever compared neo-adjuvant with adjuvant androgen deprivation in the setting of radical radiotherapy. As a result there is no clinical data that informs on the synergistic (or possibly antagonistic) interaction between these two therapy modalities. A randomised trial, in which both arms receive the same duration of hormonal therapy and same radiotherapy method, with the randomisation determining only whether the androgen deprivation starts before or after radiotherapy, would effectively control for all factors other than the interaction between hormones and radiotherapy. This strategy could provide an insight into the role that androgen deprivation plays in the radiobiology of prostate cancer and whether the biological changes induced by hormonal treatment impacts on its clinical radiosensitivity. However, in the absence of clinical data, one must turn to other evidence in order to draw a conclusion regarding the consequence of combining androgen deprivation and radiotherapy.

A study using the androgen dependent Shionogi *in vivo* spontaneous murine mammary tumour system, found that neoadjuvant androgen deprivation, in the form of orchidectomy 12 days prior to irradiation, profoundly and significantly reduced the 50% tumour control dose (TCD_{50}) when compared to adjuvant androgen deprivation (a reduction from 85.7 Gy to 43.3 Gy) [100]. If radiation therapy was deferred after the neoadjuvant androgen deprivation until an androgen independent state had been achieved and the tumour had regrown to its original volume, then the advantage of prior neoadjuvant androgen deprivation was lost (the TCD_{50} value rose to 73.3Gy). This study provided one of the first pieces of evidence for a synergistic effect between androgen ablation and irradiation and confirmed the findings of a prior study using the Dunning 3227 rat prostate cancer cell line in nude mice that was reported in abstract form only [101]. However, these results could be explained by additive cell killing, with fewer clonogens left for survival measurements. The TCD_{50} assay cannot distinguish between an additive effect on cell killing and an interaction resulting in supra-additive cell death. It must also be noted that the Shionogi model has some important distinctions from human prostate cancer. The tumour is exquisitely sensitive to androgens, with volume reductions in excess of 80% seen in the majority of tumours after neoadjuvant androgen deprivation, which contrary to the situation in human prostate cancer, leaves little for the radiotherapy to eradicate. The Shionogi tumours rapidly become androgen insensitive, with tumour regrowth to original volumes within 25 – 35 days of orchidectomy. Furthermore, the animal tumours are homogeneous rather than a mixture of benign, hyperplastic and malignant tissue as is the case in the human prostate.

In the normal prostate, androgen deprivation causes apoptotic cell death, reducing epithelial cell numbers by up to 80% [102]. However, in both animal tumour models and human prostate cancer, the dominant effect of androgen deprivation is cell cycle arrest rather than cell death [103, 104]. A study using double thymidine analogue labelling and flow cytometry of Dunning prostate R3327-G tumour-bearing rats, demonstrated a profound shift from predominantly proliferating tumour cells (65% proliferating cells) to mostly quiescent tumour cells (>90% quiescent cells) 3 days after castration [105]. The potential doubling time (Tpot) increased from 6 to 42 days. The apoptosis rate was measured at approximately 1%, equivalent to the proliferation rate, resulting in no net gain or loss of cell numbers following androgen deprivation. Similar studies using the Ki-67 labeling index have also shown that the predominant effect of androgen ablation in human prostate cancer is to reduce proliferation rather than to cause cell death [104, 106].

Quiescence and lengthening of Tpot have long been associated with radio-resistance [107]. Therefore, for neo-adjuvant or concomitant androgen deprivation to result in an improvement in radiation response, these changes must be countered by other effects such as a reduction in the clonogen repopulation rate, increased radiation induced apoptosis or enhanced intrinsic tumour radiosensitivity. Evidence from Joon *et al.* suggests that the apoptotic index following radiation may be increased by pre-treatment with androgen ablation [108]. This group also used the Dunning R3327-G tumour model and measured the peak apoptotic index following radiotherapy in androgen-deprived rats versus controls. They showed that apoptosis, measured six hours after irradiation, increased almost five-fold, suggesting a supra-additive interaction between androgen ablation and radiation due to modulation of apoptosis. Garzotto et al. have reported conflicting results using the LNCaP cell line [109]. This group demonstrated a five-fold *reduction* in postmitotic apoptosis following the deprivation of androgenic stimuli, which they attribute to cell cycle delay.

A study using androgen-sensitive LNCaP cells in culture, irradiated with 2 or 8 Gy, three days after androgen deprivation, demonstrated that despite an increase in apoptosis as measured by the TUNEL assay, clonogenic survival experiments showed no advantage over the androgen deprivation or radiotherapy alone control groups in terms of radiosensitivity [110]. These results suggest that there is no interaction between androgen deprivation and radiotherapy, when cell death is measured globally via clonogenic assay. The fact that there may have been a small degree of supra-additivity in terms of apoptosis, implies that the level of apoptosis is only a minor component of overall cell death, alternatively that the increases in apoptosis occurred in a sub-population of cells that would have been killed by the radiotherapy in any case or that the increase in apoptosis induced in one sub-population of tumour cells is countered by the induction of radioresistance in another sub-population.

Given that androgen deprivation cannot eradicate prostate cancer, with ubiquitous findings of residual cancer in prostatectomy specimens resected after primary treatment with hormones, a hypoxic environment is likely to reduce the tumour control probability for the remaining clonogens. No study has specifically addressed this issue. A report by Parker *et al.* used the Eppendorf polarographic electrode system to measure the intraprostatic pO_2 of 55 men with clinically localized prostate cancer before high-dose conformal radiotherapy [111]. They demonstrated a wide variation of tumour oxygen levels ranging between 0.2 and 57.3 mmHg. No difference was observed on the basis of whether the patient had been previously treated with androgen deprivation. However, only nine patients had received neo-adjuvant hormones, making the study underpowered to answer this question given the variability of pO_2 readings. A paired study, with measurements before and after androgen withdrawal, would be a more robust method of analysis and would control for inter-subject variation.

MRI techniques have the ability to take measurements from the entire prostate gland and characterise the nature of the component tissues. Multiple examinations are possible for every patient and the non-invasive nature of the procedure allows investigation of the true physiological environment. Padhani was the first to publish results of paired T_1-weighted DCE MRI measurements of vascular permeability before and after three months of androgen withdrawal [112]. Reductions in tumour permeability were observed ($p < 0.001$) and these reductions coincided with a decrease in serum PSA levels in 91% of patients. Further development and validation of functional MRI technology now allows the use of a combination of T_1-weighted DCE MRI, T_2*-weighted DSC MRI, diffusion weighted imaging and BOLD MRI to obtain information pertaining to vascular flow, volume, permeability, cellularity and tissue hypoxia.

1.4 Tumour Hypoxia

1.4.1 Overview

Oxygen was first identified as a factor that could influence cancer biology when its effect on radiation response was discovered in 1909 [113]. The radiation response of skin was shown to reduce when blood flow was interrupted by direct compression. Mottram in 1935 supported this hypothesis with the finding that variation in tumour radiosensitivity depends on the size of tumour islands within a mass, which in turn is governed by the proportion of cells at a significant distance from a blood vessel [114]. This was the first time diffusion dependent hypoxia was suggested as a concept. Mottram observed that this phenomenon also exists in testicular irradiation, where spermatids distant from blood vessels continue to produce spermatozoa, even when the dose given is large enough to cause sterility. In 1942, two further papers described experiments showing that anoxic mice survived higher doses of whole body radiation [115, 116]. Manipulating tissue oxygenation to overcome the hypoxia problem was shown to be feasible in a report by Hollcraft [117]. The regression of lymphosarcoma xenografts produced by a fixed dose of radiation was greatest when breathing oxygen and 5% carbon dioxide, intermediate when breathing air and least when breathing 92% Nitrogen and 8% oxygen at the time of irradiation.

The relationship of radiosensitivity to varying oxygenation was first shown in mammals by Gray et al in 1953 in an Ehrlich mouse ascites model [118]. A series of experiments showed the dependence of radiosensitivity on oxygen, consistent with studies on non-mammalian cells. Cell survival was reduced by a factor of 2.5 to 3 when irradiated in oxic conditions (100% O_2 Vs 100% nitrogen). This enhancement did not occur when densely ionising radiation was used. They also showed that the response to radiotherapy could be increased when oxygen was given to mice under 3 atmospheres compared to 1 atmosphere pressure.

Thomlinson and Gray provided the first evidence of the detrimental effects of hypoxia in human tumours [119]. A series of human lung cancers were characterised by a particular appearance, in which cords of tumour cells of varying sizes were surrounded by stroma containing vascular supply. The larger tumour cords had a necrotic centre surrounded by a rim of intact cells. All tumour cords with radii greater than 200μm exhibited necrosis but no necrosis was seen in tumour cords with a radius less than 160μm. The surrounding sheath of intact tumour cells never exceeded 180μm, irrespective of the size of the necrotic centre. Thomlinson and Gray postulated the variability of measured values obtained around the mean was due to both tumour cords not running exactly perpendicular to the plane of the section, and to partial blood vessel compression reducing oxygen concentration at the periphery of the cords. These distances are equivalent to the calculated distance that oxygen would be expected to diffuse through the tumour and imply a rim of viable cells exist in a chronically hypoxic state around the edge of the necrotic regions.

Further evidence that a sub-population of viable hypoxic cells exists in tumours came from cell survival assays of solid lymphosarcoma xenografts in mice [120]. Survival curves derived from endpoint dilution assays exhibited a steep slope at low doses and a shallower slope at higher doses. When the experiment was repeated under anoxic conditions, cell survival was increased and the slope matched the steeper gradient across the whole dose. The proportion of hypoxic cells was estimated to be about 1% from the ratio of the cell survival in each experiment. More recently, the range of hypoxic cells human tumours has been estimated to be much higher [121].

Hypoxia is an important factor in radiotherapy treatment failure and has been associated in clinical studies with poor local tumour control and relapse in carcinomas of the head and neck, prostate, bladder and cervix and also in soft tissue sarcomas [122-127].

1.4.2 The biology of tumour hypoxia

There are two distinct mechanisms that can generate regions of hypoxia within tumours. Chronic diffusion limited hypoxia, as already described, occurs in tumour cells that are situated at a distance from the nearest blood vessel. Depending on whether the nearest vessel is a venule, capillary or arteriole clinically relevant hypoxia will begin to arise at a distance of 70 – 100μm. The partial pressure of oxygen will decline further as the distance from a vessel increases up to approximately 160 - 180μm, where anoxia will lead to necrotic cell death. Diffusion limited hypoxia is relatively stable and will not vary minute-by-minute or hour-by-hour. However, over the life of an individual tumour, the balance between tumour growth and angiogenesis will affect the vascular distribution, thereby influencing the pattern of diffusion-limited hypoxia over time. It is the cells bordering the necrotic region, which are viable and clonogenic, yet exist in a hypoxic environment, that are likely to exhibit a resistant phenotype.

Evidence has emerged that another, distinct, type of hypoxia may contribute to the overall pattern of tumour oxygenation at any given point in time. Acute, transient, perfusion limited hypoxia results from temporary, reversible cessation of blood flow by closure or blockage of blood vessels within tumours. The first direct evidence for this came from experiments using the fluorescent perfusion marker Hoechst 33342 [128]. This group, based at the Gray Cancer Institute, categorised tumour cells into 10 groups depending on their proximity to a functional blood supply. This was done using a fluorescence activated cell sorter based on the cell' s Hoechst 'concentration' (i.e. ratio of fluorescence intensity and peripheral light scatter). The study demonstrated that even cells close to a blood supply might become transiently hypoxic at any particular time and that larger tumours were more prone to perfusion-limited hypoxia. These findings were confirmed using laser Doppler studies that allowed direct measurement of red cell flow in both murine and human tumours [129]. Results demonstrated that in human tumour microregions, 26% showed a change in erythrocyte flux by a factor of 2 or more over a 60 minute measurement period. More than 50% of changes were completed within 20 minutes. Within the 1 hour monitoring period at least 30% of the changes were reversed. These findings demonstrate that microregional changes in erythrocyte flux, resulting in transient, perfusion-driven changes in oxygenation, are a feature of human malignancies as well as experimental transplanted tumours.

1.4.3 The molecular basis of tumour hypoxia

The key regulator of cellular oxygen homeostasis is the dimeric hypoxia-inducible transcription factor HIF. The stability HIF-1 is oxygen dependent. Under conditions of normal oxygenation it is rapidly degraded by the ubiquitin proteosome pathway. One of the steps in the degradation process involves the hydroxylation of a HIF-1α proline residue by prolyl hydrolase. This enzyme has an absolute requirement for the presence of oxygen and ferrous (Fe^{2+}) iron as cofactors for activity. In the absence of oxygen, HIF-1α is stabilised, which allows its translocation to the nucleus where it binds with the HIF-1β sub-unit. The resultant HIF heterodimer then activates the transcription of a number of genes that participate in the normal adaptive response of the cell to hypoxia.

These genes include VEGF (angiogenesis), erythropoetin (red blood cell production), glycolytic enzymes (glucose metabolism and energy) and carbonic anhydrase (pH balance).

Like many other cellular processes, HIF is regulated by p53. This tumour suppressor gene promotes Mdm2-mediated ubiquitination and proteasomal degradation of the HIF-1α subunit. Loss of p53 in tumour cells enhances HIF-1α levels and augments HIF-1-dependent transcriptional activation of the vascular endothelial growth factor (VEGF) gene in response to hypoxia [130]. Hypoxia induces p53 and therefore causes apoptosis in cells that possess wild-type p53. However, oncogenically transformed cells that contain mutated p53 are unable to undergo apoptosis in response to hypoxia and are therefore conferred a survival advantage. By selecting for mutant p53, hypoxia not only leads to deregulation of HIF-1α and stimulation of angiogenesis but also to genetic instability and enhanced tumour progression.

Immunohistochemical studies using monoclonal antibodies to HIF-1α have demonstrated high levels of immunoreactivity in human tumour specimens compared with very low levels in normal tissues [131]. HIF-1α expression correlates with VEGF expression, microvessel density and tumour grade [132-136].This is manifest in the clinical observation that hypoxia and HIF-1α expression selects for an aggressive phenotype and poor prognosis in many tumour sites [125, 134, 137-140].

1.4.4 Hypoxia in prostate cancer

Hypoxic regions exist in human prostate carcinoma [111, 141]. Both Movsas *et al.* in 1999 and Parker *et al.* in 2004 used the Eppendorf microelectrode to characterize the range and heterogeneity of oxygen partial pressures in the prostates of men with prostate or bladder cancer. Movsas' group took 2145 individual pO_2 measurements from 12 patients. They showed that the oxygen measurements from the pathologically involved portion of the prostate were significantly lower than those from normal muscle. Similarly, higher pO_2 readings were obtained from the pathologically normal prostates than from the prostates of patients with prostate carcinoma. Increasing levels of hypoxia were observed with increasing clinical stage. Significant predictors of oxygenation included the type of tissue and clinical stage. As a confounding factor in this study, the type of anaesthesia used was also predictive of prostate oxygenation. In a subsequent report, the same investigators found that pO_2 also correlates with age [142].

Parker investigated the prostates of 55 men prior to radical radiotherapy for prostate cancer. pO_2 values ranged from 0.2 to 57.3 mmHg, with a median of 4.5 mmHg. The percentage of the 40–50 individual pO_2 measurements in each patient that were less than 5 mmHg ranged between 0 and 100%, with a median of 60%. This confirmed that biologically significant hypoxia exists in the majority of patients with clinically localized prostate cancer. No correlation was observed between pO_2 and Gleason score, prostate-specific antigen level or haemoglobin concentration. Contrary to Movsas' report, no association was found between the level of oxygenation and T-stage or age and there was no significant difference in pO_2 between prostate cancer and benign prostate tissue.

The outcome of radical radiotherapy for prostate cancer is appreciably influenced by the presence of hypoxia. Movsas' group from the Fox Chase Cancer Center, USA, prospectively studied 57 patients with localized disease [126]. A prostate : muscle pO_2 ratio of less than 0.05 resulted in significantly worse biochemical relapse-free survival at 2 years (31% versus 92%, $p < 0.0001$). Although this study was reported after a median follow-up of only 19 months, the substantial difference in relapse between the two groups is notable. Oxygenation status may therefore be another underlying biological parameter beyond the classic prognostic factors (age, clinical stage, Gleason score and prostate specific antigen) that predicts for treatment failure in prostate cancer. A modeling study based on these clinical data has predicted an oxygen enhancement ratio for prostate cancer of 1.4 (95% confidence interval of 1.2 – 1.8), which is consistent with the in vitro OER measurements of human tumour cell lines under chronic hypoxia conditions [143]. As in many other malignancies, these evaluations suggest that hypoxia is likely to be a valid therapeutic target in prostate cancer.

1.4.5 The detection and measurement of tumour hypoxia

There are a wide range of different methods to measure tissue oxygenation that have been evaluated [144, 145]. An ideal technique would be non-invasive, technically simple, reproducible, able to evaluate the whole tumour mass and give a real-time measurement of tissue pO_2 for a tumour in any body location. No such instrument exists. Each method of measurement has its own limitations and the chosen technique needs to be considered in the context of the clinical or laboratory situation in which it is to be used.

Broadly, measurements of tumour oxygenation can be divided into invasive and non-invasive techniques. Invasive methods involve inserting an electrode into the tumour or sampling the mass with a biopsy or total excision. Non-invasive approaches utilize radiological imaging **(table 1.3)**:

Table 1.3 Examples of methods for measuring tumour hypoxia

In vitro Laboratory Methods	*In-vivo* Laboratory Methods	Invasive Clinical Methods	Non-Invasive Clinical Methods
Comet Assay	Needle pO_2 probes *Eppendorf* *Oxylite*	Extrinsic Immunohistochemistry *Pimonidazole* Intrinsic Immunohistochemistry *HIF 1α* *CA9* *GLUT1*	SPECT PET *Nitroimidazoles* *^{18}F-miso* *Cu-ATSM* *EF-5* *^{18}F- FAZA* MRI *BOLD* *DCE* *MRS* *Diffusion*

Extrinsic Immunohistochemical Markers of Hypoxia – The Nitroimidazoles

The nitroimidazoles are a group of nitro-aromatic molecules originally used as anti-protozoal agents. Their investigation grew out of the findings that nitroaromatic compounds were hypoxic cell radiosensitisers. Varghese *et al.* performed experiments using ^{14}C-labelled misonidazole on Chinese hamster ovary cells in vitro and KHT murine fibrosarcoma tumour cells in vivo [146]. The radioactivity associated with the acid-insoluble precipitate from cells incubated in nitrogen in vivo was 400% higher than that of cells incubated in air. When aqueous extracts of a KHT tumour grown on a C3H mouse after intraperitoneal injection with misonidazole were analysed, the reduction product was found in higher concentration in the tumour compared with normal tissue. These experiments proved that misonidazole formed reduction products under hypoxic conditions and that they were retained within hypoxic cells. It was also the first identification of hypoxia using an 2 nitroimidazole within an in vivo tumour.

The metabolism of 2-nitroimidazoles occurs in a series of one-electron reductions **(figure 1.3)**. A nitro-radical anion, produced by the first one-electron reduction step, avidly reacts with oxygen and is oxidised back to the parent molecule so that in well-oxygenated conditions there is effectively no substrate for the second step. In low oxygen concentrations, one-electron product is further reduced to the nitroso (2 e-), hydroxylamine (4 e-), and amine (6 e-) derivatives. Eventually, the imidazole ring fragments. The reactive portions of the molecule bind to a range of macromolecular components such as thiol groups. All atoms of the ring and side-chain of the 2-nitroimidazole are retained. The side-chain also binds to cellular macromolecules because of fragmentation of the amine. Although variability in the rate of binding of nitroimidazoles by different cell lines was seen by Chapman in his work on TF MISO, an analogue of misonidasole [147], the local cellular oxygen concentration is the most important determinant of binding rate [148].

In totally anoxic conditions, binding is proportional to the square-root of the concentration of misonidazole [149]. Small quantities of oxygen convert this to first-order kinetics by reducing the concentration of a reactive free radical and so reducing its ability to react with itself by second order kinetics [150]. The oxygen-dependence of 2-nitroimidazoles binding in cells is similar to their dependence of radiosensitivity. Hodgkiss *et al.* incubated Chinese Hamster cells in vitro with NITP, a theophylline bound 2-nitroimidazole, at a range of oxygen concentrations [151]. Using a fluorescent antibody and flow cytometrical quantitation, the hypoxic;oxic differential was 1,400 ppm, similar to the value of 3800ppm for half the radiosensitising effect described by Begg [152].

A histological assessment of hypoxia in tumours provides information on relationships between hypoxia and other microregional factors. It also allows exploration of the association between hypoxia and factors such as necrosis, vascularity, proliferation, differentiation, apoptosis, and oxygen regulated protein expression. Raleigh et al raised polyclonal antibodies in rabbits to the haemocyanin adduct of CCI-103F (a hexafluorinated 2-nitroimidazole). Florescence studies showed that the marker bound within spheroids and tumour sections in patterns similar to those seen in the autoradiographic studies [153]. Subsequent testing in spontaneous canine tumours clearly showed binding occurred 10-12 cell diameters away from tumour blood vessels,

Figure 1.3 The bioreductive metabolism of Pimonidazole

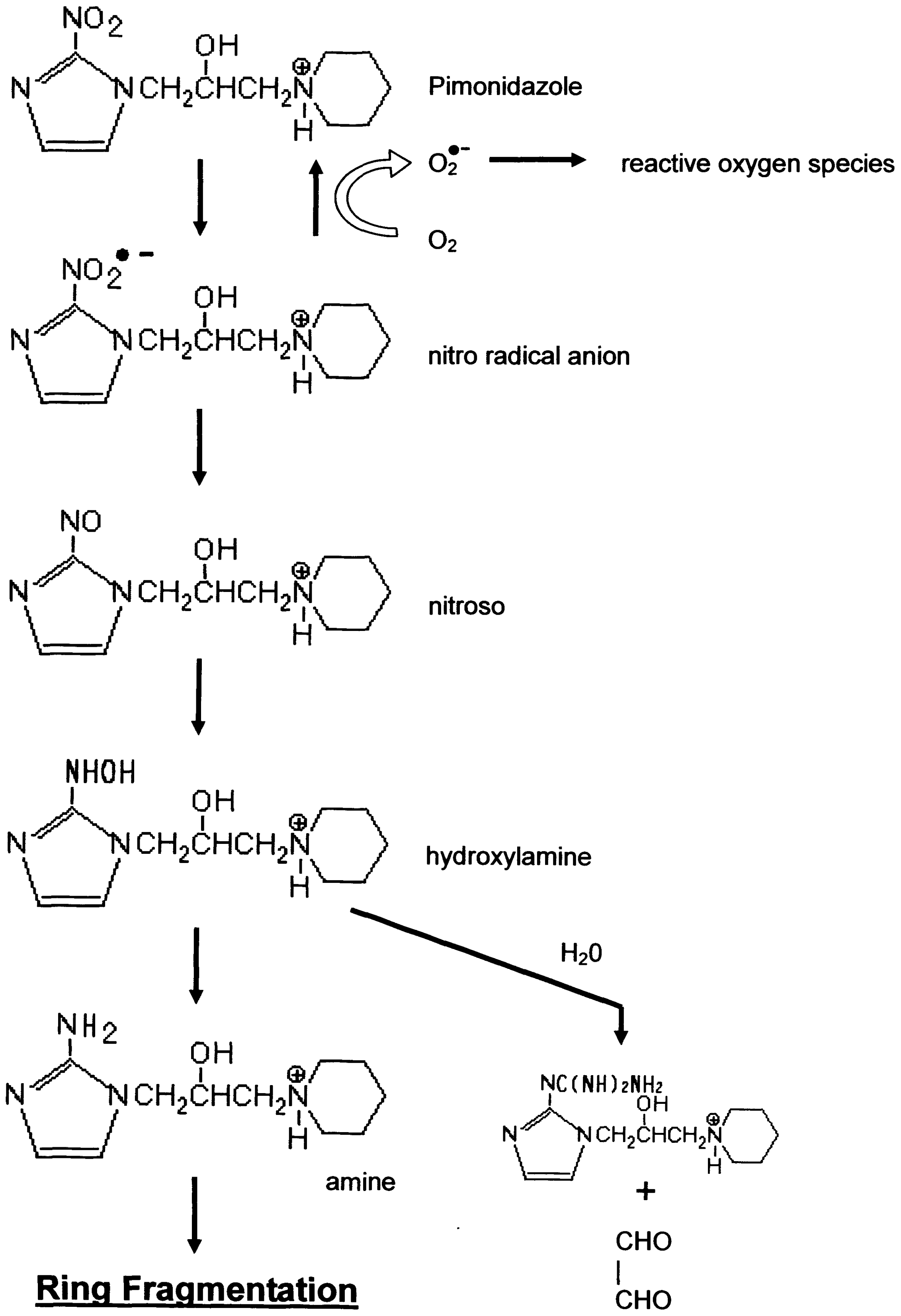

consistent with the where 'chronically' hypoxic cells would reside. The hypoxic fraction ranged from 4 to 13% according to an analysis of multiple tumour sections. Staining was seen adjacent to necrosis, although not exclusively and some binding occurred in cells close to blood vessels. Most staining was restricted to tumour cells although some staining of smooth muscle cells surrounding arterioles in some sections of normal tissue and tumour tissue was observed [154]. Further work from the same group confirmed immunohistochemistry was a feasible and straightforward method of assessing hypoxia in tumours including the development of an enzyme linked immunosorbent assay for the binding of CCI-103F [155].

In addition, the first investigation of the spatial relationship between hypoxia and proliferation was demonstrated in canine tumours using this method [156]. In this study, serial sections were stained for pre-administered CCI-103F to reveal hypoxic regions and proliferating cell nuclear antigen (PCNA) to localise proliferation. Characteristically, diffusion limited hypoxic staining away from vessels was evident, whereas proliferating cells were predominantly near blood vessels. The two cell populations showed a degree of geographical overlap. Whilst immunoglobulins could be raised to the fluorinated component of CCI-103F, it had not been clinically tested.

As a result attention turned to pimonidazole, the 2-nitroimidazole with an immunologically detectable piperidine side-chain. There was a wealth of pharmacokinetic and pharmacodynamic data supporting its safe use in humans from the radiosensitiser trials of the 1980s. It also had good chemical stability, water solubility and wide tissue distribution. Initial studies using pimonidazole showed the lifetime of hypoxic cells in canine tumours was of the order of days [157] and that the high binding of 2-nitroimidazoles in the liver did reflect normal tissue hypoxia and not native nitroreductases [158]. Pimonidazole has now been used in many experimental studies and clinical trials worldwide. At the pimonidazole dose of 0.5 g/m^2 used in hypoxia marking, pimonidazole causes neither central nervous system toxicity nor sensation (e.g., flushing). Central nervous system toxicity was of particular interest because this was the dose limiting at the higher, multiple doses used in radiosensitizer trials.

Protein adducts of reductively activated pimonidazole are effective immunogens for the production of both polyclonal and monoclonal antibodies. The antibodies have been used for immunoperoxidase analysis of formalin fixed, paraffin embedded sections and for immunofluorescence analysis of frozen fixed sections. Another attractive feature of pimonidazole is the fact that pimonidazole adducts in vivo are long-lived. This provides flexibility in the timing of biopsy taking which is an advantage in a clinical setting.

Pimonidazole binding assays provide hypoxia measurements with a high spatial resolution. Another strength of the technique is that dead cells do not generate a signal because they do not metabolize nitroimidazoles. Oxygen microelectrode measurements have been compared with the nitroimidazole binding assays in patients with squamous cell carcinomas [159]. Despite a trend that tumors with high pO_2 values measured with microelectrodes expressed less nitroimidazole binding, there was a lot of scatter in the data and no significant correlation was found between the two assays. Necrosis is suggested as being the major confounding factor. The direction of the bias is opposite for the two methods: microelectrode readings characterize necrosis as anoxic, whereas absence of nitroimidazole binding in necrotic areas would identify them as oxic. Evaluation of pimonidazole binding can be corrected for necrosis but the quantitative impact of necrosis on the result of microelectrode measurements is impossible to correct for in human tumors.

Hypoxic fraction estimated by pimonidazole binding agreed well with the hypoxic fraction measured using the comet assay in a number of animal and human tumors indicating that pimonidazole labeling can give a reliable estimate of radiobiologically relevant hypoxia [160]. The spatial relationship between tumor vasculature and pimonidazole binding was studied with a multiple staining and functional microscopic imaging technique in a human glioma xenograft model. With the perfusion marker Hoechst 33342 perfused and non-perfused vessels could be discriminated. The density of the perfused vessels was inversely related to the pimonidazole hypoxic fraction. At critical distances from perfused vessels, hypoxia occurred and the largest proportion of hypoxia was found at distances beyond 100 mm [161]. These data suggest that predominantly diffusion-limited hypoxia was detected.

Recently, it was demonstrated that there is a significant association between pimonidazole binding and loco-regional and disease-free survival in head and neck carcinomas. Of even greater interest is the observation that this association disappeared in a group of patients treated with ARCON, strongly suggesting that the nitroimidazole binding assay can provide a selection tool for hypoxia modifying treatments on an individual patient basis [162].

Pimonidazole is not the only nitroimidazole that can be detected by means of immunohistochemistry **(table 1.4)**. CCI-103F was the first and NITP was the second hypoxia marker used in this way. A disadvantage of these substances was the poor water solubility. In mice, a vehicle of DMSO and peanut oil was necessary for intraperitoneal administration, and these markers were never approved for clinical use. This led to the development of antibodies against more suitable hypoxia markers such as EF5 and pimonidazole. Unfortunately, attempts to raise antibodies against reduction products of misonidazole, the most widely used imaging agent, resulted in antibodies with relatively weak specificity that were unsuitable for general use.

Table 1.4 Nitroimidazoles as hypoxia markers

Marker name	Chemical name	Dose (species)	Minimum time to tumor excision	Approved for clinical use
Pimonidazole	(1-(2-nitro-1-imidazolyl)-3-*N*-piperidino-2-propanol)	60–80 mg/kg (mice) 0.5 g.m^{-2} (humans) 0.285 g.m^{-2} (dogs)	30–60 min (mice) >2 h (patients)	Yes (Europe, Canada and USA)
NITP (A2-nitroimidazole)	7-(4'-(2-nitroimidazol-1-yl)-butyl)-theophylline	156 mg kg^{-1} (mice)	1–2 h (mice)	No
CCI-103F	(1-(2-hydroxy-3-hexafluoroisopropoxy-propyl)-2-nitroimidazole)	60–80 mg.kg^{-1} (mice) 200 μM (rat) 40 mg.kg^{-1} (dog)	2 h (mice) 24 h (dogs)	No
EF5	[2-(2-nitro-1H-imidazol-1-yl)-*N*-(2,2,3,3,3-penta-fluoropropyl) acetamide]	100 μM (rat) 9–21 mg/kg (human)	3 h (mice) 24h (patients)	Yes (USA)

1.4.6 Carbogen Gas Breathing

1.4.6.1 Overview

Carbogen is a normobaric gas mixture of carbon dioxide and oxygen, which is usually administered at one of two concentrations (95% O_2 with 5% CO_2 or 98% O_2 with 2% CO_2). Carbogen has been demonstrated to improve the oxygenation of both experimental and human tumours. However, there is evidence to suggest that, at least in some tumours, enhanced blood flow may also contribute to its action. This gas mixture increases intravascular oxygen availability resulting in greater oxygen uptake by tumours. Carbogen also transiently opens non-functional blood vessels, likely to be a result of the CO_2 component of the gas mixture. This further increases oxygen delivery to regions of perfusion-limited hypoxia and also causes an increased leakage of molecules from the plasma to the extracellular space. Extracellular tumour pH has been shown to decline in response to carbogen gas breathing, in particular if the tumours are large and hypoxic [163].

The rationale for the use of a high oxygen-content gas to improve tumour oxygenation is that the resulting increase in arterial pO_2 will enhance the diffusion of oxygen into the tissue. The addition of 2 or 5% CO_2 was originally proposed to counteract any vasoconstriction induced by pure oxygen breathing. A study in a murine tumour model was performed to determine how the CO_2 content of the inspired gas influences radiosensitivity [164]. Gas mixtures containing 0, 1, 2.5 and 10% CO_2, balanced with oxygen, were compared with 5% CO_2 + 95% O_2. Measurements of tumour oxygenation and perfusion were also made during the breathing of each gas. The results showed that the level of radiosensitization achieved is dependent on both the CO_2 content of the inspired gas and the duration of gas breathing. No radiosensitization was evident following inhalation of 90% O_2 + 10% CO_2. All other gases elicited radiosensitization. However, that achieved with 100% O_2 disappeared at the extended pre-irradiation breathing time of 45 min. Changes in oxygenation, as measured by pO_2 electrodes, did indicate improved oxygenation status following the inhalation of the gases. However, the time course and extent of the changes did not mirror accurately the changes in radiosensitization. All the gases with a CO_2 content of 2.5% or greater induced a 10-20% reduction in microregional blood flow.

This study implies that the decreased radiosensitization seen at extended breathing times of 100% oxygen is unrelated to blood flow changes. The fact that radiosensitization is seen with extended breathing times of gases containing 2.5 & 5% CO_2, despite blood flow decreases, is indicative of other overriding physiological changes, perhaps related to oxygen utilization. The studies overall indicate that, at least in the tumour investigated, radiosensitization is maintained if the CO_2 content of the inspired gas is reduced from 5% to 2.5 or even 1%.

In humans, tolerance to carbogen can be a problem with patients feeling flushed and breathless during inhalation. These symptoms are considerably reduced if 2% CO_2 is used instead of 5% CO_2. A study comparing tumour oxygenation during inhalation of hyperoxic gas containing either 2% or 5% CO_2 has been performed [165]. Tumour pO_2 was measured in 16 patients using the Eppendorf pO_2 histograph. After breathing gas containing either 5% or 2% CO_2 an increase in median pO_2 was measured in every tumour, the frequency of low pO_2 values (less than or equal to10 mmHg) fell from 47% to 29% in the 5% group and from 55% to 17% in the 2% group. This confirms that breathing 2% CO_2 and 98% O_2 is well tolerated and effective in increasing tumour oxygenation.

1.4.6.2 Accelerated radiotherapy with Carbogen and Nicotinamide (ARCON)

Nicotinamide (niacinamide) is one of the two principal forms of the B-complex vitamin niacin. Nicotinamide, via its major metabolite NAD^{++} (nicotinamide adenine dinucleotide), is involved in a wide range of biological processes, including the production of energy, the synthesis of fatty acids, cholesterol and steroids, signal transduction and the maintenance of the integrity of the genome. It also causes vasodilation of cutaneous blood vessels.

Niacin deficiency has been found to inhibit DNA repair in cell culture models. NAD^{++} is the substrate for Poly(ADP-ribose)polymerase (PARP), an enzyme involved in DNA repair. Extensive damage to DNA results in the depletion of NAD^{++}, which can trigger cellular apoptosis. In addition, nicotinamide, via NAD^{++}, modulates the expression of the p53 tumour suppressor protein in human breast, skin and lung cells. These mechanisms may account, in part, for some of the the possible anti-cancer activity of nicotinamide.

In terms of hypoxia modification, nicotinamide appears to reduce impaired tumour blood flow and thus affects the proportion of acutely hypoxic cells. A major component of its activity is the improvement of tumour oxygenation resulting from a reduction in microregional ischaemia. Nicotinamide is known to reduce arterial blood pressure in rodents, suggesting a vascular component in its mechanism of action. A direct effect on supplying blood vessels probably contributes to the oxygenating action of nicotinamide in tumours. Athough the precise mechanism remains obscure, studies on murine tumours suggest that nicotinamide, at least at high doses, reduces the occurrence of transient decreases in microregional perfusion [166].

Both carbogen and nicotinamide have radiosensitizing properties. When used together in animal models they produce enhancement ratios of 1.9 with conventionally fractionated radiotherapy and 2.8 with accelerated radiation schedules [167, 168]. Over the past 15 years a number of early phase human studies have been conducted using ARCON in a variety of tumour sites [169-173]. All of these studies encountered significant nausea and vomiting due to the nicotinamide resulting in reduced patient compliance. The common conclusion is that a dose of 80mg/kg or higher is not feasible and future studies should proceed with a starting dose of 60mg/kg. As none of these studies were randomised, it was not possible to formally evaluate efficacy. However two studies had sufficient patient numbers and length of follow up to draw tentative conclusions in comparison with historical controls. A study in glioblastoma multiforme, ARCON seemed to have no apparent benefit and concluded with the suggestion that a phase III trial was not justified [174]. In contrast, a larger study of 215 patients with locally advanced head and neck cancer indicated very favourable rates of locoregional tumour control and overall survival [175]. The actuarial 3-year local control rates were 80% for larynx, 69% for hypopharynx, 88% for oropharynx, and 37% for oral cavity tumors. Regional control rates were 100% for N0, 93% for N1, and 74% for N2 disease.

Following promising early toxicity data, the ARCON schedule has also been tested in bladder cancer [176]. A multi-centre phase III trial (BCON) comparing 55Gy in 20 fractions of external beam with or without carbogen and nicotinamide has recently completed accrual. Results are expected by 2009.

References

1 Office for National Statistics, Registrations of cancer diagnosed in 1993-1996, England and Wales. *Health Statistics Quarterly*. 1999;4:59-70.

2 Office for National Statistics, Cancer Statistics Registrations. Registrations of cancer diagnosed in 2002, England. Series MB, no.33. *National Statistics: London*. 2005.

3 ISD Online. Information and Statistics Division, NHS Scotland. 2005.

4 Welsh Cancer Intelligence and Surveillance Unit. Cancer Incidence in Wales 1992-2002. 2005.

5 Hsing AW, Tsao L, Devesa SS. International trends and patterns of prostate cancer incidence and mortality. *Int J Cancer*. 2000;85:60-67.

6 Potosky AL, Kessler L, Gridley G, Brown CC, Horm JW. Rise in prostatic cancer incidence associated with increased use of transurethral resection. *J Natl Cancer Inst*. 1990;82:1624-1628.

7 Potosky AL, Miller BA, Albertsen PC, Kramer BS. The role of increasing detection in the rising incidence of prostate cancer. *Jama*. 1995;273:548-552.

8 Threlfall TJ, English DR, Rouse IL. Prostate cancer in Western Australia: trends in incidence and mortality from 1985 to 1996. *Med J Aust*. 1998;169:21-24.

9 Adolfsson J, Carstensen J. Natural course of clinically localized prostate adenocarcinoma in men less than 70 years old. *J Urol*. 1991;146:96-98.

10 Adolfsson J, Steineck G, Hedlund PO. Deferred treatment of clinically localized low-grade prostate cancer: actual 10-year and projected 15-year follow-up of the Karolinska series. *Urology*. 1997;50:722-726.

11 Adolfsson J, Steineck G, Hedlund PO. Deferred treatment of locally advanced nonmetastatic prostate cancer: a long-term followup. *J Urol*. 1999;161:505-508.

12 Byar DP, Corle DK. VACURG randomised trial of radical prostatectomy for stages I and II prostatic cancer. Veterans Administration Cooperative Urological Research Group. *Urology*. 1981;17:7-11.

13 Chodak GW, Thisted RA, Gerber GS, *et al*. Results of conservative management of clinically localized prostate cancer. *N Engl J Med*. 1994;330:242-248.

14 Egawa S, Go M, Kuwao S, Shoji K, Uchida T, Koshiba K. Long-term impact of conservative management on localized prostate cancer. A twenty-year experience in Japan. *Urology.* 1993;42:520-526; discussion 526-527.

15 George NJ. Natural history of localised prostatic cancer managed by conservative therapy alone. *Lancet.* 1988;1:494-497.

16 Johansson JE, Andren O, Andersson SO, *et al.* Natural history of early, localized prostate cancer. *Jama.* 2004;291:2713-2719.

17 Rana A, Chisholm GD, Khan M, Rashwan HM, Elton RA. Conservative management with symptomatic treatment and delayed hormonal manipulation is justified in men with locally advanced carcinoma of the prostate. *Br J Urol.* 1994;74:637-641.

18 Warner J, Whitmore WF, Jr. Expectant management of clinically localized prostatic cancer. *J Urol.* 1994;152:1761-1765.

19 Consensus statement: guidelines for PSA following radiation therapy. American Society for Therapeutic Radiology and Oncology Consensus Panel. *Int J Radiat Oncol Biol Phys.* 1997;37:1035-1041.

20 Thames H, Kuban D, Levy L, *et al.* Comparison of alternative biochemical failure definitions based on clinical outcome in 4839 prostate cancer patients treated by external beam radiotherapy between 1986 and 1995. *Int J Radiat Oncol Biol Phys.* 2003;57:929-943.

21 Roach M, 3rd, Hanks G, Thames H, Jr., *et al.* Defining biochemical failure following radiotherapy with or without hormonal therapy in men with clinically localized prostate cancer: recommendations of the RTOG-ASTRO Phoenix Consensus Conference. *Int J Radiat Oncol Biol Phys.* 2006;65:965-974.

22 Carter HB, Ferrucci L, Kettermann A, *et al.* Detection of life-threatening prostate cancer with prostate-specific antigen velocity during a window of curability. *J Natl Cancer Inst.* 2006;98:1521-1527.

23 Partin AW, Kattan MW, Subong EN, *et al.* Combination of prostate-specific antigen, clinical stage, and Gleason score to predict pathological stage of localized prostate cancer. A multi-institutional update. *Jama.* 1997;277:1445-1451.

24 Futterer JJ, Heijmink SW, Scheenen TW, *et al.* Prostate Cancer Localization with Dynamic Contrast-enhanced MR Imaging and Proton MR Spectroscopic Imaging. *Radiology.* 2006.

25 Hara N, Okuizumi M, Koike H, Kawaguchi M, Bilim V. Dynamic contrast-enhanced magnetic resonance imaging (DCE-MRI) is a useful modality for the precise detection and staging of early prostate cancer. *Prostate.* 2005;62:140-147.

26 Kim JK, Hong SS, Choi YJ, *et al.* Wash-in rate on the basis of dynamic contrast-enhanced MRI: usefulness for prostate cancer detection and localization. *J Magn Reson Imaging.* 2005;22:639-646.

27 Muramoto S, Uematsu H, Kimura H, *et al.* Differentiation of prostate cancer from benign prostate hypertrophy using dual-echo dynamic contrast MR imaging. *Eur J Radiol.* 2002;44:52-58.

28 Roach M, 3rd, Chen A, Song J, Diaz A, Presti J, Jr., Carroll P. Pretreatment prostate-specific antigen and Gleason score predict the risk of extracapsular extension and the risk of failure following radiotherapy in patients with clinically localized prostate cancer. *Semin Urol Oncol.* 2000;18:108-114.

29 Folkman J. Tumor angiogenesis: therapeutic implications. *N Engl J Med.* 1971;285:1182-1186.

30 Liao Z, Boileau TW, Erdman JW, Jr., Clinton SK. Interrelationships among angiogenesis, proliferation, and apoptosis in the tumor microenvironment during N-methyl-N-nitrosourea androgen-induced prostate carcinogenesis in rats. *Carcinogenesis.* 2002;23:1701-1711.

31 Haggstrom S, Lissbrant IF, Bergh A, Damber JE. Testosterone induces vascular endothelial growth factor synthesis in the ventral prostate in castrated rats. *J Urol.* 1999;161:1620-1625.

32 Jackson MW, Bentel JM, Tilley WD. Vascular endothelial growth factor (VEGF) expression in prostate cancer and benign prostatic hyperplasia. *J Urol.* 1997;157:2323-2328.

33 Brown LF, Berse B, Jackman RW, *et al.* Expression of vascular permeability factor (vascular endothelial growth factor) and its receptors in breast cancer. *Hum Pathol.* 1995;26:86-91.

34 Hatva E, Kaipainen A, Mentula P, *et al.* Expression of endothelial cell-specific receptor tyrosine kinases and growth factors in human brain tumors. *Am J Pathol.* 1995;146:368-378.

35 Plate KH, Breier G, Millauer B, Ullrich A, Risau W. Up-regulation of vascular endothelial growth factor and its cognate receptors in a rat glioma model of tumor angiogenesis. *Cancer Res.* 1993;53:5822-5827.

36 Warren RS, Yuan H, Matli MR, Gillett NA, Ferrara N. Regulation by vascular endothelial growth factor of human colon cancer tumorigenesis in a mouse model of experimental liver metastasis. *J Clin Invest.* 1995;95:1789-1797.

37 Watnick RS, Cheng YN, Rangarajan A, Ince TA, Weinberg RA. Ras modulates Myc activity to repress thrombospondin-1 expression and increase tumor angiogenesis. *Cancer Cell.* 2003;3:219-231.

38 Forsythe JA, Jiang BH, Iyer NV, *et al.* Activation of vascular endothelial growth factor gene transcription by hypoxia-inducible factor 1. *Mol Cell Biol.* 1996;16:4604-4613.

39 Hlatky L, Tsionou C, Hahnfeldt P, Coleman CN. Mammary fibroblasts may influence breast tumor angiogenesis via hypoxia-induced vascular endothelial growth factor up-regulation and protein expression. *Cancer Res.* 1994;54:6083-6086.

40 Kuwabara K, Ogawa S, Matsumoto M, *et al.* Hypoxia-mediated induction of acidic/basic fibroblast growth factor and platelet-derived growth factor in mononuclear phagocytes stimulates growth of hypoxic endothelial cells. *Proc Natl Acad Sci U S A.* 1995;92:4606-4610.

41 Mandriota SJ, Pyke C, Di Sanza C, Quinodoz P, Pittet B, Pepper MS. Hypoxia-inducible angiopoietin-2 expression is mimicked by iodonium compounds and occurs in the rat brain and skin in response to systemic hypoxia and tissue ischemia. *Am J Pathol.* 2000;156:2077-2089.

42 Maxwell PH, Dachs GU, Gleadle JM, *et al.* Hypoxia-inducible factor-1 modulates gene expression in solid tumors and influences both angiogenesis and tumor growth. *Proc Natl Acad Sci U S A.* 1997;94:8104-8109.

43 Melillo G, Musso T, Sica A, Taylor LS, Cox GW, Varesio L. A hypoxia-responsive element mediates a novel pathway of activation of the inducible nitric oxide synthase promoter. *J Exp Med.* 1995;182:1683-1693.

44 Shweiki D, Itin A, Soffer D, Keshet E. Vascular endothelial growth factor induced by hypoxia may mediate hypoxia-initiated angiogenesis. *Nature.* 1992;359:843-845.

45 Bates DO, Curry FE. Vascular endothelial growth factor increases hydraulic conductivity of isolated perfused microvessels. *Am J Physiol.* 1996;271:H2520-2528.

46 Maisonpierre PC, Suri C, Jones PF, *et al.* Angiopoietin-2, a natural antagonist for Tie2 that disrupts in vivo angiogenesis. *Science.* 1997;277:55-60.

47 Senger DR, Perruzzi CA, Feder J, Dvorak HF. A highly conserved vascular permeability factor secreted by a variety of human and rodent tumor cell lines. *Cancer Res.* 1986;46:5629-5632.

48 Yuan F, Chen Y, Dellian M, Safabakhsh N, Ferrara N, Jain RK. Time-dependent vascular regression and permeability changes in established human tumor xenografts induced by an anti-vascular endothelial growth factor/vascular permeability factor antibody. *Proc Natl Acad Sci U S A.* 1996;93:14765-14770.

49 Jain RK. Molecular regulation of vessel maturation. *Nat Med.* 2003;9:685-693.

50 Morikawa S, Baluk P, Kaidoh T, Haskell A, Jain RK, McDonald DM. Abnormalities in pericytes on blood vessels and endothelial sprouts in tumors. *Am J Pathol.* 2002;160:985-1000.

51 Chang YS, di Tomaso E, McDonald DM, Jones R, Jain RK, Munn LL. Mosaic blood vessels in tumors: frequency of cancer cells in contact with flowing blood. *Proc Natl Acad Sci U S A.* 2000;97:14608-14613.

52 Hammersen F, Endrich B, Messmer K. The fine structure of tumor blood vessels. I. Participation of non-endothelial cells in tumor angiogenesis. *Int J Microcirc Clin Exp.* 1985;4:31-43.

53 Stefanou D, Batistatou A, Kamina S, Arkoumani E, Papachristou DJ, Agnantis NJ. Expression of vascular endothelial growth factor (VEGF) and association with microvessel density in benign prostatic hyperplasia and prostate cancer. *In Vivo.* 2004;18:155-160.

54 Sinha AA, Quast BJ, Reddy PK, *et al.* Microvessel density as a molecular marker for identifying high-grade prostatic intraepithelial neoplasia precursors to prostate cancer. *Exp Mol Pathol.* 2004;77:153-159.

55 Bigler SA, Deering RE, Brawer MK. Comparison of microscopic vascularity in benign and malignant prostate tissue. *Hum Pathol.* 1993;24:220-226.

56 Bettencourt MC, Bauer JJ, Sesterhenn IA, Connelly RR, Moul JW. CD34 immunohistochemical assessment of angiogenesis as a prognostic marker for prostate cancer recurrence after radical prostatectomy. *J Urol.* 1998;160:459-465.

57 Borre M, Offersen BV, Nerstrom B, Overgaard J. Microvessel density predicts survival in prostate cancer patients subjected to watchful waiting. *Br J Cancer.* 1998;78:940-944.

58 Hall MC, Troncoso P, Pollack A, *et al.* Significance of tumor angiogenesis in clinically localized prostate carcinoma treated with external beam radiotherapy. *Urology.* 1994;44:869-875.

59 Rubin MA, Buyyounouski M, Bagiella E, *et al.* Microvessel density in prostate cancer: lack of correlation with tumor grade, pathologic stage, and clinical outcome. *Urology.* 1999;53:542-547.

60 Trojan L, Thomas D, Friedrich D, *et al.* Expression of different vascular endothelial markers in prostate cancer and BPH tissue: an immunohistochemical and clinical evaluation. *Anticancer Res.* 2004;24:1651-1656.

61 Vermeulen PB, Gasparini G, Fox SB, *et al.* Second international consensus on the methodology and criteria of evaluation of angiogenesis quantification in solid human tumours. *Eur J Cancer.* 2002;38:1564-1579.

62 Chalkley HW. Method for the quantitative morphologic analysis of tissues. *J Natl Cancer Inst.* 1943;4:47-53.

63 Burchardt T, Burchardt M, Karden J, *et al.* Reduction of endothelial and smooth muscle density in the corpora cavernosa of the streptozotocin induced diabetic rat. *J Urol.* 2000;164:1807-1811.

64 Jondet M, Letellier B, Verdys MT. Endometrial vascularization in levonorgestrel intrauterine device users; computerized microvessel measurement study. *Contraception.* 2005;71:60-64.

65 Chantrain CF, DeClerck YA, Groshen S, McNamara G. Computerized quantification of tissue vascularization using high-resolution slide scanning of whole tumor sections. *J Histochem Cytochem.* 2003;51:151-158.

66 Vertemati M, Minola E, Goffredi M, Sabatella G, Gambacorta M, Vizzotto L. Computerized morphometry of the cirrhotic liver: comparative analysis in primary biliary cirrhosis, alcoholic cirrhosis, and posthepatitic cirrhosis. *Microsc Res Tech.* 2004;65:113-121.

67 Zhang SC, Hironaka S, Ohtsu A, *et al.* Computer-assisted analysis of biopsy specimen microvessels predicts the outcome of esophageal cancers treated with chemoradiotherapy. *Clin Cancer Res.* 2006;12:1735-1742.

68 Joseph IB, Nelson JB, Denmeade SR, Isaacs JT. Androgens regulate vascular endothelial growth factor content in normal and malignant prostatic tissue. *Clin Cancer Res.* 1997;3:2507-2511.

69 Jain RK, Safabakhsh N, Sckell A, *et al.* Endothelial cell death, angiogenesis, and microvascular function after castration in an androgen-dependent tumor: role of vascular endothelial growth factor. *Proc Natl Acad Sci U S A.* 1998;95:10820-10825.

70 Joseph IB, Isaacs JT. Potentiation of the antiangiogenic ability of linomide by androgen ablation involves down-regulation of vascular endothelial growth factor in human androgen-responsive prostatic cancers. *Cancer Res.* 1997;57:1054-1057.

71 Lekas E, Johansson M, Widmark A, Bergh A, Damber JE. Decrement of blood flow precedes the involution of the ventral prostate in the rat after castration. *Urol Res.* 1997;25:309-314.

72 Shabsigh A, Chang DT, Heitjan DF, *et al.* Rapid reduction in blood flow to the rat ventral prostate gland after castration: preliminary evidence that androgens influence prostate size by regulating blood flow to the prostate gland and prostatic endothelial cell survival. *Prostate.* 1998;36:201-206.

73 Hayek OR, Shabsigh A, Kaplan SA, *et al.* Castration induces acute vasoconstriction of blood vessels in the rat prostate concomitant with a reduction of prostatic nitric oxide synthase activity. *J Urol.* 1999;162:1527-1531.

74 Matsushima H, Goto T, Hosaka Y, Kitamura T, Kawabe K. Correlation between proliferation, apoptosis, and angiogenesis in prostate carcinoma and their relation to androgen ablation. *Cancer.* 1999;85:1822-1827.

75 Huggins C, Hodges C. Studies on prostate cancer 1: the effect of castration, of oestrogen and of androgen injection on serum phosphatases in metastatic carcinoma of the prostate. *Cancer Research.* 1941;1:293-297.

76 Dalkin BL, Ahmann FR, Nagle R, Johnson CS. Randomized study of neoadjuvant testicular androgen ablation therapy before radical prostatectomy in men with clinically localized prostate cancer. *J Urol.* 1996;155:1357-1360.

77 Gleave ME, Goldenberg SL, Chin JL, *et al.* Randomized comparative study of 3 versus 8-month neoadjuvant hormonal therapy before radical prostatectomy: biochemical and pathological effects. *J Urol.* 2001;166:500-506; discussion 506-507.

78 Hugosson J, Abrahamsson PA, Ahlgren G, *et al.* The risk of malignancy in the surgical margin at radical prostatectomy reduced almost three-fold in patients given neo-adjuvant hormone treatment. *Eur Urol.* 1996;29:413-419.

79 Klotz LH, Goldenberg SL, Jewett MA, *et al.* Long-term followup of a randomized trial of 0 versus 3 months of neoadjuvant androgen ablation before radical prostatectomy. *J Urol.* 2003;170:791-794.

80 Labrie F, Cusan L, Gomez JL, *et al.* Neoadjuvant hormonal therapy: the Canadian experience. *Urology.* 1997;49:56-64.

81 Prezioso D, Lotti T, Polito M, Montironi R. Neoadjuvant hormone treatment with leuprolide acetate depot 3.75 mg and cyproterone acetate, before radical prostatectomy: a randomized study. *Urol Int.* 2004;72:189-195.

82 Schulman CC, Debruyne FM, Forster G, Selvaggi FP, Zlotta AR, Witjes WP. 4-Year follow-up results of a European prospective randomized study on neoadjuvant hormonal therapy prior to radical prostatectomy in T2-3N0M0 prostate cancer. European Study Group on Neoadjuvant Treatment of Prostate Cancer. *Eur Urol.* 2000;38:706-713.

83 Selli C, Montironi R, Bono A, *et al.* Effects of complete androgen blockade for 12 and 24 weeks on the pathological stage and resection margin status of prostate cancer. *J Clin Pathol.* 2002;55:508-513.

84 Soloway MS, Pareek K, Sharifi R, *et al.* Neoadjuvant androgen ablation before radical prostatectomy in cT2bNxMo prostate cancer: 5-year results. *J Urol.* 2002;167:112-116.

85 van der Kwast TH, Tetu B, Candas B, Gomez JL, Cusan L, Labrie F. Prolonged neoadjuvant combined androgen blockade leads to a further reduction of prostatic tumor volume: three versus six months of endocrine therapy. *Urology.* 1999;53:523-529.

86 McLeod DG, Iversen P, See WA, Morris T, Armstrong J, Wirth MP. Bicalutamide 150 mg plus standard care vs standard care alone for early prostate cancer. *BJU Int.* 2006;97:247-254.

87 Messing EM, Manola J, Sarosdy M, Wilding G, Crawford ED, Trump D. Immediate hormonal therapy compared with observation after radical prostatectomy and pelvic lymphadenectomy in men with node-positive prostate cancer. *N Engl J Med.* 1999;341:1781-1788.

88 Wirth MP, Weissbach L, Marx FJ, *et al.* Prospective randomized trial comparing flutamide as adjuvant treatment versus observation after radical prostatectomy for locally advanced, lymph node-negative prostate cancer. *Eur Urol.* 2004;45:267-270; discussion 270.

89 Crook J, Ludgate C, Malone S, *et al.* Report of a multicenter Canadian phase III randomized trial of 3 months vs. 8 months neoadjuvant androgen deprivation before standard-dose radiotherapy for clinically localized prostate cancer. *Int J Radiat Oncol Biol Phys.* 2004;60:15-23.

90 Denham JW, Steigler A, Lamb DS, *et al.* Short-term androgen deprivation and radiotherapy for locally advanced prostate cancer: results from the Trans-Tasman Radiation Oncology Group 96.01 randomised controlled trial. *Lancet Oncol.* 2005;6:841-850.

91 Laverdiere J, Nabid A, De Bedoya LD, *et al.* The efficacy and sequencing of a short course of androgen suppression on freedom from biochemical failure when administered with radiation therapy for T2-T3 prostate cancer. *J Urol.* 2004;171:1137-1140.

92 Pilepich MV, Winter K, John MJ, *et al.* Phase III radiation therapy oncology group (RTOG) trial 86-10 of androgen deprivation adjuvant to definitive radiotherapy in locally advanced carcinoma of the prostate. *Int J Radiat Oncol Biol Phys.* 2001;50:1243-1252.

93 Kumar S, Shelley M, Harrison C, Coles B, Wilt TJ, Mason MD. Neo-adjuvant and adjuvant hormone therapy for localised and locally advanced prostate cancer. *Cochrane Database Syst Rev.* 2006:CD006019.

94 Bolla M, Collette L, Blank L, *et al.* Long-term results with immediate androgen suppression and external irradiation in patients with locally advanced prostate cancer (an EORTC study): a phase III randomised trial. *Lancet.* 2002;360:103-106.

95 Pilepich MV, Winter K, Lawton CA, *et al.* Androgen suppression adjuvant to definitive radiotherapy in prostate carcinoma--long-term results of phase III RTOG 85-31. *Int J Radiat Oncol Biol Phys.* 2005;61:1285-1290.

96 Zagars GK, Johnson DE, von Eschenbach AC, Hussey DH. Adjuvant estrogen following radiation therapy for stage C adenocarcinoma of the prostate: long-term results of a prospective randomized study. *Int J Radiat Oncol Biol Phys.* 1988;14:1085-1091.
97 Hanks GE, Pajak TF, Porter A, *et al.* Phase III trial of long-term adjuvant androgen deprivation after neoadjuvant hormonal cytoreduction and radiotherapy in locally advanced carcinoma of the prostate: the Radiation Therapy Oncology Group Protocol 92-02. *J Clin Oncol.* 2003;21:3972-3978.
98 Merrick GS, Butler WM, Wallner KE, Galbreath RW, Allen ZA, Adamovich E. Androgen-deprivation therapy does not impact cause-specific or overall survival after permanent prostate brachytherapy. *Int J Radiat Oncol Biol Phys.* 2006;65:669-677.
99 Beyer DC, McKeough T, Thomas T. Impact of short course hormonal therapy on overall and cancer specific survival after permanent prostate brachytherapy. *Int J Radiat Oncol Biol Phys.* 2005;61:1299-1305.
100 Zietman AL, Prince EA, Nakfoor BM, Park JJ. Androgen deprivation and radiation therapy: sequencing studies using the Shionogi in vivo tumor system. *Int J Radiat Oncol Biol Phys.* 1997;38:1067-1070.
101 Nakfoor B, Prince E, Shipley W, Zietman A. A randomised trial comparing local tumour control following irradiation alone versus combined androgen withdrawal and irradiation in an androgen sensitive prostate cancer xenograft (Abstr. 97). *Int J Radiat Oncol Biol Phys.* 1995;32(Suppl.1):189.
102 English HF, Kyprianou N, Isaacs JT. Relationship between DNA fragmentation and apoptosis in the programmed cell death in the rat prostate following castration. *Prostate.* 1989;15:233-250.
103 Westin P, Bergh A, Damber JE. Castration rapidly results in a major reduction in epithelial cell numbers in the rat prostate, but not in the highly differentiated Dunning R3327 prostatic adenocarcinoma. *Prostate.* 1993;22:65-74.
104 Westin P, Stattin P, Damber JE, Bergh A. Castration therapy rapidly induces apoptosis in a minority and decreases cell proliferation in a majority of human prostatic tumors. *Am J Pathol.* 1995;146:1368-1375.
105 Pollack A, Joon DL, Wu CS, *et al.* Quiescence in R3327-G rat prostate tumors after androgen ablation. *Cancer Res.* 1997;57:2493-2500.
106 Oomens EH, van Steenbrugge GJ, van der Kwast TH, Schroder FH. Application of the monoclonal antibody Ki-67 on prostate biopsies to assess the fraction of human prostatic carcinoma. *J Urol.* 1991;145:81-85.
107 Denekamp J. Cell kinetics and radiation biology. *Int J Radiat Biol Relat Stud Phys Chem Med.* 1986;49:357-380.
108 Joon DL, Hasegawa M, Sikes C, *et al.* Supraadditive apoptotic response of R3327-G rat prostate tumors to androgen ablation and radiation. *Int J Radiat Oncol Biol Phys.* 1997;38:1071-1077.
109 Garzotto M, Su S, Fair W, Heston W. Irradiation-induced apoptosis of human prostate cancer requires cell division: Rationale against the use of androgen deprivation with radiation therapy for prostate cancer. *Mol Urol.* 1997;1:227 - 230.
110 Pollack A, Salem N, Ashoori F, *et al.* Lack of prostate cancer radiosensitization by androgen deprivation. *Int J Radiat Oncol Biol Phys.* 2001;51:1002-1007.
111 Parker C, Milosevic M, Toi A, *et al.* Polarographic electrode study of tumor oxygenation in clinically localized prostate cancer. *Int J Radiat Oncol Biol Phys.* 2004;58:750-757.
112 Padhani AR, MacVicar AD, Gapinski CJ, *et al.* Effects of androgen deprivation on prostatic morphology and vascular permeability evaluated with MR imaging. *Radiology.* 2001;218:365-374.
113 Schwartz G. Desensibilisierung gegen Rontgen- und Radiumstrahlen. *Munchener Medizinische Wochenschrift.* 1909;24:1-2.
114 Mottram J. *Brit J Rad.* 1935;viii:32.
115 Evans T, Goodrich J, Slaughter J. *Radiology.* 1942;xxxvii:201.
116 Lacassagne A. *Compt Rend Acad Sci.* 1942;215:231.
117 Hollcraft J, Lorenz E, Matthews M. *JNCI.* 1952;xii:751.
118 Gray LH, Conger AD, Ebert M, Hornsey S, Scott OC. The concentration of oxygen dissolved in tissues at the time of irradiation as a factor in radiotherapy. *Br J Radiol.* 1953;26:638-648.
119 Tomlinson R, Gray L. The histological structure of some human lung cancers and the possible implications for radiotherapy. *Brit J Cancer.* 1955;ix:539-549.
120 Powers W, Tolmach L. Demonstration of an anoxic component in a mouse tumour cell population by an in vivo assay of survival following irradiation. *Radiology.* 1964;83:328-336.

121 Rockwell S, Moulder J. Hypoxic fractions of human tumors xenografted into mice: a review. *Int J Radiat Oncol Biol Phys.* 1990;19:197-202.
122 Brizel DM, Dodge RK, Clough RW, Dewhirst MW. Oxygenation of head and neck cancer: changes during radiotherapy and impact on treatment outcome. *Radiother Oncol.* 1999;53:113-117.
123 Fyles AW, Milosevic M, Wong R*, et al.* Oxygenation predicts radiation response and survival in patients with cervix cancer. *Radiother Oncol.* 1998;48:149-156.
124 Nordsmark M, Overgaard M, Overgaard J. Pretreatment oxygenation predicts radiation response in advanced squamous cell carcinoma of the head and neck. *Radiother Oncol.* 1996;41:31-39.
125 Hoskin PJ, Sibtain A, Daley FM, Wilson GD. GLUT1 and CAIX as intrinsic markers of hypoxia in bladder cancer: relationship with vascularity and proliferation as predictors of outcome of ARCON. *Br J Cancer.* 2003;89:1290-1297.
126 Movsas B, Chapman JD, Hanlon AL*, et al.* Hypoxic prostate/muscle pO2 ratio predicts for biochemical failure in patients with prostate cancer: preliminary findings. *Urology.* 2002;60:634-639.
127 Nordsmark M, Hoyer M, Keller J, Nielsen OS, Jensen OM, Overgaard J. The relationship between tumor oxygenation and cell proliferation in human soft tissue sarcomas. *Int J Radiat Oncol Biol Phys.* 1996;35:701-708.
128 Chaplin D, Durand R, Olive P. Acute hypoxia in tumours: implications for modifiers of radiation effects. *Int J Radiat Biol Phys.* 1986;12:1279-1282.
129 Hill SA, Pigott KH, Saunders MI*, et al.* Microregional blood flow in murine and human tumours assessed using laser Doppler microprobes. *Br J Cancer Suppl.* 1996;27:S260-263.
130 Ravi R, Mookerjee B, Bhujwalla ZM*, et al.* Regulation of tumor angiogenesis by p53-induced degradation of hypoxia-inducible factor 1alpha. *Genes Dev.* 2000;14:34-44.
131 Talks KL, Turley H, Gatter KC*, et al.* The expression and distribution of the hypoxia-inducible factors HIF-1alpha and HIF-2alpha in normal human tissues, cancers, and tumor-associated macrophages. *Am J Pathol.* 2000;157:411-421.
132 Giatromanolaki A, Koukourakis MI, Sivridis E*, et al.* Relation of hypoxia inducible factor 1 alpha and 2 alpha in operable non-small cell lung cancer to angiogenic/molecular profile of tumours and survival. *Br J Cancer.* 2001;85:881-890.
133 Zagzag D, Zhong H, Scalzitti JM, Laughner E, Simons JW, Semenza GL. Expression of hypoxia-inducible factor 1alpha in brain tumors: association with angiogenesis, invasion, and progression. *Cancer.* 2000;88:2606-2618.
134 Aebersold DM, Burri P, Beer KT*, et al.* Expression of hypoxia-inducible factor-1alpha: a novel predictive and prognostic parameter in the radiotherapy of oropharyngeal cancer. *Cancer Res.* 2001;61:2911-2916.
135 Birner P, Schindl M, Obermair A, Breitenecker G, Oberhuber G. Expression of hypoxia-inducible factor 1alpha in epithelial ovarian tumors: its impact on prognosis and on response to chemotherapy. *Clin Cancer Res.* 2001;7:1661-1668.
136 Birner P, Gatterbauer B, Oberhuber G*, et al.* Expression of hypoxia-inducible factor-1 alpha in oligodendrogliomas: its impact on prognosis and on neoangiogenesis. *Cancer.* 2001;92:165-171.
137 Airley R, Loncaster J, Davidson S*, et al.* Glucose transporter glut-1 expression correlates with tumor hypoxia and predicts metastasis-free survival in advanced carcinoma of the cervix. *Clin Cancer Res.* 2001;7:928-934.
138 Bachtiary B, Schindl M, Potter R*, et al.* Overexpression of hypoxia-inducible factor 1alpha indicates diminished response to radiotherapy and unfavorable prognosis in patients receiving radical radiotherapy for cervical cancer. *Clin Cancer Res.* 2003;9:2234-2240.
139 Bos R, van der Groep P, Greijer AE*, et al.* Levels of hypoxia-inducible factor-1alpha independently predict prognosis in patients with lymph node negative breast carcinoma. *Cancer.* 2003;97:1573-1581.
140 Giatromanolaki A, Koukourakis MI, Sivridis E*, et al.* Expression of hypoxia-inducible carbonic anhydrase-9 relates to angiogenic pathways and independently to poor outcome in non-small cell lung cancer. *Cancer Res.* 2001;61:7992-7998.
141 Movsas B, Chapman JD, Horwitz EM*, et al.* Hypoxic regions exist in human prostate carcinoma. *Urology.* 1999;53:11-18.
142 Movsas B, Chapman JD, Greenberg RE*, et al.* Increasing levels of hypoxia in prostate carcinoma correlate significantly with increasing clinical stage and patient age: an Eppendorf pO(2) study. *Cancer.* 2000;89:2018-2024.

143 Wang JZ, Li XA, Mayr NA. Dose escalation to combat hypoxia in prostate cancer: a radiobiological study on clinical data. *Br J Radiol.* 2006;79:905-911.

144 Raleigh JA, Dewhirst MW, Thrall DE. Measuring Tumor Hypoxia. *Semin Radiat Oncol.* 1996;6:37-45.

145 Tatum JL, Kelloff GJ, Gillies RJ, *et al.* Hypoxia: importance in tumor biology, noninvasive measurement by imaging, and value of its measurement in the management of cancer therapy. *Int J Radiat Biol.* 2006;82:699-757.

146 Varghese AJ, Gulyas S, Mohindra JK. Hypoxia-dependent reduction of 1-(2-nitro-1-imidazolyl)-3-methoxy-2-propanol by Chinese hamster ovary cells and KHT tumor cells in vitro and in vivo. *Cancer Res.* 1976;36:3761-3765.

147 Chapman JD, Lee J, Meeker BE. Keynote address: cellular reduction of nitroimidazole drugs: potential for selective chemotherapy and diagnosis of hypoxic cells. *Int J Radiat Oncol Biol Phys.* 1989;16:911-917.

148 Chapman JD. Measurement of tumor hypoxia by invasive and non-invasive procedures: a review of recent clinical studies. *Radiother Oncol.* 1991;20 Suppl 1:13-19.

149 Chapman JD, Baer K, Lee J. Characteristics of the metabolism-induced binding of misonidazole to hypoxic mammalian cells. *Cancer Res.* 1983;43:1523-1528.

150 Koch CJ, Stobbe CC, Baer KA. Metabolism induced binding of 14C-misonidazole to hypoxic cells: kinetic dependence on oxygen concentration and misonidazole concentration. *Int J Radiat Oncol Biol Phys.* 1984;10:1327-1331.

151 Hodgkiss RJ, Middleton RW, Parrick J, Rami HK, Wardman P, Wilson GD. Bioreductive fluorescent markers for hypoxic cells: a study of 2-nitroimidazoles with 1-substituents containing fluorescent, bridgehead-nitrogen, bicyclic systems. *J Med Chem.* 1992;35:1920-1926.

152 Begg AC, Sheldon PW, Foster JL. Demonstration of radiosensitization of hypoxic cells in solid tumours by metronidazole. *Br J Radiol.* 1974;47:399-404.

153 Raleigh JA, Miller GG, Franko AJ, Koch CJ, Fuciarelli AF, Kelly DA. Fluorescence immunohistochemical detection of hypoxic cells in spheroids and tumours. *Br J Cancer.* 1987;56:395-400.

154 Cline JM, Thrall DE, Page RL, Franko AJ, Raleigh JA. Immunohistochemical detection of a hypoxia marker in spontaneous canine tumours. *Br J Cancer.* 1990;62:925-931.

155 Raleigh JA, Zeman EM, Rathman M, LaDine JK, Cline JM, Thrall DE. Development of an ELISA for the detection of 2-nitroimidazole hypoxia markers bound to tumor tissue. *Int J Radiat Oncol Biol Phys.* 1992;22:403-405.

156 Zeman EM, Calkins DP, Cline JM, Thrall DE, Raleigh JA. The relationship between proliferative and oxygenation status in spontaneous canine tumors. *Int J Radiat Oncol Biol Phys.* 1993;27:891-898.

157 Azuma C, Raleigh JA, Thrall DE. Longevity of pimonidazole adducts in spontaneous canine tumors as an estimate of hypoxic cell lifetime. *Radiat Res.* 1997;148:35-42.

158 Arteel GE, Thurman RG, Yates JM, Raleigh JA. Evidence that hypoxia markers detect oxygen gradients in liver: pimonidazole and retrograde perfusion of rat liver. *Br J Cancer.* 1995;72:889-895.

159 Nordsmark M, Alsner J, Keller J, *et al.* Hypoxia in human soft tissue sarcomas: adverse impact on survival and no association with p53 mutations. *Br J Cancer.* 2001;84:1070-1075.

160 Olive PL, Durand RE, Raleigh JA, Luo C, Aquino-Parsons C. Comparison between the comet assay and pimonidazole binding for measuring tumour hypoxia. *Br J Cancer.* 2000;83:1525-1531.

161 Rijken PF, Bernsen HJ, Peters JP, Hodgkiss RJ, Raleigh JA, van der Kogel AJ. Spatial relationship between hypoxia and the (perfused) vascular network in a human glioma xenograft: a quantitative multi-parameter analysis. *Int J Radiat Oncol Biol Phys.* 2000;48:571-582.

162 Kaanders JH, Wijffels KI, Marres HA, *et al.* Pimonidazole binding and tumor vascularity predict for treatment outcome in head and neck cancer. *Cancer Res.* 2002;62:7066-7074.

163 McSheehy PM, Robinson SP, Ojugo AS, *et al.* Carbogen breathing increases 5-fluorouracil uptake and cytotoxicity in hypoxic murine RIF-1 tumors: a magnetic resonance study in vivo. *Cancer Res.* 1998;58:1185-1194.

164 Hill SA, Collingridge DR, Vojnovic B, Chaplin DJ. Tumour radiosensitization by high-oxygen-content gases: influence of the carbon dioxide content of the inspired gas on PO2, microcirculatory function and radiosensitivity. *Int J Radiat Oncol Biol Phys.* 1998;40:943-951.

165 Powell ME, Collingridge DR, Saunders MI, Hoskin PJ, Hill SA, Chaplin DJ. Improvement in human tumour oxygenation with carbogen of varying carbon dioxide concentrations. *Radiother Oncol.* 1999;50:167-171.

166 Stuben G, Stuschke M, Knuhmann K, Horsman MR, Sack H. The effect of combined nicotinamide and carbogen treatments in human tumour xenografts: oxygenation and tumour control studies. *Radiother Oncol.* 1998;48:143-148.

167 Rojas A. ARCON: accelerated radiotherapy with carbogen and nicotinamide. *BJR Suppl.* 1992;24:174-178.

168 Rojas A. Radiosensitization with normobaric oxygen and carbogen. *Radiother Oncol.* 1991;20 Suppl 1:65-70.

169 Bernier J, Denekamp J, Rojas A, *et al.* ARCON: accelerated radiotherapy with carbogen and nicotinamide in non small cell lung cancer: a phase I/II study by the EORTC. *Radiother Oncol.* 1999;52:149-156.

170 Bussink J, Kaanders JH, Van der Kogel AJ. Clinical outcome and tumour microenvironmental effects of accelerated radiotherapy with carbogen and nicotinamide. *Acta Oncol.* 1999;38:875-882.

171 Kaanders JH, Pop LA, Marres HA, *et al.* Accelerated radiotherapy with carbogen and nicotinamide (ARCON) for laryngeal cancer. *Radiother Oncol.* 1998;48:115-122.

172 Lambin P, Poortmans P, Menten J, Hamers HP. Accelerated radiotherapy with carbogen and nicotinamide (ARCON) in high grade malignant gliomas. *Radiother Oncol.* 1997;43:324.

173 Saunders MI, Hoskin PJ, Pigott K, *et al.* Accelerated radiotherapy, carbogen and nicotinamide (ARCON) in locally advanced head and neck cancer: a feasibility study. *Radiother Oncol.* 1997;45:159-166.

174 Miralbell R, Mornex F, Greiner R, *et al.* Accelerated radiotherapy, carbogen, and nicotinamide in glioblastoma multiforme: report of European Organization for Research and Treatment of Cancer trial 22933. *J Clin Oncol.* 1999;17:3143-3149.

175 Kaanders JH, Pop LA, Marres HA, *et al.* ARCON: experience in 215 patients with advanced head-and-neck cancer. *Int J Radiat Oncol Biol Phys.* 2002;52:769-778.

176 Hoskin PJ, Rojas AM, Phillips H, Saunders MI. Acute and late morbidity in the treatment of advanced bladder carcinoma with accelerated radiotherapy, carbogen, and nicotinamide. *Cancer.* 2005;103:2287-2297.

Chapter 2

Introduction - MRI for the biological assessment of prostate cancer

2.1 Overview

Magnetic resonance imaging can produce images with high definition and image quality and provides the gold standard for morphological and anatomical assessment of prostate cancer. The technique utilizes the characteristic properties of protons, which vary depending on their chemical and physical environment. This environment differs between the various body tissues and in a number of pathological processes, such as malignancy. 'Weighting' the sequence that generates the image can produce various types of contrast. This is done by observing different aspects of the physical process that occur when the water protons interact with the applied magnetic field.

Given the fact that the MRI image is generated by changes that occur at the atomic level, it is not therefore surprising that this method may be useful in detecting the molecular, biochemical, physiological and metabolic changes that occur due to pathological processes within tissues. The key is to find sequences that will maximize the contrast caused by variations in a particular biological parameter, for example between areas of hypoxia and well oxygenated regions of tissue. Alternatively an exogenous contrast agent can be given and viewed over time to give measurements of perfusion and permeability of tissues, which can serve as markers for biological processes such as vascularization.

There are four functional magnetic resonance based imaging techniques: Dynamic Contrast Enhanced MRI (DCE-MRI), Intrinsic Susceptibility Weighted MRI – also known as Blood Oxygen Level Dependent (BOLD) MRI, Diffusion Weighted Imaging (DWI) and Magnetic Resonance Spectroscopy (MRS).

2.2 Dynamic Contrast Enhanced Magnetic Resonance Imaging (DCE-MRI)

2.2.1 Background

Review of the older MRI literature shows that T_1-weighted contrast enhanced images can depict prostatic zonal anatomy (not visible on unenhanced T_1-weighted images) but in general, T_2-weighted spin-echo images are better in this regard. The normal central gland enhances more than the peripheral prostate; both enhancing homogeneously. In the presence of BPH, enhancement of the central gland becomes heterogeneous [1]. Prostate cancer also enhances following contrast medium administration. Much of the early literature indicated no additional role of contrast enhancement compared to conventional T_2-weighted imaging for the assessment of prostate cancer [1, 2]. However in 1995, Brown et al. showed improved depiction of the intraprostatic location of tumours when images are obtained early after contrast administration [3], and Huch Boni et al. reported that contrast enhancement improved the detection of minimal seminal vesicle invasion by tumour [4]. Parallel developments in rapid MRI data acquisition methods lead to further clinical studies, which used a rapid series of images acquired continuously after bolus administration of contrast medium over a short period of time (1-7 minutes). This MRI technique, now called dynamic contrast enhanced MRI (DCE-MRI) has over time become established for improving lesion detection and staging and for the detection of suspected tumour recurrence. DCE-MRI is only one of many MRI methods that can directly evaluate the functional angiogenic status of tissues.

2.2.2 Dynamic contrast-enhanced MRI (DCE-MRI) technique

When a paramagnetic, low-molecular weight contrast agent is injected intravenously, it enters the tumour blood vessels and subsequently passes into the extra-vascular extra-cellular space. A high first pass extraction occurs in most normal tissues (with the exception of the brain, testes and retina) as well as in hyperplastic prostatic tissues and prostate cancer. In tumours, typically 12–45% of the contrast media leaks into the EES during the first pass [5]. Once out of the blood vessels the contrast agent is free to diffuse within the interstitial space until whole body distribution and renal excretion lowers the vascular concentration below that in the interstitial space at which stage, contrast medium passes back into the vascular space **(figure 2.1)**.

Figure 2.1 Body compartments accessed by low molecular weight contrast media injected intravenously

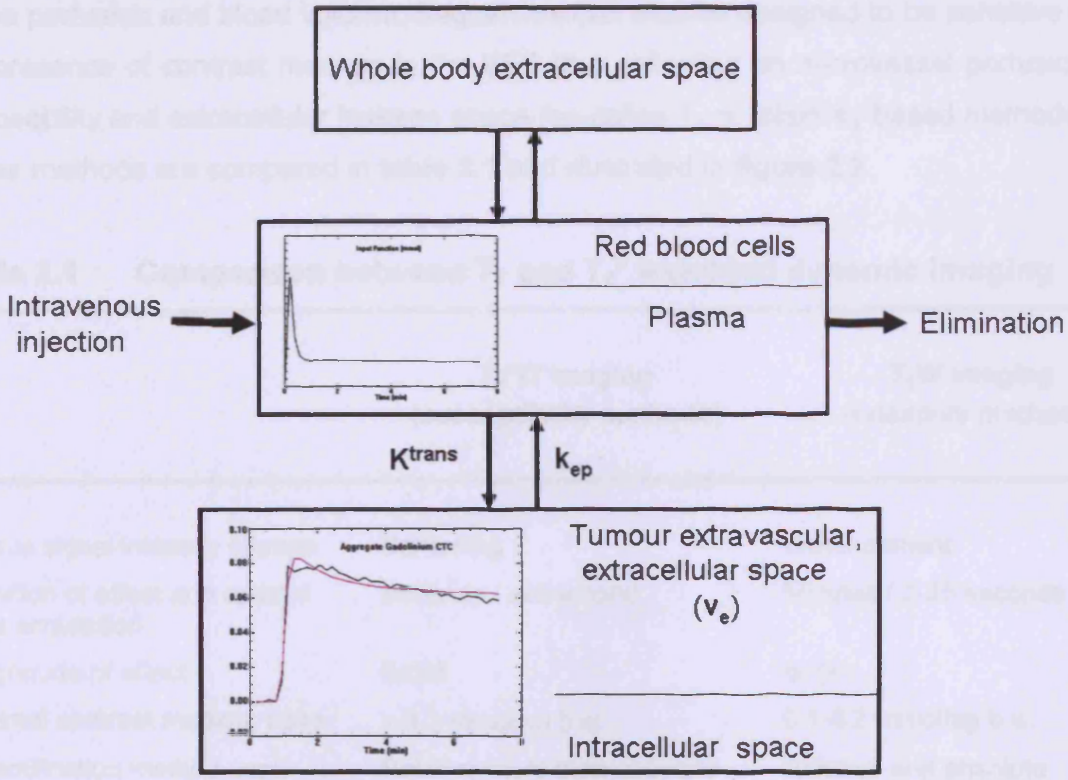

Three major factors determine the behaviour of low molecular weight contrast media in the prostate gland during the first few minutes after injection: blood perfusion (contrast agent delivery), transport of contrast agent across vessel walls and diffusion of contrast medium in the interstitial space. If the delivery of the contrast medium to a tissue is insufficient to maintain a higher vascular concentration compared to that in the EES (flow-limited situations or where vascular permeability is greater than inflow), then blood perfusion will be the dominant factor determining contrast agent kinetics; this situation is commonly found in tumours. If tissue perfusion is sufficient and transport out of the vasculature does not deplete intravascular contrast medium concentration (non-flow limited situations – e.g. in areas of fibrosis or glandular atrophy after hormonal and/or radiation treatment) then transport across the vessel wall (i.e. permeability surface area product) is the major factor that determines contrast medium kinetics. As low molecular weight contrast media do not cross cell membranes, their volume of distribution is effectively the interstitial space or EES (this excludes the glandular lumina). It is these differences in contrast agent behaviour between normal and hyperplastic prostatic tissues and tumour that are exploited by DCE-MRI to provide lesion / tissue specific information.

MR sequences can be designed to be sensitive to the vascular phase of contrast medium delivery (so-called T_2* or dynamic susceptibility contrast (DSC)), which reflect tissue perfusion and blood volume. Sequences can also be designed to be sensitive to the presence of contrast medium in the EES thus reflecting on microvessel perfusion, permeability and extracellular leakage space (so-called T_1 or relaxivity based methods). These methods are compared in **table 2.1** and illustrated in **figure 2.2**

Table 2.1 Comparison between T_1 and T_2* weighted dynamic imaging

	T_2*W imaging (susceptibility methods)	**T_1W imaging (relaxivity methods)**
Tissue signal intensity change	Darkening	Enhancement
Duration of effect and optimal data acquisition	Seconds / subsecond	Minutes / 2-25 seconds
Magnitude of effect	Small	larger
Optimal contrast medium dose	$\geq$ 0.2 mmol/kg b.w.	0.1-0.2 mmol/kg b.w.
Quantification method used	Relative more than absolute	Relative and absolute
Physiological property measured	Perfusion/blood volume	Transendothelial permeability, capillary surface area, lesion leakage space
Kinetic parameters derived	Blood volume and flow, transit time	Transfer and rate constants, leakage space
Pathological correlates	Tumour grade and microvessel vessel density	Microvessel density Vascular endothelial growth factor (VEGF)
Principle uses for prostate evaluations	Mapping of hypoxia in tumours when used with BOLD-MRI	Lesion localisation and characterisation Monitoring the effectiveness of therapy response Detecting relapsed disease

2.2.3 T_2 weighted DSC-MRI*

2.2.3.1 Data acquisition

Perfusion-weighted images can be obtained with "bolus-tracking techniques" that are sensitive to susceptibility effects caused by the passage of contrast material in a capillary bed. Bolus injection of contrast medium is essential to the success of this technique. The degree of signal intensity loss observed on susceptibility-weighted images is dependent on sequence types and parameters used, the vascular concentration of the contrast agent and microvessel size and density [6, 7] **(figure 2.2)**. The signal to noise ratio (SNR) of images can be improved by using higher doses of contrast medium (i.e., ≥ 0.2-mmol/kg body weight) [6]. MRI systems capable of rapid image acquisition are required to adequately characterize these effects. High specification, echo-planar capable machines allow rapid multi-slice data acquisition. Although such studies are possible on conventional MRI systems using standard gradient-echo sequences, data acquisition is limited to a fewer slices. When examining the prostate, even small amounts of rectal air and rectal movement can cause additional, intrinsic susceptibility artefacts that may adversely affects the quality of DSC-MRI examinations.

Figure 2.2 Comparison of the T_1-weighted DCE-MRI and T_2-weighted DSC-MRI data collections

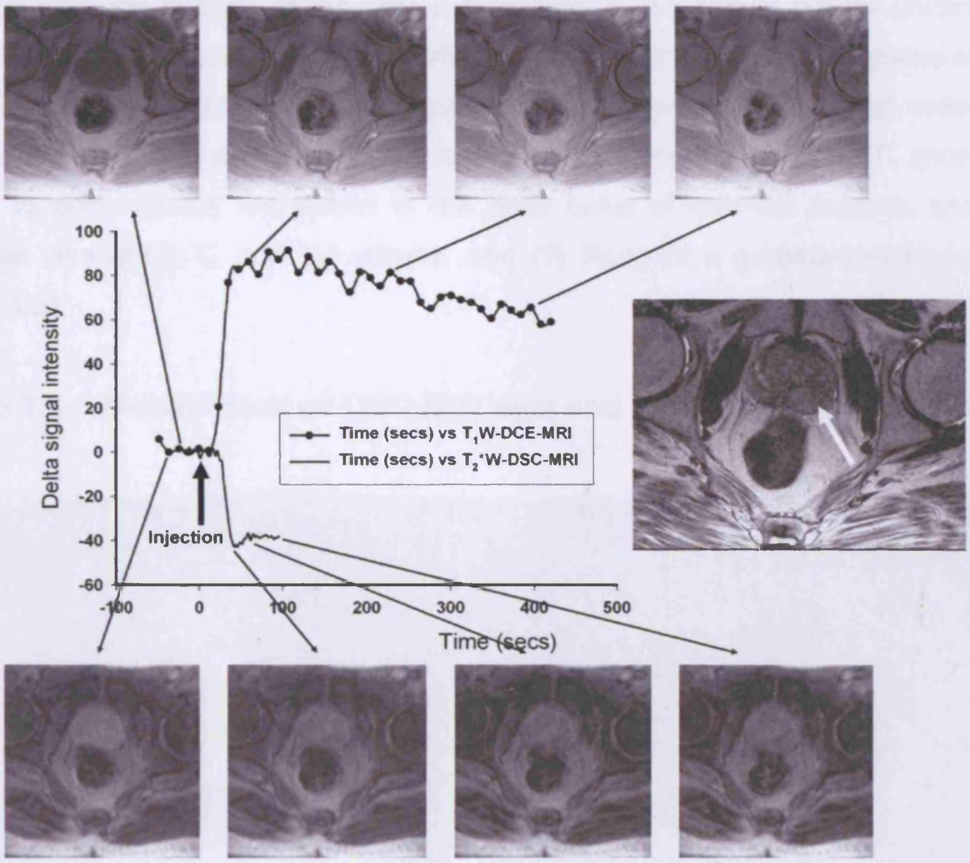

Contrast medium injection took place after the 4th data point for the T_1-weighted DCE-MRI study (time resolution 12 seconds) and after 10 data points for the DSC-MRI (time resolution 2 seconds). The zero point on the time scale represents the point of injection of contrast medium for both studies, which were performed consecutively. The data are for the region indicated by the arrow on the morphological T_2-weighted image. First pass susceptibility effects cause marked darkening of the prostate gland (Bottom row of images). Note how the signal intensity remains below the baseline due to rapid loss of compartmentalization of the Gd-DTPA. On the contrary, marked and sustained early enhancement of the prostate is seen on T_1-weighted DCE-MRI (top row). The onset and short duration of early T_2*-weighted DSC-MRI effects corresponds precisely to the upslope on the T_1-weighted enhancement curves for the same region of interest confirming that the upslope has a significant vascular contribution.

2.2.3.2 Data quantification

A linear relationship between blood concentration of the contrast agent and change in transverse relaxation time is usually assumed. Analysis also assumes that the contrast agent remains in the vascular space throughout the examination period, acting as a blood pool agent. If this were the case, tracer kinetic principles can be used to provide estimates of relative blood volume (rBV), relative blood flow (rBF) and mean transit time (MTT) derived from the first-pass of contrast agent through the microcirculation. These variables are related by the central volume theorem equation (BF = BV/MTT) [8]. In the prostate, loss of compartmentalisation of the contrast medium always occurs because of high capillary permeability. This loss of compartmentalization of the injection bolus and the T_1 enhancing effects of diluted contrast agent in the EES counters T_2* signal intensity-lowering effects, resulting in falsely lowered blood volume computations. Therefore, the conventional approach of deriving kinetic parameters obtained from the integral of the time-susceptibility curve should not be undertaken. Solutions for obtaining more reliable perfusion data under these circumstances include (1), optimisation of pulse sequence parameters to minimise T_1 signal enhancing effects, (2) pre-dosing with a small amount of contrast medium to allow T_1 shortening effects to occur before the arrival of the main bolus of contrast medium and thus minimise competing T_1 and T_2* effects, and (3) fitting of a gamma-variate function **(figure 2.3)**.

Figure 2.3 Model fitting of DSC-MRI data and parametric map formation

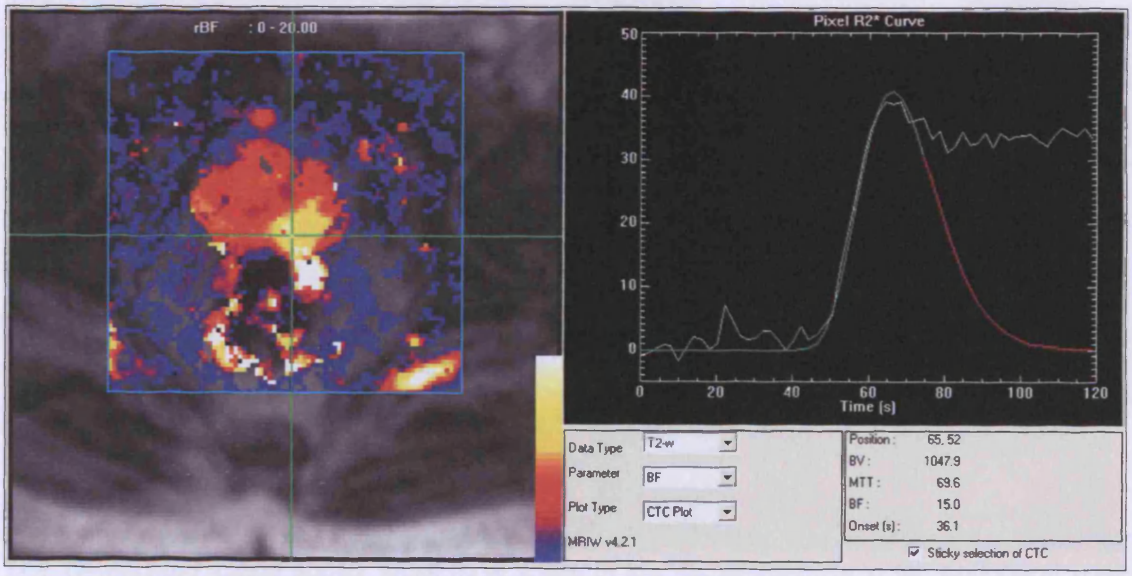

Data Type: T2-w
Parameter: BF
Plot Type: CTC Plot

Position : 65, 52
BV : 1047.9
MTT : 69.6
BF : 15.0
Onset (s) : 36.1

☑ Sticky selection of CTC

Same patient as illustrated in figure 2. T_2* signal intensity data from figure 2 is converted into R_2* (=1/T_2*) shown as the white line for the pixel at the centre of the cross-hairs on the parametric map (left) and then fitted with a gamma variate function (green then red line). Parametric map (left) representing relative blood flow (rBF; colour scale 0-20 arbitrary units) is derived on a pixel-by-pixel basis using this procedure.

2.2.3.3 Clinical experience of DSC-MRI

A limited number of studies have reported mainly in abstract form on the feasibility of using DSC-MRI to examine the prostate gland [9-11] **(figure 2.4)**. Observations have shown that it is possible to demonstrate first pass, signal intensity lowering effects and that limited tissue characterisation is possible. That is, significant differences have been noted between peripheral gland and tumour with respect to signal intensity change [9]. However, no systematic differences between BPH and tumour enhancement values have been observed. Furthermore no published studies have as yet correlated DSC-MRI with patient prostate cancer serum PSA levels, tumour stage, Gleason score, or with MVD or VEGF immunostaining. Recent work has evaluated the potential of DSC-MRI for the assessment of prostate gland and prostate cancer hypoxia [11]. In this study 20 patients were imaged with Blood Oxygen Level Dependent (BOLD)-MRI and DSC-MRI prior to radical prostatectomy and regional hypoxia assessments were undertaken using pimonidazole immunostaining. The data showed that low relative blood volumes (rBV), when used alone, had a low sensitivity (24%) for the presence of regional hypoxia but sensitivity was high (91%) as was the positive predictive value (86%).

Figure 2.4 Correlation of DCE-MRI and DSC-MRI with whole mount histology and diffusion weighted images

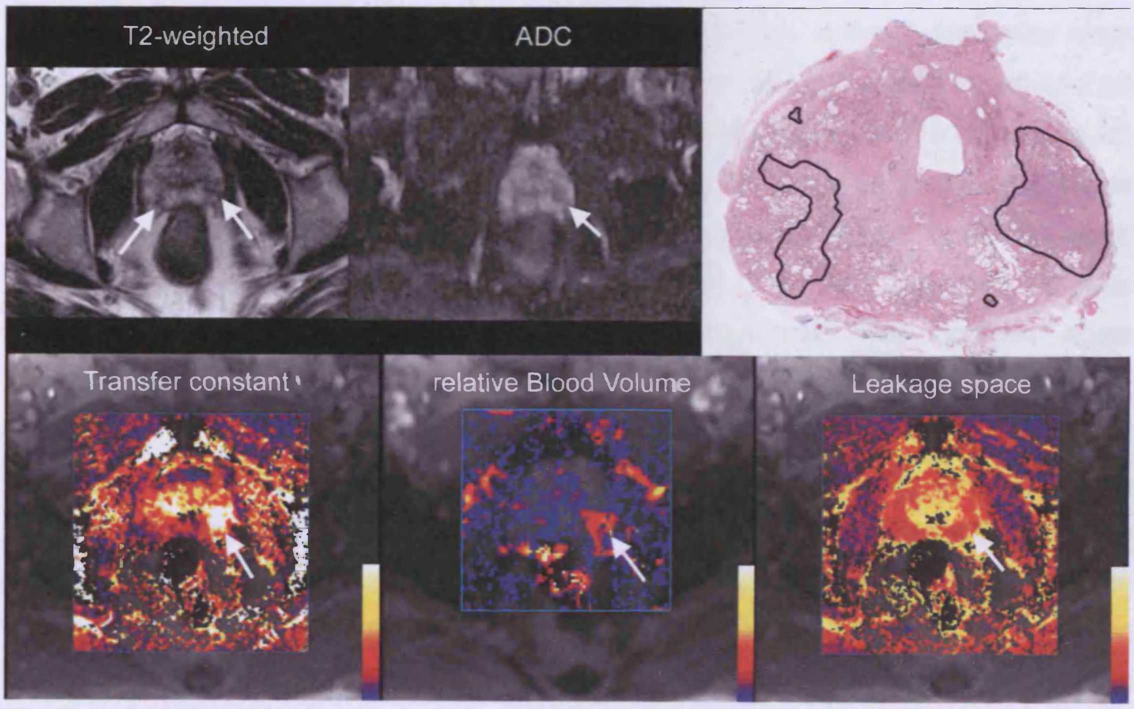

The T_2-weighted image shows small focal areas of low signal intensity in the peripheral zone (arrows) corresponding to tumour foci on histology (circled regions). The tumour nodule on the left of the gland has a high transfer constant (colour scale 0-1 min^{-1}) and relative blood volume (colour scale 0-300 arbitrary units). Tumour lesions are not visible on the leakage space map (colour scale 0-100%). Note how the central gland has high transfer constant values also.

2.2.4 T_1 weighted (relaxivity based) dynamic MRI

2.2.4.1 Data acquisition

To monitor the tissue enhancing effects of contrast agents using T_1-weighted sequences requires that confounding T_2 and T_2^* signal intensity lowering effects must be minimised. T_1-weighted gradient-echo, saturation recovery/inversion recovery snapshot sequences are often used for prostate imaging. The choice of sequence and parameters used is dependent on intrinsic advantages and disadvantages of the sequences taking into account T_1 sensitivity, anatomical coverage, acquisition times, susceptibility to artefacts arising from sources of magnetic field inhomogeneities (e.g., from rectal gas, surgical clips etc) and the need for quantification. It is recognized that high-resolution and short imaging-time are competing examination strategies on current equipment. Higher temporal resolution imaging still necessitates reduced spatial resolution, decreased anatomic coverage or a combination thereof. Higher temporal resolution techniques are essential for DSC-MRI and appear to improve tissue characterisation on T_1-weighted DCE-MRI; one study has suggested that characterisation of prostatic tissues is optimal using image acquisition times of 2 seconds [12].

In order to model tissue contrast behaviour the contrast agent concentration at each time point during the imaging procedure needs to be known. If the T_1 relaxation rates can be accurately estimated, then tissue concentration of the contrast agent can be calculated [13, 14]. Some workers assume that the change in signal intensity (delta SI) or relative signal intensity (as a percentage change) is directly proportional to tissue contrast concentration using their sequence. However, when contrast agent concentrations become large (e.g., within vessels) then this becomes a poor approximation, because signal intensity varies nonlinearly with contrast agent concentration.

Common causes for failed examinations include poor contrast medium bolus administration (particularly if manual injection techniques are used) and the presence of hip prostheses, surgical clips and rectal gas, each causing susceptibility artefacts and technical failures (poor signal to noise ratio of images or unexpected machine gain changes during the data acquisition). Patient or internal organ movements (rectal movement or bladder filling affecting prostatic position) are also not uncommon and can lead to technical failures. For example, Padhani et al. have reported that 16% of 55 patients had anterior prostatic displacements of > 5 mm due to rectal motion during

DCE-MRI examinations lasting 7 minutes and noted an inverse correlation between the degree of rectal distension of the frequency of rectal movements [15].

2.2.4.2 Quantification, uncertainties and limitations

Signal intensity enhancement on T_1-weighted DCE-MRI images can be assessed in several ways (qualitatively and quantitatively using kinetic model free variables or by the derivation of physiological indices using pharmacokinetic models). Qualitative assessments, based on the shape of the signal intensity-time curve, are useful clinically for tissue characterisation and for assessing response to treatment. Model free indices (often called semi-quantitative) describe tissue enhancement using a number of descriptors. These include onset of enhancement (time from injection or first appearance in a pelvic artery to the first increase in tissue signal intensity), initial and mean gradient of the upsweep of enhancement curves, maximum signal intensity, washout gradient and the integral areas under enhanced curves over fixed periods of time. Such model free parameters have the advantage of being relatively straightforward to calculate but have limitations including the fact that they may not accurately reflect contrast medium concentration in the tissue of interest and can be influenced by scanner settings (including gain and scaling factors).

Quantitative kinetic parameters are derived from concentration-time curves that are mathematically fitted using one of a number of recognised pharmacokinetic models [16] **(figure 2.5)**. Examples of modelling parameters include the volume transfer constant of the contrast agent (K^{trans} - formally called permeability-surface area product per unit volume of tissue), leakage space as a percentage of unit volume of tissue (v_e) and the rate constant (k_{ep} also called K_{21}). These standard parameters are related mathematically ($k_{ep} = K^{trans} / v_e$) [17].

Experience shows that observed data obtained may not fit the model chosen: each model makes a number of assumptions that may not be valid for every tissue or tumour type. For example, the application of the Tofts' model includes a standard description of the time varying blood concentration of contrast agent, also called the input function, that the supply of contrast medium is not perfusion limited and that tissue blood volume contributes negligible signal compared with that arising from contrast medium in the interstitial space [17]. Buckley has suggested that the application of commonly accepted models and their respective model-based assumptions to DCE-MRI data leads to systematic overestimation of K^{trans} [18]. Other potential sources of error arise from assumptions made for the determination of contrast medium concentration in vivo.

Figure 2.5 Converting signal intensity into contrast concentration & model fitting

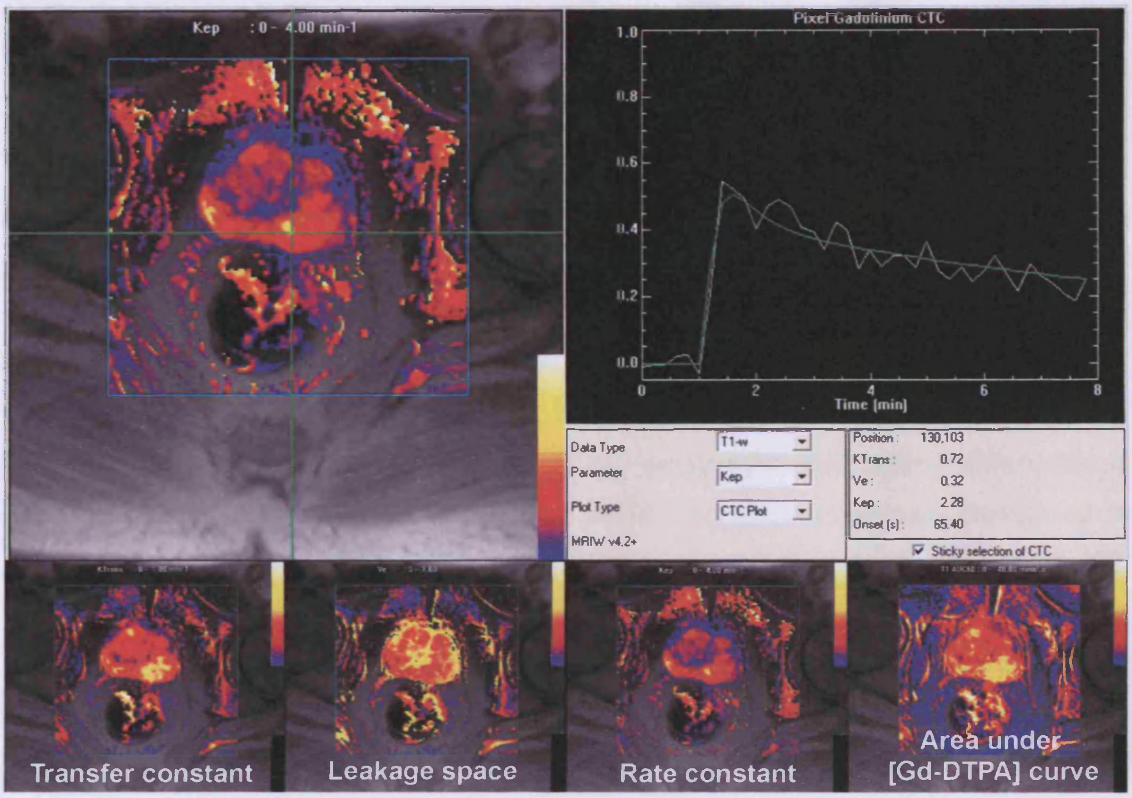

Data Type: T1-w

Parameter: Kep

Plot Type: CTC Plot

MRIW v4.2+

Position: 130,103

KTrans: 0.72

Ve: 0.32

Kep: 2.28

Onset [s]: 65.40

☑ Sticky selection of CTC

Contrast medium injection took place after the 4th data point. Time signal intensity data is first converted into contrast agent concentration and then the model fitting procedure (continuous green line) is done using the Tofts' model. Parametric maps representing transfer constant (K^{trans}; colour scale 0-1 min^{-1}), leakage space (v_e; colour scale 0-100%), rate constant (k_{ep}; colour scale 0-4 min^{-1}) are shown. The non-model dependent parameter (initial area under the Gd-DTPA concentration curve for 60 seconds ($IAUGC_{60}$); colour scale 0-40 mmol.sec) is shown for comparison.

For example, MRI contrast medium is detected only indirectly by its effect on extracellular tissue water. In tissues, extracellular water exchanges with the bulk of the water, which is intracellular. Accepting that there are outstanding issues with regard to model-based assumptions and the measurement of tissue contrast agent concentration, quantitative kinetic parameters such as K^{trans} and v_e do allow comparisons to be made between patients, in the same patient at multiple time points and between patients at different imaging centres. Furthermore physiological indices can provide valuable insights on the causes of changing enhancement patterns seen after therapeutic interventions.

2.2.4.3 Validation of T_1 weighted dynamic MRI in prostate cancer

It is possible to show characteristic differences in the enhancement patterns of peripheral prostate gland compared to the central gland and/or tumours. Studies show that prostate cancer enhances to a greater extent than the peripheral gland and that there is an overlap with the enhancement of the central gland. The enhancement patterns observed are likely to be related to underlying variations in tissue perfusion, MVD and tissue VEGF expression. Immuno-histochemical studies have found that MVD in prostate cancer and BPH are higher than in the peripheral zone. These studies also show that there is an overlap in MVD counts between tumours and BPH [19, 20]. Although many clinical studies have correlated tissue MRI enhancement with immuno-histochemical MVD measurements (see Padhani 2002 for a review [21]), no systematic correlative studies have been performed in prostate cancer. There are also no clinical studies correlating tissue MRI enhancement with immuno-histochemical VEGF staining in prostate cancer.

Although initial observations by Jager et al., suggested that poorly differentiated prostate cancer showed earlier onset and faster rate of enhancement compared to other histological grades [12], this has not been borne out by subsequent reports [22, 23]. Engelbrecht and colleagues demonstrated a weakly positive correlation between several DCE-MRI parameters and Gleason scores, with correlation coefficients ranging from –0.34 to +0.21 for peripheral zone carcinomas, with the strongest associations being for onset time and time to peak enhancement (correlation coefficients of 0.21 and 0.22 respectively) [22]. For central zone cancers, correlation coefficients ranged between –0.22 and +0.29, peak enhancement being the best correlate of Gleason score with a Pearson coefficient of 0.29. Other similar studies have shown no significant association between tumour grade and DCE-MRI kinetic parameters. Padhani et al. commented that the lack of correlation might be explained by histological sampling errors inherent in TRUS needle biopsy techniques. Engelbrecht et al. however used whole mount prostatectomy sectioning but had relatively few patients with well or poorly differentiated cancers which contributed to the lack of good correlation [22, 23].

2.2.4.4 Clinical experiences with T_1-weighted dynamic MRI

Primary diagnosis of prostate cancer

Following the widespread availability of PSA testing many men are referred for ultrasound guided biopsy with a high clinical index of suspicion that malignancy will be detected. The pre-biopsy probability of histological confirmation of cancer is up to 70% if the PSA ≥ 10ng/ml. However, a proportion of these men will have a negative biopsy, posing the clinical problem of whether this is a true-negative or false-negative result and the patient will usually be subjected to repeated biopsies. Some of these men will then be referred to MRI for diagnosis and localisation.

The investigation by DCE-MRI of men for primary detection has been limited although there are two published reports evaluating this modality in previously undiagnosed patients. Hara et al. evaluated 90 men using low temporal resolution DCE-MRI [24]. Impressively, their reported cancer detection rate was 92.9% with a specificity of 96.2%. Furthermore, the solitary false-positive case was found to have cancer following additional biopsies. The second, much smaller, study evaluated 14 patients with endorectal MRI prior to TRUS-guided biopsies [25]. Multiple MRI parameters were correlated with histology. K^{trans}, onset time, mean gradient and maximum enhancement of the gadolinium concentration-time curve showed a significant difference between tumour and normal tissue. The overall sensitivity and specificity were 59% and 74% respectively. Whilst these early reports show some promise, the case for DCE-MRI in this setting is not proven. More definitive, larger studies that take inter- and intra-observer variation into account are needed to define the role of functional MRI techniques. A more realistic approach, given current evidence, would be to use a multifunctional imaging approach combining DCE-MRI, 1H-MRS and DW-MRI to determine areas of the prostate associated with a high probability of cancer, thereby allowing targeted re-biopsy of a particular prostate region in addition to standard sector sampling. However, as a caveat to this strategy, it should be noted once a prostate gland has been needled, reactive enhancement in areas devoid of cancer, which is often diffuse, can obscure any tumour for a prolonged period of time.

Localisation and staging of prostate cancer

Despite the fact that there is debate regarding the optimal technique for T_1-weighted dynamic data acquisition, numerous studies have found dynamic sequences superior to conventional T_2-weighted sequences in terms of accuracy, sensitivity and specificity using histopathological confirmation as the gold standard **(table 2.2)**. Jager et al in 1997 reported on 57 patients that were imaged conventionally and with dynamic sequences [12]. Dynamic imaging improved sensitivity from 57.5% to 73.5% and accuracy from 72% to 77.5%, whilst not affecting specificity (80.5% versus 81% respectively). Namimoto supported this finding reporting a diagnostic accuracy of 75% for T2-weighted images, and 79% for dynamic images [26]. The accuracy of the combination of dynamic MR images with postcontrast T_1-weighted images was 82%. It was concluded that dynamic MR imaging was useful in the differentiation of low intensity lesions in the peripheral zone. Recently, a prospective study using whole-mount histopathology from radical prostatectomy specimens for correlation examined 34 prostates using T_2-weighted MRI, DCE-MRI and ^{1}H-MRS [27]. Localization accuracy and ROI-based receiver operating characteristic (ROC) curves were calculated. Areas under the ROC curve for T_2-weighted MR, DCE-MRI, and ^{1}H-MRS were 0.68, 0.91, and 0.80, respectively. Furthermore, reader accuracy in tumour localization with dynamic MRI was significantly better than that with quantitative spectroscopic imaging ($P < 0.01$) in both the peripheral and central gland.

Although one would expect more accurate tumour localization to lead to better staging performance, there is only limited direct clinical evidence to confirm this. It would appear that DCE-MRI can help in patients with equivocal capsular penetration, seminal vesicle or neurovascular bundle involvement. A study designed to compare the staging accuracy of experienced versus less experienced readers, once again using whole-mount histopathology from radical prostatectomy specimens for comparison, showed that DCE-MRI improved the performance of less experience readers [28]. Staging performance for the less experienced readers with DCE-MRI resulted in significant improvement of the area under the receiver operating characteristics curve compared with T2-weighted MR imaging alone (0.66 and 0.82, respectively; $P = 0.01$). More experienced readers gained little from the addition of dynamic sequences.

Table 2.2 Studies comparing dynamic sequences with conventional T2-weighted sequences for prostate tumour localisation

Study	Year	Number of Patients	Tumour/ segment number	Sensitivity (%)		Specificity (%)		Accuracy (%)		Histo-pathological correlation
				T2	dyn	T2	dyn	T2	dyn	
Jager	1997	57	102	57.5	73.5	80.5	81	72	77.5	Prostatectomy
Namimoto	1998	42	44	95	86	57	74	75	79	TRUS+Biopsy
Ogura	2001	38	85	-	59	-	88	-	72	prostatectomy
Muramoto	2002	34	34	-	100	-	85	-	92	Both
Ito	2003	31	122	-	87	-	74	-	82	TRUS+Biopsy
Kiessling	2004	27	27	-	70*	-	88*	-	-	prostatectomy
Schlemmer	2004	28	28	79[†]	68[†]	-	-	-	-	prostatectomy
Hara	2005	82	3444[‡]	-	92.9	-	96.2	-	80.5	TRUS+Biopsy
Kim	2005	53	53	65	96	60	82	62	88	prostatectomy
Kozlowski	2006	14	14	-	59	-	74	-	-	Both
Futterer	2006	34	476	67[§]	69-95[§]	74[§]	80-96[§]	71[§]	81-91[§]	prostatectomy

*for Slope$_{52}$

[†] for peripheral zone lesions only

[‡] 14 cores per patient, each core divided into 3; 82x14x3=3444

[§] 2 readers evaluated each image. Best results presented

2.3 Blood Oxygen Level Dependent Magnetic Resonance Imaging (BOLD-MRI)

2.3.1 Background

It has previously been extremely difficult to characterise the oxygen status of an individual prostate tumour prior to treatment. Immunostaining for hypoxia can only be performed once the tumour has been removed from the body. ^{19}F nuclear magnetic resonance oximetry of perfluorocarbons (PFCs) has not been the subject of human trials and is limited by the limited distribution of PFC emulsions. Direct tumour measurement with electrodes (Eppendorf) is imprecise because of the inability of the operator to determine tumour regions within the prostate using the trans-rectal ultrasond probe. A non-invasive technique that accurately and repetitively measures tumour oxygenation may find broad applications in clinical and basic cancer research.

BOLD-MRI capitalizes on the differing magnetic properties of oxygenated and deoxygenated blood. Oxyhaemoglobin contains iron in the Fe^{3+} (diamagnetic) state, deoxyhaemoglobin contains iron in the Fe^{2+} (paramagnetic) state. Deoxyhemoglobin serves as an intravascular contrast agent because it brings about an increase in the transverse relaxation rates of blood and surrounding tissues. Microscopic field gradients in the vicinity of red blood cells and vessels are modulated by changes in the paramagnetic deoxyhaemoglobin concentration, which leads to signal attenuation in susceptibility weighted MRI sequences (T_2*). In other words, the blood oxygen level itself is acting as a contrast agent. As the oxygenation of hemoglobin is closely related to the pO_2 of blood (described by the oxygen-haemoglobin dissociation curve), which is assumed to be in equilibrium with tissue pO_2, BOLD MRI is expected to provide a sensitive index of the oxygenation status of tissue immediately adjacent to perfused microvessels. Tissues with increased deoxyhaemoglobin concentration are seen as higher signal on the resulting BOLD MRI image.

The BOLD MRI effect can be quantified by plotting the natural log of signal intensity against the echo time to derive tissue relaxivity (the power of the exponent is $1/T_2^*$ or R_2^*, the rate of relaxation). This is performed for each imaging voxel and parametric R_2^* maps are produced **(figure 2.6).**

This phenomenon was first demonstrated in the brain by Ogawa and colleagues [29]. Its success in detecting the changes in oxygenation caused by neuronal activity has led to a number of clinical applications for its use in the field of neurology, including the assessment of haemodynamic changes, multiple sclerosis, stroke, degenerative brain disease, spinal injury and uses in psychology.

Figure 2.6 Calculation of R_2*

-R2* = slope of log (signal intensity) – echo time plot
Slope ~ deoxyhaemaglobin concentration
[deoxyHB] ~ intravascular pO_2 ~ tissue pO_2

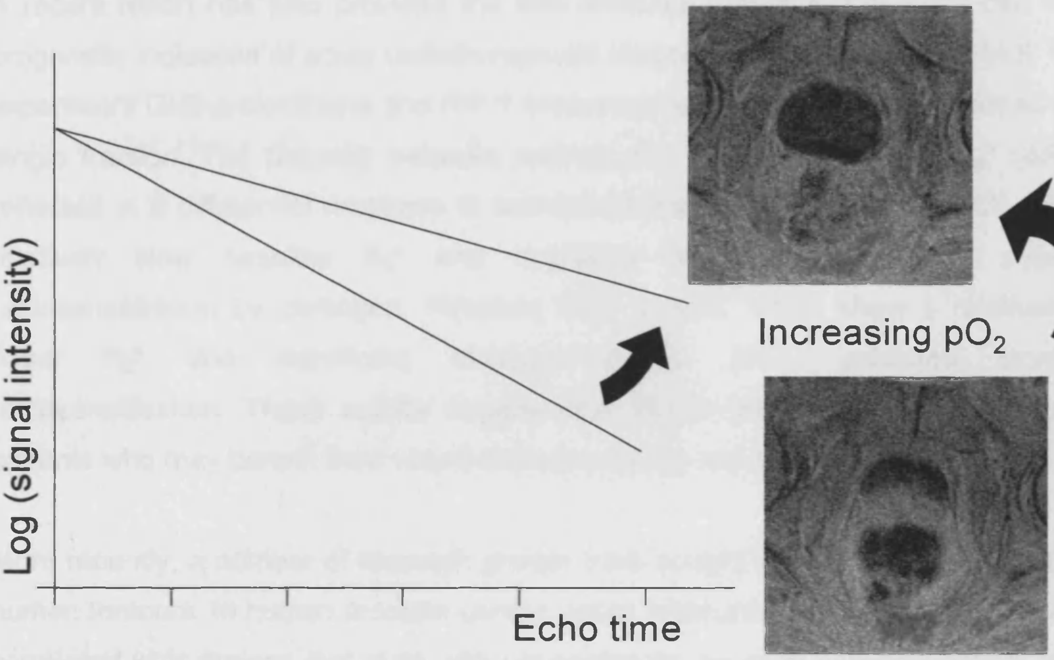

Its use in oncology is less prevalent and largely experimental at present. In 1994 the first report was published showing that T_2* weighted MRI images may be useful in the detection of tumour hypoxia in an animal model [30]. Rats bearing an adenocarcinoma xenograft were imaged breathing air and 100% O_2, with portions of the tumour exhibiting an increase in signal intensity of up to 50% following hyperoxia. Following this there has been demonstration of the enhancement effect of increased oxygenation on the BOLD image in a number of other experimental tumour models [31] and evidence that T_2* weighted images can differentiate tumours from normal tissue [32].

2.3.2 Validation

Validation of the technique has been achieved by correlation with direct microelectrode measurements [33, 34], intravital microscopy [35] and immunohistochemistry [36]. In rodent tumors, changes in the BOLD signal in response to vasomodulation, particularly by exposure to inhaled carbogen, mirror changes in tissue pO_2 [33, 34, 37-39].

Carbogen inhalation affects BOLD MRI imaging for GH3 prolactinomas and RIF-1 fibrosarcomas in different ways [31] most likely reflecting the underlying vascular status, including vascular volume, vessel size, and perfusion. Large decreases in signal are observed in GH3 tumors, suggesting oxygenation of deoxyhemoglobin in response to carbogen. RIF-1 tumors however, show less response, suggesting poorer oxygenation. For RIF-1 tumors, many areas may not be perfused, whereas GH3 tumors are fairly well perfused.

A recent report has also provided the first evidence that BOLD contrast can offer a prognostic indication of acute radiotherapeutic response in rodent tumours [40]. In this experiment GH3 prolactinona and RIF-1 fibrosarcoma xenografts were irradiated with a single fraction. The disparity between intrinsic R_2^* and the change in R_2^* (ΔR_2^*) is reflected in a differential response to radiation therapy. RIF-1 tumors, which exhibit a relatively slow baseline R_2^* and negligible ΔR_2^* with carbogen, show no radiosensitization by carbogen. Whereas GH3 tumors, which show a relatively fast basal R_2^* and significant carbogen-induced ΔR_2^*, exhibited significant radiosensitisation. These results suggest that BOLD MRI can be used to identify patients who may benefit from vasomodulation during radiotherapy.

More recently, a number of research groups have sought to validate this application in human tumours. In human prostate cancer, areas highlighted by the T_2^* sequences are correlated with regions that stain with pimonidazole, an immunohistochemical marker for tumour hypoxia [41]. A further study has demonstrated BOLD imaging responses in a number of tumour types [42] and this technique is also a valuable tool in differentiating areas of prostate cancer from regions of benign prostatic hypertrophy in humans, as demonstrated by a study validated by histopathological comparison between prostatectomy specimens and corresponding BOLD images [43].

A preliminary report has suggested that R_2^* correlates with pimonidazole staining In the prostate gland. It appears to be most sensitive for identifying hypoxic regions within tumors but not within benign prostate hyperplasia [11]. A study reported by Hoskin *et al.* showed that the sensitivity of R_2^* in depicting tumour hypoxia was high (88%), improving with the addition of low blood volume information (95%) without changing specificity (36% and 29% respectively) [44]. Fast R_2^* increased the positive predictive value for hypoxia by 6% (70% to 76%); conversely, slow R_2^* decreased the likelihood of hypoxia being present by 24% (70% to 46%; and by 41% when combined with rBV information). This early study indicates that R_2^* maps from BOLD-MRI have high sensitivity but low specificity for defining intraprostatic tumour hypoxia. The high negative predictive value (70%) when combined with blood volume information indicates that BOLD-MRI may be a suitable technique for mapping prostatic tumour oxygenation.

2.3.3 Limitations

The BOLD MRI signal can reflect the hypoxic status of tumors but does not directly measure pO_2 values. The R_2^* quantity depends upon the total number of deoxyhaemoglobin molecules within each imaging voxel. The proportion of blood that is deoxygenated (i.e. the deoxyhaemoglobin : oxyhaemoglobin ratio) is not reflected. Therefore, if two similar regions with equivalent pO_2 are compared, the region that simply contains more blood volume will exhibit a higher R_2^* value because it contains more deoxyhaemoglobin molecules. In other words, BOLD-MRI is blood volume and therefore blood flow dependent (blood flow = blood volume / transit time). Obtaining perfusion measurements from the same region of interest can compensate for this. This can be achieved by combining BOLD-MRI with dynamic susceptibility contrast MRI, dynamic CT, diffusion weighted MRI or even Doppler ultrasound.

The R_2^* rate is related to the presence of deoxyhaemoglobin molecules within the red blood cell, however the parameter of interest is pO_2. The relationship between the proportion of haemoglobin that is oxygenated and the intravascular pO_2 is described by the sigmoidal oxygen-haemoglobin dissociation curve **(figure 2.7).** At pO_2 levels below about 40mmHg, the relationship is virtually linear. This indicates that for quantifying clinically relevant tumour hypoxia (<10mmHg), R_2^* is likely to be proportional to intravascular pO_2. For well-oxygenated regions, with pO_2 values that approach that of arterial blood, the relative increase in haemoglobin saturation for any given rise in pO_2, is much less. Therefore, BOLD-MRI should be more capable of discriminating between changes in low pO_2 levels than changes in high pO_2 levels. Image contrast on BOLD MRI can also be affected by carbon dioxide tension, hematocrit, pH, temperature and the presence of 2,3-diphosphoglycerate because of their effect on the oxygen-haemoglobin dissociation curve.

By virtue of the fact that the BOLD signal is created by blood cells, this technique can only reflect intravascular pO_2. There is no MRI 'probe' of the extravascular space. Tumour cells exist in the extravascular compartment, it is therefore the tissue pO_2 that influences tumour biology. Consequently, BOLD-MRI assumes that intravascular pO_2 is a reflection of the surrounding tissue pO_2. Oxygen diffuses from the vascular stroma into tumour, where it is consumed by the tumour cells. As a result there is a pO_2 gradient surrounding each tumour capillary up to a diffusion distance of about 180μm where cells are unable to survive and become necrotic. Therefore the intravascular pO_2 does not give a true representation of the extracellular environment surrounding each tumour cell. Despite this, given the high vascular permeability within tumours, it is highly unlikely that a hypoxic tumour would contain blood vessels with a high intravascular pO_2 or a well oxygenated tumour would contain a high volume of deoxygenated blood.

Figure 2.7 The oxygen-haemoglobin dissociation curve

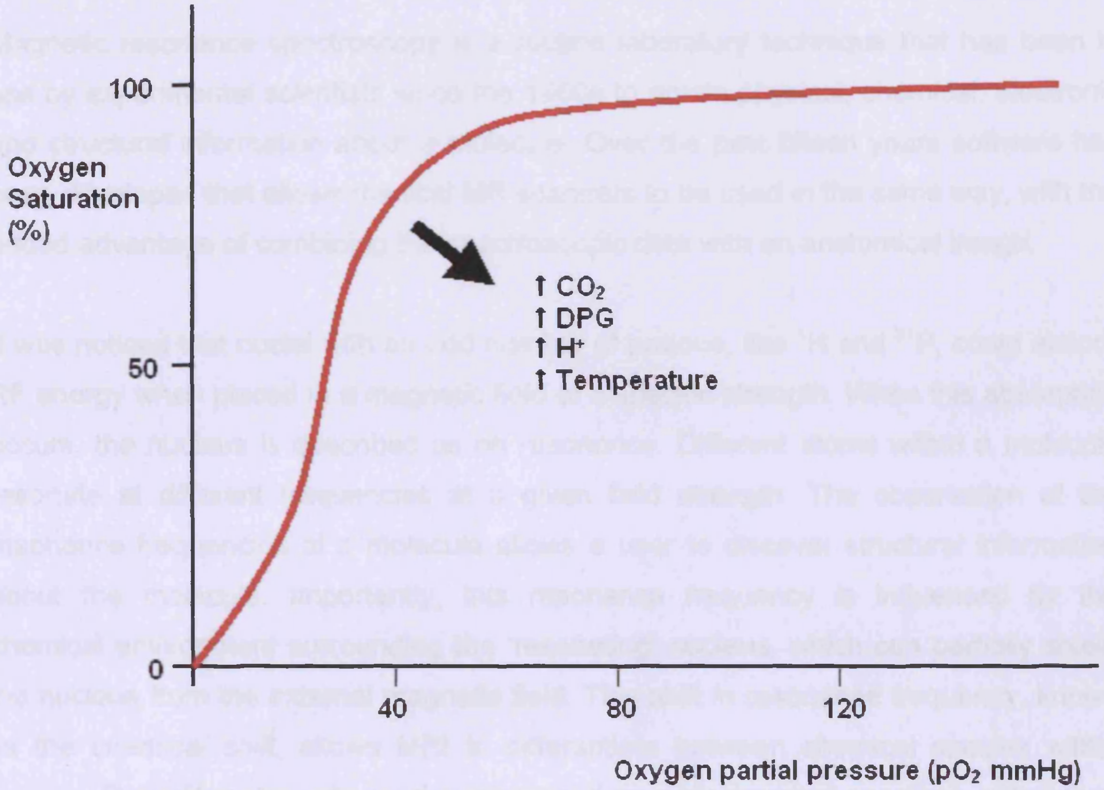

R_2* maps minimize, but do not completely eliminate, inflow effects that can contribute to contrast on single-echo gradient-echo images, while retaining sensitivity to oxygenation changes that may be caused by alterations in blood flow. Other limitations with particular relevance to imaging of the prostate gland include susceptibility artefacts generated by large quantities of rectal gas and movement of the gland caused by rectal filling during the image acquisition time. These may be partially reduced by asking patients to empty their bowels before the scan.

2.4 Magnetic Resonance Spectroscopy (MRS)

2.4.1 Background

Magnetic resonance spectroscopy is a routine laboratory technique that has been in use by experimental scientists since the 1950s to obtain physical, chemical, electronic and structural information about a molecule. Over the past fifteen years software has been developed that allows medical MR scanners to be used in the same way, with the added advantage of combining the spectroscopic data with an anatomical image.

It was noticed that nuclei with an odd number of protons, like ^{1}H and ^{31}P, could absorb RF energy when placed in a magnetic field of a specific strength. When this absorption occurs, the nucleus is described as on *resonance*. Different atoms within a molecule resonate at different frequencies at a given field strength. The observation of the resonance frequencies of a molecule allows a user to discover structural information about the molecule. Importantly, this resonance frequency is influenced by the chemical environment surrounding the 'resonating' nucleus, which can partially shield the nucleus from the external magnetic field. This shift in resonance frequency, known as the *chemical shift*, allows MRI to differentiate between chemical species within tissues. The information obtained is presented as a biochemical spectrum rather than an image, providing a variety of quantitative data depending on the nucleus involved and the chemical environment that surrounds it. Disease processes, such as cancer, have altered chemical environments compared to the surrounding normal tissue and therefore produce a different spectrum of nuclear magnetic resonance. **(figure 2.8)**

Most clinical MRS in oncology is concerned with signals from ^{1}H or ^{31}P atoms that occur naturally in body tissues. ^{19}F signals from anticancer drugs can be used to analyse pharmacokinetics and pharmacodynamics. Synthetic ^{13}C-labelled molecules are also used to assess the biochemical and physiological parameters of tumours and their response to treatment.

Spectroscopy is being used with increasing frequency in oncology especially in cases of brain and prostate cancer. One of the biggest challenges in prostate radiotherapy is determining the pattern of malignant change within a gland that is also heterogeneously filled with areas of benign hypertrophy. Dose escalation to the whole gland is limited by urethral and rectal toxicity. Spectroscopy is being evaluated as a method by which the malignant regions of the organ can be selectively identified [45], thereby allowing dose escalation to limited portions of the gland and sparing excessive dose to the normal tissues.

Figure 2.8a Magnetic resonance spectroscopy of the prostate gland

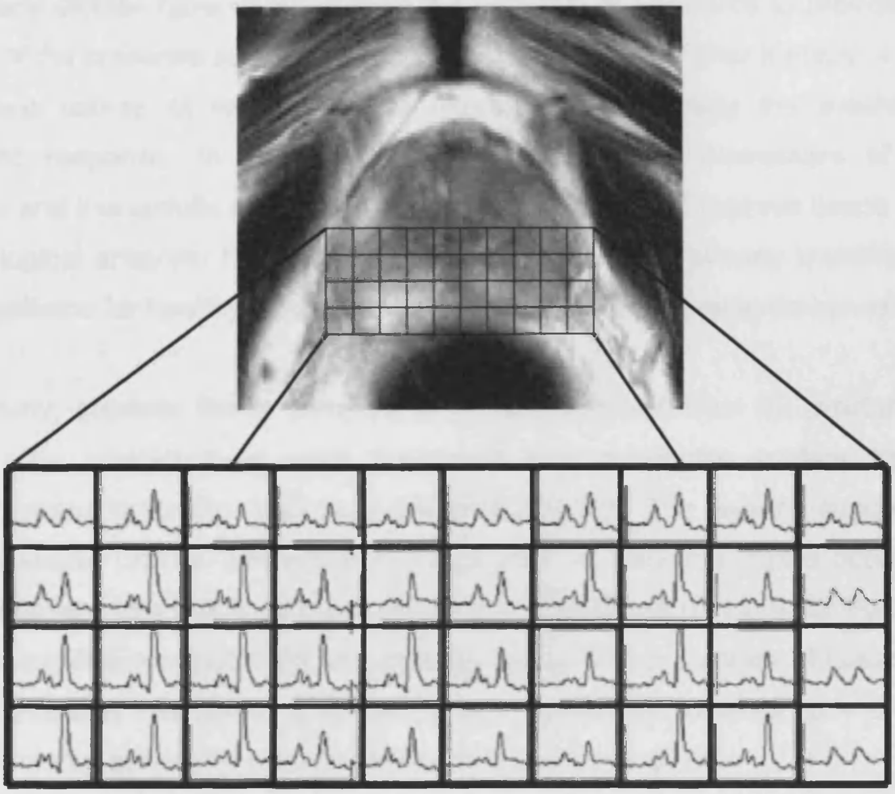

Figure 2.8b The spectrum produced in the benign and malignant prostate

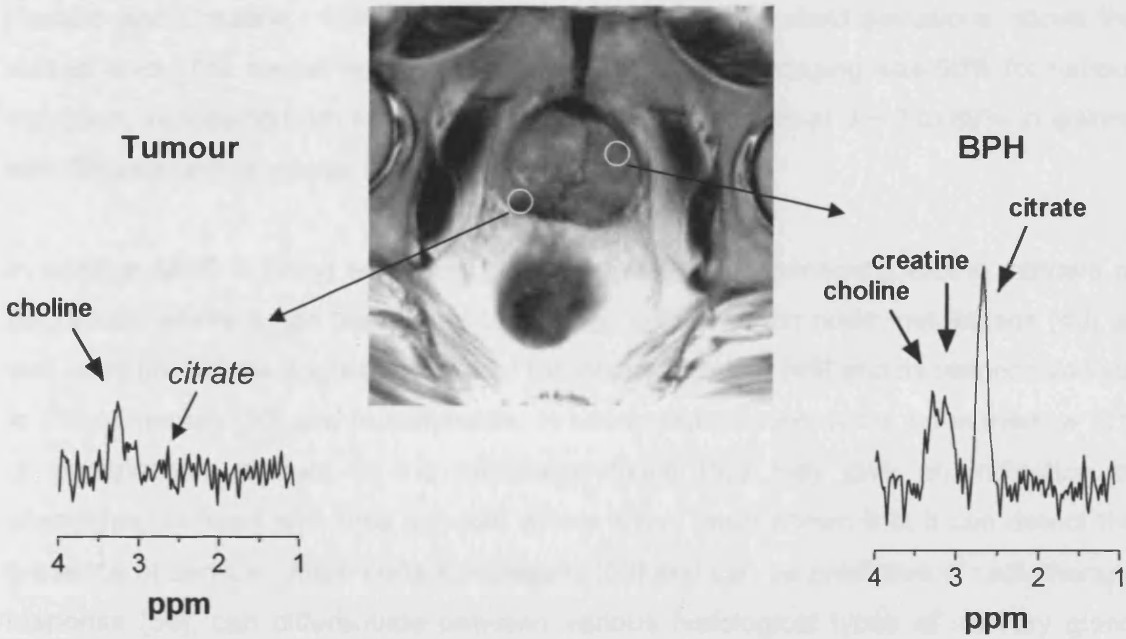

Recent studies in pre-prostatectomy patients have indicated that the metabolic information provided by MRS combined with the anatomical information provided by MRI can significantly improve the assessment of cancer location and extent within the prostate, extracapsular spread, and cancer aggressiveness. Additionally, pre- and post-therapy studies have demonstrated the potential of MRI/MRS to provide a direct measure of the presence and spatial extent of prostate cancer after therapy, a measure of the time course of response, and information concerning the mechanism of therapeutic response. In addition to detecting metabolic biomarkers of disease behaviour and therapeutic response, MRI/MRSI guidance can improve tissue selection for pathological analysis. High-resolution MRS studies have already identified unique spectral patterns for healthy glandular and stromal tissues and prostate cancer.

In one study, prostate tissue samples ($n = 199$) obtained from 82 prostate cancer patients after prostatectomy were compared with metabolite profiles from high-resolution proton magnetic resonance spectroscopy [46]. The findings suggested that tissue metabolite profiles differentiated malignant from benign samples obtained from the same patient ($p < 0.005$) and correlated with PSA levels ($p < 0.006$). Furthermore, metabolite profiles obtained from histologically benign tissue samples of Gleason score 6 and 7 prostates delineated a subset of less aggressive tumours ($p < 0.008$) and predicted tumour perineural invasion within the subset ($p < 0.03$).

In another report, spectral profiles from 123 patients who underwent endorectal MR imaging and MR spectroscopic imaging were compared with the corresponding pathology [47]. Voxels in the peripheral zone were considered suspicious for cancer if Choline and Creatine : Citrate ratio was at least two standard deviations above the normal level. The overall sensitivity of MR spectroscopic imaging was 56% for tumour detection, increasing from 44% in lesions with Gleason score of 3 + 3 to 89% in lesions with Gleason score greater than or equal to 4 + 4.

In addition MRS is being evaluated as a diagnostic and monitoring tool in cancers of the breast, where it has been used to identify axillary lymph node metastases [48] as well as to predict the aggressiveness of the primary tumour [49] and its responsiveness to chemotherapy [50] and in leukaemia, in which examination of the bone marrow [51] or phospholipid content of the peripheral blood [52] may give an indication of phenotype. In head and neck cancers where it has been shown that it can detect the presence of cervical lymph node metastases [53] and can be predictive of radiotherapy response [54], can differentiate between various histological types of salivary gland neoplasm [55] and can distinguish benign from malignant thyroid nodules [56]. MRS has also been successfully tried in cancers of the colon, cervix, pancreas, oesophagus and soft tissue sarcomas. There have also been preliminary reports of using spectroscopy of body fluids such as bile or semen to detect the presence of malignant cells as a diagnostic test for hepato-biliary or prostate cancer respectively [57, 58].

MR spectroscopy has the ability to detect biochemical and molecular targets that have prognostic significance. It does this without the need for any tissue to be removed from the body and provides an assessment of the whole tumour in its intact living state with no artefacts generated by cutting and fixing the tissue. As most cancer patients will undergo imaging as part of their diagnostic and planning work-up these prognostic analyses can be incorporated within existing procedures, thereby negating the need for additional predictive tests.

MRS is not without its problems. A common difficulty is magnetic field distortion, chiefly resulting in inadequate water suppression and distorted spectral line-shapes. In some cases, metabolite signals are hidden under much stronger lipid or water resonances. Often several metabolites are present at relatively high concentrations in a particular tissue, however the MR sensitivity for their detection is poor due to their signal energy being spread over a large number of closely spaced resonances or from signal cancellation of overlapping resonances. For example, glutamate is present at a similar concentration as N-acetyl aspartate, though in practice its signal is barely detectable. Another area for future improvement in MRS is undoubtedly in the area of improved spectral analysis, which will need to overcome the presence of low signal to noise ratios and unknown lipid, water or macromolecular baseline signals. With the realisation that MRS is a potentially powerful clinical tool that may solve some difficult clinical dilemmas, development is progressing rapidly. Also, due to the fact that it is entirely non-invasive and adds little to the imaging time and department throughput, MRS is quickly gaining popularity.

2.4.2 Magnetic resonance spectroscopy of fluorinated nitroimidazoles for the dectection of tumour hypoxia

MRS provides details of tissue chemistry from several administered nuclei including ^{1}H, ^{31}P, ^{13}C, ^{23}Na. The para-magnetic nucleus, ^{19}F can be relatively easily conjugated other molecules to allow particular aspects of the tissue of interest to be evaluated. Fluorinated 2- nitroimidazoles have been produced to allow hypoxic cells to be identified by this method. Raleigh *et al.* synthesised a hexafluorinated 2-nitroimidazole (CCI-103F) [59]. In Balb/C mice it was preferentially bound within tumour with a plasma-to-tumour ratio of 0.8. Li et al used this technique in SCCVII tumours finding that the signal obtained positively correlated with tumour size consistent with the fact that larger SCCVII tumours have larger hypoxic fractions [60]. Further analysis of the fraction of surviving tumour cells after a single fraction of 10Gy irradiation revealed that tumours that retained larger amounts of CCI-103F had higher surviving fractions. Further studies established the proof of principle that fluorinated probes were suitable MRS directed markers of hypoxia [61].The same analogue was evaluated with another fluorinated 2-nitroimidazole (Ro 07-0741) by Maxwell et al [62]. Ro 07-0741 is a mono-fluorinated probe and was found to be less lipophilic than its hexafluorinated counterpart. Signal was readily detectable by MRS in EMT6 tumour, liver, and brain soon after i.v. injection in BALB/c mice. Tumour levels remained constant up to 10 hours after injection whilst there was a reduction in signal intensity from brain and liver. The work was repeated in KHT and RIF-1 tumours in C3H/He mice. RIF-1 tumours have a lower hypoxic fraction than KHT tumours and the comparative signal obtained reflected this difference. However, the problem of the lipophilic nature of these compounds remains to be solved: a hydrophilic compound would not only be less neurotoxic, but also be less susceptible to metabolism by non-nitroreductive pathways. This was the rational for the design of SR4554, that consists of a hydrophilic side chain, three fluorine atoms to enhance magnetic detection and the 2-nitroimidazole ring to bioreduce only within hypoxic cells [63]. In vivo and clinical studies are in progress.

2.5 Diffusion Weighted Imaging (DWI)

Diffusion imaging is essentially a method of measuring the Brownian motion of molecules, which in biological tissue means the diffusion of water molecules. In living tissues water does not diffuse equally in all directions, preferring to follow the direction of ordered tissue planes, fibres and other structural elements within the organ, with its flow restricted by natural barriers such as cell membranes, macromolecules and variations in interstitial pressure. As a result the diffusion image can be seen as a measure of three-dimensional spatial order within an organ. Cancer, by its very nature, tends to produce disorder, destroying natural tissue layers, distorting fibres and altering the usual motion of water molecules.

All forms of anti-cancer therapy tend to cause cellular breakdown, necrosis and a reduction of tumour interstitial fluid pressure. This leads to an increase in the movement of water between the various fluid compartments and a subsequent increase in the 'apparent diffusion coefficient' (ADC) measured by MRI. Therefore an increase in ADC value can be interpreted as a response to treatment. In this way diffusion imaging offers a new way of assessing and studying cancer in-vivo.

Diffusion data is obtained by applying extra opposing gradient pulses of differing duration and amplitude to T_2-weighted MR sequences. If there is no net movement of water molecules during this period of time, there will be exact cancelling out of the applied balanced gradients and therefore no change in signal intensity. If there is water movement there will be imbalance which results in a signal change in the images obtained. The degree of diffusion weighting is indicated by the b-value (measured in s/mm^2). The larger the b-value, the greater the decrease in measured signal intensity. The gradient of the ln[signal intensity] time plot for a number of b-values gives the apparent diffusion coefficient (ADC).

The only established clinical use of diffusion-weighted imaging at present is the detection of ischaemic stroke in the acute phase [64]. Little is known about its potential in oncology although a number of pre-clinical and early phase clinical studies have begun to investigate its usefulness. It has been shown in a number of tumour types that diffusion imaging can help differentiate between benign and malignant tumours [65, 66] and has possible implications for radiotherapy treatment planning [67]. As with spectroscopy, diffusion imaging may be able to differentiate between recurrent malignant glioma and radiation induced necrosis [68]. As a prognostic indicator, diffusion weighted imaging has also shown promise. In a pre-clinical study using rat mammary tumours, a low pre-chemotherapy ADC value has been shown to correlate with response [69]. Similarly, in a study of 14 patients with colorectal cancer, the ADC maps were predictive of response to neo-adjuvant chemo-radiotherapy [70].

In prostate cancer, diffusion imaging has shown early promise in the improvement of tumour detection, with sensitivity and specificity values for the discrimination of tumour from benign hypertrophy and normal peripheral zone frequently exceeding 80% [71-75] **(figure 2.9)**. However its potential is more far-reaching. The overall apparent diffusion coefficient (ADC) encompasses both the diffusion of water molecules within tissue as well as contributions from the flow of water molecules within vessels [76]. It is possible to distinguish between these two components of measured water diffusion by altering the degree of diffusion weighting. With the use of lower b-values (<100 s/mm^2) water movement caused by flow within vessels will be the predominant factor determining ADC. For higher b-values, the movement of water molecules in the extravascular space is preferentially measured, reflecting the cellularity of the extracellular matrix. As a result, diffusion weighted MRI can be used to measure perfusion or cellular density.

Larger clinical trials are required to evaluate whether this technique can offer predictive information in cancer medicine and the extent to which it can help guide treatment planning.

Figure 2.9 Diffusion MRI of the prostate gland

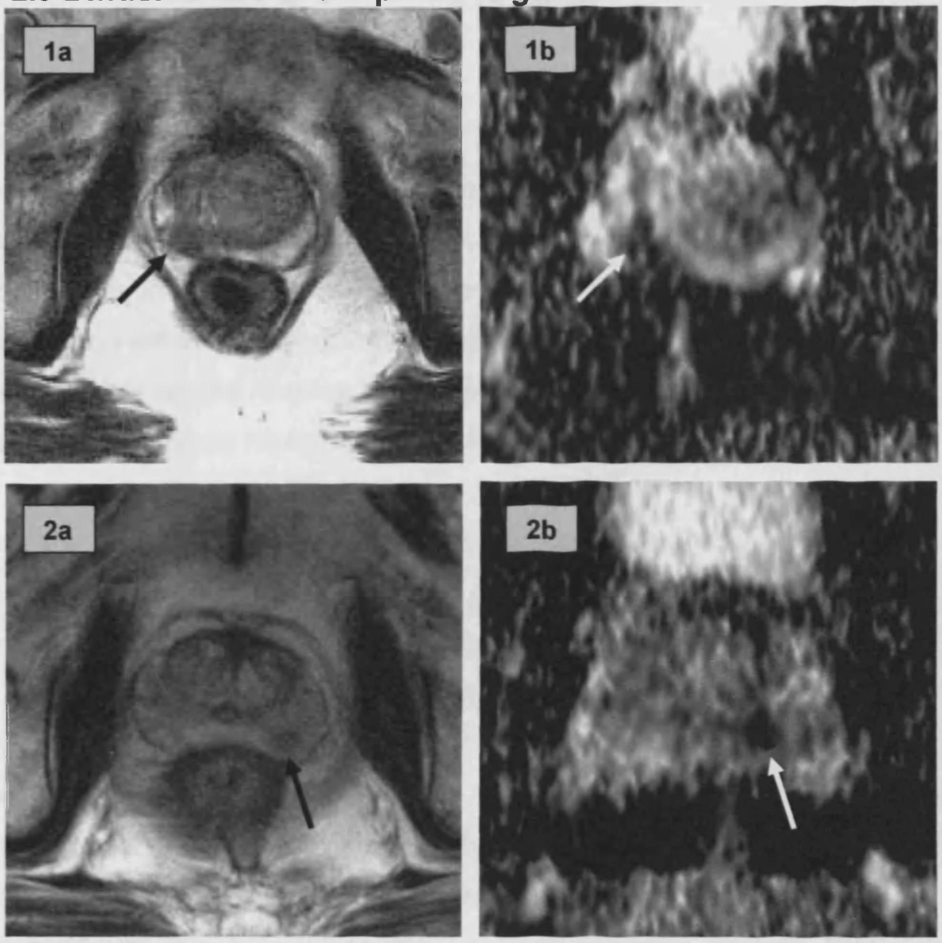

Two patients are shown with tumour indicated by an arrow. T_2-weighted images (left column) are compared with diffusion weighted ADC maps (right column). In the top row the patient has tumour in the right posterior peripheral zone and in the bottom row the patient has a small focus of tumour in the left posterior peripheral zone. Regions with low ADC value correspond to areas of low signal intensity on the T_2-weighted images.

2.6 Functional imaging for radiotherapy planning

Modern computer software and improvements in linear accelerator design now allow the radiation oncologist to design irregularly shaped fields that conform accurately to the desired target volume and also permit modulation of the radiation beam intensity within that volume. The use of 'intensity modulated radiation therapy' (IMRT) has proliferated in recent years with the expectation that the very precise dose distributions that are now possible will minimize normal tissue side-effects and allow escalation of radiation dose to the tumour. In the 'pre-conformal' era the weighting and energy of each radiation beam was decided depending on the patient's contour, the depth of the tumour from each entry portal and the relative position of any structures that need to be avoided. This 'forward-planning' approach was also used in the early, non-conformal CT-based planning systems, the only difference being that a computer program calculated the absorbed dose-distribution more accurately based on the pixel intensity of the cross sectional imaging used, allowing greater refinement of each beam parameter.

It is now possible to approach the planning process in reverse. The starting point being the specification of the required dose in the target volume and dose limits within other specified volumes that contain normal tissues. An iterative computer algorithm then calculates the optimum beam intensities that will generate the desired homogenous dose-distribution within the target volume without exceeding the specified normal-tissue dose limits. This is termed 'inverse treatment planning' and is currently used to produce the most highly conformal radiotherapy plans in use today.

However, it is possible to go a step further. Throughout the history of radiotherapy the goal has been to produce a homogenous dose distribution across the target volume. Tumours, on the other hand, are not homogenous blocks of tissue. Within each tumour volume there are areas that are proliferating and areas that are quiescent, hypoxic regions and well oxygenated regions and portions with altered vascularity, varying metabolism and genetically determined differences in radiation resistance lying adjacent to each other. The use of functional imaging techniques to identify these biological variations within the tumour results in functional 'maps' which can be superimposed onto the standard anatomical cross-sectional imaging, highlighting sub-volumes within the target that may require a higher radiation dose. These sub-volumes could represent areas of increased proliferation or relative radioresistance, such as hypoxia. It is also possible to use functional imaging to differentiate areas of tumour from areas of benign change, within an organ that has traditionally been treated in its entirety, with a view to only irradiating the malignant areas, for example with prostate cancer.

In order to target these biological sub-volumes with a higher absorbed dose than the surrounding tissue requires the intentional creation of dose-inhomogeneity. This technique of dose 'painting' (in 2D) or dose 'sculpting' (in 3D) as originally described by Ling and colleagues [77], involves the same inverse planning technique as previously described, with the addition of a 'biological target volume' within the planning target volume which can be assigned a separate, higher, dose level, essentially resulting in a hot-spot of absorbed dose over this new, functionally guided, biological target. **(Figure 2.10)**

Figure 2.10 Radiotherapy planning with DCE-MRI

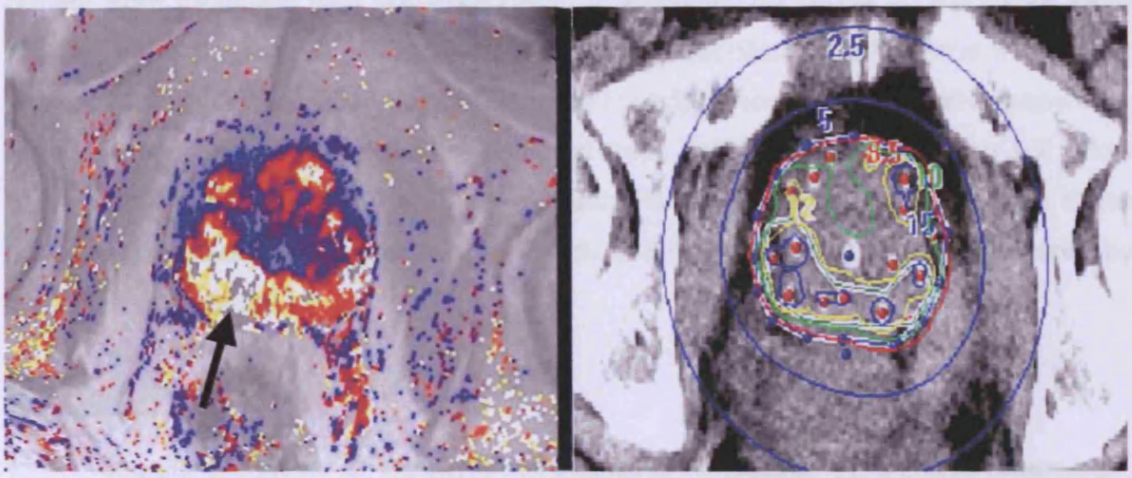

A simulated high dose-rate brachytherapy plan (right image) conforming to the 'biological target' as determined by a K^{trans} map of the prostate (left image). The dynamic MRI image has shown an area of high K^{trans} values (arrow) in the posterior aspect of the prostate gland. The red line on the radiotherapy plan indicates the 8.5 Gray (per fraction) isodose, this is the dose prescribed to the whole gland. The yellow line shows the 15 Gray isodose (a boost of 175%), directed at the biological target.

There are a number of theoretical and practical advantages with this approach. Firstly, despite sophisticated planning techniques, conventional dose escalation will ultimately result in dose limits defined by normal tissue toxicity. For example, in the case of prostate cancer (where there is a proven case for dose escalation [78]), IMRT can safely deliver 80–82Gy to the whole prostate with acceptable normal tissue toxicity [79]. However, despite the fact that highly conformal dose distributions can be theoretically produced to deliver doses approaching 100Gy in some patients, with a rectal dose volume histogram (DVH) that is within tolerance, this treatment is unacceptable. This is because of unavoidable urethral toxicity, a structure that, because of its position running through the centre of the target volume, can never be avoided even with the most advanced planning algorithms. Dose sculpting, on the other hand, provides a mechanism by which the portions of the prostate that require the highest radiation dose because of their intrinsic biology, can be dose escalated separately from the remainder of the gland, thereby increasing the probability of achieving the required dose level without exceeding any normal tissue dose limit.

Secondly, the functional information gained in the planning stages of the radiotherapy process may lead to the optimal choice of treatment modality, or combination of treatment modalities. If the tumour is found to be very hypoxic, radiotherapy could be combined with hypoxic sensitizers or the breathing of high oxygen containing gas mixtures. Highly proliferating cancers may be more appropriately treated with combined chemo-radiotherapy or in conjunction with other biological agents. Tumours with extensive evidence of neo-vascularization or expression of vascular growth factors may benefit from treatment with anti-angiogenic or anti-vascular drugs. In the future there may be ways to target specific steps in tumour metabolism or offer gene therapy for specific defects defined by molecular imaging in conjunction with localized therapy. Finally, the prognostic information obtained from the functional approach will allow better risk stratification and therefore a greater ability to discriminate between those patients that require an aggressive approach and those who are likely to be cured by less intensive efforts.

References

1 Mirowitz SA, Brown JJ, Heiken JP. Evaluation of the prostate and prostatic carcinoma with gadolinium-enhanced endorectal coil MR imaging. *Radiology.* 1993;186:153-157.

2 Quinn SF, Franzini DA, Demlow TA, *et al.* MR imaging of prostate cancer with an endorectal surface coil technique: correlation with whole-mount specimens. *Radiology.* 1994;190:323-327.

3 Brown G, Macvicar DA, Ayton V, Husband JE. The role of intravenous contrast enhancement in magnetic resonance imaging of prostatic carcinoma. *Clin Radiol.* 1995;50:601-606.

4 Huch Boni RA, Boner JA, Lutolf UM, Trinkler F, Pestalozzi DM, Krestin GP. Contrast-enhanced endorectal coil MRI in local staging of prostate carcinoma. *J Comput Assist Tomogr.* 1995;19:232-237.

5 Daldrup HE, Shames DM, Husseini W, Wendland MF, Okuhata Y, Brasch RC. Quantification of the extraction fraction for gadopentetate across breast cancer capillaries. *Magn Reson Med.* 1998;40:537-543.

6 Bruening R, Berchtenbreiter C, Holzknecht N, *et al.* Effects of three different doses of a bolus injection of gadodiamide: assessment of regional cerebral blood volume maps in a blinded reader study. *AJNR Am J Neuroradiol.* 2000;21:1603-1610.

7 Dennie J, Mandeville JB, Boxerman JL, Packard SD, Rosen BR, Weisskoff RM. NMR imaging of changes in vascular morphology due to tumor angiogenesis. *Magn Reson Med.* 1998;40:793-799.

8 Collins DJ, Padhani AR. Dynamic magnetic resonance imaging of tumor perfusion. Approaches and biomedical challenges. *IEEE Eng Med Biol Mag.* 2004;23:65-83.

9 Gibbs P, Young BJ, Turnbull LS. Diagnostic utility of perfusion weighted imaging of the prostate. In: Proceeding of the UK Radiological Congress; 2001; London; 2001. p. 53.

10 Noseworthy MN, Morton G, Wright GA. Comparison of normal and cancerous prostate using dynamic TI and T2* weighted MRI. In: Proceedings of the 7th annual meeting of the international society for magnetic resonance in medicine; 1999; Philadelphia; 1999. p. 2148.

11 Hoskin PJ, Carnell DM, Taylor NJ, *et al.* Hypoxia in prostate cancer: correlation of BOLD-MRI with pimonidazole immunohistochemistry-initial observations. *Int J Radiat Oncol Biol Phys.* 2007;68:1065-1071.

12 Jager GJ, Ruijter ET, van de Kaa CA, *et al.* Dynamic TurboFLASH subtraction technique for contrast-enhanced MR imaging of the prostate: correlation with histopathologic results. *Radiology.* 1997;203:645-652.

13 Buckley DL, Kerslake RW, Blackband SJ, Horsman A. Quantitative analysis of multi-slice Gd-DTPA enhanced dynamic MR images using an automated simplex minimization procedure. *Magn Reson Med.* 1994;32:646-651.

14 Donahue KM, Burstein D, Manning WJ, Gray ML. Studies of Gd-DTPA relaxivity and proton exchange rates in tissue. *Magn Reson Med.* 1994;32:66-76.

15 Padhani AR, Khoo VS, Suckling J, Husband JE, Leach MO, Dearnaley DP. Evaluating the effect of rectal distension and rectal movement on prostate gland position using cine MRI. *Int J Radiat Oncol Biol Phys.* 1999;44:525-533.

16 Tofts PS, Brix G, Buckley DL, *et al.* Estimating kinetic parameters from dynamic contrast-enhanced T(1)-weighted MRI of a diffusable tracer: standardized quantities and symbols. *J Magn Reson Imaging.* 1999;10:223-232.

17 Tofts PS. Modeling tracer kinetics in dynamic Gd-DTPA MR imaging. *J Magn Reson Imaging.* 1997;7:91-101.

18 Buckley DL. Uncertainty in the analysis of tracer kinetics using dynamic contrast-enhanced T1-weighted MRI. *Magn Reson Med.* 2002;47:601-606.

19 Sinha AA, Quast BJ, Reddy PK, *et al.* Microvessel density as a molecular marker for identifying high-grade prostatic intraepithelial neoplasia precursors to prostate cancer. *Exp Mol Pathol.* 2004;77:153-159.

20 Trojan L, Thomas D, Friedrich D, *et al.* Expression of different vascular endothelial markers in prostate cancer and BPH tissue: an immunohistochemical and clinical evaluation. *Anticancer Res.* 2004;24:1651-1656.

21 Padhani AR. Dynamic contrast-enhanced MRI in clinical oncology: current status and future directions. *J Magn Reson Imaging.* 2002;16:407-422.

22 Engelbrecht MR, Huisman HJ, Laheij RJ, *et al.* Discrimination of prostate cancer from normal peripheral zone and central gland tissue by using dynamic contrast-enhanced MR imaging. *Radiology.* 2003;229:248-254.

23 Padhani AR, Gapinski CJ, Macvicar DA, *et al.* Dynamic contrast enhanced MRI of prostate cancer: correlation with morphology and tumour stage, histological grade and PSA. *Clin Radiol.* 2000;55:99-109.

24 Hara N, Okuizumi M, Koike H, Kawaguchi M, Bilim V. Dynamic contrast-enhanced magnetic resonance imaging (DCE-MRI) is a useful modality for the precise detection and staging of early prostate cancer. *Prostate.* 2005;62:140-147.

25 Kozlowski P, Chang SD, Jones EC, Berean KW, Chen H, Goldenberg SL. Combined diffusion-weighted and dynamic contrast-enhanced MRI for prostate cancer diagnosis--correlation with biopsy and histopathology. *J Magn Reson Imaging.* 2006;24:108-113.

26 Namimoto T, Morishita S, Saitoh R, Kudoh J, Yamashita Y, Takahashi M. The value of dynamic MR imaging for hypointensity lesions of the peripheral zone of the prostate. *Comput Med Imaging Graph.* 1998;22:239-245.

27 Futterer JJ, Heijmink SW, Scheenen TW, *et al.* Prostate Cancer Localization with Dynamic Contrast-enhanced MR Imaging and Proton MR Spectroscopic Imaging. *Radiology.* 2006.

28 Futterer JJ, Engelbrecht MR, Huisman HJ, *et al.* Staging prostate cancer with dynamic contrast-enhanced endorectal MR imaging prior to radical prostatectomy: experienced versus less experienced readers. *Radiology.* 2005;237:541-549.

29 Ogawa S, Lee TM. Magnetic resonance imaging of blood vessels at high fields: in vivo and in vitro measurements and image simulation. *Magn Reson Med.* 1990;16:9-18.

30 Karczmar GS, River JN, Li J, Vijayakumar S, Goldman Z, Lewis MZ. Effects of hyperoxia on T2* and resonance frequency weighted magnetic resonance images of rodent tumours. *NMR Biomed.* 1994;7:3-11.

31 Robinson SP, Rodrigues LM, Ojugo AS, McSheehy PM, Howe FA, Griffiths JR. The response to carbogen breathing in experimental tumour models monitored by gradient-recalled echo magnetic resonance imaging. *Br J Cancer.* 1997;75:1000-1006.

32 Kuperman V, River JN, Lewis MZ, Lubich LM, Karczmar GS. Changes in T2*-weighted images during hyperoxia differentiate tumors from normal tissue. *Magn Reson Med.* 1995;33:318-325.

33 Al-Hallaq HA, River JN, Zamora M, Oikawa H, Karczmar GS. Correlation of magnetic resonance and oxygen microelectrode measurements of carbogen-induced changes in tumor oxygenation. *Int J Radiat Oncol Biol Phys.* 1998;41:151-159.

34 Maxwell RJ, Robinson SP, McIntyre DJO, Griffiths JR, Vojnovic B. Comparison of changes in gradient-echo 1H MR image intensity and pO2 in rodent tumours in response to carbogen breathing. *Proc I. S. M. R. M 7th Annual Meeting.* 1999:495 (abstract).

35 Neeman M, Dafni H, Bukhari O, Braun RD, Dewhirst MW. In vivo BOLD contrast MRI mapping of subcutaneous vascular function and maturation: validation by intravital microscopy. *Magn Reson Med.* 2001;45:887-898.

36 Robinson SP, Rijken PF, Howe FA, *et al.* Tumor vascular architecture and function evaluated by non-invasive susceptibility MRI methods and immunohistochemistry. *J Magn Reson Imaging.* 2003;17:445-454.

37 Baudelet C, Gallez B. How does blood oxygen level-dependent (BOLD) contrast correlate with oxygen partial pressure (pO2) inside tumors? *Magn Reson Med.* 2002;48:980-986.

38 Howe FA, Robinson SP, Rodrigues LM, Griffiths JR. Flow and oxygenation dependent (FLOOD) contrast MR imaging to monitor the response of rat tumors to carbogen breathing. *Magn Reson Imaging.* 1999;17:1307-1318.

39 Robinson SP, Collingridge DR, Howe FA, Rodrigues LM, Chaplin DJ, Griffiths JR. Tumour response to hypercapnia and hyperoxia monitored by FLOOD magnetic resonance imaging. *NMR Biomed.* 1999;12:98-106.

40 Rodrigues LM, Howe FA, Griffiths JR, Robinson SP. Tumor R2* is a prognostic indicator of acute radiotherapeutic response in rodent tumors. *J Magn Reson Imaging.* 2004;19:482-488.

41 Taylor NJ, Baddeley H, Goodchild KA, *et al.* BOLD MRI of human tumor oxygenation during carbogen breathing. *J Magn Reson Imaging.* 2001;14:156-163.

42 Griffiths JR, Taylor NJ, Howe FA, *et al.* The response of human tumors to carbogen breathing, monitored by Gradient-Recalled Echo Magnetic Resonance Imaging. *Int J Radiat Oncol Biol Phys.* 1997;39:697-701.

43 Diergarten T, Martirosian P, Kottke R, *et al.* Functional characterization of prostate cancer by integrated magnetic resonance imaging and oxygenation changes during carbogen breathing. *Invest Radiol.* 2005;40:102-109.

44 Hoskin P, Carnell D, Taylor N, *et al.* Hypoxia in prostate cancer: correlation of BOLD-MRI with pimonidazole immunohistochemistry. *Int J Radiat Oncol Biol Phys.*In Press.

45 Kurhanewicz J, Swanson MG, Nelson SJ, Vigneron DB. Combined magnetic resonance imaging and spectroscopic imaging approach to molecular imaging of prostate cancer. *J Magn Reson Imaging.* 2002;16:451-463.

46 Cheng LL, Burns MA, Taylor JL, *et al.* Metabolic characterization of human prostate cancer with tissue magnetic resonance spectroscopy. *Cancer Res.* 2005;65:3030-3034.

47 Zakian KL, Sircar K, Hricak H, *et al.* Correlation of proton MR spectroscopic imaging with gleason score based on step-section pathologic analysis after radical prostatectomy. *Radiology.* 2005;234:804-814.

48 Seenu V, Pavan Kumar MN, Sharma U, Gupta SD, Mehta SN, Jagannathan NR. Potential of magnetic resonance spectroscopy to detect metastasis in axillary lymph nodes in breast cancer. *Magn Reson Imaging.* 2005;23:1005-1010.

49 Lean C, Doran S, Somorjai RL, *et al.* Determination of grade and receptor status from the primary breast lesion by magnetic resonance spectroscopy. *Technol Cancer Res Treat.* 2004;3:551-556.

50 Meisamy S, Bolan PJ, Baker EH, *et al.* Neoadjuvant chemotherapy of locally advanced breast cancer: predicting response with in vivo (1)H MR spectroscopy--a pilot study at 4 T. *Radiology.* 2004;233:424-431.

51 Jensen KE, Jensen M, Grundtvig P, Thomsen C, Karle H, Henriksen O. Localized in vivo proton spectroscopy of the bone marrow in patients with leukemia. *Magn Reson Imaging.* 1990;8:779-789.

52 Kuliszkiewicz-Janus M, Tuz MA, Baczynski S. Application of 31P MRS to the analysis of phospholipid changes in plasma of patients with acute leukemia. *Biochim Biophys Acta.* 2005;1737:11-15.

53 Mukherji SK, Schiro S, Castillo M, Kwock L, Muller KE, Blackstock W. Proton MR spectroscopy of squamous cell carcinoma of the extracranial head and neck: in vitro and in vivo studies. *AJNR Am J Neuroradiol.* 1997;18:1057-1072.

54 Bezabeh T, Odlum O, Nason R, *et al.* Prediction of treatment response in head and neck cancer by magnetic resonance spectroscopy. *AJNR Am J Neuroradiol.* 2005;26:2108-2113.

55 King AD, Yeung DK, Ahuja AT, *et al.* Salivary gland tumors at in vivo proton MR spectroscopy. *Radiology.* 2005;237:563-569.

56 Russell P, Lean CL, Delbridge L, May GL, Dowd S, Mountford CE. Proton magnetic resonance and human thyroid neoplasia. I: Discrimination between benign and malignant neoplasms. *Am J Med.* 1994;96:383-388.

57 Averna TA, Kline EE, Smith AY, Sillerud LO. A decrease in 1H nuclear magnetic resonance spectroscopically determined citrate in human seminal fluid accompanies the development of prostate adenocarcinoma. *J Urol.* 2005;173:433-438.

58 Khan SA, Cox IJ, Thillainayagam AV, Bansi DS, Thomas HC, Taylor-Robinson SD. Proton and phosphorus-31 nuclear magnetic resonance spectroscopy of human bile in hepatopancreaticobiliary cancer. *Eur J Gastroenterol Hepatol.* 2005;17:733-738.

59 Raleigh JA, Franko AJ, Treiber EO, Lunt JA, Allen PS. Covalent binding of a fluorinated 2-nitroimidazole to EMT-6 tumors in Balb/C mice: detection by F-19 nuclear magnetic resonance at 2.35 T. *Int J Radiat Oncol Biol Phys.* 1986;12:1243-1245.

60 Li SJ, Jin GY, Moulder JE. Prediction of tumor radiosensitivity by hexafluoromisonidazole retention monitored by [1H]/[19F] magnetic resonance spectroscopy. *Cancer Commun.* 1991;3:133-139.

61 Raleigh JA, Franko AJ, Kelly DA, Trimble LA, Allen PS. Development of an in vivo 19F magnetic resonance method for measuring oxygen deficiency in tumors. *Magn Reson Med.* 1991;22:451-466.

62 Maxwell RJ, Workman P, Griffiths JR. Demonstration of tumor-selective retention of fluorinated nitroimidazole probes by 19F magnetic resonance spectroscopy in vivo. *Int J Radiat Oncol Biol Phys.* 1989;16:925-929.

63 Aboagye EO, Kelson AB, Tracy M, Workman P. Preclinical development and current status of the fluorinated 2-nitroimidazole hypoxia probe N-(2-hydroxy-3,3,3-trifluoropropyl)-2-(2-nitro-1-imidazolyl) acetamide (SR 4554, CRC 94/17): a non-invasive diagnostic probe for the measurement of tumor hypoxia by magnetic resonance spectroscopy and imaging, and by positron emission tomography. *Anticancer Drug Des.* 1998;13:703-730.

64 Huisman TA. Diffusion-weighted imaging: basic concepts and application in cerebral stroke and head trauma. *Eur Radiol.* 2003;13:2283-2297.

65 Habermann CR, Gossrau P, Graessner J, *et al.* Diffusion-weighted echo-planar MRI: a valuable tool for differentiating primary parotid gland tumors? *Rofo.* 2005;177:940-945.

66 Sato C, Naganawa S, Nakamura T, *et al.* Differentiation of noncancerous tissue and cancer lesions by apparent diffusion coefficient values in transition and peripheral zones of the prostate. *J Magn Reson Imaging.* 2005;21:258-262.

67 Jena R, Price SJ, Baker C, *et al.* Diffusion tensor imaging: possible implications for radiotherapy treatment planning of patients with high-grade glioma. *Clin Oncol (R Coll Radiol).* 2005;17:581-590.

68 Hein PA, Eskey CJ, Dunn JF, Hug EB. Diffusion-weighted imaging in the follow-up of treated high-grade gliomas: tumor recurrence versus radiation injury. *AJNR Am J Neuroradiol.* 2004;25:201-209.

69 Roth Y, Tichler T, Kostenich G, *et al.* High-b-value diffusion-weighted MR imaging for pretreatment prediction and early monitoring of tumor response to therapy in mice. *Radiology.* 2004;232:685-692.

70 Dzik-Jurasz A, Domenig C, George M, *et al.* Diffusion MRI for prediction of response of rectal cancer to chemoradiation. *Lancet.* 2002;360:307-308.

71 Pickles MD, Gibbs P, Sreenivas M, Turnbull LW. Diffusion-weighted imaging of normal and malignant prostate tissue at 3.0T. *J Magn Reson Imaging.* 2006;23:130-134.

72 Miao H, Fukatsu H, Ishigaki T. Prostate cancer detection with 3-T MRI: comparison of diffusion-weighted and T2-weighted imaging. *Eur J Radiol.* 2007;61:297-302.

73 Tanimoto A, Nakashima J, Kohno H, Shinmoto H, Kuribayashi S. Prostate cancer screening: the clinical value of diffusion-weighted imaging and dynamic MR imaging in combination with T2-weighted imaging. *J Magn Reson Imaging.* 2007;25:146-152.

74 Reinsberg SA, Payne GS, Riches SF, *et al.* Combined use of diffusion-weighted MRI and 1H MR spectroscopy to increase accuracy in prostate cancer detection. *AJR Am J Roentgenol.* 2007;188:91-98.

75 Desouza NM, Reinsberg SA, Scurr ED, Brewster JM, Payne GS. Magnetic resonance imaging in prostate cancer: value of apparent diffusion coefficients for identifying malignant nodules. *Br J Radiol.* 2007.

76 Patterson DM, Padhani AR, Collins DJ. Technology insight: water diffusion MRI--a potential new biomarker of response to cancer therapy. *Nat Clin Pract Oncol.* 2008;5:220-233.

77 Ling CC, Humm J, Larson S, *et al.* Towards multidimensional radiotherapy (MD-CRT): biological imaging and biological conformality. *Int J Radiat Oncol Biol Phys.* 2000;47:551-560.

78 Bolla M. What is the role of radiation dose escalation in the treatment of localized prostate cancer? *Nat Clin Pract Urol.* 2008.

79 Zelefsky MJ, Fuks Z, Hunt M, *et al.* High-dose intensity modulated radiation therapy for prostate cancer: early toxicity and biochemical outcome in 772 patients. *Int J Radiat Oncol Biol Phys.* 2002;53:1111-1116.

Chapter 3

The reproducibility of and correlation between quantitative and semi-quantitative dynamic, blood oxygen level dependent and diffusion MRI parameters in the malignant human prostate

3.1 Aim

To determine the reproducibility of T_1-weighted dynamic contrast enhanced MRI, T_2*-weighted dynamic susceptibility contrast MRI, BOLD MRI and diffusion-weighted imaging for the prostate as a whole, prostate tumour, normal prostatic peripheral zone and benign prostatic central zone, in patients with prostate cancer, before and after three months of androgen deprivation. Also, to correlate the various MRI parameters obtained.

3.2 Introduction

All quantitative biological measurements exhibit variability. This is caused by natural variation in the quantity being measured, variation in the measurement process and errors introduced during analysis. For any measurement to be useful in the determination of whether a change has occurred, for example as a result of treatment, knowledge of its reproducibility is required. An estimate of measurement error enables interpretation of whether a change in an observation has occurred as a result of parameter variability or whether the difference is real. This estimate of error can be calculated for the study group as a whole or on an individual patient-by-patient basis.

With regard to dynamic and intrinsic susceptibility-weighted magnetic resonance imaging studies of the prostate, variability can occur at several stages of the examination. Patient movement can be minimised with careful explanation of the procedure and ensuring comfort and relaxation during the examination. Internal prostate movement is largely unavoidable but can be slightly reduced by asking the patient to empty their rectum before the scan. A study using cine-MRI has demonstrated significant prostatic movement in 58% of patients during a seven minute acquisition, with correlation between the incidence of prostate movement and the degree of rectal distension [1]. Measurement factors such as MRI scanner type and settings, data acquisition technique and number of imaging sites may introduce variability between departments and between studies. For comparative studies, the ability to image the same plane through the prostate on successive examinations will influence reproducibility. This in turn is influenced by the extent to which any intervention between examinations alters the morphological appearance, size and shape of the prostate gland. Analysis methods, including the mathematical model used, parameter derived, assumptions made, input function measurement and inter- and intra -observer variability in ROI placement will also affect the overall reproducibility of the measurement.

The International Standards Organisation (ISO: 5725, 1994 [2]) definitions of repeatability and reproducibility are as follows:

1. Repeatability refers to test conditions that are as constant as possible, where the same operator using the same equipment within a "short time interval" obtains independent test results with the same method on identical items in the same laboratory.

2. Reproducibility refers to test conditions under which results are obtained with the same method on identical test items, but in different laboratories with different operators using different equipment.

Repeatability refers to the ability of a measurement system to provide consistent readings on a given object with control over external sources of error. Repeatability therefore informs on equipment variation. An MRI test-retest examination, without moving the patient over a short period of time, is considered a repeatability study.

Reproducibility on the other hand is the ability for multiple experiments, performed in different departments at different times, to achieve consistent results on identical objects. Thus, reproducibility measures the typical error between observers when each observes the same quantity. Reproducibility informs on appraiser / experimental variation. An MRI measurement repeated on a patient several days apart is considered to be a reproducibility study. Even if the equipment and analysis technique used for the two measurements is identical, the experimental conditions are different because of the timing element.

In general, high precision is obtained when both repeatability and reproducibility errors are small.

There are a limited number of published reports documenting the reproducibility of dynamic and susceptibility-weighted MR imaging in normal human tissues and tumours.

A study of 19 patients assessed the reproducibility of the T1-weighted DCE MRI parameters K^{trans}, v_e and maximum contrast medium accumulation (MCMA) in pelvic muscle, bone marrow and fat [3]. Results showed high variability in bone marrow and fat, making these tissues unsuitable for obtaining reliable kinetic parameter estimates. This study also demonstrated low, statistically non-significant, variance ratios for pelvic muscle, suggesting that the *within-subject* variance was large compared to the *between-subject* variance. In a similar study of 21 patients with a variety of tumour types, the reproducibility of semi-quantitative (gradient, enhancement and AUC) and quantitative (K^{trans}, v_e and k_{ep}) parameters was compared [4]. $v_{e,}$ enhancement and AUC were shown to be highly reproducible DCE-MRI parameters. K^{trans}, k_{ep} and gradient had greater variability, with larger changes in individuals required to be statistically significant, but were nevertheless sufficiently reproducible to detect changes greater than 14-17%.

Reproducibility of T_1 and T_2* -weighted parameters, including R_2*, in a variety of pelvic tumours (predominantly ovarian or uterine in origin) has been reported by Lankester *et al* [5]. These are the only published data regarding the reproducibility of T_2* or R_2*-weighted parameters in extra-cranial human tumours. Of the quantitative T_1-weighted measurements, K^{trans} was again shown to be the least reproducible with a wCV of 20.3%. v_e and k_{ep} had wCV values of 8.3% and 17.4% respectively. The T_2* reproducibility statistics for rBV and rBF gave wCV values of 19.7% and 16.8% respectively, although on an individual patient basis a change of ±54.5% for rBV and ±46.4% for rBF would be required to be considered a significant change at the 95% confidence level. For R_2*, wCV was 17.5% with a 48.6% change required for significance.

These studies all conclude that a measure of reproducibility is essential for valid assessment of treatment effect and should be incorporated into any clinical research protocol that utilises dynamic or susceptibility weighted MRI parameters for response assessment. A benchmark of reproducibility values has been provided that can now be used as a comparison with future studies.

3.3 General Description of Statistical Measures of Reproducibility

Spontaneous variability of parameter estimates:

Within-subject coefficient of variation (wCV):

This is the within-subject standard deviation divided by the mean, multiplied by 100 to give a percentage.

Variance ratio (F):

Is the ratio of the between-patient variance and within-patient variance. A parameter with a larger variance in the patient population, but a small variance within individual patients (wCV) would have a higher variance ratio

Measurement error:

Interclass correlation coefficient (ICC):

A measure of the precision of parameter estimates. It is the average correlation coefficient across all possible orderings of the data when there is no obvious choice of X and Y axis for each of the pairs of measurements.

Repeatability statistic:

The threshold value (as a percentage change) below which the absolute difference between two measurements on the same patient (n=1) is expected to lie for 95% of the pairs of observations. From this, one can calculate the number of patients in the group that achieved a parameter change that would be considered significant, at the 95% confidence level, as a real change rather than simply being due to measurement variability.

3.4 Patients and Methods

3.4.1 General

The reproducibility analysis was carried out as part of the androgen deprivation study, using the same 20 patients **(chapter 6)**.

As depicted in **figure 6.1**, **page 189** each patient was examined with five multi-parameter MRI scans. The first two scans and the last two scans were used for the assessment of reproducibility. Scans one and two were performed a few days apart prior to the commencement of androgen deprivation in order to determine the reproducibility of each of the MRI parameters in the baseline physiological state without endocrine manipulation. Scans four and five were performed a few days apart three months after the commencement of androgen deprivation in order to determine the reproducibility of each of the MRI parameters in the androgen deprived state. The mean number of days between scans one and two was 2.75 days (range 1 – 8 days) and the mean number of days between scans four and five was 2.55 days (range 1 – 14 days).

3.4.2 MRI Protocol

As the reproducibility study was incorporated within the androgen deprivation study, the MRI protocols and methods for image analysis are identical to those described in chapter 5 and as a result will not be repeated here. The same parameters were measured or calculated.

3.4.3 Statistical Methods for Reproducibility Calculations

The standard consensus approach to assessing reproducibility was used [6-8].

For each patient, the difference between the measurements of a parameter at each reproducibility scan, *d*, was calculated.

The distribution of *d* was tested for normality using the Shapiro-Wilk test.

In order to establish whether the size of *d* was dependent upon the parameter value, Kendall's tau for correlation of the absolute value of *d* against the mean parameter value for the two scans was calculated [7]. If this test demonstrated that error was indeed proportional to the mean, at the 95% confidence level, then the data were transformed using natural logarithms (*ln*). The Shapiro-Wilk and Kendall's tau test were then repeated.

The following statistical measures of reproducibility were then obtained from a one way analysis of variance (ANOVA) on the original or transformed data:

The mean squared difference (*dsd*) was calculated:

$$dsd = \sqrt{\frac{\sum d^2}{n}}$$

The within-patient standard deviation (wSD) was calculated:

$$\text{wSD} = \frac{dsd}{\sqrt{2}}$$

The within patient coefficient of variance was calculated:

a) For original data: $\text{wCV} = \frac{wSD}{mean}$

b) For *ln* transformed data wCV = Exp(wSD)-1

The repeatability parameter, r, was calculated as follows:

a) For original data: $\text{r\%} = \left(\frac{r}{mean}\right) \times 100$

b) For *ln* transformed data $\text{r\%} = \frac{100 \times Exp(\ln mean \pm r)}{mean}$

The variance ratio (F)

The ratio of the between patient variance and within patient variance can be mathematically described by:

$$\text{F} = \frac{\chi_n^2 / n}{\chi_d^2 / d}$$

where n=numerator and d=denominator

The Interclass correlation coefficient (ICC) was calculated as follows:

$$\text{ICC} = \frac{mSS_B - SS_T}{(m-1)SS_T}$$

where m is the number of observations per subject, SSB is the sum of squared between subjects and SST is the total sum of squares (as per one way ANOVA above).

In order to determine whether there were any significant correlation between any of the baseline kinetic parameter values, Spearman's ρ (rho) was calculated.

Statistical analysis was performed using the StatsDirect statistical software package (StatsDirect, Cheshire, UK) and Microsoft® Excel 2000 (Microsoft Corporation, Washington State, USA).

3.5 Results

3.5.1 General

Patient characteristics and scheduling details were the same as for the androgen deprivation study **(tables 6.1 and 6.2, p187&193)**. The median time between the first two examinations and the last two examinations was 2 days and 1.5 days respectively.

Due to patient movement and other reasons that are described in **section 6.4.1, p192** it was not possible to generate all of various parametric maps from every scan. The numbers of data pairs used for each reproducibility calculation are given in **tables 3.1 – 3.5**. The baseline means of the median kinetic parameter values for whole prostate are given in tables **tables 3.1 – 3.5**. In general these values are comparable with literature values for normal human tissues and human tumours [3-5, 9, 10].

3.5.2 Results of the reproducibility analysis

Reproducibility statistics are also shown in **tables 3.1 – 3.5**. No parameter, either for baseline pairs or pairs after three months of androgen deprivation, had a mean difference significantly different from zero. In other words, there was no systematic change in parameter value, in either direction, between the paired sets of scans either at baseline or at three months **(appendix C)**. This confirms that the first scan of the pair has no influence on the second scan, which may have been the case if there had been significant contrast retention in the prostatic tissues from the first scan at the time of the second scan, which has been occasionally observed **(figure 3.1)**.

The distribution of each parameter was not significantly different from normal, either at baseline or at three months. The Kendall's tau test confirmed the proportionality of error and mean value for K^{trans}, k_{ep}, AUC_{60}, rBV and rBF. As a result the data for these five parameters were logarithmically transformed (*ln*). After transformation, Kendall's tau was no longer significant, indicating no further dependence of error on the mean, thereby allowing calculation of valid reproducibility statistics. The difference between values for v_e, R_2*, ADC (b-values 0 – 1000 s/mm^2), ADC (b-values 0 – 50 s/mm^2) and ADC (b-values 150 – 1000 s/mm^2) showed no dependence on the mean and therefore no transformation was required for these data.

When assessed by the within-patient coefficient of variance (wCV), the most consistently reproducible region of interest was whole prostate. The variance ratio also demonstrated the whole prostate ROI to be highly reproducible although not as reliably as with wCV. The least reproducible ROI was undoubtedly the normal peripheral zone, whichever reproducibility statistic was used. Tumour ROIs were generally slightly less reproducible than whole prostate ROIs but more reproducible than peripheral zone, other than for the diffusion-weighted ADC parameters, in which the tumour ROIs were consistently the least reproducible.

For whole prostate, tumour and central zone ROIs, there was a consistent deterioration in reproducibility following three months of androgen deprivation (when measured by wCV or variance ratio) other than for the R_2* parameter (see below). The reproducibility of peripheral zone ROIs tended to improve following androgen withdrawal, other than for ADC measurements, although the initial reproducibility of this ROI was poor, as previously described.

Consistent with the findings of Lankester [5], Galbraith [4] and Padhani [3], v_e was the most reproducible T_1-weighted DCE-MRI parameter. AUC_{60} was almost as reproducible as v_e, with slightly more variability in terms of wCV and variance ratio for most ROIs. K^{trans} also demonstrated good reproducibility, with wCV values for whole prostate and tumour being slightly superior to that previously described in the literature for pelvic tumours (13.9% for whole prostate and 20.1% for prostate tumour, compared with 20.3% reported by Lankester and 24% reported by Galbraith). The T_2*-weighted parameters demonstrated poor reproducibility, with variance ratios ranging between 2.5 and 5.5 for baseline rBV measurements and between 2.2 and 3.9 for baseline rBF readings, indicating a large variation within patients compared to the variation between patients.

The effect of androgen deprivation on the reproducibility of K^{trans} was essentially neutral, with wCV and variance ratio worsening for whole prostate and central zone ROIs, and improving for tumour and peripheral zone ROIs. For the other T_1-weighted parameters and the T_2*-weighted measurements, the effect of androgen deprivation tended to worsen reproducibility.

R_2* proved to be a notable exception, with a consistent and considerable improvement in reproducibility following androgen deprivation therapy. The baseline wCV values for whole prostate and tumour (21.7% and 23.3% respectively), with a requirement of a 60.1% change for whole prostate ROIs and a 64.6% change for tumour ROIs required to indicate a significant change for an individual patient at the 95% confidence level, compared unfavourably with the results reported by Lankester (who showed a wCV of 17.5% with a 48.6% change to demonstrate significance, in a variety of pelvic tumours). After androgen deprivation, R_2* reproducibility improved with a wCV of 12.3%

for whole prostate and 11.8% for tumour, with 34.1% and 32.8% changes required for significance, respectively. This resulted in R_2* becoming one of the most reproducible MRI parameters of all, with only baseline v_e having superior values.

As for other published studies [3, 11], R_2* was calculated for normal pelvic muscle (obturator internus). This normal tissue demonstrated exceptional reproducibility, with a baseline wCV of 4% and 3 month wCV of only 1.2%. After androgen deprivation, a change of 3.3% would be sufficient to demonstrate a significant change in an individual patient, at the 95% confidence level.

3.5.3 Correlation between MRI parameters

The reproducibility statistics for the diffusion-weighted ADC measurements suffered from poor patient numbers, with only seven patients in each reproducibility cohort. Despite this, whole prostate ADC maps demonstrated reasonable reproducibility (wCV of 10.3 – 16.2% at baseline, 10.5 – 23.3% at 3 months). Given the patient numbers, it is not possible to comment on the effect of androgen withdrawal on the reproducibility of ADC values with any degree of certainty.

Correlation between the different parameters at baseline is shown in **tables 3.6 to 3.9**. For whole prostate ROIs, AUC_{60} was found to correlate very strongly with K^{trans} ($p = 0.95$, $p < 0.0001$) and strongly with v_e ($\rho = 0.74$, $p = 0.0003$). K^{trans} also correlated strongly with v_e ($\rho = 0.79$, $p < 0.0001$). Even stronger correlations were observed for tumour measurements: AUC_{60} versus K^{trans} ($\rho = 0.98$, $p < 0.0001$) and AUC_{60} versus k_{ep} ($\rho = 0.83$, $p < 0.0001$). Many other kinetic parameter values exhibited significant correlation with each other. Relative blood flow and relative blood volume exhibit extremely high correlation ($p = 0.98$ for both whole prostate and tumour, $p < 0.0001$) reflecting their close mathematical relationship and the narrow range of mean transit time (MTT) values observed (rBF = rBV/MTT).

R_2* did not correlate with any other parameter for whole prostate, tumour or central gland although did exhibit a degree of correlation with K^{trans}, k_{ep} and AUC_{60} for peripheral zone. ADC values generally did not exhibit significant correlation with other parameters reflecting the low numbers of patients that underwent diffusion weighted imaging.

Table 3.1 Reproducibility and Repeatability Statistics – T_1-weighted DCE - MRI

K^{trans}

Whole Prostate - K^{trans} Baseline	
Number of patients	19
Mean ROI size (pixels)	6725
Mean number of pixels	6060
Mean value ($mins^{-1}$)	0.206
Repeatability for n=1 (%)	-30.3 to 43.4
Variance ratio (F)	12.5
P-value for F	< 0.0001
ICC	0.84
wCV	13.9%

Whole Prostate - K^{trans} 3 Months	
Number of patients	20
Mean ROI size (pixels)	5222
Mean number of pixels	3864
Mean value ($mins^{-1}$)	0.146
Repeatability for n=1 (%)	-33.4 to 50.2
Variance ratio (F)	10.0
P-value for F	< 0.0001
ICC	0.81
wCV	15.8%

Tumour - K^{trans} Baseline	
Number of patients	19
Mean ROI size (pixels)	1046
Mean number of pixels	987
Mean value ($mins^{-1}$)	0.273
Repeatability for n=1 (%)	-39.8 to 66.2
Variance ratio (F)	11.2
P-value for F	< 0.0001
ICC	0.83
wCV	20.1%

Tumour - K^{trans} 3 Months	
Number of patients	19
Mean ROI size (pixels)	614
Mean number of pixels	425
Mean value ($mins^{-1}$)	0.130
Repeatability for n=1 (%)	-38.6 to 62.8
Variance ratio (F)	23.2
P-value for F	< 0.0001
ICC	0.91
wCV	19.2%

Peripheral Zone - K^{trans} Baseline	
Number of patients	18
Mean ROI size (pixels)	162
Mean number of pixels	136
Mean value ($mins^{-1}$)	0.126
Repeatability for n=1 (%)	-62.1 to 163.8
Variance ratio (F)	3.3
P-value for F	0.008
ICC	0.51
wCV	41.9%

Peripheral Zone - K^{trans} 3 Months	
Number of patients	18
Mean ROI size (pixels)	116
Mean number of pixels	86
Mean value ($mins^{-1}$)	0.069
Repeatability for n=1 (%)	-41.0 to 69.4
Variance ratio (F)	13.5
P-value for F	< 0.0001
ICC	0.85
wCV	21.0%

Central Zone - K^{trans} Baseline	
Number of patients	18
Mean ROI size (pixels)	174
Mean number of pixels	172
Mean value ($mins^{-1}$)	0.253
Repeatability for n=1 (%)	-40.5 to 68.2
Variance ratio (F)	14.9
P-value for F	< 0.0001
ICC	0.87
wCV)	20.6%

Central Zone - K^{trans} 3 Months	
Number of patients	18
Mean ROI size (pixels)	126
Mean number of pixels	123
Mean value ($mins^{-1}$)	0.206
Repeatability for n=1 (%)	-50.8 to 103.3
Variance ratio (F)	6.6
P-value for F	0.0001
ICC	0.73
wCV	29.2%

v_e

Whole Prostate – v_e Baseline	
Number of patients	19
Mean ROI size (pixels)	6725
Mean number of pixels	6060
Mean value (%)	41.6
Repeatability for n=1 (%)	-24.7 to 24.7
Variance ratio (F)	13.4
P-value for F	< 0.0001
ICC	0.85
wCV	8.9%

Whole Prostate - v_e 3 Months	
Number of patients	20
Mean ROI size (pixels)	5222
Mean number of pixels	3864
Mean value (%)	47.3
Repeatability for n=1 (%)	-33.1 to 33.1
Variance ratio (F)	7.6
P-value for F	< 0.0001
ICC	0.76
wCV	11.9%

Tumour – v_e Baseline	
Number of patients	19
Mean ROI size (pixels)	1046
Mean number of pixels	987
Mean value (%)	41.2
Repeatability for n=1 (%)	-34.6 to 34.6
Variance ratio (F)	11.0
P-value for F	< 0.0001
ICC	0.82
wCV	12.5%

Tumour - v_e 3 Months	
Number of patients	19
Mean ROI size (pixels)	614
Mean number of pixels	425
Mean value (%)	45.3
Repeatability for n=1 (%)	-48.6 to 48.6
Variance ratio (F)	5.9
P-value for F	0.0002
ICC	0.70
wCV	17.5%

Peripheral Zone – v_e Baseline	
Number of patients	18
Mean ROI size (pixels)	162
Mean number of pixels	136
Mean value (%)	29.2
Repeatability for n=1 (%)	-41.1 to 41.1
Variance ratio (F)	11.7
P-value for F	< 0.0001
ICC	0.83
wCV	14.8%

Peripheral Zone – v_e 3 Months	
Number of patients	18
Mean ROI size (pixels)	116
Mean number of pixels	86
Mean value (%)	35.2
Repeatability for n=1 (%)	-76.7 to 76.7
Variance ratio (F)	4.5
P-value for F	0.001
ICC	0.62
wCV	27.7%

Central Zone – v_e Baseline	
Number of patients	18
Mean ROI size (pixels)	174
Mean number of pixels	172
Mean value (%)	32.6
Repeatability for n=1 (%)	-36.1 to 36.1
Variance ratio (F)	19.3
P-value for F	< 0.0001
ICC	0.90
wCV	13.0%

Central Zone – v_e 3 Months	
Number of patients	18
Mean ROI size (pixels)	126
Mean number of pixels	123
Mean value (%)	42.2
Repeatability for n=1 (%)	-35.1 to 35.1
Variance ratio (F)	10.7
P-value for F	< 0.0001
ICC	0.82
wCV	12.7%

k_{ep}

Whole Prostate – k_{ep} Baseline	
Number of patients	19
Mean ROI size (pixels)	6725
Mean number of pixels	6060
Mean value ($mins^{-1}$)	0.513
Repeatability for n=1 (%)	-30.3 to 43.6
Variance ratio (F)	5.7
P-value for F	0.0002
ICC	0.69
wCV	13.9%

Whole Prostate – k_{ep} 3 Months	
Number of patients	20
Mean ROI size (pixels)	5222
Mean number of pixels	3864
Mean value ($mins^{-1}$)	0.327
Repeatability for n=1 (%)	-39.1 to 64.2
Variance ratio (F)	4.1
P-value for F	0.0014
ICC	0.59
wCV	19.6%

Tumour – k_{ep} Baseline	
Number of patients	19
Mean ROI size (pixels)	1046
Mean number of pixels	987
Mean value ($mins^{-1}$)	0.680
Repeatability for n=1 (%)	-44.8 to 81.3
Variance ratio (F)	4.9
P-value for F	0.0006
ICC	0.65
wCV	24.0%

Tumour – k_{ep} 3 Months	
Number of patients	19
Mean ROI size (pixels)	614
Mean number of pixels	425
Mean value ($mins^{-1}$)	0.311
Repeatability for n=1 (%)	-60.6 to 153.7
Variance ratio (F)	2.6
P-value for F	0.023
ICC	0.42
wCV	39.9%

Peripheral Zone - k_{ep} Baseline	
Number of patients	18
Mean ROI size (pixels)	162
Mean number of pixels	136
Mean value ($mins^{-1}$)	0.461
Repeatability for n=1 (%)	-66.8 to 201.4
Variance ratio (F)	2.0
P-value for F	0.008
ICC	0.30
wCV	48.9%

Peripheral Zone – k_{ep} 3 Months	
Number of patients	18
Mean ROI size (pixels)	116
Mean number of pixels	86
Mean value ($mins^{-1}$)	0.217
Repeatability for n=1 (%)	-58.4 to 140.4
Variance ratio (F)	1.5
P-value for F	< 0.0001
ICC	0.18
wCV	37.2%

Central Zone – k_{ep} Baseline	
Number of patients	18
Mean ROI size (pixels)	174
Mean number of pixels	172
Mean value ($mins^{-1}$)	0.808
Repeatability for n=1 (%)	-35.8 to 55.8
Variance ratio (F)	9.5
P-value for F	< 0.0001
ICC	0.80
wCV	17.4%

Central Zone – k_{ep} 3 Months	
Number of patients	18
Mean ROI size (pixels)	126
Mean number of pixels	123
Mean value ($mins^{-1}$)	0.500
Repeatability for n=1 (%)	-58.1 to 138.9
Variance ratio (F)	2.6
P-value for F	0.0001
ICC	0.43
wCV	37.0%

AUC_{60}

Whole Prostate – AUC Baseline		Whole Prostate – AUC 3 Months	
Number of patients	19	Number of patients	20
Mean ROI size (pixels)	6725	Mean ROI size (pixels)	5222
Mean number of pixels	6620	Mean number of pixels	5024
Mean value (mmol.s)	10.84	Mean value (mmol.s)	7.46
Repeatability for n=1 (%)	-32.3 to 47.7	Repeatability for n=1 (%)	-41.0 to 69.4
Variance ratio (F)	10.9	Variance ratio (F)	8.6
P-value for F	< 0.0001	P-value for F	< 0.0001
ICC	0.82	ICC	0.78
wCV	15.1%	wCV	21.0%

Tumour – AUC Baseline		Tumour – AUC 3 Months	
Number of patients	19	Number of patients	19
Mean ROI size (pixels)	1046	Mean ROI size (pixels)	614
Mean number of pixels	1041	Mean number of pixels	590
Mean value (mmol.s)	14.23	Mean value (mmol.s)	7.28
Repeatability for n=1 (%)	-36.3 to 57.1	Repeatability for n=1 (%)	-49.4 to 97.7
Variance ratio (F)	23.0	Variance ratio (F)	15.7
P-value for F	< 0.0001	P-value for F	< 0.0001
ICC	0.91	ICC	0.87
wCV	17.7%	wCV	27.9%

Peripheral Zone – AUC Baseline		Peripheral Zone – AUC 3 Months	
Number of patients	18	Number of patients	18
Mean ROI size (pixels)	162	Mean ROI size (pixels)	116
Mean number of pixels	153	Mean number of pixels	108
Mean value (mmol.s)	7.32	Mean value (mmol.s)	4.84
Repeatability for n=1 (%)	-58.5 to 140.8	Repeatability for n=1 (%)	-45.0 to 81.9
Variance ratio (F)	4.5	Variance ratio (F)	6.0
P-value for F	0.0014	P-value for F	0.0002
ICC	0.62	ICC	0.70
wCV	37.3%	wCV	24.1%

Central Zone – AUC Baseline		Central Zone – AUC 3 Months	
Number of patients	18	Number of patients	18
Mean ROI size (pixels)	174	Mean ROI size (pixels)	126
Mean number of pixels	173	Mean number of pixels	126
Mean value (mmol.s)	13.02	Mean value (mmol.s)	12.01
Repeatability for n=1 (%)	-32.8 to 48.9	Repeatability for n=1 (%)	-44.5 to 80.2
Variance ratio (F)	16.2	Variance ratio (F)	8.4
P-value for F	< 0.0001	P-value for F	< 0.0001
ICC	0.88	ICC	0.78
wCV	15.5%	wCV	23.7%

Table 3.2 Reproducibility and Repeatability Statistics – T_2*-weighted DSC – MRI

rBV

Whole Prostate – rBV Baseline	
Number of patients	19
Mean ROI size (pixels)	648
Mean number of pixels	500
Mean value (AU)	141.42
Repeatability for n=1 (%)	-68.6 to 218.3
Variance ratio (F)	3.5
P-value for F	0.005
ICC	0.53
wCV	51.9%

Whole Prostate – rBV 3 Months	
Number of patients	20
Mean ROI size (pixels)	448
Mean number of pixels	289
Mean value (AU)	47.94
Repeatability for n=1 (%)	-84.0 to 525.2
Variance ratio (F)	1.6
P-value for F	0.15
ICC	0.21
wCV	93.8%

Tumour – rBV Baseline	
Number of patients	18
Mean ROI size (pixels)	126
Mean number of pixels	97
Mean value (AU)	251.77
Repeatability for n=1 (%)	-81.1 to 427.7
Variance ratio (F)	2.5
P-value for F	0.033
ICC	0.40
wCV	82.3%

Tumour – rBV 3 Months	
Number of patients	18
Mean ROI size (pixels)	68
Mean number of pixels	37
Mean value (AU)	34.18
Repeatability for n=1 (%)	-81.2 to 430.6
Variance ratio (F)	4.6
P-value for F	0.001
ICC	0.63
wCV	82.7%

Peripheral Zone – rBV Baseline	
Number of patients	17
Mean ROI size (pixels)	45
Mean number of pixels	32
Mean value (AU)	86.97
Repeatability for n=1 (%)	-88.2 to 747.21
Variance ratio (F)	5.5
P-value for F	0.0006
ICC	0.67
wCV	116.3%

Peripheral Zone – rBV 3 Months	
Number of patients	17
Mean ROI size (pixels)	30
Mean number of pixels	17
Mean value (AU)	23.69
Repeatability for n=1 (%)	-80.0 to 399.7
Variance ratio (F)	1.6
P-value for F	0.17
ICC	0.21
wCV	78.7%

Central Zone – rBV Baseline	
Number of patients	17
Mean ROI size (pixels)	43
Mean number of pixels	36
Mean value (AU)	164.80
Repeatability for n=1 (%)	-81.5 to 440.7
Variance ratio (F)	3.7
P-value for F	0.005
ICC	0.56
wCV	83.9%

Central Zone – rBV 3 Months	
Number of patients	17
Mean ROI size (pixels)	36
Mean number of pixels	27
Mean value (AU)	72.60
Repeatability for n=1 (%)	-93.3 to 1384.4
Variance ratio (F)	1.4
P-value for F	0.26
ICC	0.13
wCV	164.8%

rBF

Whole Prostate – rBF Baseline	
Number of patients	19
Mean ROI size (pixels)	648
Mean number of pixels	500
Mean value (AU)	2.37
Repeatability for n=1 (%)	-62.5 to 166.7
Variance ratio (F)	3.7
P-value for F	0.003
ICC	0.56
wCV	42.5%

Whole Prostate – rBF 3 Months	
Number of patients	20
Mean ROI size (pixels)	448
Mean number of pixels	289
Mean value (AU)	0.98
Repeatability for n=1 (%)	-83.3 to 499.0
Variance ratio (F)	1.3
P-value for F	0.30
ICC	0.09
wCV	90.8%

Tumour – rBF Baseline	
Number of patients	18
Mean ROI size (pixels)	126
Mean number of pixels	97
Mean value (AU)	4.20
Repeatability for n=1 (%)	-77.9 to 351.5
Variance ratio (F)	2.2
P-value for F	0.05
ICC	0.35
wCV	72.3%

Tumour – rBF 3 Months	
Number of patients	18
Mean ROI size (pixels)	68
Mean number of pixels	37
Mean value (AU)	0.78
Repeatability for n=1 (%)	-78.8 to 371.9
Variance ratio (F)	4.2
P-value for F	0.002
ICC	0.60
wCV	75.1%

Peripheral Zone – rBF Baseline	
Number of patients	17
Mean ROI size (pixels)	45
Mean number of pixels	32
Mean value (AU)	1.54
Repeatability for n=1 (%)	-83.8 to 516.0
Variance ratio (F)	2.9
P-value for F	0.017
ICC	0.47
wCV	92.8%

Peripheral Zone – rBF 3 Months	
Number of patients	17
Mean ROI size (pixels)	30
Mean number of pixels	17
Mean value (AU)	0.52
Repeatability for n=1 (%)	-80.1 to 401.3
Variance ratio (F)	0.9
P-value for F	0.59
ICC	-0.09
wCV	79.0%

Central Zone – rBF Baseline	
Number of patients	17
Mean ROI size (pixels)	43
Mean number of pixels	36
Mean value (AU)	2.82
Repeatability for n=1 (%)	-75.9 to 314.5
Variance ratio (F)	3.9
P-value for F	0.004
ICC	0.57
wCV	67.1%

Central Zone – rBF 3 Months	
Number of patients	17
Mean ROI size (pixels)	36
Mean number of pixels	27
Mean value (AU)	1.22
Repeatability for n=1 (%)	-90.9 to 1000.0
Variance ratio (F)	1.6
P-value for F	0.18
ICC	0.19
wCV	137.7%

Table 3.3 Reproducibility and Repeatability Statistics – BOLD MRI

R_2^*

Whole Prostate - R_2^* Baseline	
Number of patients	20
Mean ROI size (pixels)	6804
Mean number of pixels	6804
Mean value (s^{-1})	17.24
Repeatability for n=1 (%)	-60.1 to 60.1
Variance ratio (F)	2.5
P-value for F	0.025
ICC	0.40
wCV	21.7%

Whole Prostate - R_2^* 3 Months	
Number of patients	20
Mean ROI size (pixels)	5534
Mean number of pixels	5534
Mean value (s^{-1})	20.73
Repeatability for n=1 (%)	-34.1 to 34.1
Variance ratio (F)	5.1
P-value for F	0.0003
ICC	0.66
wCV	12.3%

Tumour - R_2^* Baseline	
Number of patients	19
Mean ROI size (pixels)	924
Mean number of pixels	924
Mean value (s^{-1})	16.59
Repeatability for n=1 (%)	-64.6 to 64.6
Variance ratio (F)	2.3
P-value for F	0.039
ICC	0.37
wCV	23.3%

Tumour - R_2^* 3 Months	
Number of patients	19
Mean ROI size (pixels)	668
Mean number of pixels	668
Mean value (s^{-1})	23.41
Repeatability for n=1 (%)	-32.8 to 32.8
Variance ratio (F)	3.6
P-value for F	0.004
ICC	0.55
wCV	11.8%

Peripheral Zone - R_2^* Baseline	
Number of patients	18
Mean ROI size (pixels)	155
Mean number of pixels	155
Mean value (s^{-1})	14.09
Repeatability for n=1 (%)	-115.7 to 115.7
Variance ratio (F)	2.1
P-value for F	0.06
ICC	0.34
wCV	41.8%

Peripheral Zone - R_2^* 3 Months	
Number of patients	18
Mean ROI size (pixels)	121
Mean number of pixels	121
Mean value (s^{-1})	19.66
Repeatability for n=1 (%)	-61.0 to 61.0
Variance ratio (F)	3.1
P-value for F	0.011
ICC	0.49
wCV	22.0%

Central Zone - R_2^* Baseline	
Number of patients	18
Mean ROI size (pixels)	190
Mean number of pixels	190
Mean value (s^{-1})	10.35
Repeatability for n=1 (%)	-140.4 to 140.4
Variance ratio (F)	1.7
P-value for F	0.15
ICC	0.22
wCV	50.7%

Central Zone - R_2^* 3 Months	
Number of patients	18
Mean ROI size (pixels)	145
Mean number of pixels	145
Mean value (s^{-1})	13.73
Repeatability for n=1 (%)	-81.4 to 81.4
Variance ratio (F)	3.3
P-value for F	0.008
ICC	0.51
wCV	29.4%

Table 3.4 Reproducibility and Repeatability Statistics – BOLD MRI

R_2^* - *Normal Tissue (Obturator Internus Muscle)*

Obturator Internus Muscle - R_2^* Baseline	
Number of patients	20
Mean ROI size (pixels)	11632
Mean number of pixels	11632
Mean value (s^{-1})	25.02
Repeatability for n=1 (%)	-11.2 to 11.2
Variance ratio (F)	8.07
P-value for F	< 0.0001
ICC	0.77
wCV	4.0%

Obturator Internus Muscle - R_2^* 3 Months	
Number of patients	20
Mean ROI size (pixels)	10956
Mean number of pixels	10956
Mean value (s^{-1})	25.01
Repeatability for n=1 (%)	-3.3 to 3.3
Variance ratio (F)	71.7
P-value for F	< 0.0001
ICC	0.97
wCV	1.2%

Table 3.5 Reproducibility and Repeatability Statistics
Diffusion Weighted Imaging

ADC (b-values 0 – 1000 s/mm^2)

Whole Prostate – ADC Baseline	
Number of patients	7
Mean ROI size (pixels)	6804
Mean number of pixels	6804
Mean value (x10^{-3}mm^{2}s^{-1})	130.4
Repeatability for n=1 (%)	-28.5 to 28.5
Variance ratio (F)	2.4
P-value for F	0.13
ICC	0.35
wCV	10.3%

Whole Prostate – ADC 3 Months	
Number of patients	7
Mean ROI size (pixels)	5534
Mean number of pixels	5534
Mean value (x10^{-3}mm^{2}s^{-1})	131.0
Repeatability for n=1 (%)	-29.0 to 29.0
Variance ratio (F)	4.6
P-value for F	0.033
ICC	0.59
wCV	10.5%

Tumour – ADC Baseline	
Number of patients	7
Mean ROI size (pixels)	924
Mean number of pixels	924
Mean value (x10^{-3}mm^{2}s^{-1})	62.7
Repeatability for n=1 (%)	-131.3 to 131.3
Variance ratio (F)	1.8
P-value for F	0.23
ICC	0.20
wCV	47.4%

Tumour – ADC 3 Months	
Number of patients	7
Mean ROI size (pixels)	668
Mean number of pixels	668
Mean value (x10^{-3}mm^{2}s^{-1})	53.8
Repeatability for n=1 (%)	-190.4 to 190.4
Variance ratio (F)	0.4
P-value for F	0.88
ICC	-0.52
wCV	68.7%

Peripheral Zone – ADC Baseline	
Number of patients	7
Mean ROI size (pixels)	155
Mean number of pixels	155
Mean value (x10^{-3}mm^{2}s^{-1})	149.4
Repeatability for n=1 (%)	-38.3 to 38.3
Variance ratio (F)	6.0
P-value for F	0.016
ICC	0.67
wCV	13.8%

Peripheral Zone – ADC 3 Months	
Number of patients	7
Mean ROI size (pixels)	121
Mean number of pixels	121
Mean value (x10^{-3}mm^{2}s^{-1})	119.2
Repeatability for n=1 (%)	-88.8 to 88.8
Variance ratio (F)	2.9
P-value for F	0.09
ICC	0.43
wCV	32.1%

Central Zone – ADC Baseline	
Number of patients	7
Mean ROI size (pixels)	190
Mean number of pixels	190
Mean value (x10^{-3}mm^{2}s^{-1})	152.0
Repeatability for n=1 (%)	-17.9 to 17.9
Variance ratio (F)	13.3
P-value for F	0.0016
ICC	0.84
wCV	6.5%

Central Zone – ADC 3 Months	
Number of patients	7
Mean ROI size (pixels)	145
Mean number of pixels	145
Mean value (x10^{-3}mm^{2}s^{-1})	142.1
Repeatability for n=1 (%)	-29.6 to 29.6
Variance ratio (F)	1.8
P-value for F	0.24
ICC	0.20
wCV	10.7%

Early ADC (b-values 0 – 50 s/mm^2)

Whole Prostate – Early ADC Baseline		**Whole Prostate – Early ADC 3 Months**	
Number of patients	7	Number of patients	7
Mean ROI size (pixels)	6804	Mean ROI size (pixels)	5534
Mean number of pixels	6804	Mean number of pixels	5534
Mean value $(x10^{-3}mm^2s^{-1})$	414.9	Mean value $(x10^{-3}mm^2s^{-1})$	381.4
Repeatability for n=1 (%)	-44.8 to 44.8	Repeatability for n=1 (%)	-64.5 to 64.5
Variance ratio (F)	0.8	Variance ratio (F)	0.7
P-value for F	0.62	P-value for F	0.67
ICC	-0.21	ICC	-0.26
wCV	16.2%	wCV	23.3%

Tumour – Early ADC Baseline		**Tumour – Early ADC 3 Months**	
Number of patients	7	Number of patients	7
Mean ROI size (pixels)	924	Mean ROI size (pixels)	668
Mean number of pixels	924	Mean number of pixels	668
Mean value $(x10^{-3}mm^2s^{-1})$	385.5	Mean value $(x10^{-3}mm^2s^{-1})$	434.8
Repeatability for n=1 (%)	-85.3 to 85.3	Repeatability for n=1 (%)	-271.6 to 271.6
Variance ratio (F)	5.7	Variance ratio (F)	0.3
P-value for F	0.018	P-value for F	0.92
ICC	0.66	ICC	-0.59
wCV	30.8%	wCV	98.0%

Peripheral Zone – Early ADC Baseline		**Peripheral Zone – Early ADC 3 Months**	
Number of patients	7	Number of patients	7
Mean ROI size (pixels)	155	Mean ROI size (pixels)	121
Mean number of pixels	155	Mean number of pixels	121
Mean value $(x10^{-3}mm^2s^{-1})$	405.8	Mean value $(x10^{-3}mm^2s^{-1})$	357.2
Repeatability for n=1 (%)	-77.9 to 77.9	Repeatability for n=1 (%)	-157.0 to 157.0
Variance ratio (F)	3.0	Variance ratio (F)	1.2
P-value for F	0.09	P-value for F	0.38
ICC	0.44	ICC	0.02
wCV	28.1%	wCV	56.7%

Central Zone – Early ADC Baseline		**Central Zone – Early ADC 3 Months**	
Number of patients	7	Number of patients	7
Mean ROI size (pixels)	190	Mean ROI size (pixels)	145
Mean number of pixels	190	Mean number of pixels	145
Mean value $(x10^{-3}mm^2s^{-1})$	366.1	Mean value $(x10^{-3}mm^2s^{-1})$	361.1
Repeatability for n=1 (%)	-72.8 to 72.8	Repeatability for n=1 (%)	-75.9 to 75.9
Variance ratio (F)	3.0	Variance ratio (F)	0.9
P-value for F	0.09	P-value for F	0.52
ICC	0.44	ICC	-0.11
wCV	26.3%	wCV	27.4%

Late ADC (b-values 150 – 1000 s/mm^2)

Whole Prostate – Late ADC Baseline		**Whole Prostate – Late ADC 3 Months**	
Number of patients	7	Number of patients	7
Mean ROI size (pixels)	6804	Mean ROI size (pixels)	5534
Mean number of pixels	6804	Mean number of pixels	5534
Mean value (x10^{-3}mm^{2}s^{-1})	104.0	Mean value (x10^{-3}mm^{2}s^{-1})	87.3
Repeatability for n=1 (%)	-36.4 to 36.4	Repeatability for n=1 (%)	-51.7 to 51.7
Variance ratio (F)	3.5	Variance ratio (F)	3.1
P-value for F	0.064	P-value for F	0.081
ICC	0.50	ICC	0.46
wCV	13.1%	wCV	18.7%

Tumour – Late ADC Baseline		**Tumour – Late ADC 3 Months**	
Number of patients	7	Number of patients	7
Mean ROI size (pixels)	924	Mean ROI size (pixels)	668
Mean number of pixels	924	Mean number of pixels	668
Mean value (x10^{-3}mm^{2}s^{-1})	42.3	Mean value (x10^{-3}mm^{2}s^{-1})	38.6
Repeatability for n=1 (%)	-201.1 to 201.1	Repeatability for n=1 (%)	-255.7 to 255.7
Variance ratio (F)	0.9	Variance ratio (F)	0.5
P-value for F	0.545	P-value for F	0.79
ICC	-0.13	ICC	-0.39
wCV	72.6%	wCV	92.3%

Peripheral Zone – Late ADC Baseline		**Peripheral Zone – Late ADC 3 Months**	
Number of patients	7	Number of patients	7
Mean ROI size (pixels)	155	Mean ROI size (pixels)	121
Mean number of pixels	155	Mean number of pixels	121
Mean value (x10^{-3}mm^{2}s^{-1})	126.8	Mean value (x10^{-3}mm^{2}s^{-1})	91.7
Repeatability for n=1 (%)	-41.2 to 41.2	Repeatability for n=1 (%)	-123.5 to 123.5
Variance ratio (F)	7.4	Variance ratio (F)	2.5
P-value for F	0.009	P-value for F	0.124
ICC	0.73	ICC	0.37
wCV	14.9%	wCV	44.6%

Central Zone – Late ADC Baseline		**Central Zone – Late ADC 3 Months**	
Number of patients	7	Number of patients	7
Mean ROI size (pixels)	190	Mean ROI size (pixels)	145
Mean number of pixels	190	Mean number of pixels	145
Mean value (x10^{-3}mm^{2}s^{-1})	134.4	Mean value (x10^{-3}mm^{2}s^{-1})	121.7
Repeatability for n=1 (%)	-30.6 to 30.6	Repeatability for n=1 (%)	-55.8 to 55.8
Variance ratio (F)	5.5	Variance ratio (F)	0.5
P-value for F	0.021	P-value for F	0.076
ICC	0.65	ICC	-0.37
wCV	11.0%	wCV	20.2%

Figure 3.1 Example of contrast retention between two MRI scans on consecutive days

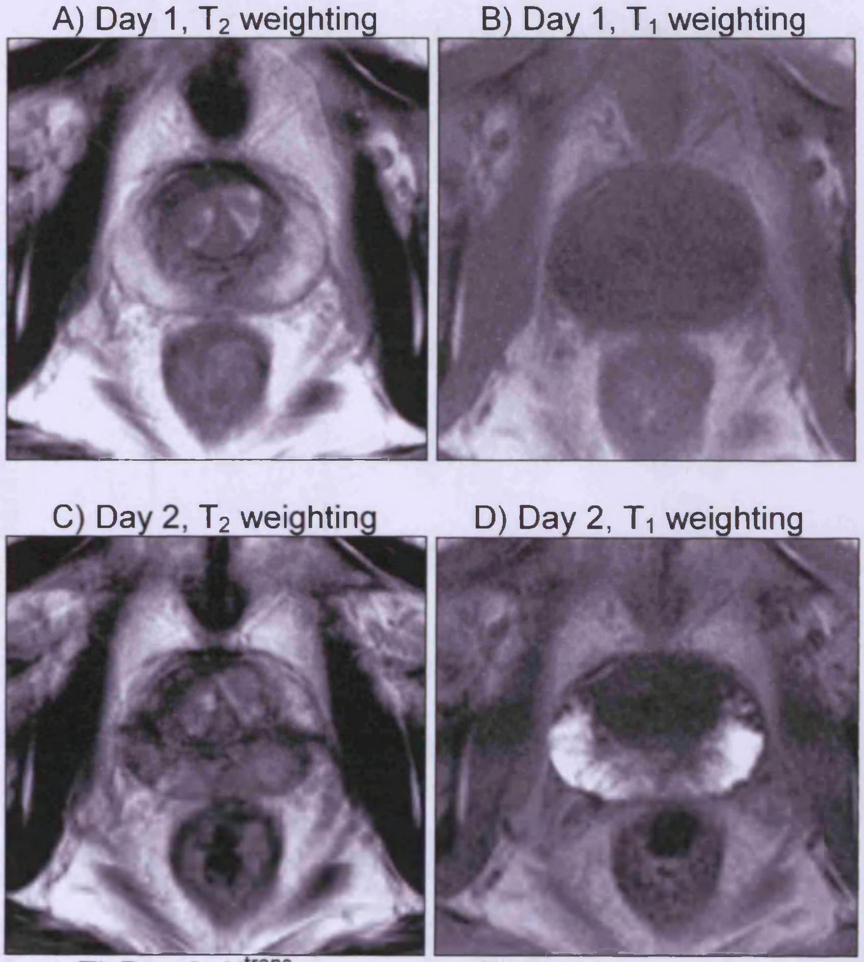

A) Day 1, T_2 weighting

B) Day 1, T_1 weighting

C) Day 2, T_2 weighting

D) Day 2, T_1 weighting

The pre-contrast T_1 image (B) demonstrates low signal intensity throughout the prostate. The following day, a similar pre-contrast image (D) exhibits prominent high signal intensity in the posterior peripheral gland. As no intervention has occurred between the two scans, the only reasonable explanation for this effect is pooling of Gd-DTPA from day 1 to day 2. The effect on the dynamic images is shown (E – J). As there is already saturation of the tissues with gadolinium there is little or no increase in gadolinium concentration after bolus injection, resulting in poor curve fitting and loss of data from the affected regions. In this study this effect was seen on three occasions, two at baseline and one after 3 months of androgen deprivation. The most striking example is shown.

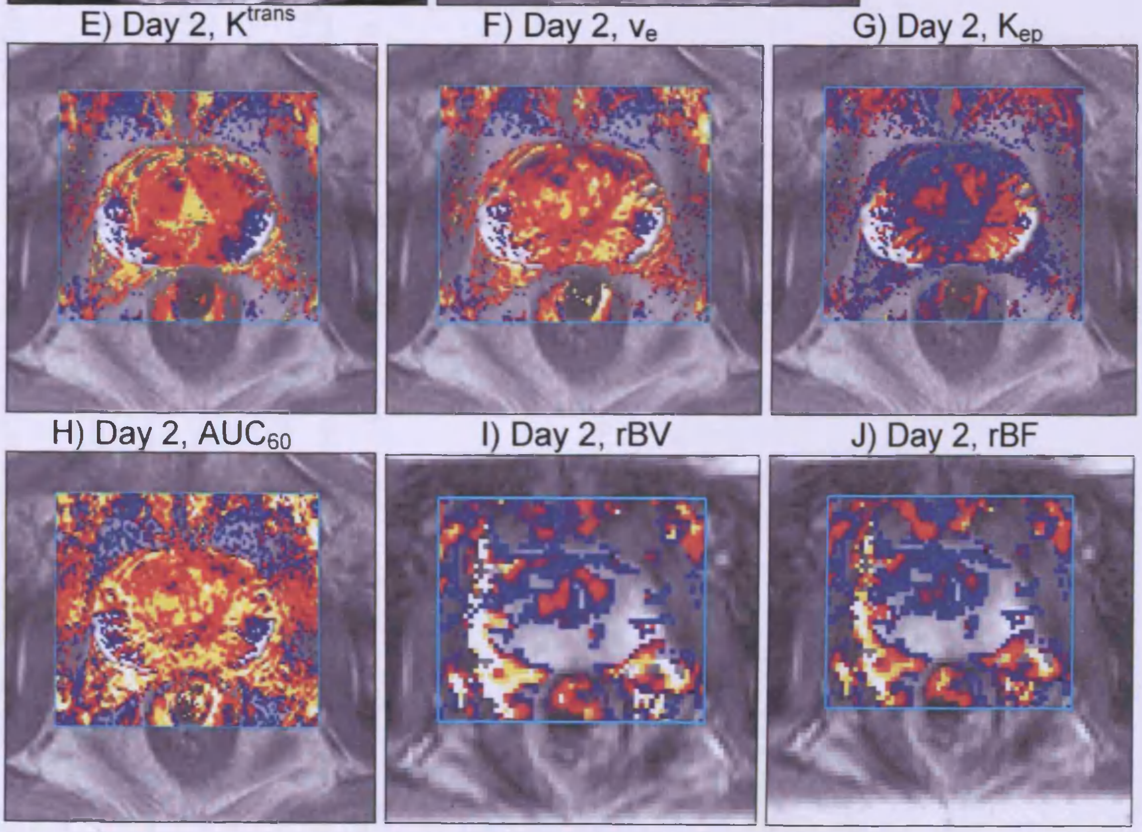

E) Day 2, K^{trans}

F) Day 2, v_e

G) Day 2, K_{ep}

H) Day 2, AUC_{60}

I) Day 2, rBV

J) Day 2, rBF

Table 3.6 Correlation coefficients (ρ) for T_1 and T_2^* weighted DCE-MRI, R_2^* and ADC parameters at baseline

Whole Prostate

	v_e		k_{ep}		AUC_{60}		rBV		rBF		R_2^*		ADC (b-val 0-1000)		ADC (b-val 0-50)		ADC (b-val 150-1000)	
	ρ	p-value	ρ	p-value	ρ	p-value	ρ	p-value	ρ	p-value	ρ	p-value	ρ	p-value	ρ	p-value	ρ	p-value
K^{trans}	0.79	<0.0001	0.57	0.009	0.95	<0.0001	0.68	0.0012	0.66	0.002	0.17	ns	-0.5	ns	-0.54	ns	-0.5	ns
v_e			0.05	ns	0.74	0.0003	0.38	ns	0.31	ns	0.10	ns	-0.43	ns	-0.79	0.034	-0.43	ns
k_{ep}					0.62	0.0046	0.68	0.0013	0.70	0.0009	0.26	ns	0.04	ns	0.14	ns	0.04	ns
AUC_{60}							0.70	0.0008	0.67	0.0016	0.22	ns	-0.5	ns	-0.54	ns	-0.5	ns
rBV									0.98	<0.0001	0.06	ns	-0.29	ns	0.04	ns	-0.29	ns
rBF											0.10	ns	-0.29	ns	0.04	ns	-0.29	ns
R_2^*													0.43	ns	-0.21	ns	0.42	ns
ADC (b-val 0-1000)															0.43	ns	1.0	0.0004
ADC (b-val 0-50)																	0.43	ns

ns = not significant

Table 3.7 Correlation coefficients (ρ) for T_1 and T_2* weighted DCE-MRI, R_2* and ADC parameters at baseline

Tumour

	v_e		k_{ep}		AUC_{60}		rBV		rBF		R_2*		ADC (b-val 0-1000)		ADC (b-val 0-50)		ADC (b-val 150-1000)	
	ρ	p-value	ρ	p-value	ρ	p-value	ρ	p-value	ρ	p-value	ρ	p-value	ρ	p-value	ρ	p-value	ρ	p-value
K^{trans}	0.57	0.008	0.80	<0.0001	0.98	<0.0001	0.56	0.0138	0.59	0.0086	0.29	ns	0.36	ns	-0.5	ns	0.36	ns
v_e			0.16	ns	0.49	0.033	0.33	ns	0.35	ns	0.19	ns	0.64	ns	-0.32	ns	0.57	ns
k_{ep}					0.83	<0.0001	0.58	0.011	0.59	0.0082	0.18	ns	0.14	ns	-0.29	ns	0.04	ns
AUC_{60}							0.59	0.0094	0.62	0.0055	0.36	ns	0.43	ns	-0.54	ns	0.50	ns
rBV									0.98	<0.0001	-0.12	ns	0.25	ns	0.57	ns	0.00	ns
rBF											-0.09	ns	0.04	ns	0.42	ns	-0.18	ns
R_2*													0.00	ns	-0.14	ns	0.57	ns
ADC (b-val 0-1000)															0.21	ns	0.75	ns
ADC (b-val 0-50)																	0.11	ns

ns = not significant

Table 3.8 Correlation coefficients (ρ) for T_1 and T_2^* weighted DCE-MRI, R_2^* and ADC parameters at baseline

Peripheral Zone

	v_e		k_{ep}		AUC_{60}		rBV		rBF		R_2^*		ADC (b-val 0-1000)		ADC (b-val 0-50)		ADC (b-val 150-1000)	
	ρ	p-value	ρ	p-value	ρ	p-value	ρ	p-value	ρ	p-value	ρ	p-value	ρ	p-value	ρ	p-value	ρ	p-value
K^{trans}	0.59	0.011	0.67	0.0029	0.99	<0.0001	0.38	ns	0.38	ns	0.50	0.035	0.00	ns	0.36	ns	-0.18	ns
v_e			-0.12	ns	0.61	0.0079	0.19	ns	0.16	ns	0.22	ns	-0.18	ns	0.07	ns	-0.29	ns
k_{ep}					0.65	0.0046	0.26	ns	0.29	ns	0.47	0.05	0.21	ns	0.46	ns	0.07	ns
AUC_{60}							0.41	ns	0.41	ns	0.50	0.0354	0.00	ns	0.36	ns	-0.18	ns
rBV									0.98	<0.0001	-0.17	ns	-0.04	ns	-0.11	ns	0.00	ns
rBF											-0.10	ns	-0.04	ns	-0.11	ns	0.00	ns
R_2^*													0.11	ns	0.76	0.048	-0.11	ns
ADC (b-val 0-1000)															0.00	ns	0.96	0.0028
ADC (b-val 0-50)																	-0.18	ns

ns = not significant

Table 3.9 Correlation coefficients (ρ) for T_1 and T_2* weighted DCE-MRI, R_2* and ADC parameters at baseline

Central Zone

	v_e		k_{ep}		AUC_{60}		rBV		rBF		R_2*		ADC (b-val 0-1000)		ADC (b-val 0-50)		ADC (b-val 150-1000)	
	ρ	p-value	ρ	p-value	ρ	p-value	ρ	p-value	ρ	p-value	ρ	p-value	ρ	p-value	ρ	p-value	ρ	p-value
K^{trans}	0.77	0.0003	0.59	0.0105	0.96	<0.0001	0.47	ns	0.57	0.0137	0.29	ns	-0.07	ns	0.43	ns	-0.29	ns
v_e			0.02	ns	0.82	<0.0001	0.14	ns	0.27	ns	0.11	ns	-0.71	ns	0.25	ns	-0.89	0.0067
k_{ep}					0.53	0.0244	0.52	0.0277	0.52	0.027	0.25	ns	0.64	ns	0.50	ns	0.54	ns
AUC_{60}							0.42	ns	0.55	0.0198	0.22	ns	-0.21	ns	0.50	ns	-0.43	ns
rBV									0.95	<0.0001	-0.09	ns	0.39	ns	0.43	ns	0.39	ns
rBF											-0.08	ns	0.39	ns	0.43	ns	0.39	ns
R_2*													0.68	ns	0.00	ns	0.43	ns
ADC (b-val 0-1000)															0.07	ns	0.89	0.0123
ADC (b-val 0-50)																	-0.07	ns

ns = not significant

3.6 Discussion

This analysis has shown considerable difference in the variability of the four prostate regions of interest, namely whole prostate, tumour, normal peripheral zone and benign central gland. The fact that peripheral zone is the least reproducible is not surprising. This cohort of patients was made up of men about to undergo neo-adjuvant androgen deprivation prior to external beam radiotherapy. Given the fact that radical prostatectomy and the increasingly popular low dose-rate brachytherapy treatments are reserved for men with more limited, low-stage disease, the external-beam radiotherapy patient population in prostate cancer tends to have more extensive localised disease. 75% of men in this study had stage 2c disease or greater. As a result, the region of peripheral gland that met the criteria for ROI placement (i.e. homogeneous high signal intensity on non-contrast enhanced T_2-weighted sequences) was usually small. This is reflected in the number of pixels used for parameter calculation, which for peripheral gland was only 2.2 – 6.4% of the number of pixels used for whole prostate calculations, depending on the parameter in question. With such low numbers of pixels to average, small differences in ROI placement between scans, spurious pixel values and gland movement during the scan will all have a proportionally greater influence on the final parameter value and thereby increase variability.

For whole prostate ROIs the reverse is true, making it the most reproducible region for analysis. For biological observations, whole prostate values may seem the least informative, being comprised of various different tissues, each of which may respond differently to any given intervention, thereby only giving a 'global' assessment of effect on the gland. However, with increasing evidence that a proportion of tumour cell kill results from vascular effects rather than direct cytotoxicity, a global assessment of prostate vascular status is becoming ever more relevant [12-15].

Tumour regions of interest are generally the most relevant, given that the tumour is the intended target for prostate cancer therapy. Differentiation of tumour from benign peripheral zone is often difficult and as a result is the most frequent subject of radiological publications concerning the prostate gland [16-30]. In this study great care was taken to utilise all the available information for tumour ROI delineation, including combinations of T_2-weighted, contrast enhanced T_1-weighted and diffusion ADC maps. In general, an irregular mass of low signal intensity in the peripheral zone seen on the T_2-weighted images was considered to represent tumour. All regions were checked by a highly experienced radiologist with a specialist interest in prostate cancer (ARP).

Given the challenges in defining tumour regions, it is encouraging that the reproducibility of tumour ROIs was generally not substantially inferior to whole prostate regions for T_1 parameters (variance ratios of 4.9 to 23 for tumour compared with 5.7 to 13.4 for whole prostate), T_2* parameters (variance ratios of 2.2 to 2.5 for tumour versus 3.5 – 3.7 for whole prostate) and for R_2* (variance ratios of 2.3 for tumour versus 2.5 for whole prostate). This is despite a considerably smaller ROI size. The coefficients of variance are comparable to values published in the literature. For example, in this study the wCV for tumour K^{trans} was 20.1% compared with 20.3% reported by Lankester [5] and 24% reported by Galbraith [4]. This is despite the fact that both of these studies investigated much more readily definable tumours such as ovarian, uterine and renal carcinomas as well as pelvic or thoracic sarcomas. Similar comparisons can be made for the other T_1 parameters.

The reproducibility of the prostate T_2* parameters rBV and rBF was poor, with variance ratios of 2.5 – 5.5 for baseline rBV and 2.2 – 3.9 for baseline rBF. wCV values were also disappointing, ranging from 42.5% to 116.3%. This is much worse than the only other reported reproducibility measures for T_2* parameters, in gynaecological malignancy, of 12.1% for rBV and 16.8% for rBF [5]. Given the fact that the image matrix size for the T_2* acquisition is half that of the T_1 images (128 x 128 pixels as opposed to 256 x 256 pixels), resulting in each pixel being four times larger, one would expect a reduction in reproducibility. However, this factor alone cannot explain the poor results. Susceptibility-weighted MRI methods are more liable to be affected by susceptibility artefacts generated by changes in the volume of rectal gas. These artefacts tend to influence the posterior prostate due to its close proximity to the rectum. As a result tumour and peripheral zone ROIs are likely to be most affected by this phenomenon, given that these regions tended to lie posteriorly. Accordingly, wCV for tumour and peripheral zone (72.3% - 116.3%) is worse than wCV for whole prostate (42.5% - 51.9%). Central zone T_2* reproducibility is also likely to be affected by the fact that this region of the prostate is very heterogenous, with nodules of benign hyperplasia interspersed with normal glandular tissue and fibrosis. As a result blood flow is likely to vary considerably between these tissue types and small differences in ROI placement may result in large variations in blood volume and blood flow measurements.

The reproducibility of R_2* in pelvic muscle is extremely good (wCV of 4%, $F = 8.07$ at baseline). This suggests that the measurement technique itself exhibits very low variability. However, when R_2* is measured in tumours, reproducibility is significantly worse (wCV of 23.3%, $F = 2.3$). This may be explained by our understanding of tumour vasculature, which has chaotic structure, poorly formed, fragile vessels with high permeability to macromolecules. There is arteriovenous shunting, high vascular tortuosity and vasodilatation leading to intermittent or unstable flow due to transient rises in already raised interstitial pressure. This results in intermittent changes in blood flow causing periods of transient acute hypoxia. The variability of R_2* may therefore reflect the intrinsic biology of prostate tumours rather than measurement error. This hypothesis is supported by the consistent improvement in the reproducibility of tumour R_2* following androgen deprivation. Androgen withdrawal causes tumour vascular regression and a reduction in the proportion of abnormal blood vessels. As a result there is stabilisation of blood flow and less fluctuation of pO_2 levels.

The decline in reproducibility of the T_1-and T_2*-weighted parameters following androgen deprivation is difficult to explain. In general, the reductions are modest and mixed in comparison with the consistent improvements seen in R_2*. Using the same argument as for R_2*, one would expect an improvement in the reproducibility of the values of relative blood flow and volume. The worsening of reproducibility may in part be due to the fact that these measures are relative because the absolute arterial input function is not known, making comparisons between studies more difficult. The technical difficulties of T_2* methods due to susceptibility artefacts may also mask any physiological stabilisation to the tumour blood flow. Changes in the T_1 parameters before and after androgen deprivation are smaller, with declines only occurring for certain measures (whole prostate and central zone K^{trans}, whole prostate, peripheral and central zone v_e, whole prostate, tumour and central zone k_{ep} and whole prostate, tumour and central zone AUC_{60}).

The deterioration in reproducibility for whole prostate, tumour and central gland regions of interest following androgen withdrawal may have a simpler explanation. Androgen deprivation causes a reduction in prostate volume (by an average of 34% in this study), thereby reducing the number of pixels for whole prostate analysis. The distinction between tumour and normal peripheral zone becomes even harder to discern following the reduction in peripheral zone signal intensity on T_2-weighted sequences, making the definition of these regions less reliable. Similarly, the altered prostate morphology makes accurate recreation of central zone ROIs from examination to examination more difficult, thereby increasing variability.

The strong correlation observed between AUC_{60} and the quantitative T_1 parameters confirms the observations reported by Lankester, validating the use of this semi-quantitative parameter, which is not dependent on mathematical modelling of gadolinium concentration – time curves, as a 'global' measure of vascularity. The interdependence between K^{trans} and v_e, K^{trans} and k_{ep} and both K^{trans} and k_{ep} with rBv and rBV reflect the intrinsic relationship between blood flow, vascular permeability, distribution within the extravascular compartment and re-entry of contrast into the vasculature. The fact that nothing correlates with R_2* suggests that, for this series at least, the vascular deoxyhaemoglobin concentration is independent of flow or volume effects.

3.7 Conclusion

This study documents the variability and repeatability of T_1-and T_2*-weighted DCE-MRI, R_2* and apparent diffusion coefficients for the various regions of the human prostate gland. Together with published data for prostate gland and other tumour sites, data are emerging regarding the suitability of the various MRI parameters as measures of response to treatment in a variety of malignant tumours [4, 5, 11, 31]. Specifically, this study has served to provide estimates of variability, within the 20 patients imaged as part of this study, so as to determine the effect of androgen deprivation on the prostate gland accurately and to calculate, on an individual patient-by-patient basis, whether a parameter change following androgen withdrawal is statistically significant.

References

1 Padhani AR, Khoo VS, Suckling J, *et al.* Evaluating the effect of rectal distension and rectal movement on prostate gland position using cine MRI. *Int J Radiat Oncol Biol Phys* 1999;44:525-533.

2 Accuracy (trueness and precision) of measurement methods and results. General principles and definitions (BS ISO 5725-1). 1994.

3 Padhani AR, Hayes C, Landau S, *et al.* Reproducibility of quantitative dynamic MRI of normal human tissues. *NMR Biomed* 2002;15:143-153.

4 Galbraith SM, Lodge MA, Taylor NJ, *et al.* Reproducibility of dynamic contrast-enhanced MRI in human muscle and tumours: comparison of quantitative and semi-quantitative analysis. *NMR Biomed* 2002;15:132-142.

5 Lankester K, Taylor N, Stirling J, *et al.* Dynamic MRI for Imaging Tumour Microvasculature: Comparison of Susceptibility and Relaxivity Techniques in Pelvic Tumours. *J Magn Reson Imaging* 2007;25:In press.

6 Bland JM, Altman DG. Measurement error. *Bmj* 1996;313:744.

7 Bland JM, Altman DG. Measurement error proportional to the mean. *Bmj* 1996;313:106.

8 Bland JM, Altman DG. Measurement error and correlation coefficients. *Bmj* 1996;313:41-42.

9 Hunter GJ, Hamberg LM, Choi N, *et al.* Dynamic T1-weighted magnetic resonance imaging and positron emission tomography in patients with lung cancer: correlating vascular physiology with glucose metabolism. *Clin Cancer Res* 1998;4:949-955.

10 Padhani AR, Gapinski CJ, Macvicar DA, *et al.* Dynamic contrast enhanced MRI of prostate cancer: correlation with morphology and tumour stage, histological grade and PSA. *Clin Radiol* 2000;55:99-109.

11 Hoskin P, Carnell D, Taylor N, *et al.* Hypoxia in prostate cancer: correlation of BOLD-MRI with pimonidazole immunohistochemistry. *Int J Radiat Oncol Biol Phys*;In Press.

12 Hayek OR, Shabsigh A, Kaplan SA, *et al.* Castration induces acute vasoconstriction of blood vessels in the rat prostate concomitant with a reduction of prostatic nitric oxide synthase activity. *J Urol* 1999;162:1527-1531.

13 Lekas E, Johansson M, Widmark A, *et al.* Decrement of blood flow precedes the involution of the ventral prostate in the rat after castration. *Urol Res* 1997;25:309-314.

14 Matsushima H, Goto T, Hosaka Y, *et al.* Correlation between proliferation, apoptosis, and angiogenesis in prostate carcinoma and their relation to androgen ablation. *Cancer* 1999;85:1822-1827.

15 Shabsigh A, Chang DT, Heitjan DF, *et al.* Rapid reduction in blood flow to the rat ventral prostate gland after castration: preliminary evidence that androgens influence prostate size by regulating blood flow to the prostate gland and prostatic endothelial cell survival. *Prostate* 1998;36:201-206.

16 Engelbrecht MR, Huisman HJ, Laheij RJ, *et al.* Discrimination of prostate cancer from normal peripheral zone and central gland tissue by using dynamic contrast-enhanced MR imaging. *Radiology* 2003;229:248-254.

17 Engelbrecht MR, Jager GJ, Laheij RJ, *et al.* Local staging of prostate cancer using magnetic resonance imaging: a meta-analysis. *Eur Radiol* 2002;12:2294-2302.

18 Futterer JJ, Heijmink SW, Scheenen TW, *et al.* Prostate Cancer Localization with Dynamic Contrast-enhanced MR Imaging and Proton MR Spectroscopic Imaging. *Radiology* 2006.

19 Hara N, Okuizumi M, Koike H, *et al.* Dynamic contrast-enhanced magnetic resonance imaging (DCE-MRI) is a useful modality for the precise detection and staging of early prostate cancer. *Prostate* 2005;62:140-147.

20 Huch Boni RA, Boner JA, Lutolf UM, *et al.* Contrast-enhanced endorectal coil MRI in local staging of prostate carcinoma. *J Comput Assist Tomogr* 1995;19:232-237.

21 Jager GJ, Ruijter ET, van de Kaa CA, *et al.* Local staging of prostate cancer with endorectal MR imaging: correlation with histopathology. *AJR Am J Roentgenol* 1996;166:845-852.

22 Jager GJ, Ruijter ET, van de Kaa CA, *et al.* Dynamic TurboFLASH subtraction technique for contrast-enhanced MR imaging of the prostate: correlation with histopathologic results. *Radiology* 1997;203:645-652.

23 Kahn T, Burrig K, Schmitz-Drager B, *et al.* Prostatic carcinoma and benign prostatic hyperplasia: MR imaging with histopathologic correlation. *Radiology* 1989;173:847-851.

24 Kiessling F, Lichy M, Grobholz R, *et al.* Simple models improve the discrimination of prostate cancers from the peripheral gland by T1-weighted dynamic MRI. *Eur Radiol* 2004;14:1793-1801.

25 Kozlowski P, Chang SD, Jones EC, *et al.* Combined diffusion-weighted and dynamic contrast-enhanced MRI for prostate cancer diagnosis--correlation with biopsy and histopathology. *J Magn Reson Imaging* 2006;24:108-113.

26 Muramoto S, Uematsu H, Kimura H, *et al.* Differentiation of prostate cancer from benign prostate hypertrophy using dual-echo dynamic contrast MR imaging. *Eur J Radiol* 2002;44:52-58.

27 Namimoto T, Morishita S, Saitoh R, *et al.* The value of dynamic MR imaging for hypointensity lesions of the peripheral zone of the prostate. *Comput Med Imaging Graph* 1998;22:239-245.

28 Quinn SF, Franzini DA, Demlow TA, *et al.* MR imaging of prostate cancer with an endorectal surface coil technique: correlation with whole-mount specimens. *Radiology* 1994;190:323-327.

29 Scheidler J, Hricak H, Vigneron DB, *et al.* Prostate cancer: localization with three-dimensional proton MR spectroscopic imaging--clinicopathologic study. *Radiology* 1999;213:473-480.

30 Schiebler ML, Tomaszewski JE, Bezzi M, *et al.* Prostatic carcinoma and benign prostatic hyperplasia: correlation of high-resolution MR and histopathologic findings. *Radiology* 1989;172:131-137.

31 Rijpkema M, Kaanders JH, Joosten FB, *et al.* Effects of breathing a hyperoxic hypercapnic gas mixture on blood oxygenation and vascularity of head-and-neck tumors as measured by magnetic resonance imaging. *Int J Radiat Oncol Biol Phys* 2002;53:1185-1191.

Chapter 4

Experiments to evaluate the validity and reproducibility of Blood Oxygen Level Dependent MRI and its response to hyperoxia, in two human prostate cancer xenografts.

4.1 Aims

1) To evaluate the correlation between the quantity and distribution of pimonidazole immunostaining and the BOLD-MRI derived R_2* parameter in DU145 and PC3 human prostate tumour xenografts.

2) To assess the reproducibility of R_2* in these xenografts.

3) To determine the effect of carbogen gas breathing on the R_2* parameter.

4.2 Introduction

This chapter contains details of the experiments performed to determine whether BOLD MRI is a valid technique to evaluate the oxygen status of prostate carcinoma and to determine the effect of an increased inspired oxygen concentration on tumour oxygenation.

Animal experiments were performed in order to evaluate the validity and reproducibility of this MR technique in a highly controlled environment without the confounding factors that are present in the clinical setting. Prostate cancer xenografts are suitable for imaging studies because they consist of solid tumour masses. Longer continuous acquisition times could be used with mice compared with human subjects because they could be rendered motionless using sedation. There is also more control in obtaining tumour sections in the same orientation as the MRI scan because there is no requirement for detailed pathological staging, which must always take priority to sectioning for research purposes in patients that undergo radical prostatectomy.

The DU145 cell line was originally isolated from a lesion in the brain of a patient with metastatic carcinoma of the prostate and a 3 year history of lymphocytic leukaemia [1, 2]. It forms adenocarcinoma (grade II) consistent with a prostatic primary. The cell line is not detectably hormone sensitive, is only weakly positive for acid phosphatase and isolated cells form colonies in soft agar. The cells do not express prostate specific antigen. Ultrastructural analyses of both the cell line and original tumour reveals microvilli, tonofilaments, desmosomes, mitochondria, well developed Golgi and heterogenous lysosomes.

The PC-3 cell line was initiated from a bone metastasis of a stage IV prostate adenocarcinoma in a 62-year-old male Caucasian [3]. The line is not detectably hormone sensitive. Cells exhibit low acid phosphatase and testosterone-5-alpha reductase activities.

4.3 Materials and Methods

All animal experiments were performed in full compliance with government regulations and UKCCCR guidelines on animal welfare and were approved by the local Ethical Review Committee (Home office licence number 70/5823).

4.3.1 Cell Culture

DU145 and PC3 cells were incubated under 19.6% O_2, 5% CO_2 and 75.4% N_2 at 37°C. The cells were maintained in Dulbecco's Modified Eagle Media (DMEM) media supplemented with 10% foetal calf serum (FCS), 2mM L-glutamine, 100 units/ml penicillin and 100µg/ml streptomycin.

4.3.2 Implant

Tumours were initiated by injecting 0.05ml containing $2x10^6$ cells (subcutaneously) onto the rear dorsum of 8-10 week old SCID mice. Animals were selected for treatment when their tumours reached 8-10mm geometric mean diameter (GMD).

4.3.3 Imaging

Three experiments were performed on each mouse using two imaging sessions over two days:

Mice were sedated for each MRI scan using 200µl of 1 : 10 hypnorm in water, injected into the peritoneal cavity. The sedated mouse was then placed in a six centimetre diameter quadrature birdcage coil (Varian, Palo Alto, CA, USA) in a 4.7 Tesla Varian MR system. A hot air blower with continuous temperature monitoring was used to maintain body temperature.

Day 1

Baseline BOLD measurement:

Initial T_1-weighted sagital and transverse scans were obtained for localisation. Multiple spoiled gradient echo (GRE) images were acquired on a single central slice with increasing TE times (4ms - 48ms, in 4ms steps), with TR 117 ms, flip angle (α) 45°, slice thickness 1 mm and field of view 40 x 45 mm.

Carbogen breathing experiment:

Scanning time was divided into three gas-breathing periods with the mouse breathing air, carbogen (95% O_2 and 5% CO_2) and then air again. The first air breathing period lasted four minutes, followed by 10 minutes of carbogen breathing and then a further four minutes breathing air. All gases were administered at 1 l.min^{-1} (gases obtained from BOC, UK). A vacuum- based gas scavenger was used to minimise changes in oxygen content within the magnet bore. GRE images with the same imaging parameters that were used for the baseline scan were acquired every minute throughout the experiment.

The mouse was returned to the animal house overnight.

Day 2

Pimonidazole administration:

Each mouse was weighed. Pimonidazole hydrochloride, made up to a concentration of 6mg/ml was administered at a dose of 60mg/kg by intra-peritoneal injection one hour before the scan.

Imaging:

Sedation and immobilisation was performed as for day one. The imaging protocol was identical to the baseline scan on day one with the mouse breathing air only. The tumour was imaged in the same plane and at the same level as on the previous day. The animal was returned to its cage after the scan.

Euthanasia:

The mouse was killed by cervical dislocation two hours after the pimonidazole injection (i.e. about 20 minutes after imaging was complete). The tumour was immediately dissected.

4.3.4 Histology and Immunohistochemical Analysis

These are detailed in the histological methods section – **appendix A**.

4.3.5 Animal MR Image Analysis (Figure 4.1)

Multi-echo single-slice sequence images were processed using Matlab version 5 (The Mathworks, Nantick, MA, USA). A region of interest (ROI) was drawn around the tumour using the initial T_1-weighted image. R_2* (s^{-1}) pixel-maps were then calculated for the baseline scan, for each time-point of the carbogen series and for the scans on day 2. A grid-based analysis was then performed for each of the scans. The in-house analysis program written for the Matlab software created a 1mm x 1mm grid across the tumour. R_2* pixel maps were generated for each grid element.

Animated GIF images were generated by the Matlab program and used to check for movement with the GIMP animation playback feature (GNU Image Manipulation Program, www.gimp.org). If movement was seen to occur, the individual image was excluded and the ROI re-positioned for subsequent analysis. Animals were excluded if there was movement through the imaging plane during the experiment.

4.3.6 Experimental Design

Validation

The validation experiment compared the level and distribution of R_2* with the distribution of pimonidazole staining in the corresponding histological section. The median R_2* value for the whole tumour ROI from day 2 of the experiment was compared with the whole tumour pimonidazole staining percentage (with and without the exclusion of necrotic areas). R_2* from each grid element was also compared with the pimonidazole staining percentage from the corresponding grid element in the matching histological section. The grid-based analysis was only performed for non-necrotic tumour grid elements. The day 2 MRI parameter values were chosen for the histological comparison because this imaging procedure was performed only 20-30 minutes prior to the excision and formalin fixation of the tumour. As a result there was minimal time for the oxygenation status of the tumour xenograft to change between the time-points of the MRI and immunohistochemical measurements of hypoxia.

Figure 4.1 **Animal MR Image Analysis**

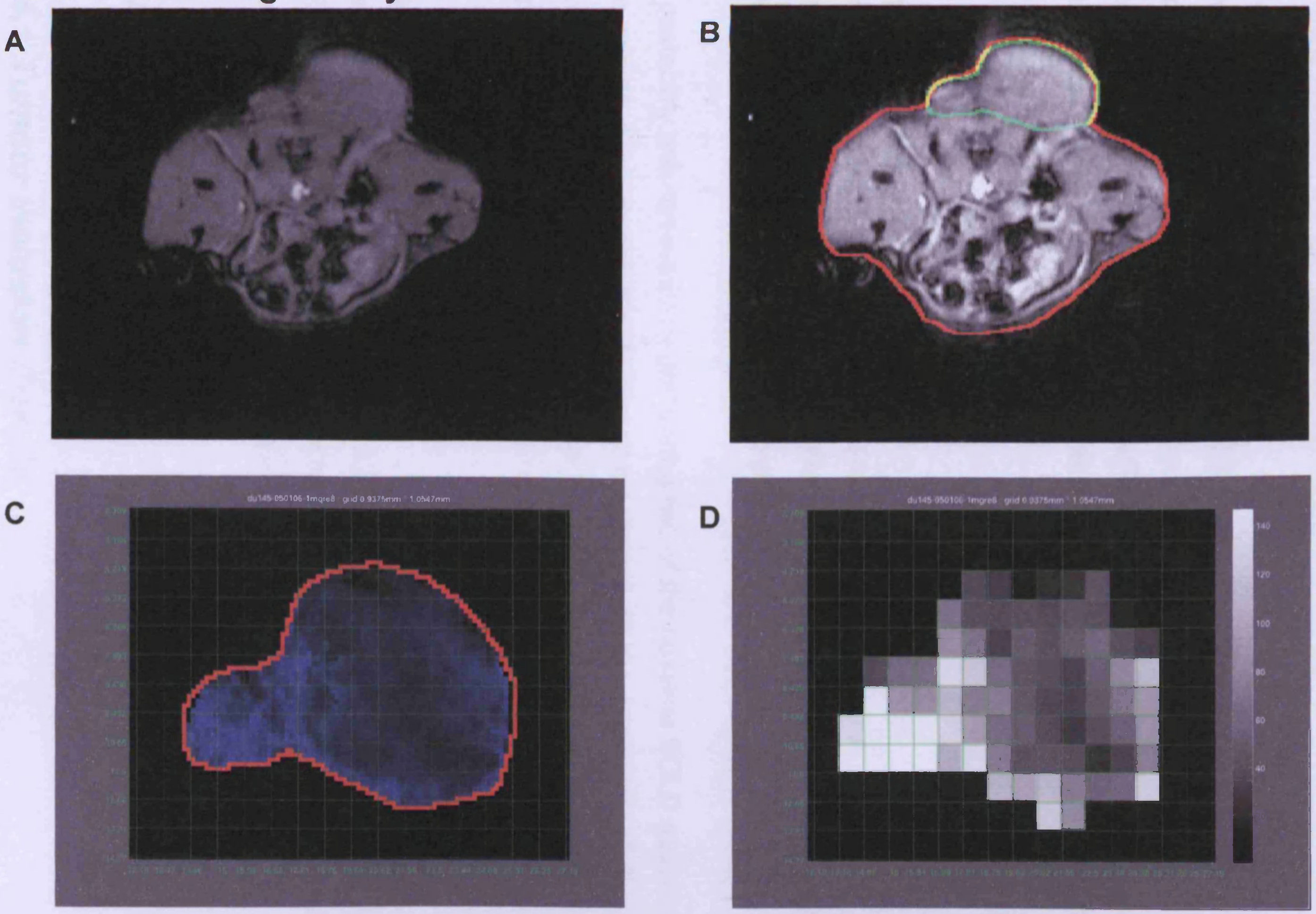

(A) shows the initial T_1-weighted image the entire mouse in cross section. A region of interest was drawn around each tumour (B). R_2^* (s^{-1}) pixel-maps were then calculated (C). A grid-based analysis (1 x 1mm) was then performed for each scan (D).

The distribution of each set of results was tested for normality using the Shapiro-Wilk test. For normally distributed data, correlation was assessed using the Pearson correlation coefficient (r). For non-parametric data the Spearman-Rank correlation coefficient was used. The Mann-Whitney U test was used to test for a significant difference between two categorical data sets, for example when the percentage of necrosis between the two xenografts was being compared.

A receiver operating characteristic (ROC) curve was plotted for both the whole tumour and grid-based data for the DU145 tumours. This calculation provided an estimation of the sensitivity and specificity of BOLD MR when used to depict tumour hypoxia. It also established the R_2* value with the optimum power to predict hypoxia within a grid element.

Reproducibility

The reproducibility experiment compared the whole tumour baseline R_2* values between day 1 and day 2 for each mouse. The standard consensus approach to assessing reproducibility was used (see page 89).

Repeatability was assessed by comparing two of the baseline BOLD sequences taken one minute apart during the air breathing period at the beginning of the carbogen experiment on day 1 (time-points two and three). Again the standard consensus approach was used.

Carbogen breathing

The effect of hyperoxia on R_2* was evaluated using the time series of repeated BOLD MRI scans during carbogen breahing. Changes in R_2* for the whole xenograft and for every grid element of each tumour were calculated.

4.4 Results

4.4.1 Tumour Inclusion Criteria

Twenty-four DU145 and twenty PC3 prostate tumour xenografts were imaged.

For four DU145 tumours and three PC3 tumours the tumour became fragmented on dissection. For these tumours only average whole tumour measurements were possible. Very poor anatomical correlation between the MRI and histological section made grid based analysis impossible. Pimonidazole staining failed in two DU145 tumours for unknown reasons; these tumours were excluded from the immunohistochemical analysis. In one of the DU145 experiments no data was obtained for the day 2 MRI scan because of a temporary fault with the MRI software. In this case reproducibility analysis was not possible. The day 1 MRI scan was used for pathological correlation. In one DU145 tumour and three PC3 tumours there were no results for the carbogen breathing experiment. In each case this was due to data corruption during the MR image acquisition.

The following numbers of tumour xenografts were used for each analysis:

Table 4.1 The number of tumour xenografts used for analysis

	Whole Tumour Pathological Correlation	Grid Based Pathological Correlation	Reproducibility	Carbogen
DU145	22	19	23	23
PC3	20	17	20	17

4.4.2 Tumour Characteristics

Notable differences were identified between the two tumour types:

1) PC3 tumours were significantly more necrotic than DU145 tumours with a median of 18.1% of the total cross-sectional PC3 tumour area being necrotic compared with 9.4% for DU145 tumours ($p = 0.034$, Mann-Whitney U test). **Figure 4.2**.
2) PC3 tumours contain significantly more blood vessels than DU145 tumours. The mean vascular endothelial cross sectional area as a proportion of the whole tumour cross-sectional area for PC3 tumours was 17.3% compared with 3.8% for DU145 tumours ($p < 0.0001$, Mann-Whitney U test). **Figure 4.3**.
3) The DU145 tumours were significantly more hypoxic than the PC3 tumours, this is compatible with the difference in vascularity. The median proportion of cells staining with pimonidazole was 22.5% for DU145 tumours versus 10.6% for PC3 xenografts, $p = 0.018$ (20.3% and 10.7% respectively if necrosis is excluded, $p = 0.015$, Mann-Whitney U test). **Figure 4.4**.

Figure 4.2

The difference in the percentage of necrosis between DU145 and PC3 xenografts

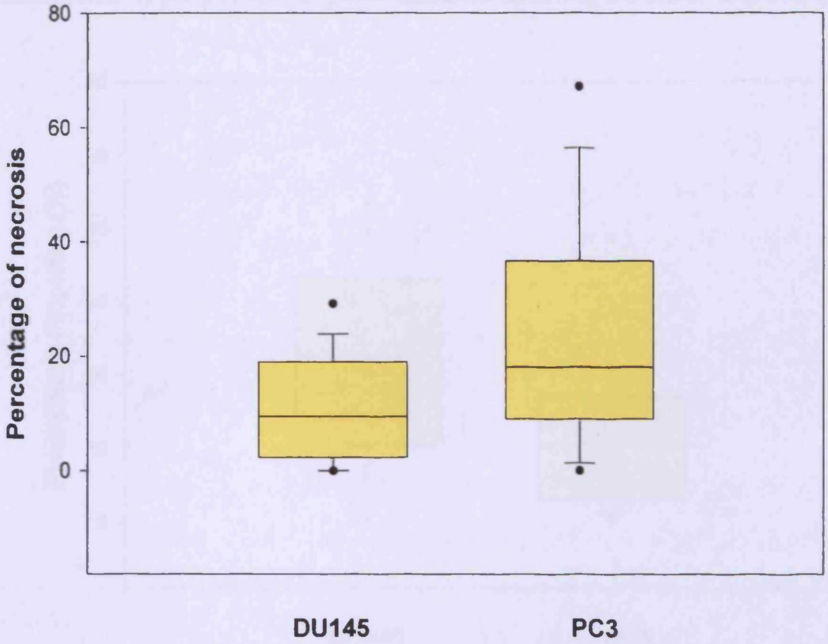

Figure 4.3

The difference in proportion of CD31 staining between DU145 and PC3 tumours

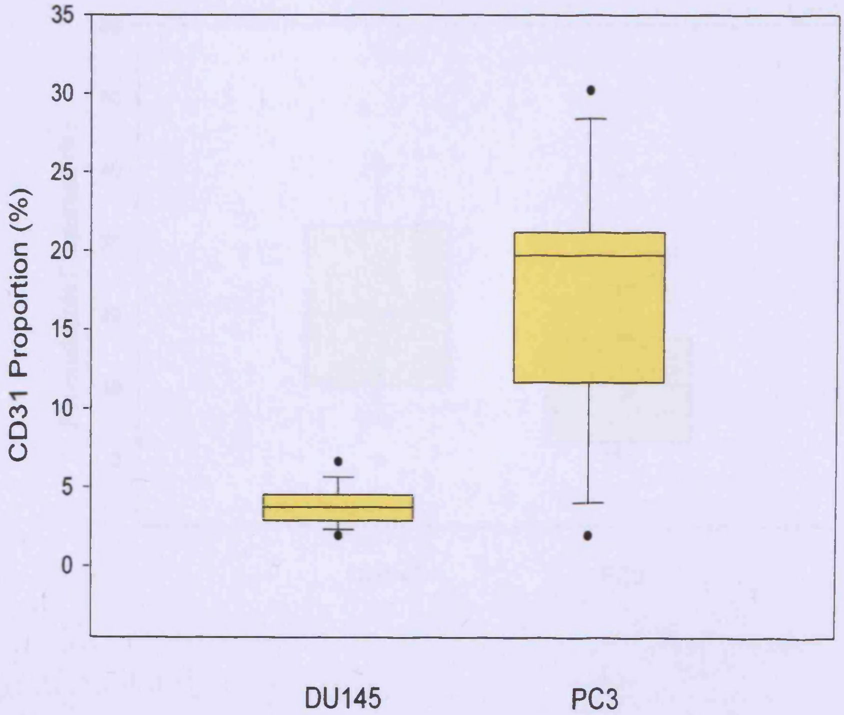

Figure 4.4

The difference in proportion of pimonidazole staining between DU145 and PC3 tumours

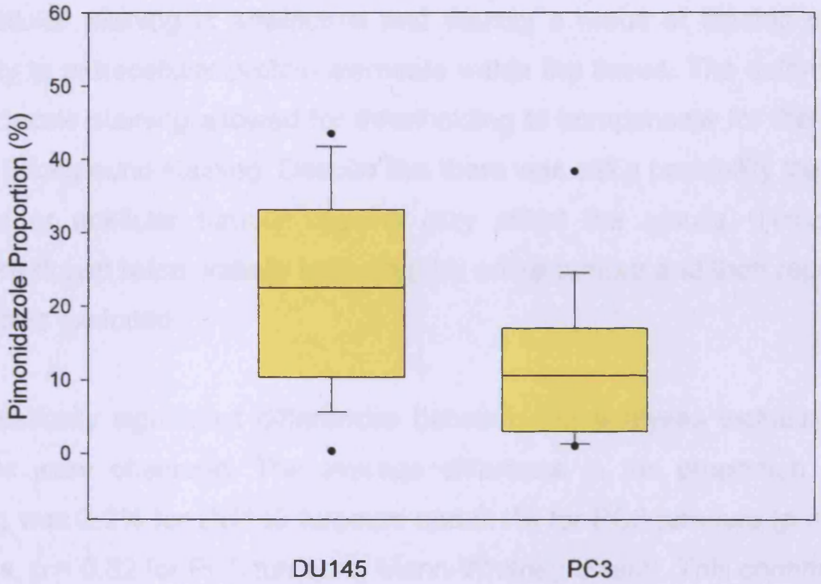

The difference in proportion of pimonidazole staining between DU145 and PC3 tumours with areas of necrosis excluded

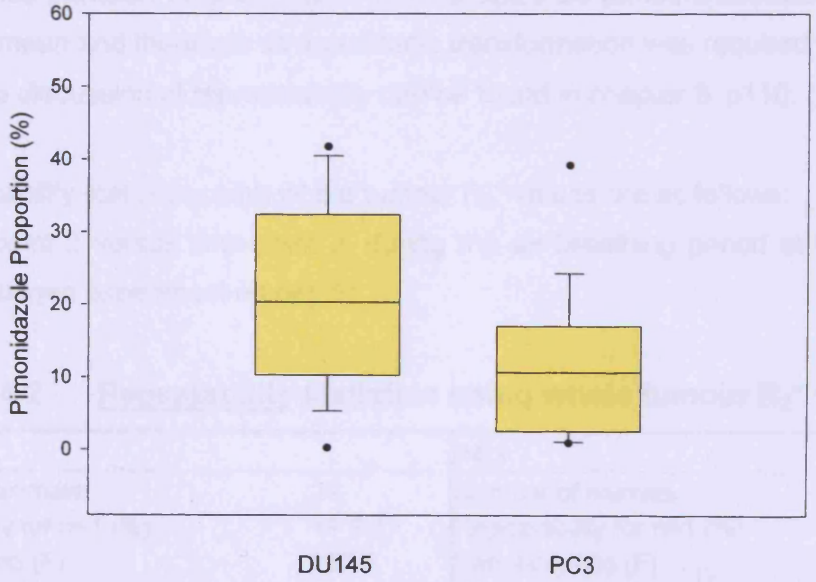

4.4.3 Exclusion of necrosis

Intact living cells take up pimonidazole in an active process. Areas of necrosis should not, in theory, stain for pimonidazole. Pimonidazole labelling can be considered 'positive' if the brown staining is cytoplasmic or nuclear, in other words the pimonidazole is bound within the cell as a result of the cell's low oxygen environment. Extracellular staining is artefactual and usually a result of binding of the secondary antibody to extracellular protein elements within the tissue. The automated analysis of pimonidazole staining allowed for thresholding to compensate for the small amount of diffuse background staining. Despite this there was still a possibility that the inclusion of necrotic or acellular tumour regions may affect the results. Tumours ROIs were therefore drawn twice, initially including the entire tumour and then repeated with areas of necrosis excluded.

No statistically significant differences between the analyses including and excluding necrosis were observed. The average difference in the proportion of pimonidazole staining was 2.2% for DU145 tumours and 0.1% for PC3 tumours (p = 0.69 for DU145 tumours, p = 0.82 for PC3 tumours, Mann-Whitney U test). This confirms the specificity of pimonidazole binding and indicates that background, extracellular staining was minimal and statistically irrelevant.

4.4.4 Reproducibility Analysis

The distribution of each parameter was not significantly different form normal. The difference between values for both DU145 and PC3 tumours showed no dependence on the mean and therefore no logarithmic transformation was required for these data. A detailed discussion of reproducibility can be found in chapter 3, p110.

Repeatability statistics using whole tumour R_2* values are as follows:

(Time-point 2 versus time-point 3, during the air breathing period at the beginning of the carbogen experiment on day 1)

Table 4.2 Repeatability statistics using whole tumour R_2* values

DU145		**PC3**	
Number of animals	23	Number of animals	17
Repeatability for n=1 (%)	+/- 9.3	Repeatability for n=1 (%)	+/- 6.3%
Variance ratio (F)	287.8	Variance ratio (F)	1580.2
P-value for F	< 0.0001	P-value for F	< 0.0001
Interclass correlation coefficient (ICC)	0.99	Interclass correlation coefficient (ICC)	0.99
Coefficient of variation (wCV)	3.4%	Coefficient of variation (wCV)	2.2%

The test proved to be extremely repeatable in both DU145 and PC3 tumours. For an individual mouse, a reduction in R_2* of 9.3% for DU145 tumours and 6.3% for PC3 tumours could be considered significant at the 95% confidence level (i.e. not simply a result of test variability). A very high degree of repeatability was seen for both tumour types in terms of both ICC and wCV.

Reproducibility statistics using whole tumour R_2* values are as follows:
(Day 1 versus Day 2)

Table 4.3 <u>Reproducibility</u> statistics using whole tumour R_2* values

DU145		**PC3**	
Number of animals	23	Number of animals	20
Variance ratio (F)	10.3	Variance ratio (F)	23.6
P-value for F	< 0.0001	P-value for F	< 0.0001
Interclass correlation coefficient (ICC)	0.81	Interclass correlation coefficient (ICC)	0.91
Coefficient of variation (wCV)	5.2%	Coefficient of variation (wCV)	9.1%

A high degree of reproducibility was seen for both tumour types in terms of both ICC and wCV.

4.4.5 Histological Correlation

<u>Whole Tumour Measurements</u>

There is a statistically significant positive correlation between the R_2* rate and the proportion of pimonidazole labelling within DU145 and PC3 human prostate cancer xenografts. **(figures 4.5 & 4.6)**. Pearson's product moment correlation coefficient (r) was calculated for both tumour types with necrosis included and excluded:

Table 4.4 The correlation between R_2* and pimonidazole labelling

	Necrosis Included		Necrosis Excluded	
	r	p-value	r	p-value
DU145	0.75	< 0.0001	0.75	< 0.0001
PC3	0.73	0.0006	0.73	0.0006

Figure 4.5

Scatter plot showing the relationship between whole DU145 tumour R_2^* and the proportion of pimonidazole staining in corresponding tumour sections

(regression line shown in black)

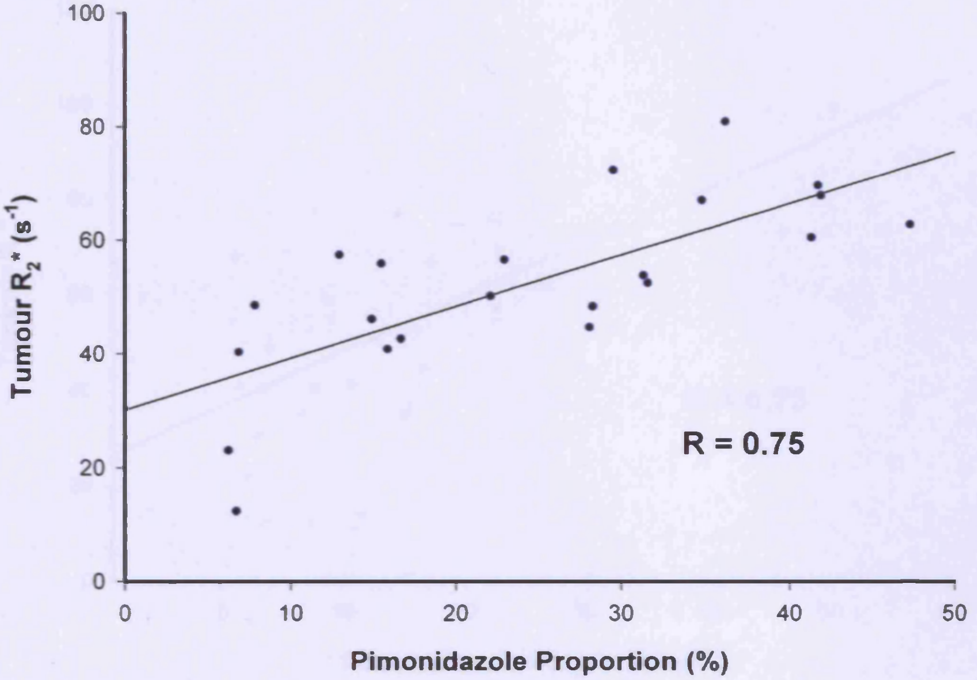

Scatter plot showing the relationship between whole DU145 tumour R_2^* and the proportion of pimonidazole staining in corresponding tumour sections.
Necrosis Excluded
(regression line shown in black)

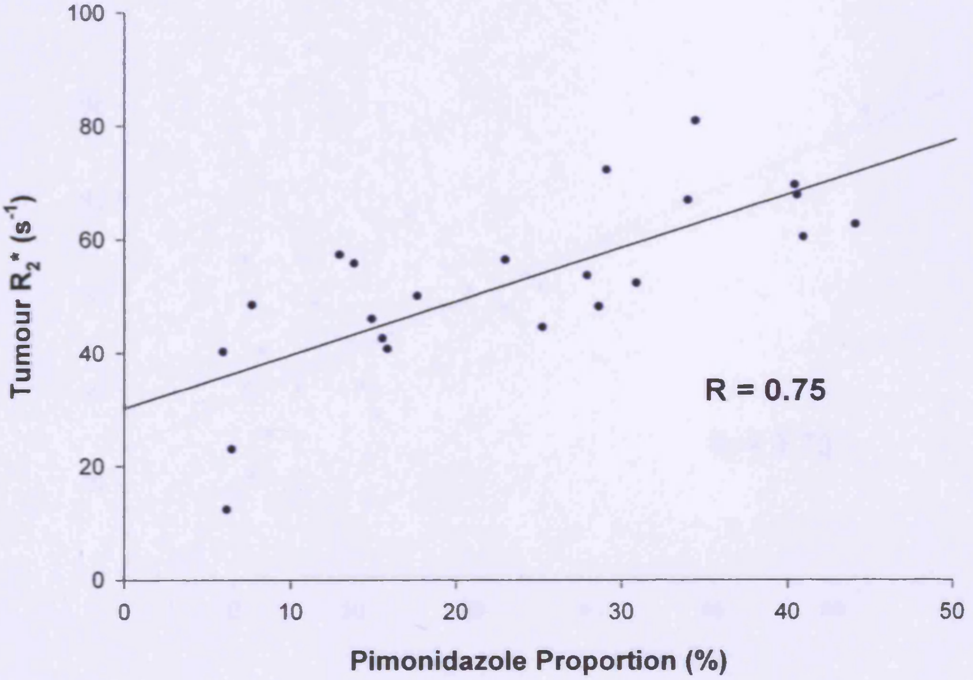

Figure 4.6

Scatter plot showing the relationship between whole PC3 tumour R_2^* and the proportion of pimonidazole staining in corresponding tumour sections

(regression line shown in black)

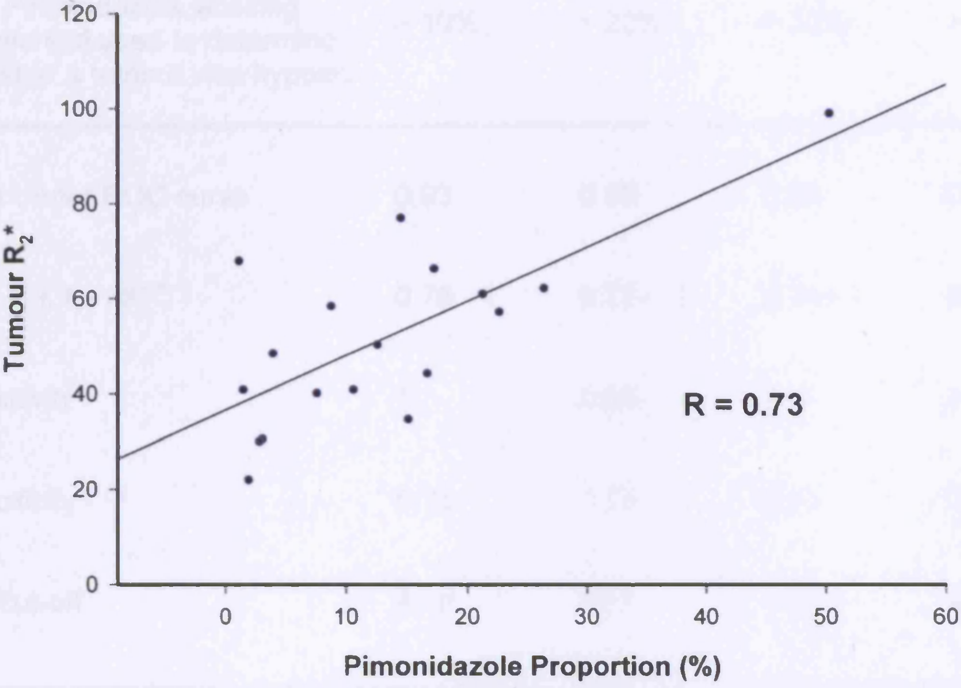

Scatter plot showin the relationship between whole PC3 tumour R_2^* and the proportion of pimonidazole staining in corresponding tumour sections
Necrosis Excluded
(regression line shown in black)

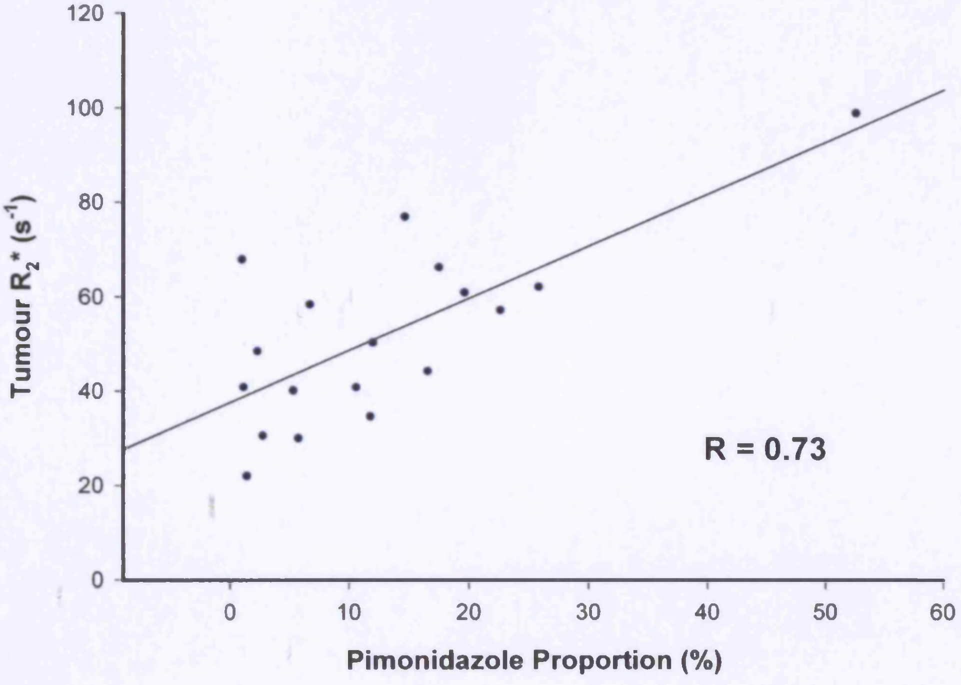

The ROC analysis is dependent upon the pimonidazole-staining threshold above which a tumour was considered hypoxic. As a result four calculations were performed with increasing cut-off values **(figure 4.7)**:

Table 4.5 ROC analysis – whole tumour

Pimonidazole labelling threshold used to determine whether a tumour was hypoxic	> 10%	> 20%	> 30%	> 40 %
Area Under ROC curve	0.93	0.88	0.88	0.86
95% C.I. for ROC	0.78 - 1	0.73 – 1	0.74 - 1	0.70 - 1
Sensitivity	1	0.85	1	1
Specificity	0.75	0.78	0.71	0.83
R2* cut-off	40.8	50.1	52.43	60.52

Figure 4.7 ROC analysis – whole DU145 tumour

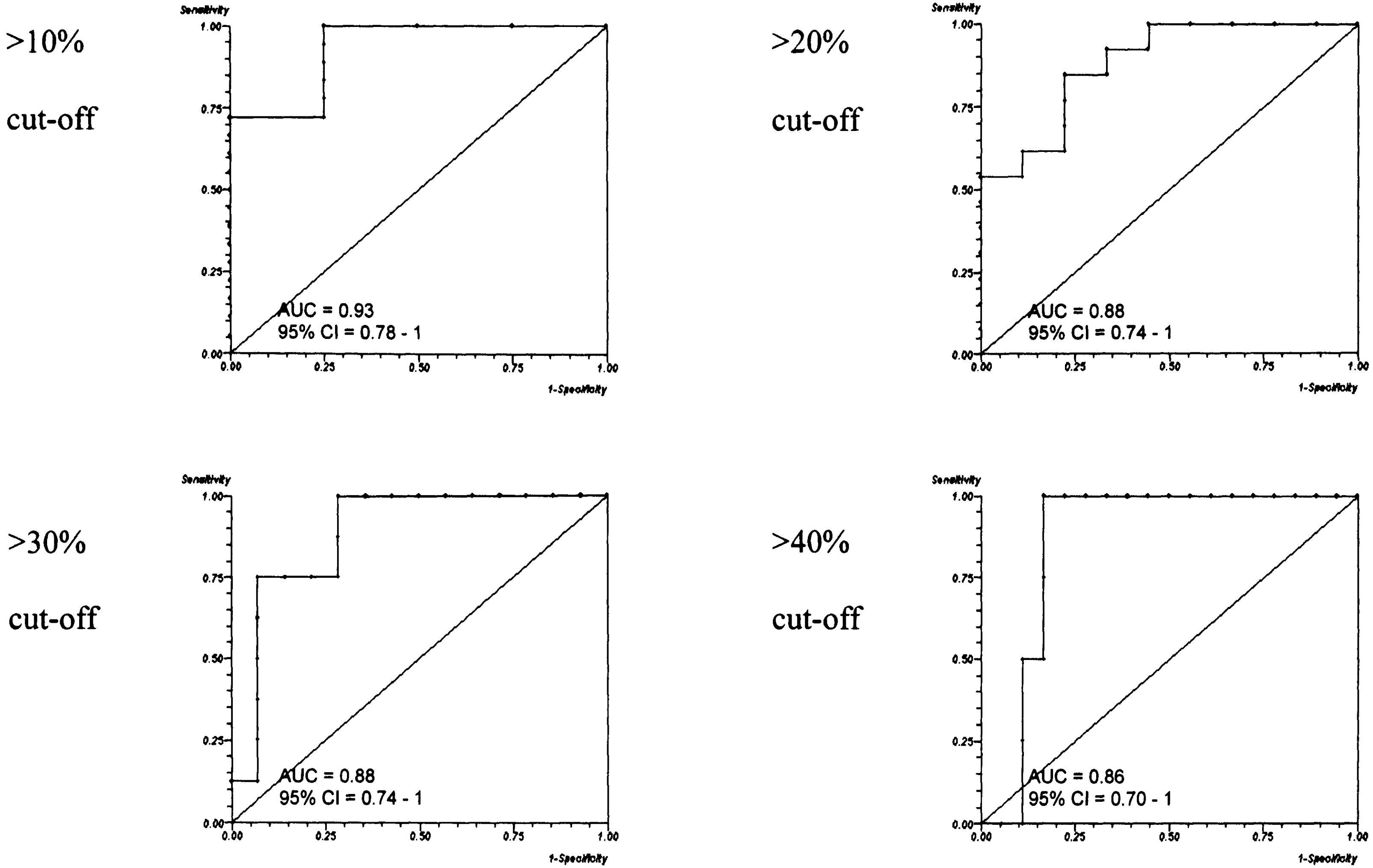

>10% cut-off

>20% cut-off

>30% cut-off

>40% cut-off

Grid Analysis

917 DU145 and 864 PC3 corresponding grid pairs were identified between the MR images and the histological sections. For each MRI grid the median R_2* value was used. The calculation of the percentage of pimonidazole proportion for each grid element involved the division of the area of staining by the total grid area. As a result, only grid squares that contained 100% tumour could be used for analysis. This left 536 DU145 grid pairs and 412 PC3 grid pairs. Grid elements that contained necrosis were also excluded leaving a final number of grid pairs for analysis of 431 for DU145 and 319 for PC3.

A weak, but highly statistically significant correlation was seen between R_2* and pimonidazole labelling in the DU145 grid-based analysis ($r = 0.28$, $p < 0.0001$) **(figure 4.8)**. No correlation was seen in the poorly staining PC3 tumours **(figure 4.9)**.

The ROC for the grid based analysis for DU145 tumours gave the following results **(figure 4.10)**:

Table 4.6 ROC analysis – grids

Pimonidazole labelling threshold used to determine whether a tumour was hypoxic	> 10%	> 20%	> 30%	> 40 %
Area Under ROC curve	0.64	0.62	0.63	0.62
95% C.I. for ROC	0.56–0.71	0.55–0.69	0.57-0.70	0.54-0.68
Sensitivity	0.31	0.26	0.51	0.38
Specificity	0.95	0.96	0.72	0.83
R2* cut-off	54.6	47.9	47.9	54.7

Figure 4.8

Graph showing the correlation between R_2^* and the proportion of pimonidazole labelling in 19 DU145 tumours analysed using a 1x1mm grid

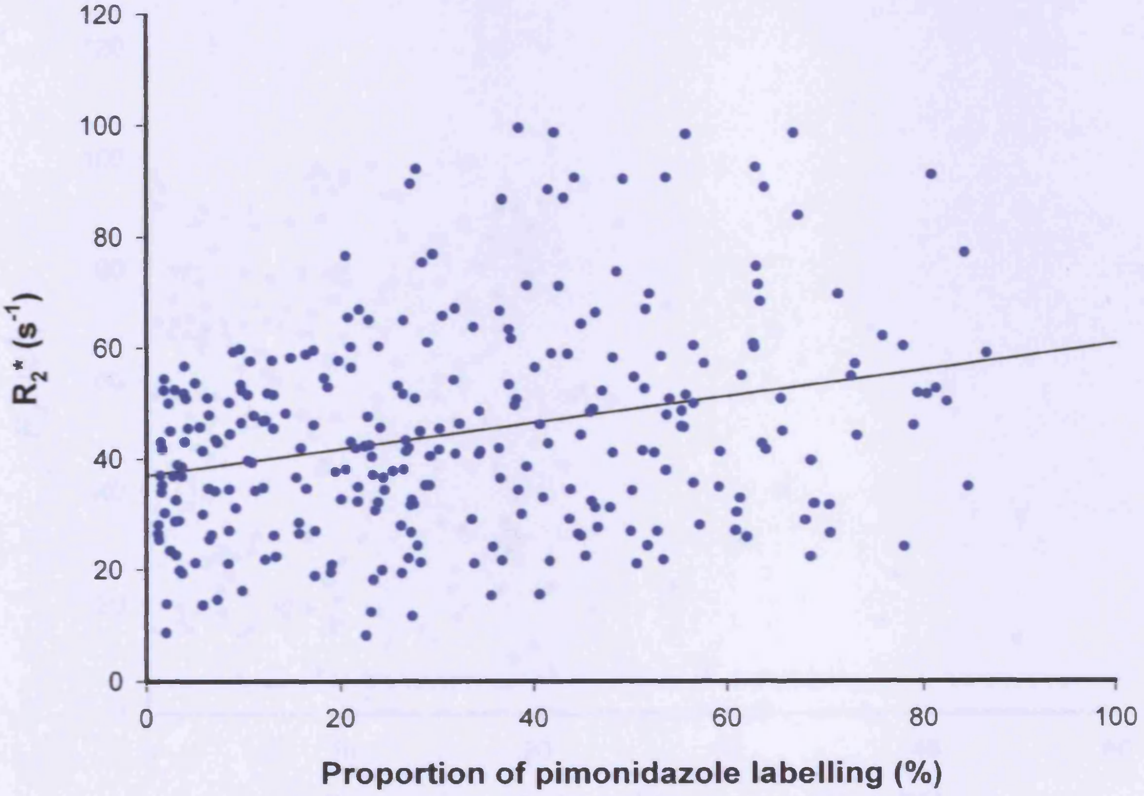

Figure 4.9

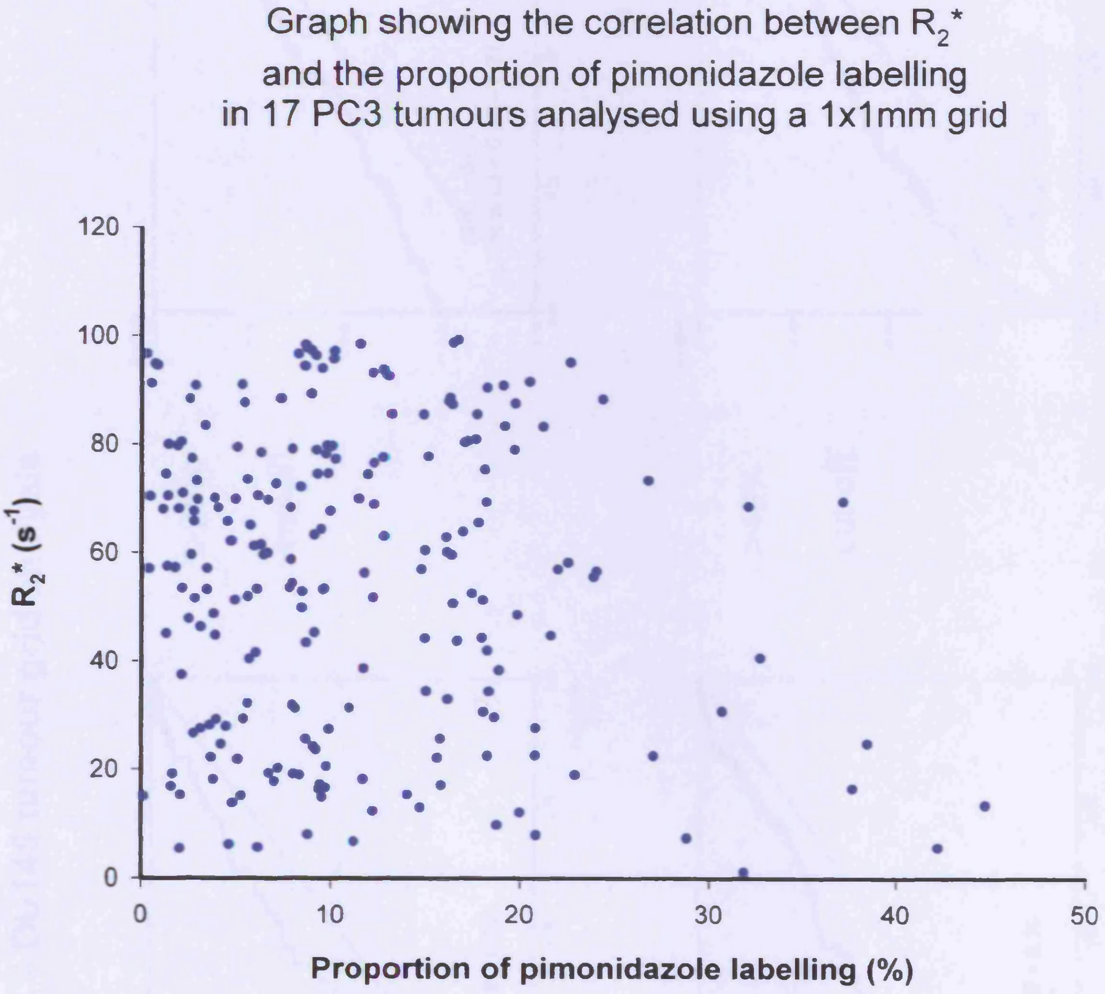
Graph showing the correlation between R_2*
and the proportion of pimonidazole labelling
in 17 PC3 tumours analysed using a 1x1mm grid
R_2* (s^{-1})
120
100
80
60
40
20
0
0
10
20
30
40
50
Proportion of pimonidazole labelling (%)

Figure 4.10 ROC analysis – DU145 tumour grid analysis

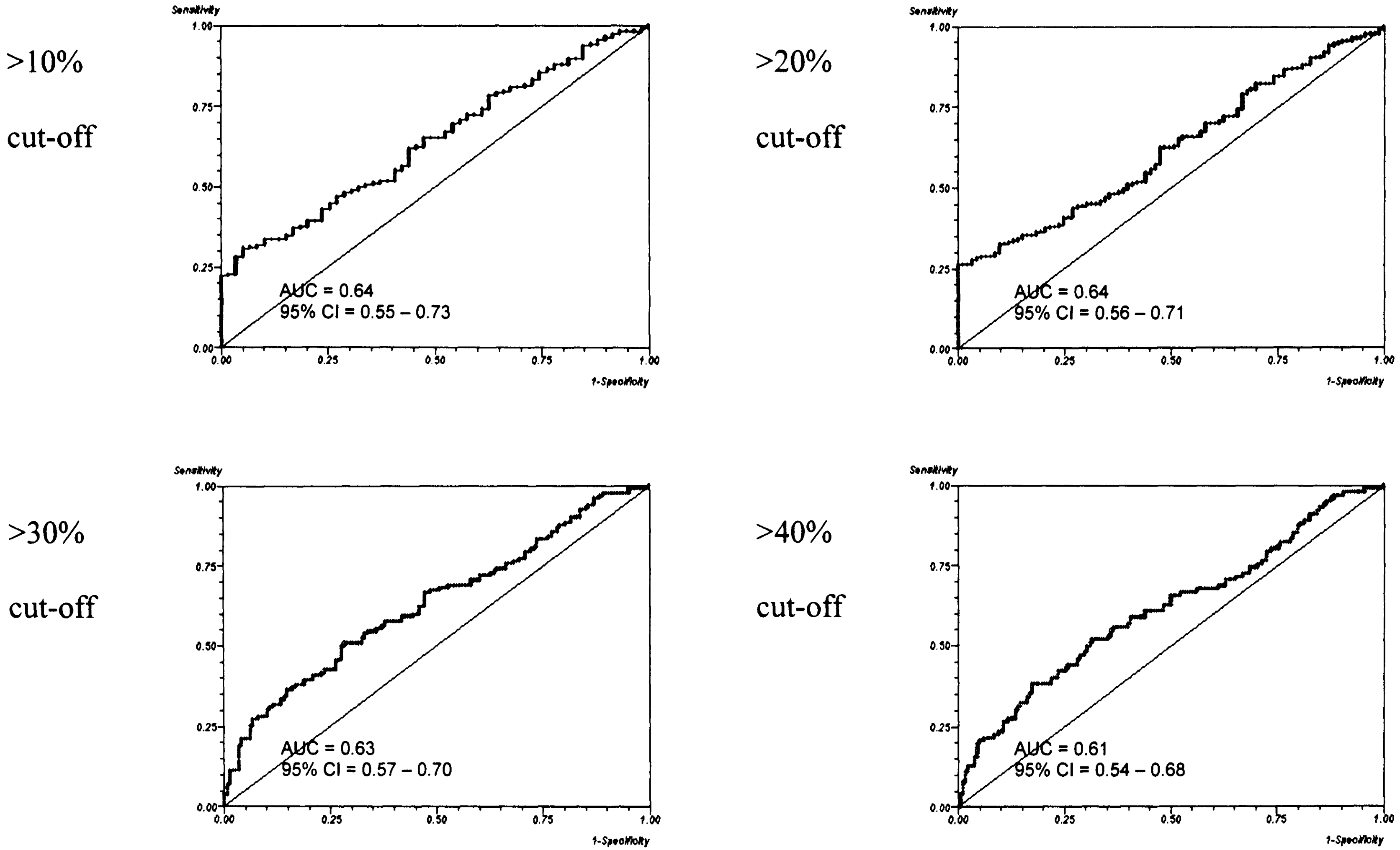

>10% cut-off

>20% cut-off

>30% cut-off

>40% cut-off

4.4.6 Carbogen Breathing

BOLD MRI measurements were made every minute during the carbogen experiment. The first four baseline R_2^* measurements, before the carbogen gas exposure was initiated, were averaged to give a single baseline value. The remaining R_2^* values (measurements 5 – 18) were subtracted from the baseline measurement to give a ΔR_2^* value, i.e. the change in R_2^* from baseline.

Analysis on an individual tumour by tumour basis for DU145 and PC3 tumours showed that four DU145 bearing mice and five PC3 bearing mice had a reduction in R_2^* during carbogen exposure that could be considered statistically significant and distinguishable from test variability at the 95% confidence level **(figure 4.11)**. Analysis of the two groups as a whole showed a mean reduction in R_2^* of $3.52s^{-1}$ ($p = 0.0032$) for the DU145 tumours and $6.01s^{-1}$ ($p = 0.092$) for the PC3 tumours, using the paired student's t-test.

The carbogen time series graphs demonstrate the temporal effect of carbogen breathing on the oxygenation of the prostate cancer xenografts **(figure 4.12)**. R_2^* values fall rapidly after the commencement of carbogen breathing as tumour oxygen levels increase. By the end of the experiment the R_2^* values have essentially returned to baseline. Interestingly, in both DU145 and PC3 tumours, R_2^* values seem to begin a return towards their baseline reading before the carbogen exposure has been terminated. For DU145 tumours this occurs after approximately nine minutes and with PC3 tumours the effect is seen earlier, at about four to five minutes. Also, in the DU145 experiments there is a suggestion of a 'rebound' phenomenon in which the final R_2^* values appear to be higher than they were to start with. This effect was not statistically significant and not seen in the PC3 xenografts.

Grid analysis for the carbogen experiments

1110 individual tumour grid elements were evaluated from the 23 DU145 tumours. 979 grids were evaluated from the 17 PC3 tumours. Grids exhibiting R_2^* values less than $5s^{-1}$ and greater than $100s^{-1}$ at baseline were excluded from the analysis because these values were likely to be artefactual. This left 882 DU145 and 796 PC3 grid elements for analysis. Because of the large volume of data, only five time points were used for the grid analysis; baseline (average of the first four pre-carbogen measurements), early carbogen (average of measurements 6 to 9), mid-carbogen (average of measurements 9 to 12), late carbogen (average of measurements 12 to 15) and post carbogen (average of measurements 15 to 18).

Figure 4.11

The effect of carbogen gas on individual DU145 tumours

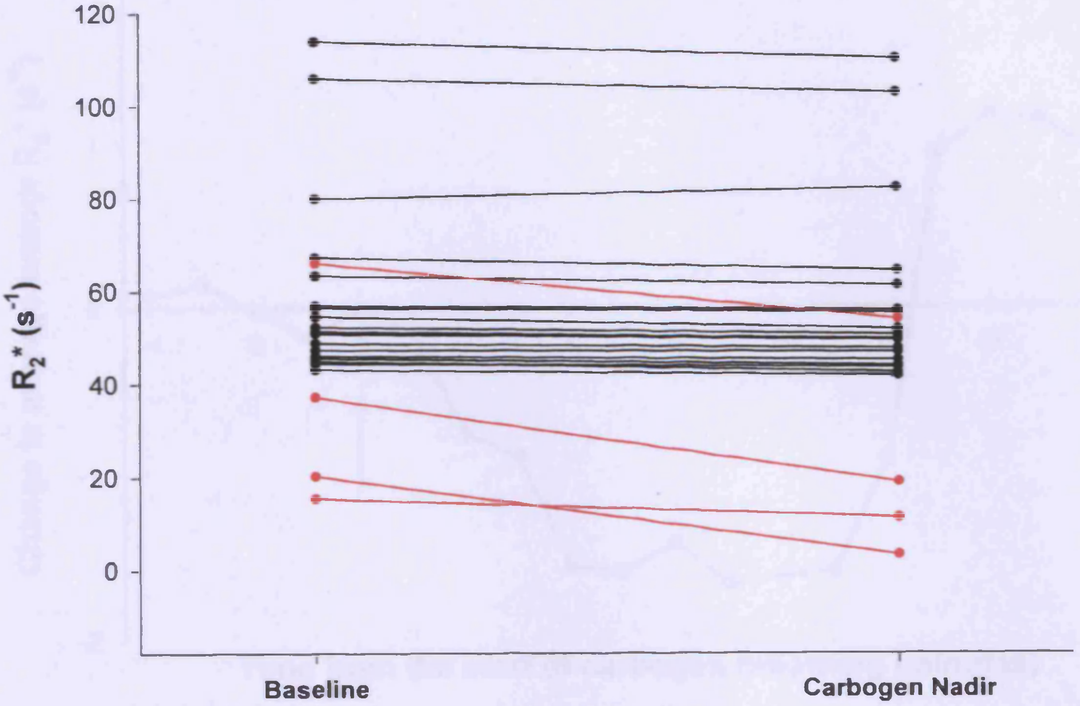

The effect of carbogen gas on individual PC3 tumours

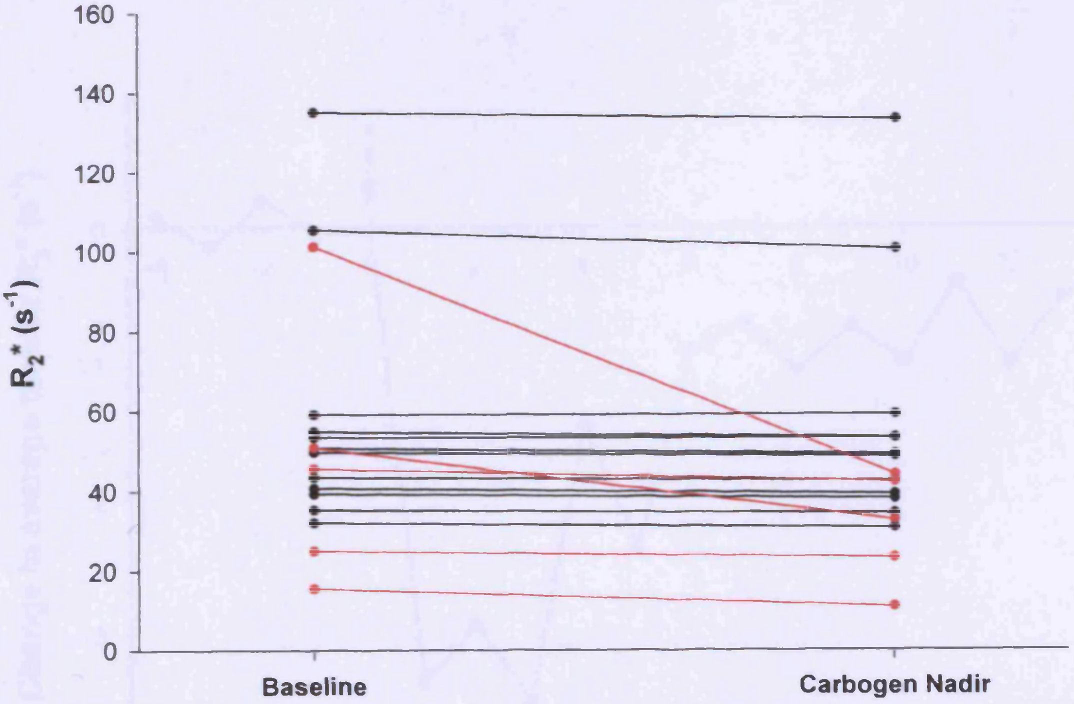

Individual tumours that demonstrated a statistically significant reduction in R_2^* are shown in red.

Figure 4.12

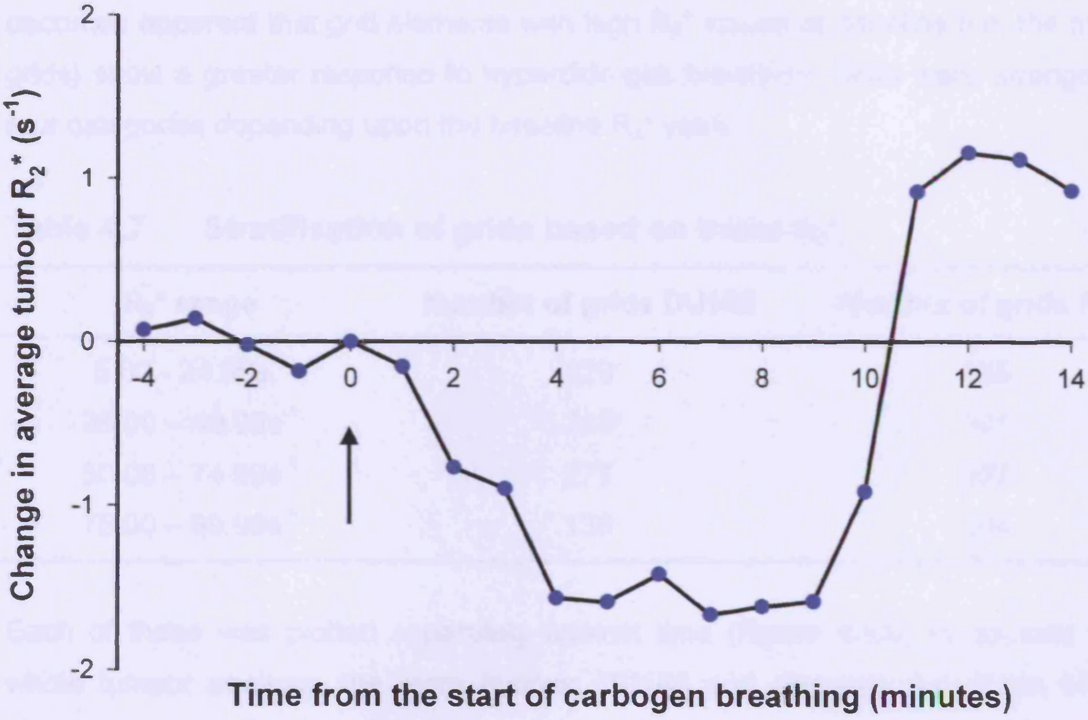

The effect of carbogen gas breathing over time - DU145 tumours

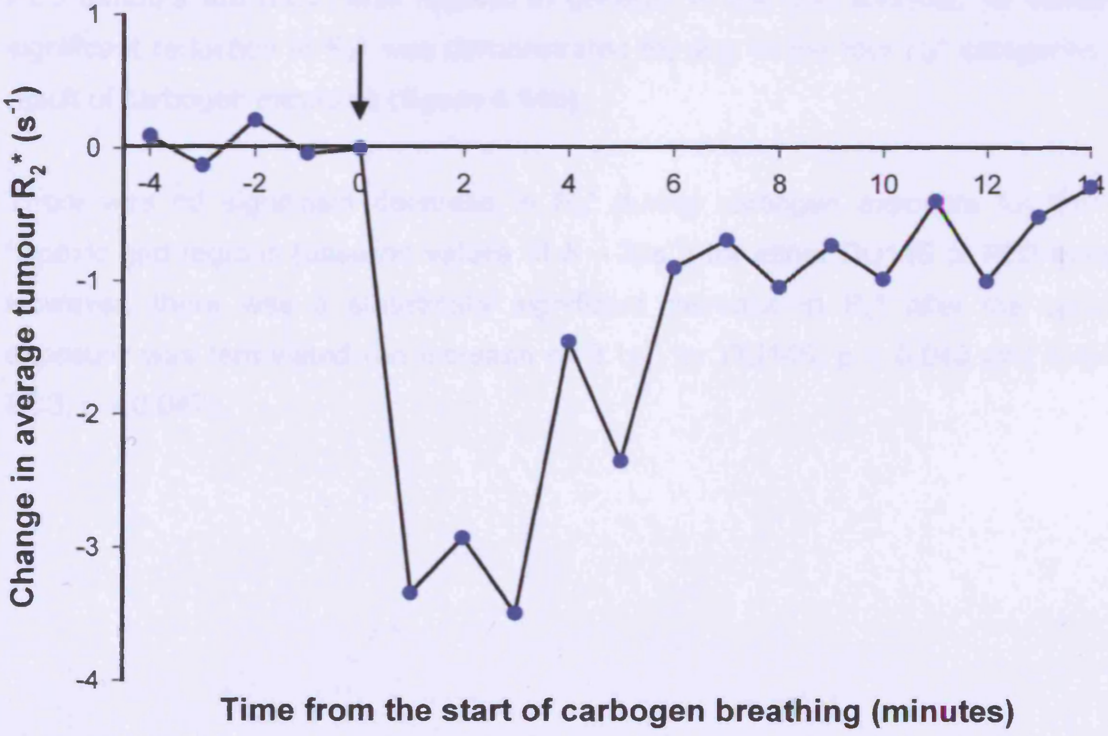

The effect of carbogen gas breathing over time - PC3 tumours

Figure 4.13 demonstrates that if all grid elements are averaged together, carbogen seems to have little effect on the R_2^* parameter value.

However, when the grids were stratified according to their baseline R_2^* value it becomes apparent that grid elements with high R_2^* values at baseline (i.e. the hypoxic grids) show a greater response to hyperoxic gas breathing. Grids were arranged into four categories depending upon the baseline R_2^* value:

Table 4.7 Stratification of grids based on initial R_2^*

R_2^* range	Number of grids DU145	Number of grids PC3
5.00 - 24.99s^{-1}	129	155
25.00 – 49.99s^{-1}	338	301
50.00 – 74.99s^{-1}	277	237
75.00 – 99.99s^{-1}	138	104

Each of these was plotted separately against time **(figure 4.14)**. In contrast to the whole tumour analysis, the more hypoxic DU145 grid elements (i.e. those with the highest baseline R_2^*) showed the greatest carbogen response **(figure 4.14a)**. In fact only grid elements with baseline R_2^* of between 75 and 100 s^{-1} show a statistically significant reduction in R_2^* in response to carbogen exposure (a difference between baseline and mid-carbogen exposure of 3.0s^{-1}, $p = 0.038$).

PC3 tumours are much less hypoxic in general. In the grid analysis, no statistically significant reduction in R_2^* was demonstrated for any of the four R_2^* categories as a result of carbogen exposure **(figure 4.14b)**.

There was no significant decrease in R_2^* during carbogen exposure for the least hypoxic grid regions (baseline values of 5 – 25s^{-1}) for either DU145 or PC3 tumours. However, there was a statistically significant *increase* in R_2^* after the carbogen exposure was terminated (an increase of 3.1s^{-1} for DU145, $p = 0.049$ and 3.4s^{-1} for PC3, $p = 0.047$).

Figure 4.13

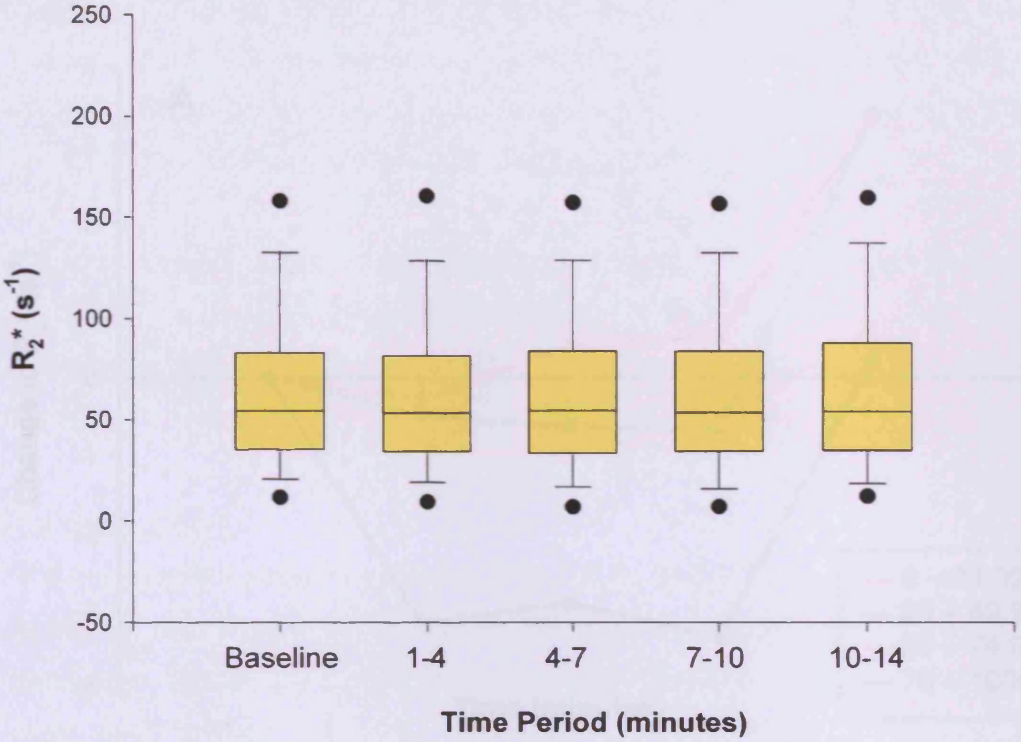
The effect of carbogen breathing.
Grid based analysis of DU145 tumours

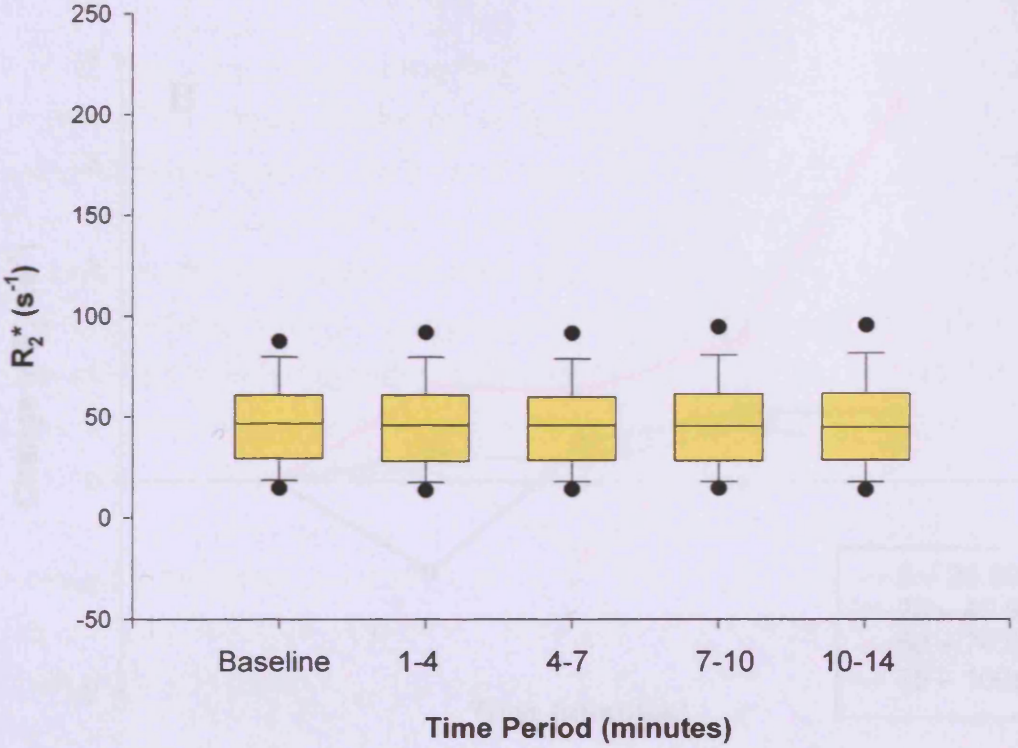
**The effect of carbogen breathing.
Grid based analysis of PC3 tumours**

Figure 4.14

The change in R_2^* with carbogen exposure stratified for baseline R_2^* DU145 tumours

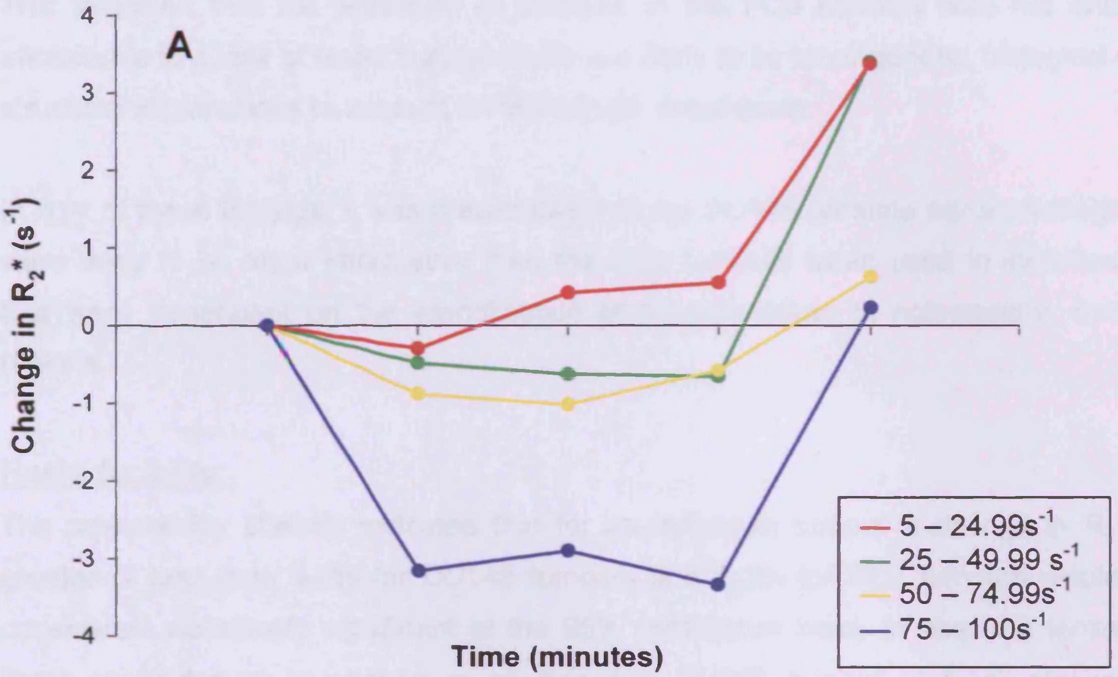

Change in R_2^* with carbogen exposure stratified for baseline R_2^* PC3 tumours

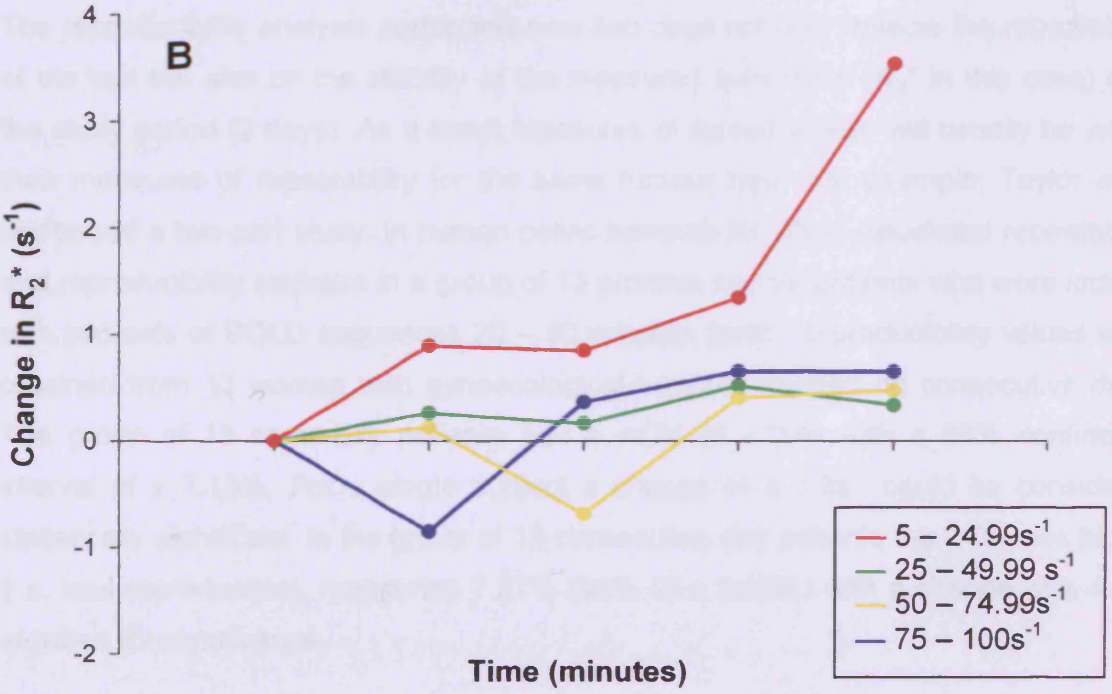

4.5 Discussion

Tumour Characteristics

DU145 tumours contained fewer blood vessels and were consequently more hypoxic than the PC3 xenografts. In contrast, the PC3 tumours were significantly more necrotic. This indicated that the presence of necrosis in the PC3 tumours was not entirely attributable to a lack of blood supply. There are likely to be other genetic, biological and structural explanations to account for the cellular breakdown.

In light of these findings, it was predictable that the DU145 prostate cancer xenografts were likely to be more informative than the PC3 tumours when used in experiments that were dependent on the identification of hypoxic areas in non-necrotic tumour regions.

Reproducibility:

The repeatability statistic indicates that for an individual tumour a change in R_2* of greater or less than 9.3% for DU145 tumours and 6.3% for PC3 tumours would be considered statistically significant at the 95% confidence level. In absolute terms, in these study groups, a change in an individual DU145 tumour of $5.1s^{-1}$ and in an individual PC3 tumour of $3.5s^{-1}$ in either direction can be considered real and not simply a result of test variability. The repeatability statistic informs on the test itself rather than reflecting biological parameters that may change over time. Therefore, these results suggest that BOLD MRI is a highly repeatable test in this experimental setting.

The reproducibility analysis performed over two days not only reflects the repeatability of the test but also on the stability of the measured parameter (R_2* in this case) over the study period (2 days). As a result measures of reproducibility will usually be worse than measures of repeatability for the same tumour type. For example, Taylor *et al.* performed a two-part study, in human pelvic tumours [4]. They calculated repeatability and reproducibility statistics in a group of 13 prostate cancer patients who were imaged with two sets of BOLD sequences 20 – 30 minutes apart. Reproducibility values were obtained from 13 women with gynaecological tumours imaged on consecutive days. The group of 13 same-day patients had a wCV of 2.78% with a 95% confidence interval of ± 2.13%. For a single subject a change of ± $1.8s^{-1}$ could be considered statistically significant. In the group of 13 consecutive day patients the wCV was higher (i.e. less reproducible), measuring 7.57% (95% CI ± 5.82%) with a change of ± $4.4s^{-1}$ required for significance.

The reproducibility of the R_2* parameter in DU145 xenografts appears to be extremely good. A wCV value of 5.2% and a variance ratio of 10.3 are comparable to the human data previously described and better than that reported by Lankester *et al.* (wCV of 17.5% in human pelvic tumours [5]). The PC3 tumours exhibited slightly less reproducibility in terms of wCV (9.1%). This may in part be due to the fact that there were fewer numbers (20 versus 23). The intra-class correlation coefficient demonstrated excellent reproducibility for both xenografts (0.81 and 0.91 for DU145 and PC3 respectively).

BOLD-MRI is a technique with sufficient reproducibility to be useful in the assessment of changes to the R_2* parameter in DU145 and PC3 prostrate cancer xenografts.

Histological Correlation

Studies that attempt to correlate histological sections with imaging slices will always be subject to inherent errors. To start with, the correlation can only ever be as good as the accuracy to which the excised tumour is cut. A slight discrepancy between the level or plane of the tumour section may result in a mismatch of part or all of the slice. In this study, a 4μm immunohistologial section has been compared to a 1000μm MRI slice, a 250-fold variation in thickness. There is no way to compensate for this disparity. Increasing tissue thickness would result in inadequate staining and poor cellular definition. Reducing MRI slice thickness is not possible within the current constraints of machine spatial resolution. Furthermore, the MRI scan evaluates the tumour in its intact living state whereas the histological specimen has been subject to excision, fixation and staining. As a result the final immunohistological section is contracted and distorted, bearing only a general resemblance to the shape of the original tumour. Despite the fact that the analysis process compensates for the two-dimensional change in shape with respect to the overall x and y diameter of the tumour, asymmetrical distortions can not be taken into account.

With these difficulties in mind, one can appreciate that even a perfect imaging test that measures exactly the same parameter as its histological correlate, will demonstrate imperfect correlation between to two modalities.

The correlation between R_2* and the proportion of pimonidazole staining has other limitations. Pimonidazole is a lipid soluble nitroimidazole with a high partition coefficient, which diffuses freely throughout the tissues. R_2* can only reflect on the oxygenation status of blood and on tissues adjacent to perfused vessels. The resolution of immunohistochemical analysis is at a cellular level of only a few micrometres, the MRI pixel dimension is approximately 175µm^2, thus pimonidazole immunostaining represents hypoxia with greater spatial resolution than the R2* image.

BOLD MRI captures its parametric map over a period of seconds whereas pimonidazole is distributed over the two-hour period between injection and euthanasia. As a result, the MR image represents a near-instantaneous snapshot of oxygenation at a given moment, while pimonidazole represents the overall level and distribution of oxygen over a much longer time frame. Given that acute vascular effects have been demonstrated over 20 minute periods [6], the relative contributions of acute and chronic hypoxia may be represented differently using the two modalities.

Despite the differences at a microscopic and cellular level, there is likely to be a large degree of overlap between the processes measured by BOLD MRI and pimonidazole labelling at a macroscopic level. When assessing an entire tumour, or a substantial region within it, the degree of pimonidazole staining, whether caused by acute or chronic hypoxia effects, is likely to reflect an 'average' tissue pO_2 level for that particular area at the time of the investigation. Similarly, given the association between tissue pO_2 and intravascular deoxyhaemoglobin saturation, R_2* is likely to reflect and average tissue pO_2 over the time period of the examination. Therefore, as long as the two examinations are carried out within a reasonable time of each other and acceptable anatomical correlation is achieved between the image slice and the histological section, reasonable correlation should be possible.

The results in this study confirm this. Whole tumour measurements exhibited reasonable correlation between pimonidazole labelling and R_2* ($r = 0.75$, $p < 0.0001$ and $r = 0.73$, $p = 0.0006$ for DU145 and PC3 respectively). The ROC analysis emphasises this point. If pimonidazole staining is considered the 'gold-standard', R_2* is able to detect hypoxia with an area under the ROC curve of between 0.86 and 0.93 depending on the pimonidazole threshold used. The sensitivity of the test ranged between 85 and 100% and specificity varied between 71 and 83%. This indicates that despite the differences in the physiological processes being measured by the two techniques, they give similar results at the macroscopic level.

It would appear that it makes no difference whether necrosis is included or excluded from the analysis **(figures 4.5 & 4.6)**. This finding is consistent with the original descriptions of pimonidazole immunohistochemistry [7]. Necrotic tissues do not take up pimonidazole, which involves an active process, and generate a low R_2* signal because of its dependency upon intact red blood cells. Therefore, there should be minimal discrepancy between evaluations made between the two modalities, in regard to necrosis. However, there is a degree of background brown staining within necrotic areas of sections stained for pimonidazole caused by secondary antibody effects. It is clear from the results that the automated thresholding capability of the analysis software effectively excludes the extracellular staining, thereby negating any artefact it may cause.

The whole tumour results indicate that R_2^* correlates with pimonidazole labelling between tumours. From the ROC analysis in these tumour types, an R_2^* value above about $50s^{-1}$ predicts for pimonidazole staining most accurately (with an area under the ROC curve of 0.86 – 0.93). Pimonidazole is known to stain cells in regions with a tissue pO_2 of less than 10mmHg [8, 9]. It can therefore be inferred that for the DU145 prostate cancer xenografts in a mouse model, an R_2^* value of $50s^{-1}$ or more is predictive of relevant tumour hypoxia.

The discrepancy between the whole tumour assessment and the grid-based analysis is difficult to explain in terms of biology. The whole tumour analysis assessed the correlation between pimonidazole staining and R_2^* *between* tumours, whereas the grid based analysis assessed the correlation between pimonidazole staining and R_2^* *within* tumours. Despite this difference, the analysis was performed on the same immunohistochemical sections and same MR images. It is fair to assume that because whole tumours that generally stain heavily with pimonidazole have high R_2^* values, it would follow that there would be a similar correlation for regions *within* the tumours. However the results for the grid-based analysis showed only a weak correlation for the DU145 tumours ($r = 0.28$, $p < 0.0001$) and no correlation at all for the PC3 xenografts.

One explanation lies with the analysis itself. Reducing the 'functional unit' of evaluation from a whole tumour region of interest down to a 1 x 1 mm square inevitably exacerbates all of the problems related to anatomical registration and distortion between the MR and histology slices. A small mismatch between the MRI and histology grids of only a fraction of a millimetre could result in grids from one region of the histology slice being compared to a different part of the tumour on the MR image. Furthermore, for the PC3 tumours there was a reduced number of grid squares suitable for analysis and a lower level of pimonidazole labelling.

This may be sufficient to explain the inconsistency in correlation as one moves from a whole tumour level down to a regional level. However, a biological explanation may lie with the fact that regional variations in blood volume become more apparent at this resolution. To explain this hypothesis one could imagine a hypothetical situation in which an MR scanner was available with a spatial resolution of only a few micrometres and perfect anatomical registration with an immunohistochemical image was possible. In this situation, if one were to image a tumour voxel that contained red blood cells, such as in or around a blood vessel, then a meaningful BOLD signal would be produced and correlation with immunohistochemistry would be feasible. However, if one were to image an adjacent voxel without red blood cells, minimal BOLD signal would be produced and R_2* would not correlate with any immunohistochemical measure of oxygenation. At a macroscopic level, the blood volume component is averaged out across all voxels in the section. As voxel size decreases, the analysis becomes more dependent upon blood volume. In this experiment the voxel diameter of 175µm is of similar order to the oxygen diffusion distance in tumours of approximately 100µm, with necrosis appearing at a distance of 160 - 180µm from the nearest vessel. It is therefore possible that micro-regional variations in blood volume are influencing the correlation seen.

Carbogen

Carbogen has been demonstrated to improve the oxygenation of both experimental and human tumours (see introduction, page 41). In human prostate cancer, BOLD-MRI during carbogen gas breathing has been used to improve diagnostic localisation of tumour within the heterogeneously enhancing malignant gland [10]. A significant signal intensity increase was found in normal central gland and peripheral zone ($p = 0.004$). Signal enhancement was significantly lower in carcinoma when compared to the contralateral normal side ($p = 0.004$). A series of experiments using the Dunning prostate R3327 rat tumour model has investigated this effect using needle electrode measurements and 19F NMR echo planar imaging after direct intratumoural injection of hexafluorobenzene [11-13]. Administration of carbogen gas reduced the hypoxic fraction (defined as measurements <10mmHg) from 59% to 22% ($p < 0.0001$). A further study using an anaplastic variant of the Dunning R3327 model attempted to determine whether microelectrode measurements predicted the avidity of two hypoxic markers in prostate tumour tissue [14]. In the course of the experiments carbogen gas was used. Median pO_2 values were found to increase significantly in response to carbogen breathing ($p = 0.001$). A study using the Eppendorf pO_2 histograph has specifically investigated the effects of carbogen breathing on DU145 and PC3 xenografts [15]. An average increase of 8.3 mmHg was seen in the DU145 tumours and of 9.8 mmHg was seen in the PC3 tumours.

Prostate cancers exhibit regions of clinically relevant hypoxia [16, 17]. These reports suggest that the oxygenation of prostate tumours can be affected by carbogen breathing. However, no previous study has specifically examined the use of BOLD-MRI to quantify the changes induced by carbogen breathing in a prostate cancer model.

Only the DU145 tumours showed a statistically significant change from baseline following carbogen exposure, with a mean reduction in R_2^* of $3.52s^{-1}$ ($p = 0.0032$). The PC3 tumours exhibited a greater mean reduction of $6.01s^{-1}$ but this was not significant, possibly due to the fewer numbers (17 versus 23). The ΔR_2^* versus time plots **(figure 4.12)** suggest a trend of decreasing R_2^* as a result of carbogen breathing followed by a return to baseline following the resumption of air breathing. The pimonidazole staining demonstrated that the average proportion of each tumour that was considered to be hypoxic was only 22.5% for DU145 tumours and 12.5% for PC3 tumours. As a result, the whole tumour R_2^* measurements included all of the well-oxygenated tumour regions that were unlikely to respond to carbogen exposure. This may, at least in part, explain why the PC3 tumours did not exhibit a change that was statistically significant.

The grid analysis compensated for this effect by stratifying for baseline R2*. Using this method the most hypoxic regions of the tumour could be examined separately. For the DU145 tumours a statistically significant reduction was then seen for tumour areas that started with a baseline R_2^* of above $75s^{-1}$ ($p = 0.038$), **figure 4.14**.

In both tumour types there is a suggestion that R_2^* begins to return to its baseline value before the cessation of carbogen breathing **(figure 4.12)**. This phenomenon has been previously described. The early studies that investigated the use of carbogen gas as a radiosensitising agent identified optimum pre-irradiation breathing times. Chaplin reported that in KHT murine sarcomas, the minimum survival level for tumour cells was reached after approximately ten minutes of carbogen gas inspiration [18]. Longer breathing times gave a considerable range of surviving fraction values which suggested a slow reduction in tumour sensitisation relative to air. Further work from the same group confirmed these results in murine SCCVII tumours [19]. In this tumour the optimum breathing time appeared to be between 10 and 30 minutes with no sensitising effect observed after 90 minutes. The addition of nicotinamide reversed the time related reduction in radiosensitisation, resulting in the observation of a fully aerobic radiation response during 90 minutes of carbogen exposure.

It is possible that the physiological explanation lies in the development of perfusion-limited hypoxia as a result of tumour blood flow variations induced by prolonged carbogen exposure. These effects may, in turn, account for the apparent overshoot in R_2* seen in the whole DU145 tumour measurements and the rise in R_2* measured in the non-hypoxic grids (baseline R_2* of 5 - $25s^{-1}$) in both xenografts following the cessation of carbogen breathing. Nicotinamide is thought to act by reducing microregional alterations in tumour perfusion, thereby reducing this effect. It may therefore play a role in future studies that attempt to use carbogen gas to increase oxygenation in prostate tumours.

The carbogen experiments demonstrated a difference between DU145 and PC3 tumours. Only the DU145 tumours exhibited a significant R_2* reduction in response to carbogen. The PC3 tumours showed a more rapid return to baseline R2* levels during carbogen breathing and only the DU145 tumours displayed a ‘rebound’ phenomenon (although this was not statistically significant). This cannot simply be a result of differences in vascular density because the CD31 staining has shown that the poorly responding PC3 tumours contained many more blood vessels **(figure 4.3)** and would therefore be assumed to have received greater oxygen delivery. Part of the altered carbogen response may be attributable to differences within the blood vessels, such as the proportion of mature and immature vessels (which affects their CO_2 reactivity) and whether those vessels present may not be perfused. It would be interesting to test whether the incorporation of blood volume information would predict for response to carbogen gas breathing.

4.6 Conclusion

BOLD MRI is a repeatable and reproducible biological imaging technique. The above experiment has confirmed that R_2* can predict for pimonidazole staining in DU145 and PC3 prostate cancer xenografts with moderate accuracy, although it is arguable whether the R_2* parameter alone would provide sufficient precision in mapping tumour hypoxia for specific targeting, as would be required for radiotherapy dose-painting. Despite this, there is sufficient credibility in these data to support the hypothesis that BOLD MRI is a valid non-invasive hypoxia imaging modality in prostate cancer, accordingly, human testing is justifiable and warranted.

This experiment has made no attempt to include blood volume or blood flow information. As described in chapter 2, these physiological parameters are important in the interpretation of the BOLD image. Further testing of the BOLD-MRI technique for the assessment of tumour hypoxia in human prostate cancer requires concomitant acquisition of R_2* and quantitative blood flow data in order to assess whether this improves the diagnostic accuracy for hypoxia detection **(see chapter 5)**.

Furthermore, the experiment has confirmed that prostate cancer xenografts respond to carbogen exposure. As hypoxia is a firmly established cause of radioresistance, demonstration of this effect in human prostate cancer may provide a strategy to address this hurdle in the clinical setting.

References

1 Mickey DD, Stone KR, Wunderli H, *et al.* Heterotransplantation of a human prostatic adenocarcinoma cell line in nude mice. *Cancer Res* 1977;37:4049-4058.
2 Stone KR, Mickey DD, Wunderli H, *et al.* Isolation of a human prostate carcinoma cell line (DU 145). *Int J Cancer* 1978;21:274-281.
3 Kaighn ME, Narayan KS, Ohnuki Y, *et al.* Establishment and characterization of a human prostatic carcinoma cell line (PC-3). *Invest Urol* 1979;17:16-23.
4 Taylor N, Lankester K, Stirling J, *et al.* Reproducibility of human tumour R2* maps obtained from BOLD images. *Proc I. S. M. R. M 10th Annual Meeting* 2002:p 2065 abstract no. 2065.
5 Lankester K, Taylor N, Stirling J, *et al.* Dynamic MRI for Imaging Tumour Microvasculature: Comparison of Susceptibility and Relaxivity Techniques in Pelvic Tumours. *J Magn Reson Imaging* 2007;25:In press.
6 Chaplin D, Durand R, Olive P. Acute hypoxia in tumours: implications for modifiers of radiation effects. *Int J Radiat Biol Phys* 1986;12:1279-1282.
7 Raleigh JA, Chou SC, Bono EL, *et al.* Semiquantitative immunohistochemical analysis for hypoxia in human tumors. *Int J Radiat Oncol Biol Phys* 2001;49:569-574.
8 Arteel GE, Thurman RG, Raleigh JA. Reductive metabolism of the hypoxia marker pimonidazole is regulated by oxygen tension independent of the pyridine nucleotide redox state. *Eur J Biochem* 1998;253:743-750.
9 Arteel GE, Thurman RG, Yates JM, *et al.* Evidence that hypoxia markers detect oxygen gradients in liver: pimonidazole and retrograde perfusion of rat liver. *Br J Cancer* 1995;72:889-895.
10 Diergarten T, Martirosian P, Kottke R, *et al.* Functional characterization of prostate cancer by integrated magnetic resonance imaging and oxygenation changes during carbogen breathing. *Invest Radiol* 2005;40:102-109.
11 Hunjan S, Zhao D, Constantinescu A, *et al.* Tumor oximetry: demonstration of an enhanced dynamic mapping procedure using fluorine-19 echo planar magnetic resonance imaging in the Dunning prostate R3327-AT1 rat tumor. *Int J Radiat Oncol Biol Phys* 2001;49:1097-1108.
12 Zhao D, Constantinescu A, Hahn EW, *et al.* Tumor oxygen dynamics with respect to growth and respiratory challenge: investigation of the Dunning prostate R3327-HI tumor. *Radiat Res* 2001;156:510-520.
13 Zhao D, Constantinescu A, Hahn EW, *et al.* Differential oxygen dynamics in two diverse Dunning prostate R3327 rat tumor sublines (MAT-Lu and HI) with respect to growth and respiratory challenge. *Int J Radiat Oncol Biol Phys* 2002;53:744-756.
14 Iyer RV, Haynes PT, Schneider RF, *et al.* Marking hypoxia in rat prostate carcinomas with beta-D-[125I]azomycin galactopyranoside and. *J Nucl Med* 2001;42:337-344.
15 Teicher BA, Schwartz GN, Dupuis NP, *et al.* Oxygenation of human tumor xenografts in nude mice by a perfluorochemical emulsion and carbogen breathing. *Artif Cells Blood Substit Immobil Biotechnol* 1994;22:1369-1375.
16 Movsas B, Chapman JD, Horwitz EM, *et al.* Hypoxic regions exist in human prostate carcinoma. *Urology* 1999;53:11-18.
17 Parker C, Milosevic M, Toi A, *et al.* Polarographic electrode study of tumor oxygenation in clinically localized prostate cancer. *Int J Radiat Oncol Biol Phys* 2004;58:750-757.
18 Siemann DW, Hill RP, Bush RS. The importance of the pre-irradiation breathing times of oxygen and carbogen (5% CO2: 95% O2) on the in vivo radiation response of a murine sarcoma. *Int J Radiat Oncol Biol Phys* 1977;2:903-911.
19 Chaplin DJ, Horsman MR, Siemann DW. Further evaluation of nicotinamide and carbogen as a strategy to reoxygenate hypoxic cells in vivo: importance of nicotinamide dose and pre-irradiation breathing time. *Br J Cancer* 1993;68:269-273.

Chapter 5.

Intrinsic susceptibility weighted MRI as a method for quantifying and mapping hypoxia in human prostate cancer

5.1 Aims

1) To determine whether the numerical value and distribution of the MRI derived R_2^* parameter correlates with the degree of pimonidazole labelling in the human prostate.

2) To assess whether the inclusion of blood volume information from dynamic susceptibility contrast MRI improves the sensitivity and specificity for hypoxia detection.

3) To determine whether carbogen breathing influences the ability to detect hypoxia in the human prostate and the extent to which it alters the oxygenation of prostate cancer.

4) To evaluate the repeatability of BOLD-MRI in the human prostate.

5.2 Introduction

This chapter contains details of experiments performed to determine whether BOLD and DSC-MRI are useful and valid techniques to evaluate the oxygen status of prostate carcinoma in patients about to undergo radical prostatectomy surgery. Information regarding the effect of carbogen breathing gas on prostate carcinoma was also obtained, which may have relevance in terms of radiosensitisation.

5.3 Patients and Methods

5.3.1 Patients, Treatment and Examination Schedule

Between November 2003 and July 2007, 17 patients with prostate cancer (age 56-76 years, Gleason grade 6-8, PSA 1.9-32.0 ng/ml) that were due to be treated with a radical prostatectomy procedure were recruited. The histological diagnosis of prostate cancer was made by core biopsy in all patients. Details of tumour pathology, staging

Table 5.1 MRI Study population

Patient Number	Age (years)	PSA (ng/ml)	Clinical 'T' Stage	Pathological 'T' Stage	Gleason Grade (Biopsy)	Gleason Grade (Prostatectomy)	Resection Margins
1	62	9.0	2c	2c	3+3=6	3+3=6	Negative
2	66	17.3	2c	3a	4+3=7	3+4=7	Positive
3	71	11.0	1c	2b	3+3=6	3+3=6	Negative
4	76	6.7	1b	2c	3+3=6	3+3=7	Negative
5	64	23.4	2a	2b	4+3=7	4+3=7	Negative
6	61	12.7	1c	3a	3+4=7	3+4=7	Positive
7	63	6.8	1c	2c	4+3=7	4+3=7	Negative
8	75	7.65	2a	2c	4+4=8	4+3=7	Negative
9	62	17.98	1c	3b	3+3=6	3+4=7	Positive
10	61	9.8	2a	2b	3+4=7	3+4=7	Negative
11	67	32	2c	3a	3+4=7	4+3=7	Positive
12	56	4.0	2c	3a	3+3=6	3+4=7	Positive
13	63	11.7	1c	3a	3+4=7	4+3=7	Positive
14	56	4.2	1c	3a	3+4=7	3+3=6	Positive
15	67	1.9	2c	2c	3+3=6	3+3=6	Positive
16	63	4.8	1c	3a	3+3=6	3+4=7	Positive
17	69	8.3	2c	3a	3+4=7	3+4=7	Positive

and treatment are shown in **table 5.1**. Inclusion criteria were: (1) Histologically-proven primary prostate carcinoma, (2) Intention to have the whole prostate gland removed surgically (3) Ability to give written informed consent and (4) Age over 18 years. Exclusion criteria were: (1) Contra-indication to MRI, (2) Known allergy to gadopentetate dimeglumine (Gd-DTPA) and (3) Known allergy to pimonidazole hydrochloride.

Each patient was examined with a multi-parameter MRI scan before surgery. The intention was to scan the patient on the day before surgery in order to minimise the time interval between the two measurements of oxygenation (namely the BOLD MRI and the pimonidazole immunohistochemistry). An intravenous pimonidazole infusion was administered 16 – 24 hours before surgery.

5.3.2 Imaging

All MRI investigations were performed at the Paul Strickland Scanner Centre at Mount Vernon Hospital, Northwood, UK. Patients were imaged in a Symphony 1.5T MRI scanner (Siemens Medical Systems, Erlangen, Germany) using a phased array pelvic coil. The MRI protocols are detailed in **appendix B**. Patients were imaged using the following schedule:

1. Small field-of-view T_1 and T_2-weighted anatomical scans perpendicular to the urethra were used to stage tumours and to identify tumour slice locations. Images were inspected for the presence of a peripheral zone abnormality consistent with cancer. The central slice for functional imaging was chosen to contain a satisfactory tumour region for data analysis.
2. Initial BOLD MRI (breathing room air): To determine baseline R_2* values for comparison with immunohistochemistry.
3. Second BOLD MRI (breathing room air): Performed immediately after the first BOLD scan to establish the repeatability of the BOLD technique.
4. Carbogen breathing commences.
5. Third BOLD scan initiated after 10 minutes of carbogen breathing. Carbogen is continued for the duration of the BOLD acquisition.
6. A ten minute period of breathing room air.
7. T_1-weighted Dynamic Contrast Enhanced MRI (DCE-MRI).
8. T_2*-weighted Dynamic Susceptibility Contrast MRI (DSC-MRI).

5.3.3 Carbogen Breathing:

A 98% O_2 and 2% CO_2 mixture was used. A previous study has shown equivalent efficacy and increased tolerability with 2% CO_2 over 5% CO_2 [1]. Before entering the MRI scanner, each patient was allowed to breathe carbogen for several minutes to experience and adjust to the altered sensations that are caused by breathing the hypercapnic gas mixture **(figure 5.1a)**. The patients were then asked to lie in the scanner and the equipment was positioned **(figure 5.1b)**. The mask was positioned over the patient's face. The initial air breathing period was performed with the mask in place but without the carbogen tubing connected. This was to reduce patient movement during the scan at the point when the carbogen gas was connected. A pulse oximeter recorded the subject's heart rate and peripheral blood oxygen saturation. The tubing was disconnected as soon as the third BOLD scan was complete. The remaining imaging protocol was performed breathing room air without a mask.

Figure 5.1 Carbogen gas breathing during MR imaging

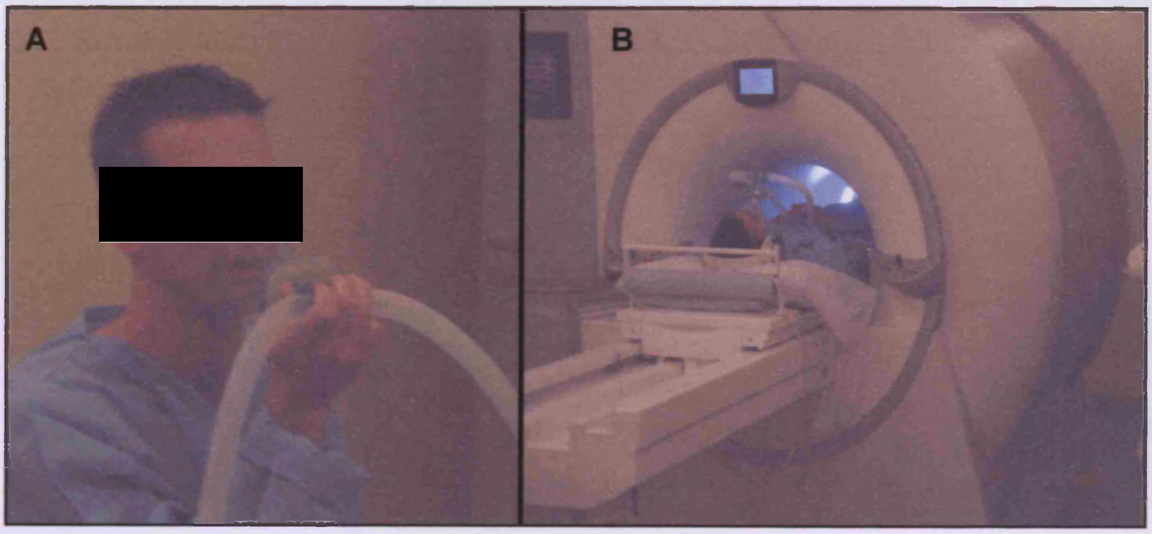
[redacted]

5.3.4 Pimonidazole Infusion

Pimonidazole infusion occurred between 16 and 24 hours before surgery. Patients were weighed and their height was measured. Body surface area (BSA) was calculated using the DuBois method (BSA = ($Weight^{0.425}$ x $Height^{0.725}$) x 0.007184). The dose of Pimonidazole was $0.5g/m^2$ with a maximum dose of 1g. This was administered in 100mls of normal saline over 20 minutes via a 20 gauge venous cannula using a screened photosensitive drug giving set.

5.3.5 Histology and Immunohistochemical Analysis

Prostate gland removal, sectioning, slide preparation, staining and immunohistochemical analysis methods are detailed in **appendix A**

5.3.6 Human MR Image Analysis

The procedures for the generation of functional parametric data are detailed in **appendix B** and **Chapter 2**.

5.4 Experimental Design and Statistical Methods

MRI characteristics

Differences between each prostate region for each of the parametric MRI values was assessed using the Kruskal-Wallis test

Tumour Localisation

Using the grid based analysis system described in **appendix B**, it was possible to determine how good each MRI parameter was at discriminating between benign prostate tissue and tumour. For each of the 17 patients a 5x5mm grid was superimposed on the anatomical T_2 image. The same grid could then be used to derive functional parametric data for each grid element using BOLD, DCE and DSC MRI. Only grid elements that were fully occupied by prostate tissue were included:

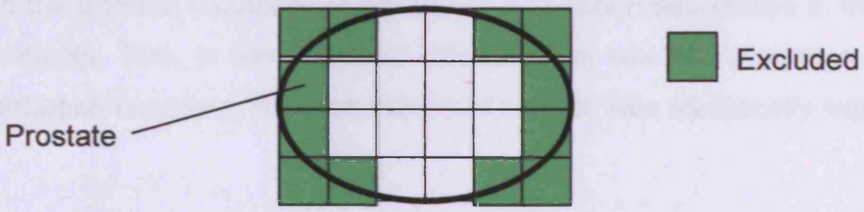

ROC analysis was then used to determine the sensitivity, specificity and overall accuracy of each MRI parameter for tumour detection.

Validation

The validation experiment compared the numerical value and distribution of R_2* with the distribution of pimonidazole staining in the corresponding whole-mount histological section. The mean of the two baseline (air breathing) median R_2* values for the whole prostate, tumour, benign prostate peripheral zone and benign prostate central zone ROIs was compared with the pimonidazole staining percentage from the corresponding immunohistochemical sections (calculated as described in **appendix A**). R_2* from each grid element was also compared with the pimonidazole staining percentage from the corresponding grid element in the matching histological section.

The distribution of each set of results was tested for normality using the Shapiro-Wilk test. For normally distributed data, correlations were assessed using the Pearson correlation coefficient (r).

Receiver operating characteristic (ROC) curves were plotted for the grid-based data. These calculations provided an estimation of the sensitivity and specificity of BOLD MR and T_2*-weighted DSC-MRI data when used to depict tumour hypoxia. They also established the R_2* and rBV values with the optimum power to predict hypoxia within a grid element.

Repeatability

The repeatability experiment for the BOLD sequences compared the R_2* values between air breathing scans 1 and 2 for each patient. The analysis was performed for whole prostate, tumour, benign prostate peripheral zone and benign prostate central zone ROIs separately. The standard consensus approach to assessing reproducibility was used **(see Chapter 3, page 89).** The procedure was repeated using each individual grid element from the grid-based analysis. The results of these experiments determined the intrinsic variability of the BOLD acquisition sequences in this particular group of patients. This, in turn, allowed calculation of whether a change in R_2* as a result of carbogen exposure, for each individual patient, was statistically significant.

Carbogen breathing

The effect of increased inspired oxygen concentration on the BOLD image was evaluated by comparing the baseline R_2* measurements (an average of the first two air-breathing BOLD sequences) and R_2* measurements made after 10 minutes of carbogen breathing. Changes in R_2* for the whole prostate, tumour, benign prostate peripheral zone and benign prostate central zone were calculated separately. A 5x5mm grid-based analysis was performed to determine the changes within each region of interest **(appendix B)**.

5.5 Results

5.5.1 General (table 5.2)

All 17 patients completed two baseline BOLD scans. One patient was unable to tolerate carbogen breathing, due to a feeling of claustrophobia whilst in the MRI scanner wearing a facemask, although he was able to complete the remainder of the imaging protocol without the mask. All 17 patients were imaged using both T_1 and T_2* weighted dynamic sequences. In one patient, rectal filling between the first and second BOLD scan caused such severe prostate movement that repeatability analysis was impossible. In another patient, transient gas filling caused a susceptibility artefact obscuring the tumour ROI. Every patient then went on to receive a pimonidazole infusion (without complication) and subsequent prostatectomy. Pathological staging details are given in **table 5.1**. In two cases, the 5mm histological section corresponding to the imaging slice did not contain any tumour, although tumour was found elsewhere in the prostatectomy specimen. As a result these patients were analysed in terms of whole prostate, benign peripheral zone and benign central zone only. Analysis of the correlation between tumour R_2* and pimonidazole staining therefore only includes 15 patients. The following numbers of patients were used for each analysis:

Table 5.2 The numbers of patients used for analysis

	Pathological Correlation		Repeatability		Carbogen		Dynamic Analysis	
	Benign	Tumour	Benign	Tumour	Benign	Tumour	Benign	Tumour
Patient numbers	17	15	16	13	16	14	17	15

5.5.2 Overall Characteristics

On average there were 2.25 tumour foci in the imaging slice (range 0 – 11). The mean proportion by surface area of the prostate that was malignant was 8.2% (range 0.2-29.1%) **(Figure 5.2)**. The proportion of each prostate region that stained for pimonidazole is given in **table 5.3** and shown graphically in **figure 5.3.**

Table 5.3 Pimonidazole Staining Proportion

Tumour	40.6% (range 0.6 – 90.0%)
Peripheral Zone	34.6% (range 0.2 – 71.4%)
Central Zone	38.5% (range 0.7 – 91.0%)
Whole Prostate	36.7% (range 0.6 – 76.9%)

Figure 5.2 H&E stained whole-mounts (tumour outlined in black)

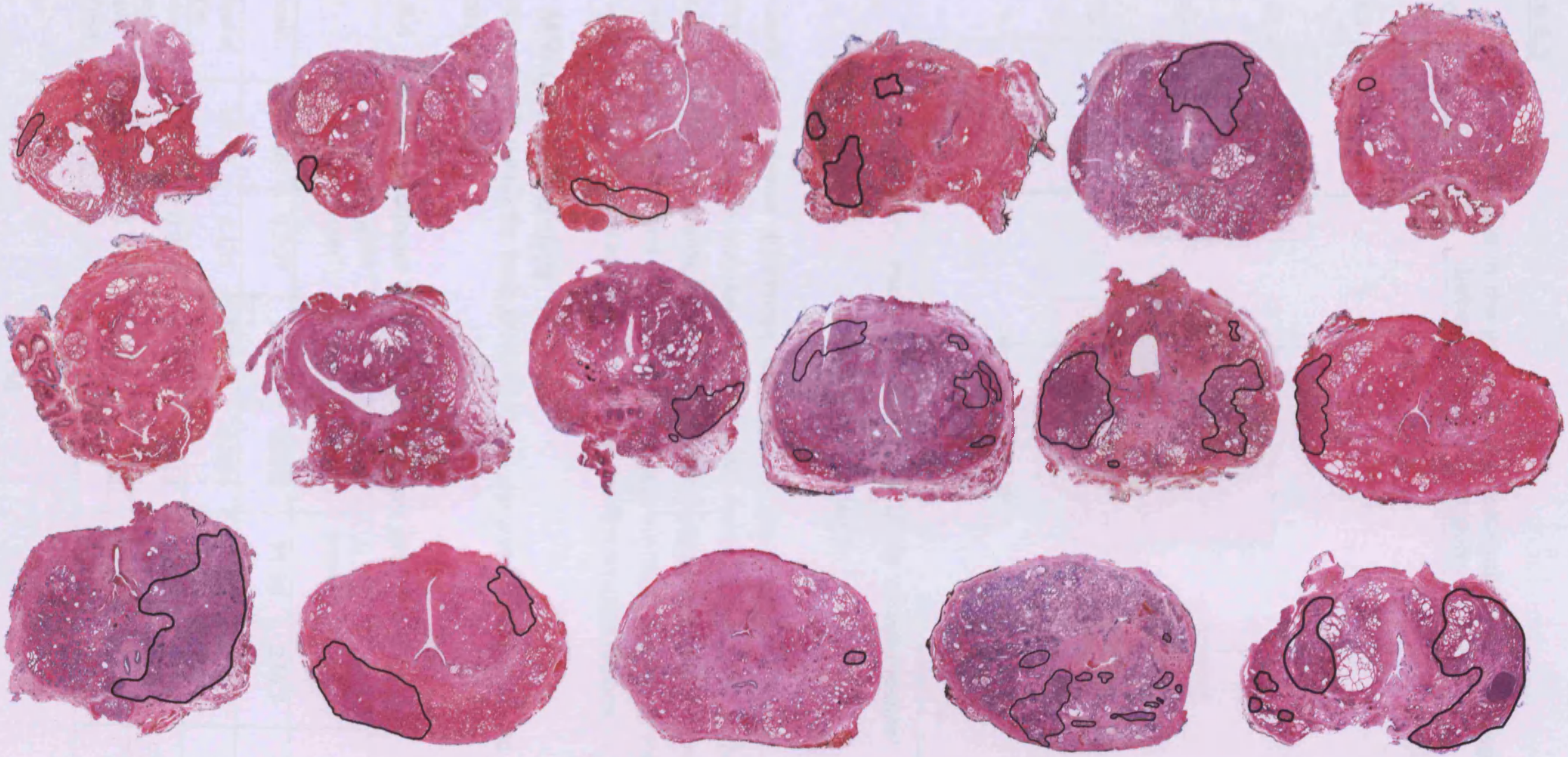

Figure 5.3

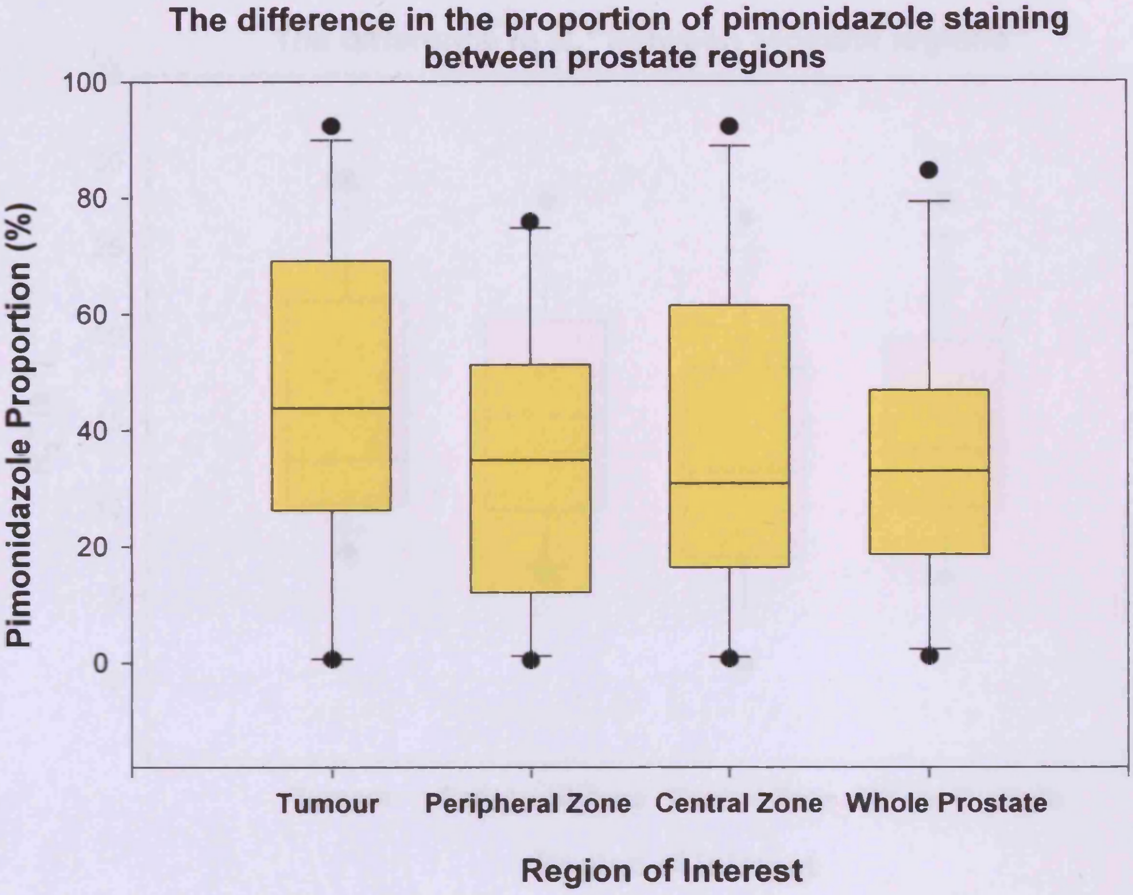

There were no statistical differences between the four regions in terms of the proportion of pimonidazole staining (Kruskal-Wallis test). As described in previous reports [2, 3], there was a wide variation in hypoxia between patients. Pimonidazole scores varied between 0.2 and 91%, mirroring the pO_2 readings reported by Parker *et al.* of 0.2 to 57.3 mm Hg. This seems to be true for all of the prostate regions.

5.5.3 MRI Characteristics

The functional MRI values for each prostate region are given in **table 5.4** and shown graphically in **figure 5.4**.

Table 5.4 Mean functional MRI values for each prostate region

	R_2^* (s^{-1})	K^{trans} (min^{-1})	v_e (x100%)	k_{ep} (min^{-1})	AUC_{60} ($mmol.s^{-1}$)	rBV (au)	rBF (au)
Tumour	16.55	0.207	0.367	0.602	11.98	219.7	4.16
Peripheral Zone	15.79	0.125	0.320	0.391	7.87	108.3	2.08
Central Zone	13.20	0.277	0.401	0.713	15.47	131.8	2.61
Whole Prostate	15.13	0.183	0.374	0.492	11.37	110.7	2.22

Figure 5.4 The difference in MR parameters between prostate regions

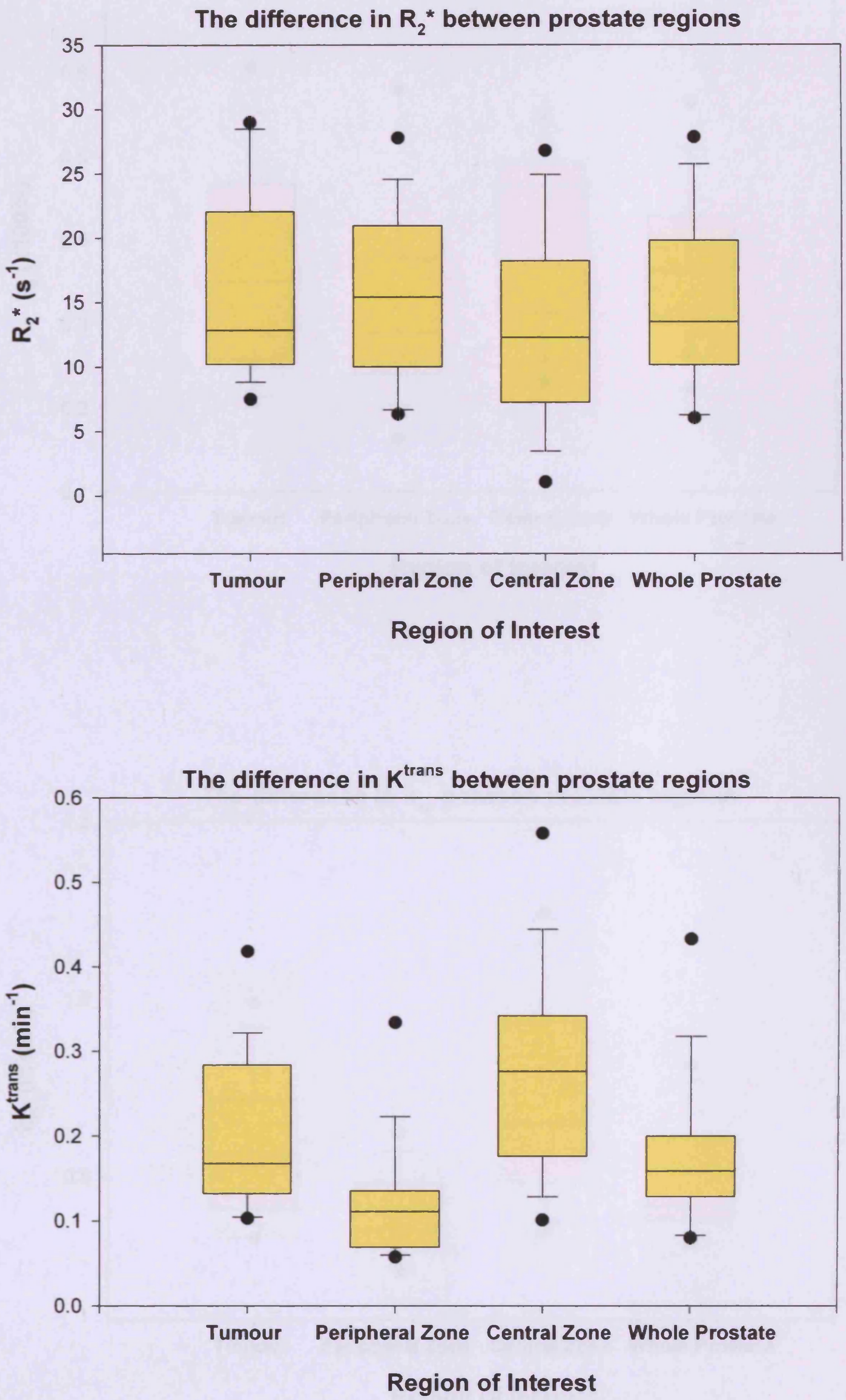

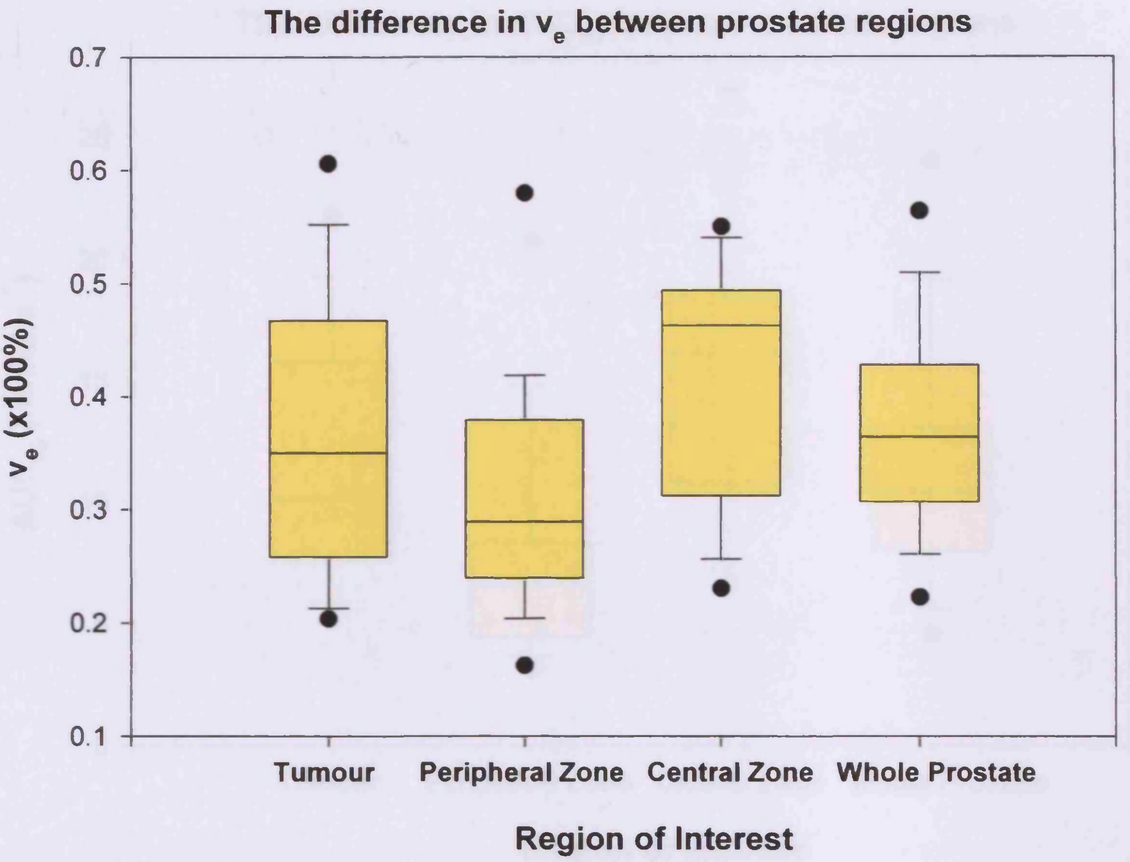

The difference in v_e between prostate regions

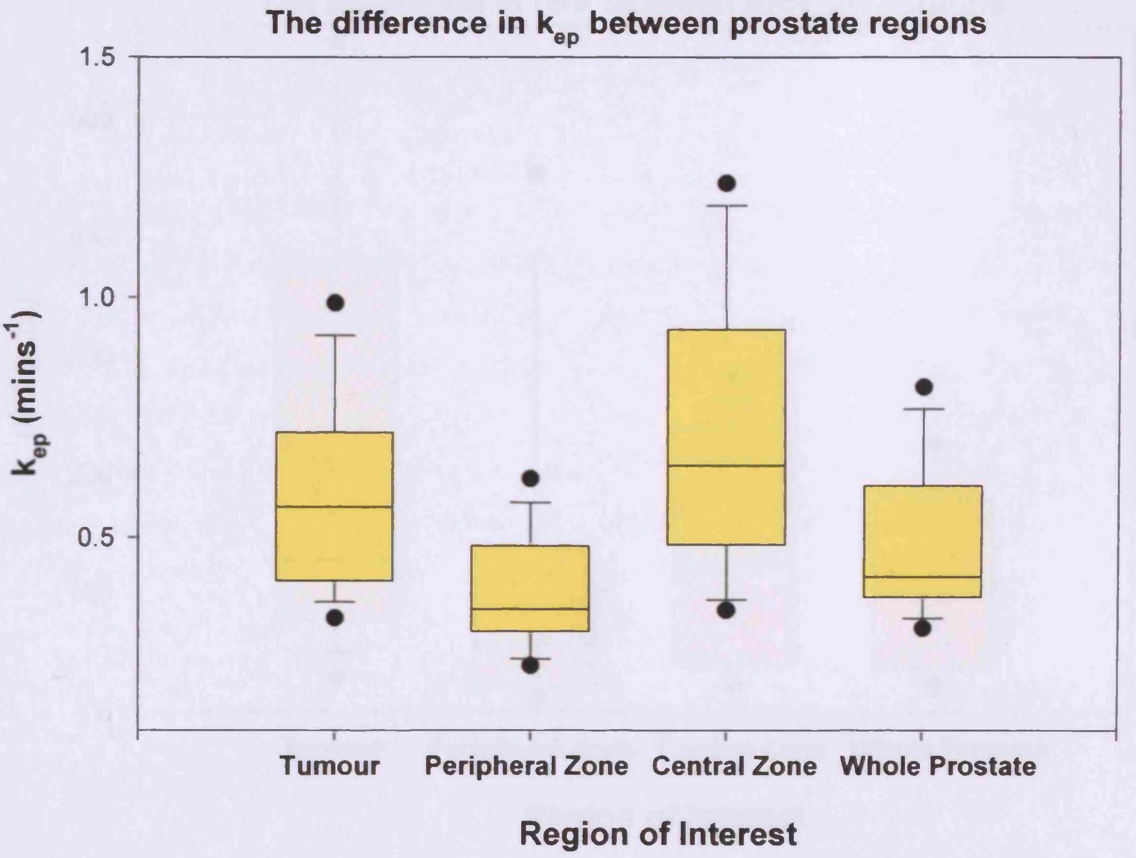

The difference in k_{ep} between prostate regions

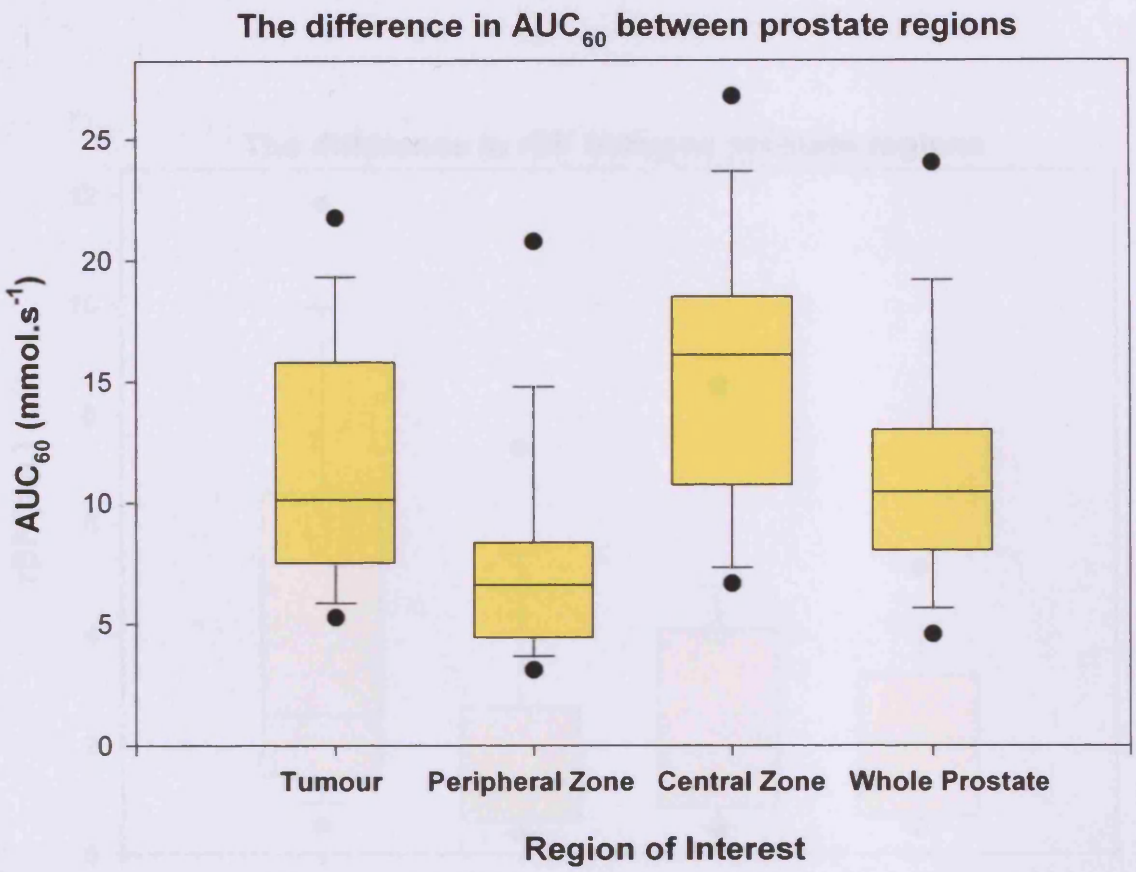
The difference in AUC60 between prostate regions
AUC60 (mmol.s-1)
0
5
10
15
20
25
Tumour
Peripheral Zone
Central Zone
Whole Prostate
Region of Interest

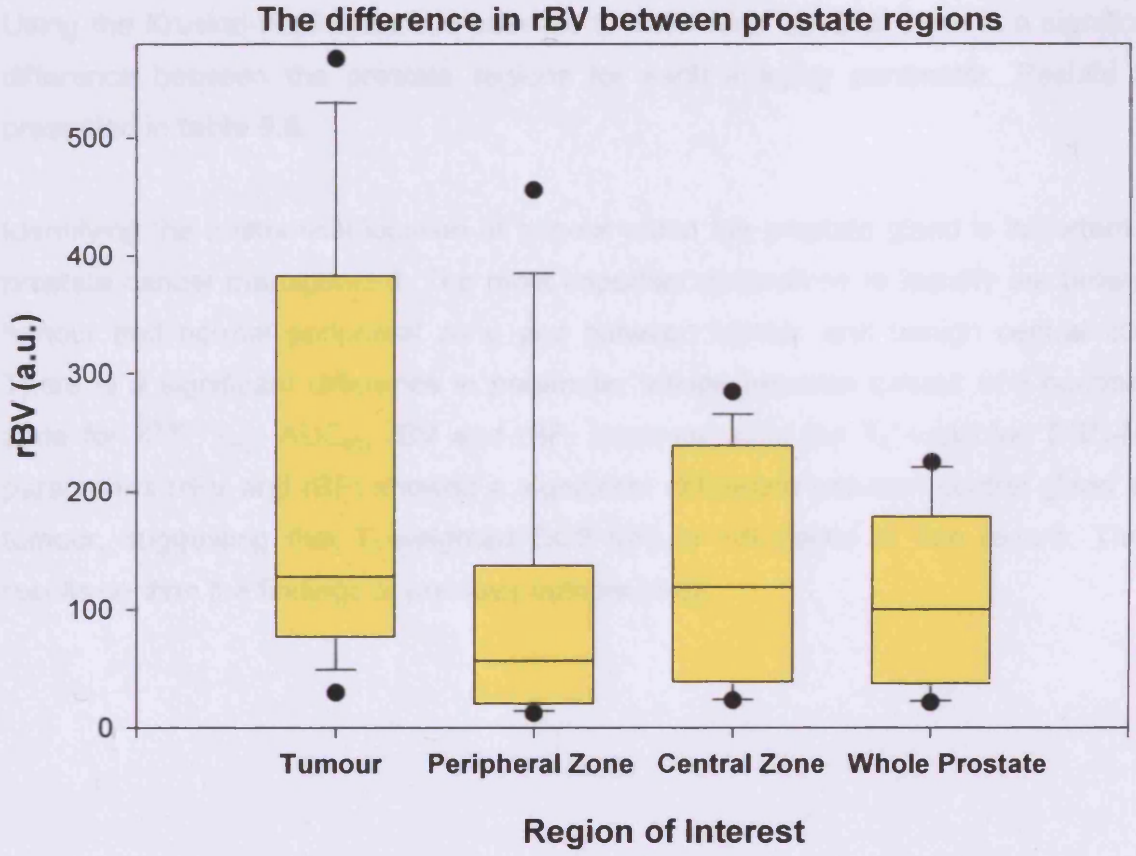
The difference in rBV between prostate regions
rBV (a.u.)
0
100
200
300
400
500
Tumour
Peripheral Zone
Central Zone
Whole Prostate
Region of Interest

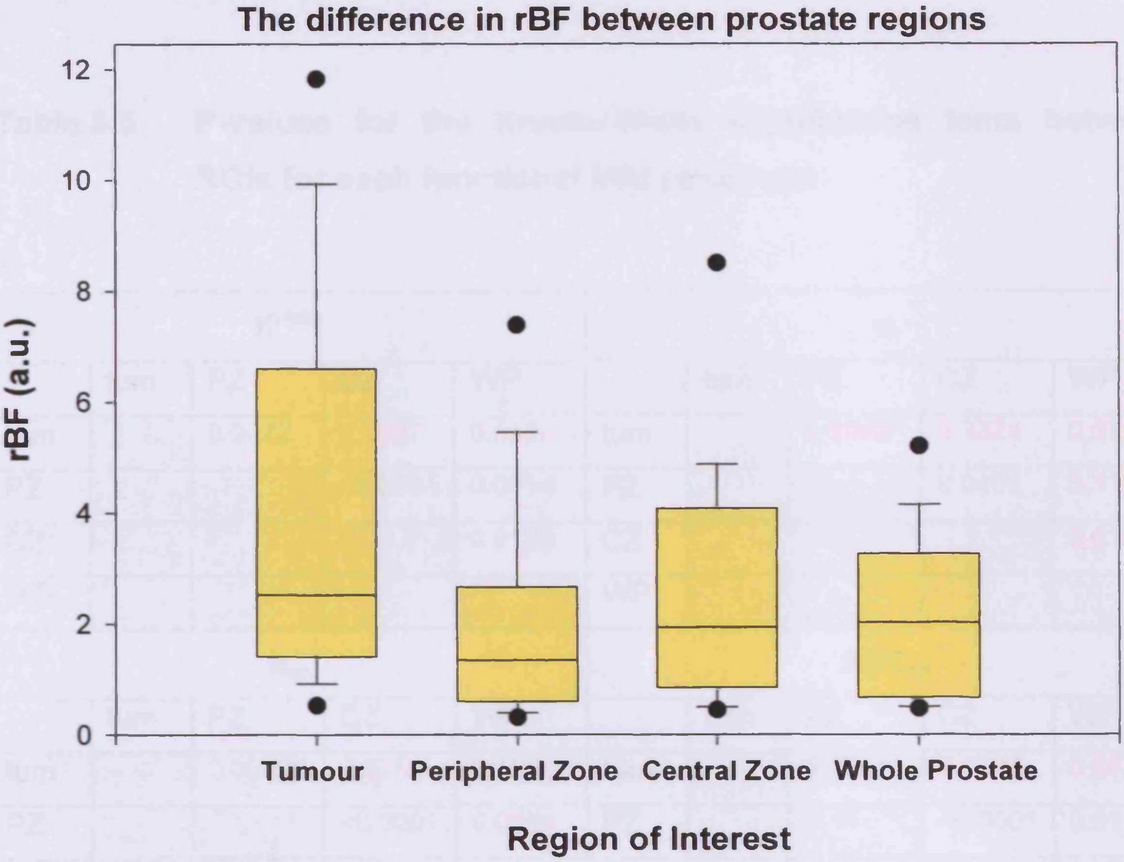

Using the Kruskal-Wallis test it is possible to determine whether there is a significant difference between the prostate regions for each imaging parameter. Results are presented in **table 5.5**.

Identifying the anatomical location of tumour within the prostate gland is important for prostate cancer management. The most important distinctions to identify are between tumour and normal peripheral zone and between tumour and benign central zone. There is a significant difference in parameter values between tumour and peripheral zone for K^{trans}, k_{ep}, AUC_{60}, rBV and rBF. However, only the T_2*-weighted DSC-MRI parameters (rBV and rBF) showed a significant difference between central gland and tumour, suggesting that T_1-weighted DCE-MRI is not useful in this regard. These results confirm the findings of previous authors [4-6].

Table 5.5 P-values for the Kruskal-Wallis significance tests between ROIs for each functional MRI parameter

K^{trans}				
	tum	PZ	CZ	WP
tum		0.0022	0.0897	0.5524
PZ			<0.0001	0.0094
CZ				0.0195
WP				

v_e				
	tum	PZ	CZ	WP
tum		0.2963	0.3324	0.6319
PZ			0.0401	0.1181
CZ				0.6107
WP				

k_{ep}				
	tum	PZ	CZ	WP
tum		0.0009	0.3752	0.1005
PZ			<0.0001	0.0654
CZ				0.0104
WP				

AUC_{60}				
	tum	PZ	CZ	WP
tum		0.0111	0.0806	0.8677
PZ			<0.0001	0.0139
CZ				0.0491
WP				

rBV				
	tum	PZ	CZ	WP
tum		<0.0001	0.0027	<0.0001
PZ			0.1634	0.4488
CZ				0.0336
WP				

rBF				
	tum	PZ	CZ	WP
tum		<0.0001	0.0013	<0.0001
PZ			0.403	0.7513
CZ				0.2503
WP				

R_2*				
	tum	PZ	CZ	WP
tum		0.8502	0.2814	0.6389
PZ			0.3578	0.7719
CZ				0.5276
WP				

Green values show a statistically significant difference at the 95% confidence level

Red values do not show a statistically significant difference at the 95% confidence level

5.5.4 Tumour Localisation

Total number of grid elements	827
Number of fully occupied grid elements	637
Number of tumour containing grids	121
Number of benign central zone grids	262
Number of benign peripheral zone grids	254

Table 5.6 ROC analysis for each MRI parameter

Parameter	Area Under ROC curve	95% C.I. for ROC	Sensitivity	Specificity	Optimum threshold
K^{trans}	0.71	0.66 – 0.77	0.68	0.67	0.13 min^{-1}
v_e	0.56	0.50 – 0.63	0.60	0.57	35%
k_{ep}	0.71	0.65 – 0.76	0.40	0.80	0.48 min^{-1}
AUC_{60}	0.67	0.61 – 0.73	0.64	0.62	8.01mmols^{-1}
rBV	0.52	0.46 – 0.58	0.90	0.18	219 a.u.
rBF	0.51	0.44 – 0.57	0.58	0.47	1.00 a.u.
R_2*	0.53	0.47 – 0.60	0.35	0.75	21.2s^{-1}

For an area under the ROC curve to be considered statistically significant its confidence interval must not cross 0.5. Therefore it can be seen that only the DCE-MRI parameters (K^{trans}, v_e, k_{ep} and AUC_{60}) were reliable in this regard. The most reliable parameter for locating tumour proved to be K^{trans}, with a sensitivity of 68%, a specificity of 67% and an overall accuracy of 68% using a threshold of 0.13 min^{-1} **(figure 5.5)**

5.5.5 Hypoxia detection - Regional Prostate Measurements

There is a statistically significant correlation between the level of R_2* seen on the MRI image and the proportion of pimonidazole labelling within prostate tumour and for the benign prostate peripheral zone. There was no correlation for benign central gland or for the whole prostate ROI **(figure 5.6)**. Pearson's product moment correlation coefficient (r) was calculated for the four prostate regions:

Table 5.7 Correlation coefficients (r) for the four prostate regions

	r	p-value
Prostate Tumour	0.64	0.0103
Peripheral Zone	0.49	0.0461
Central Zone	0.20	0.4486
Whole Prostate	0.41	0.0984

Figure 5.5

The use of the K^{trans} DCE-MRI parameter for tumour localisation

(Tumour shown with arrows)

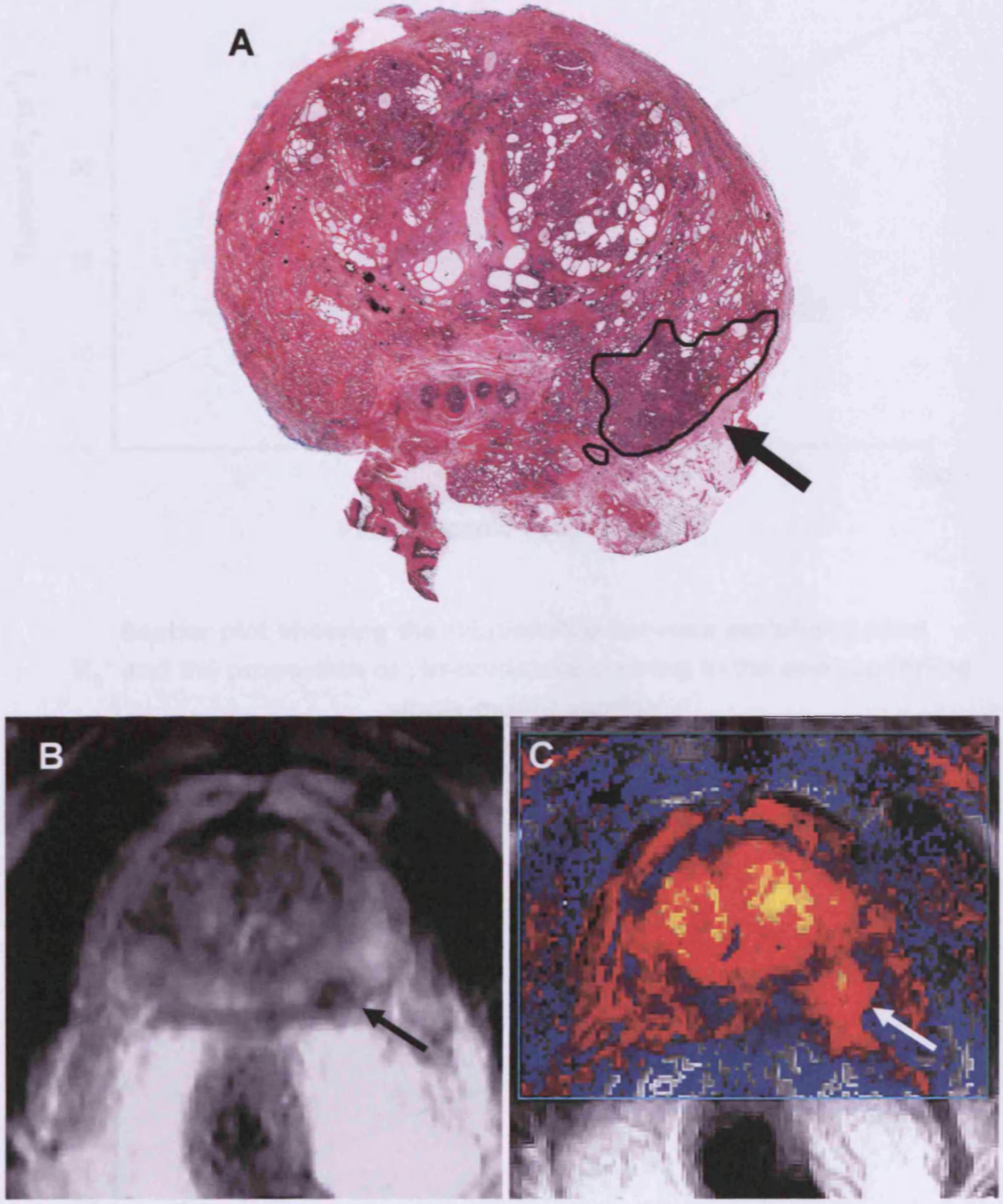

A 62 year old gentleman who presented with a PSA of 17.98 had a clinically-staged T1c adenocarcinoma of the prostate (Gleason 3+3=6 on biopsy). The radical prostatectomy specimen revealed a margin-positive T3b, Gleason 3+4 tumour (**image A**). The preoperative T_2-weighted MR image showed a low signal intensity region in the left posterior peripheral zone (arrow, **image B**). In the DCE-MRI image (**image C**) the median K^{trans} value for the tumour region (arrowed) measured 0.23 min^{-1} compared to the median value for the remainder of the benign peripheral zone of 0.13 min^{-1}.

Figure 5.6

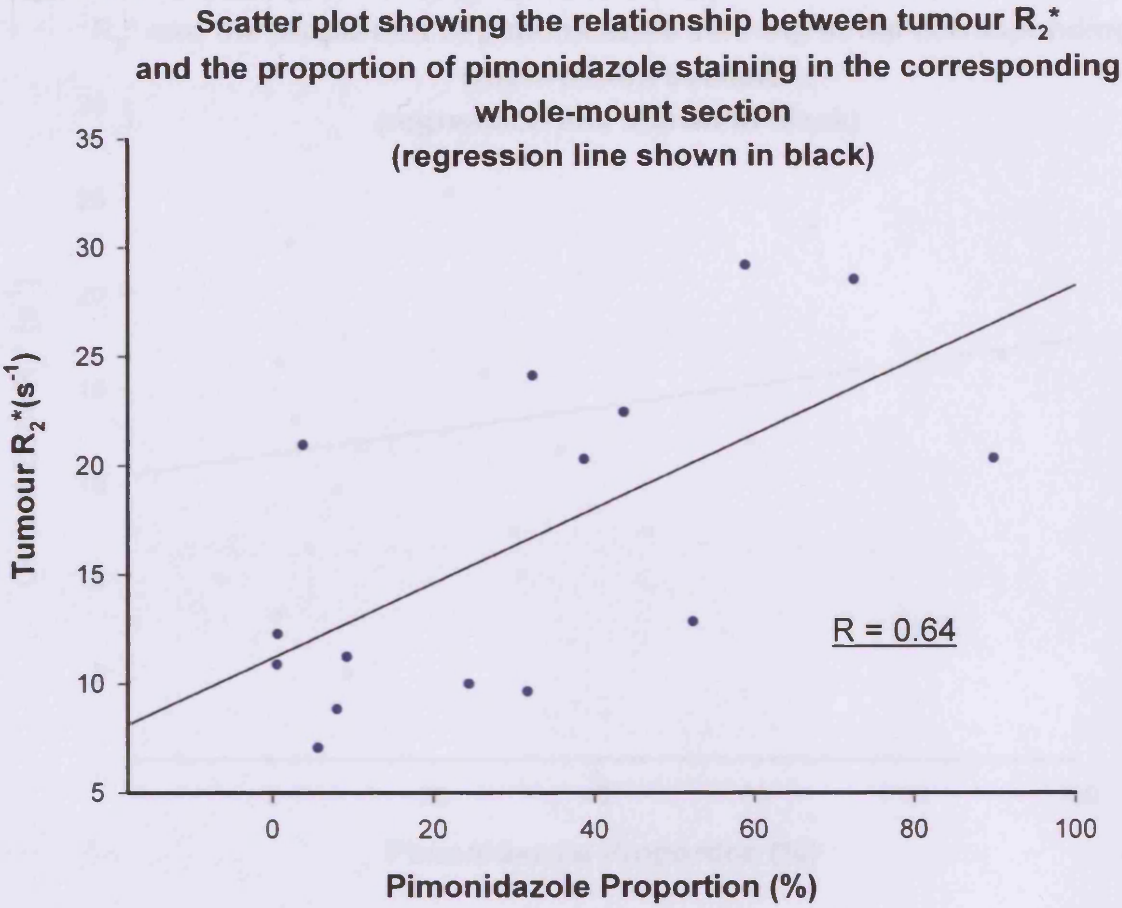
Scatter plot showing the relationship between tumour R_2* and the proportion of pimonidazole staining in the corresponding whole-mount section (regression line shown in black)

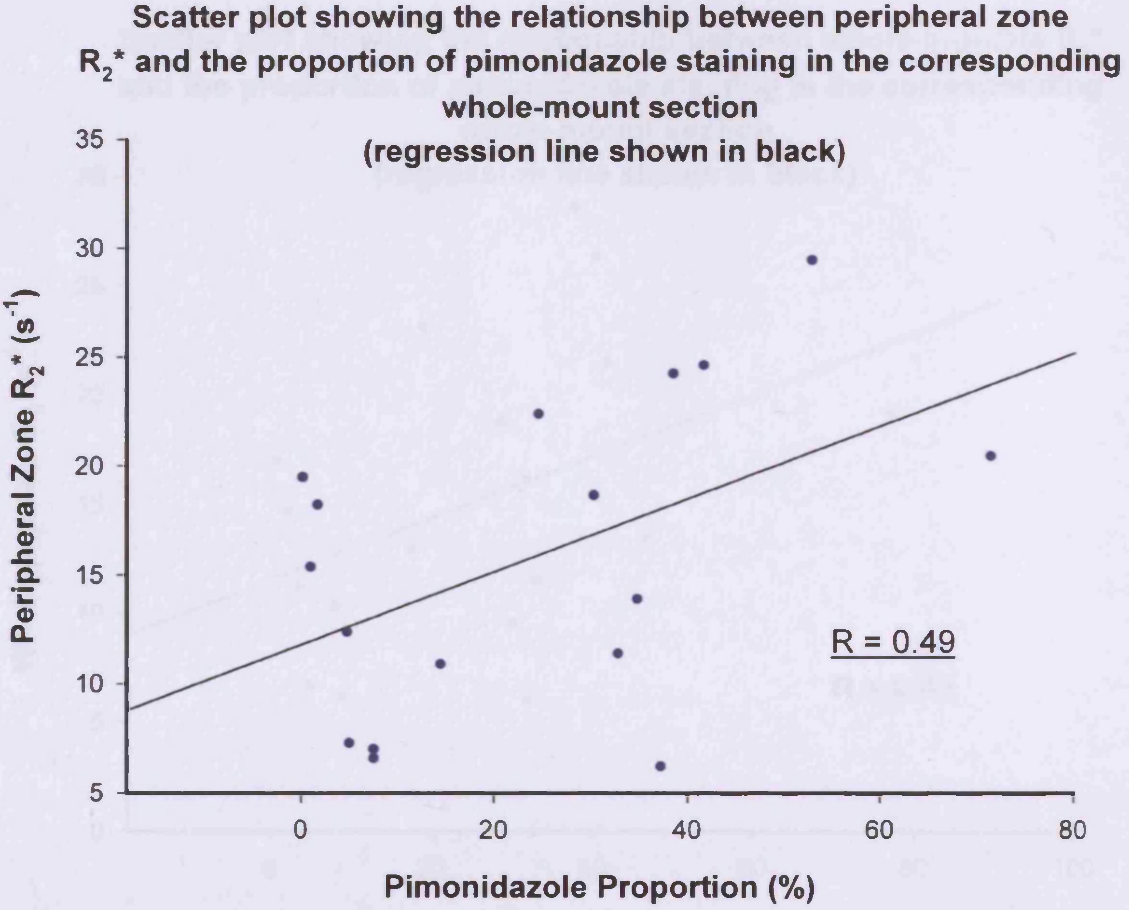
Scatter plot showing the relationship between peripheral zone R_2* and the proportion of pimonidazole staining in the corresponding whole-mount section (regression line shown in black)

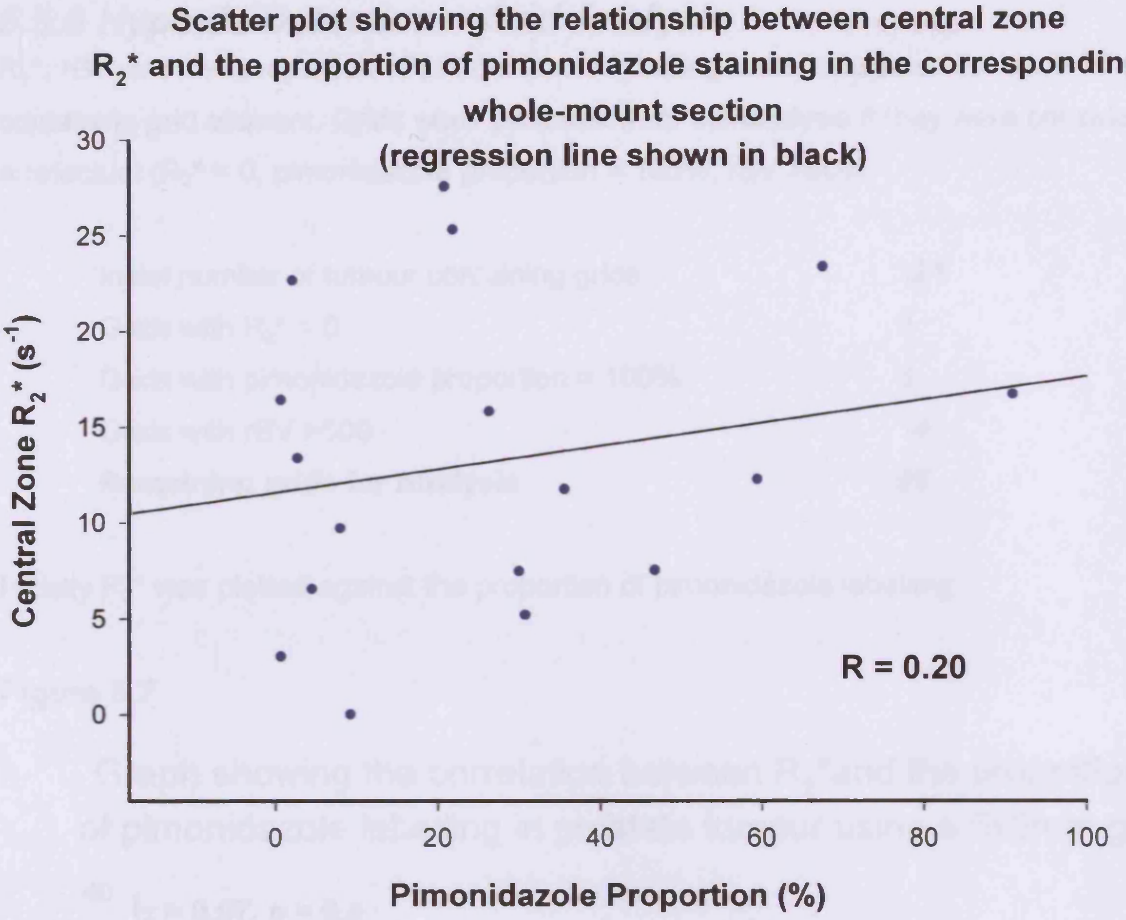
Scatter plot showing the relationship between central zone R_2* and the proportion of pimonidazole staining in the corresponding whole-mount section (regression line shown in black)

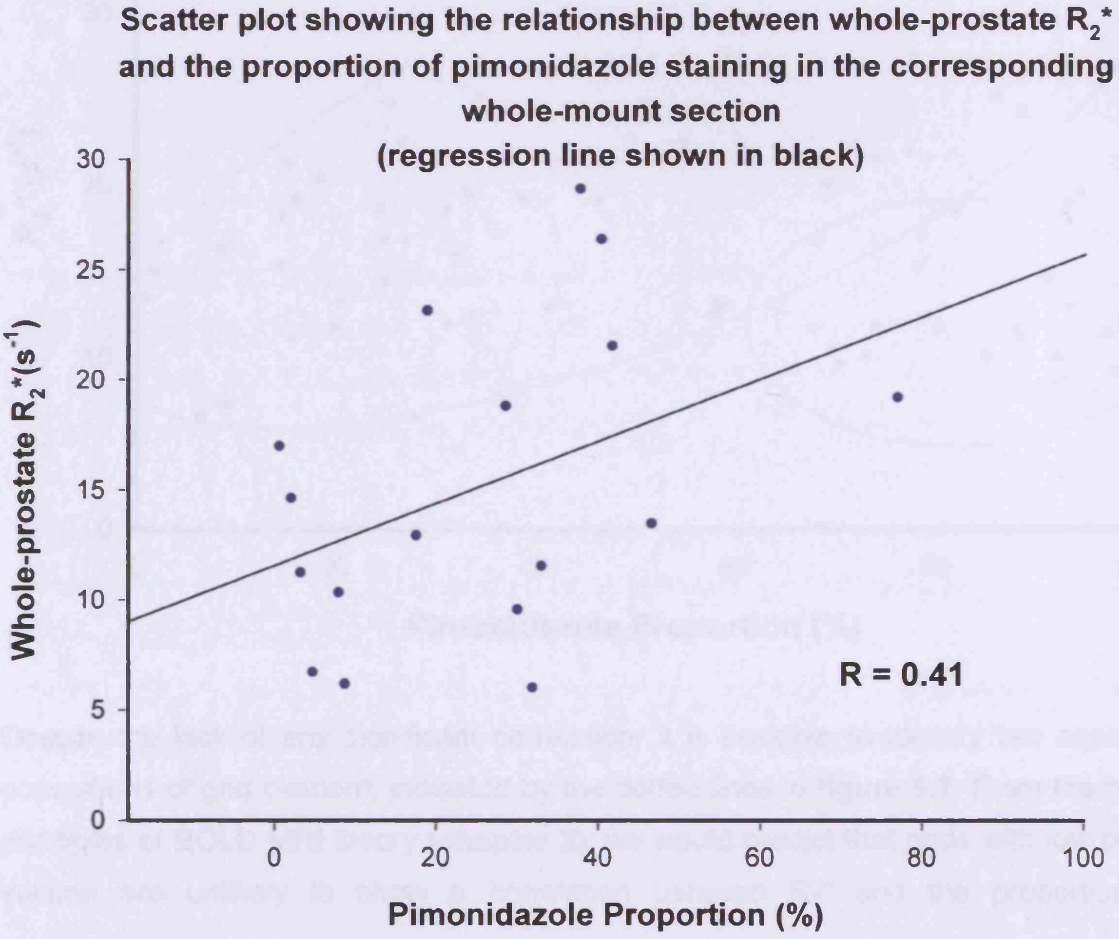
Scatter plot showing the relationship between whole-prostate R_2* and the proportion of pimonidazole staining in the corresponding whole-mount section (regression line shown in black)

5.5.6 Hypoxia Detection – Grid Analysis

R_2*, rBV and the proportion of pimonidazole labelling were calculated for each tumour containing grid element. Grids were excluded from the analysis if they were considered artefactual (R_2* = 0, pimonidazole proportion = 100%, rBV >500)

Initial number of tumour containing grids	121
Grids with R_2* = 0	3
Grids with pimonidazole proportion = 100%	8
Grids with rBV >500	14
Remaining grids for Analysis	**96**

Initially R_2* was plotted against the proportion of pimonidazole labelling:

Figure 5.7

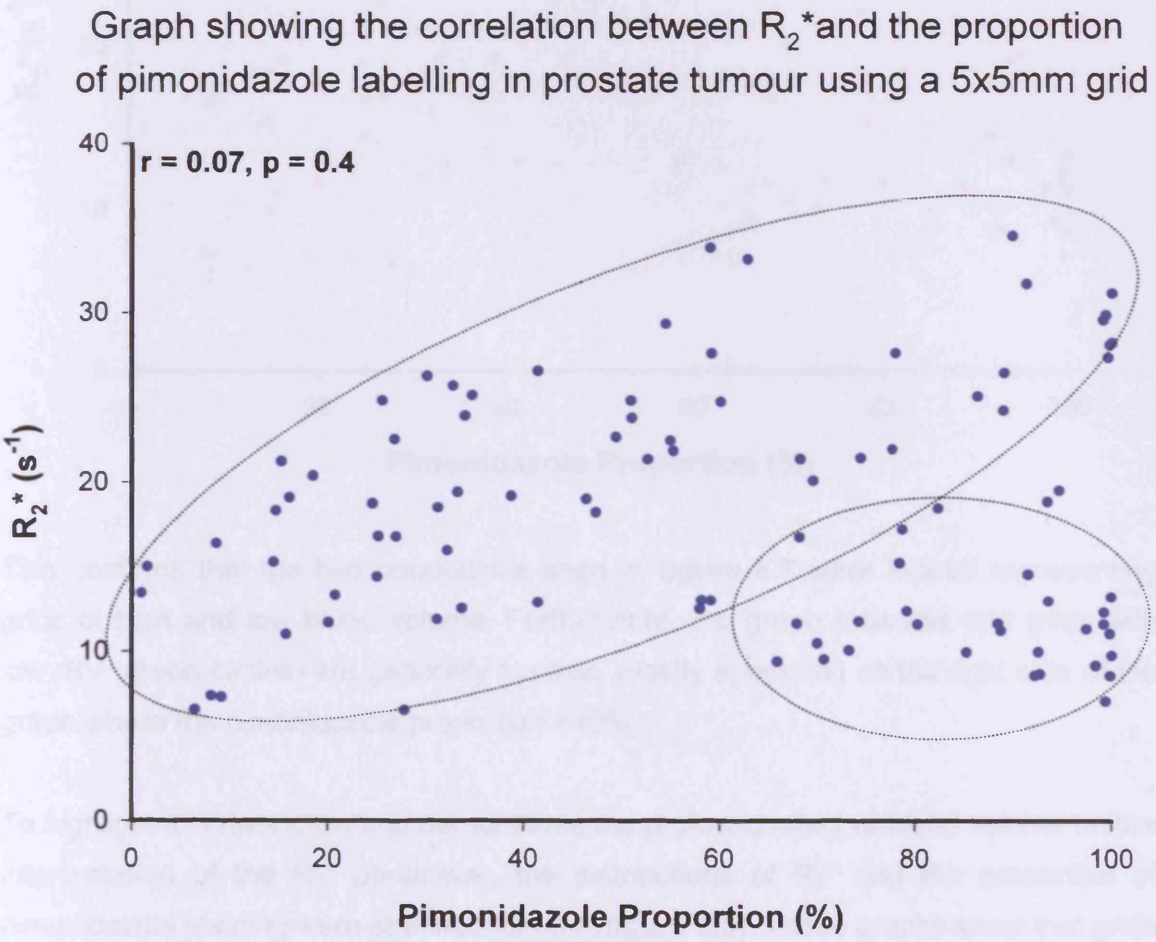

Despite the lack of any significant correlation, it is possible to identify two separate populations of grid element, indicated by the dotted lines in **figure 5.7**. From the basic principles of BOLD MRI theory **(chapter 2)**, we would predict that grids with low blood volume are unlikely to show a correlation between R_2* and the proportion of pimonidazole labelling, due to the general lack of haemoglobin molecules available to cause the BOLD effect. Conversely, grids with sufficient blood volume may possibly show a relationship.

Grid elements were then stratified for blood volume, using an rBV threhold of 40 au:

Figure 5.8

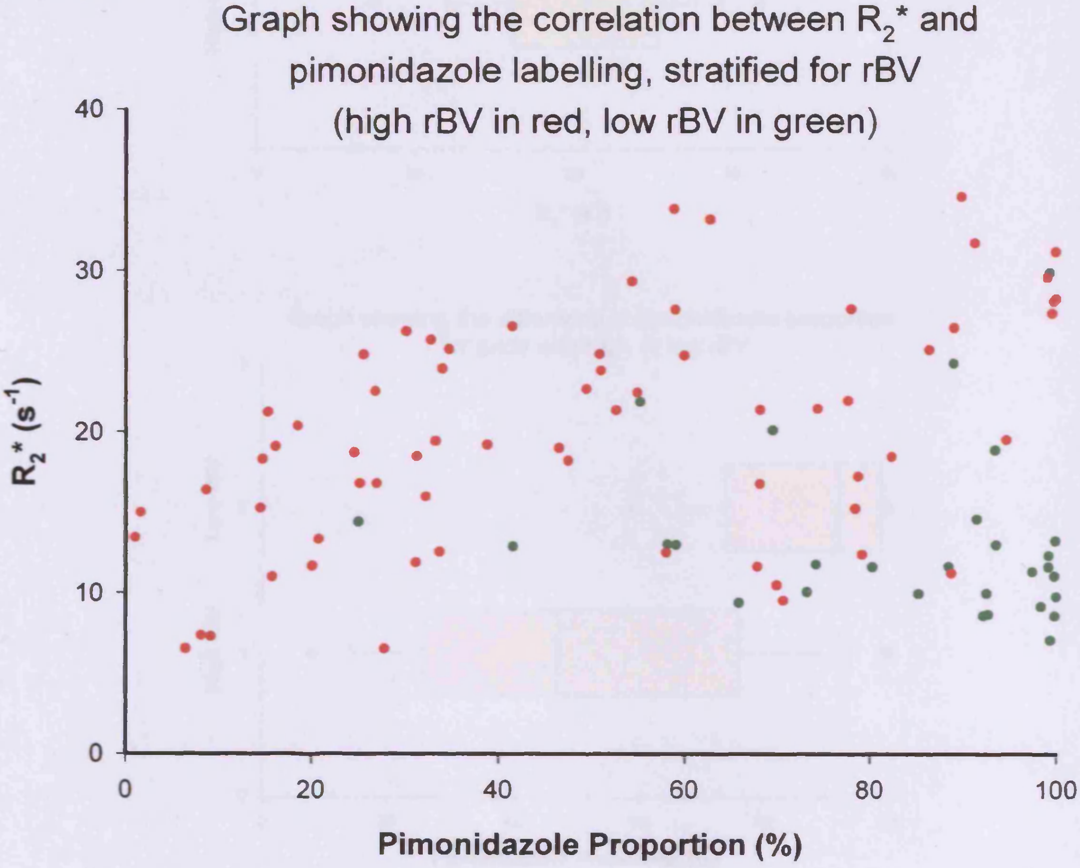

This confirms that the two populations seen in **figure 5.7** were indeed representing grids of high and low blood volume. Furthermore, the graph indicates that grids with low rBV (green circles) are generally hypoxic, mostly appearing on the right side of the graph where the pimonidazole proportion >40%.

To highlight this distinction and demonstrate the profound effect of blood volume on the interpretation of the R_2* parameter, the distributions of R_2* and the proportion of pimonidazole staining were stratified for rBV **(figure 5.9)**. These graphs show that grids with low rBV are more hypoxic than grids with high rBV in view of the higher proportion of pimonidazole labelling (89.1% versus 49.1%, $p < 0.0001$). Despite this, grids with low rBV exhibit significantly lower R_2* values ($11.2s^{-1}$ versus $20.7s^{-1}$, $p < 0.0001$) because of their inability to impart a BOLD effect due to the lack of haemoglobin delivery.

Figure 5.9

Graph showing the difference in R_2*for grids with high or low rBV

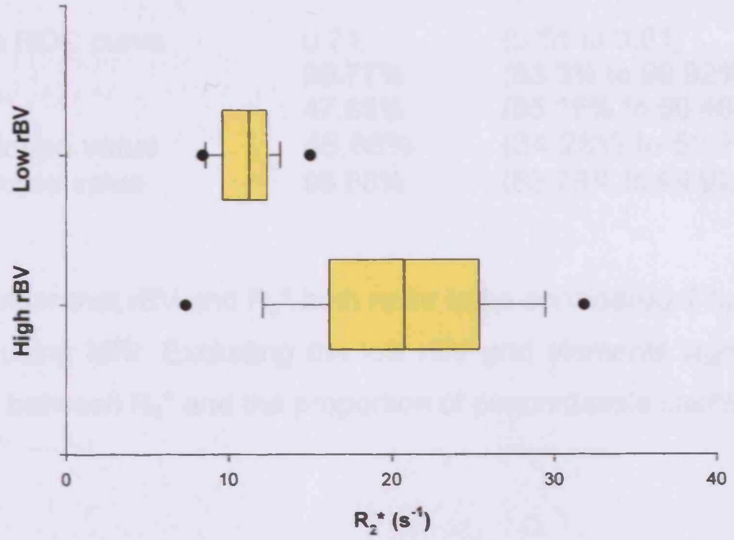

Graph showing the difference in pimonidazole proportion for grids with high or low rBV

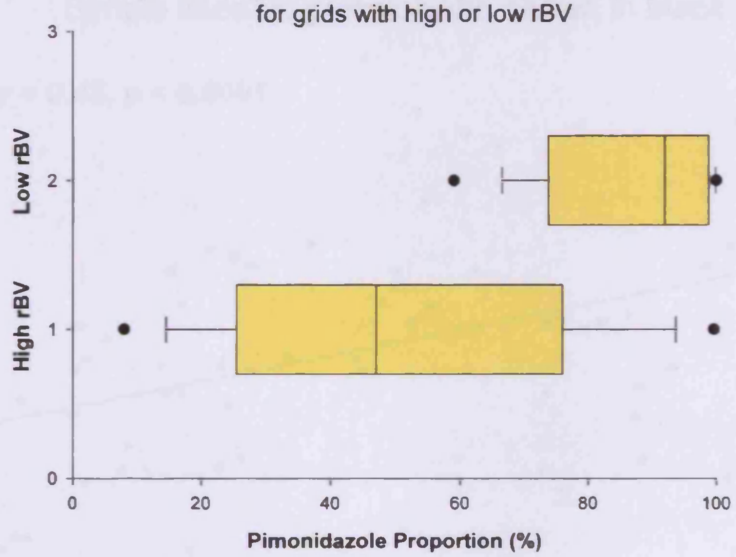

Using rBV alone it is possible to discriminate hypoxic and non-hypoxic grids with excellent sensitivity but with low specificity. ROC analysis shows that the optimum cut-off for rBV in this data set is 42.08:

Figure 5.10

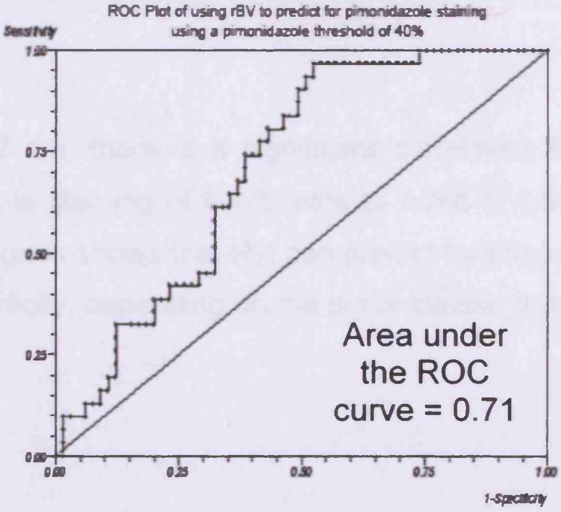
ROC Plot of using rBV to predict for pimonidazole staining using a pimonidazole threshold of 40%

Using the 42.08 cut-off, rBV alone gives:

Area under the ROC curve	0.71	(0.61 to 0.81)
Sensitivity	96.77%	(83.3% to 99.92%)
Specificity	47.69%	(35.15% to 60.46%)
Positive predictive value	46.88%	(34.28% to 59.77%)
Negative predictive value	96.88%	(83.78% to 99.92%)

It is therefore clear that rBV and R_2* both need to be considered if hypoxia maps are to be generated using MRI. Excluding the low rBV grid elements significantly increases the correlation between R_2* and the proportion of pimonidazole staining:

Figure 5.11

Correlation between R_2* and pimonidazole labelling. Low rBV grids excluded. Simple linear regression line shown in black

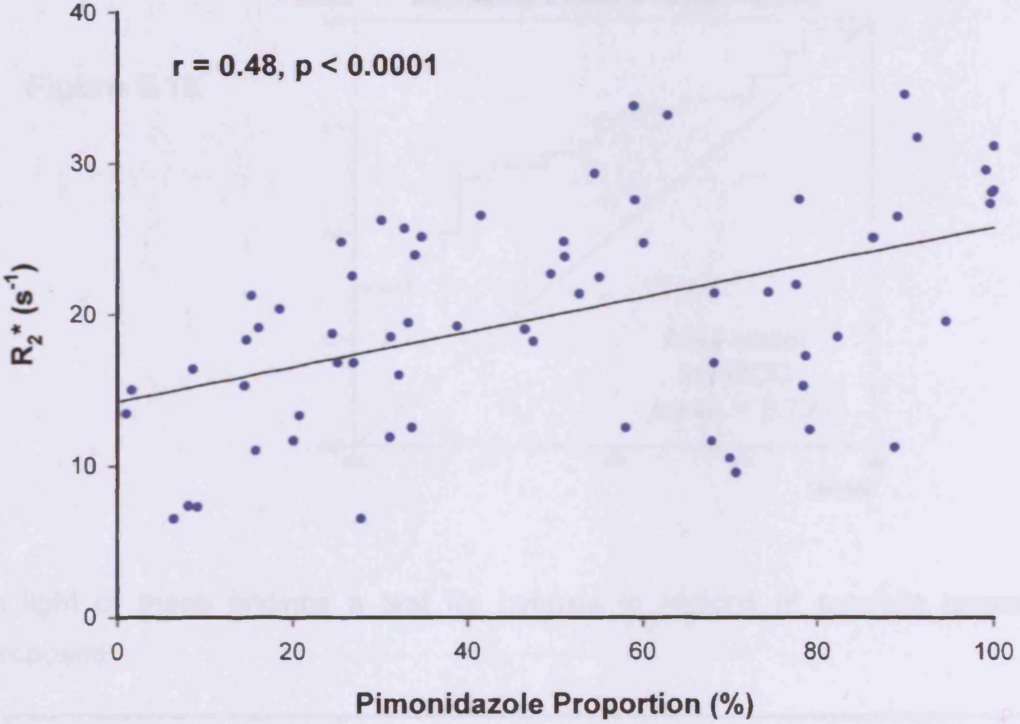

For grids with rBV > 42 a.u. there is a significant correlation between R_2* and the proportion of pimonidazole staining of 0.478 (95% CI 0.268 to 0.644, $p < 0.0001$). ROC analysis of the high rBV grids shows that R_2* can predict for pimonidazole labeling with high sensitivity and specificity, depending on the pimonidazole threshold used:

Table 5.8 ROC analysis of the high rBV grids (>42 a.u.)

Pimonidazole labelling threshold used to determine whether a tumour was hypoxic	> 10%	> 20%	> 30%	> 40 %
Area Under ROC curve	0.87	0.77	0.77	0.72
95% C.I. for ROC	0.76 – 0.98	0.65 – 0.89	0.65 – 0.88	0.59 – 0.84
Sensitivity	0.74	0.54	0.58	0.63
Specificity	1.00	1.00	0.90	0.80
R_2* cut-off	16.8	21.3	21.3	21.3

Figure 5.12

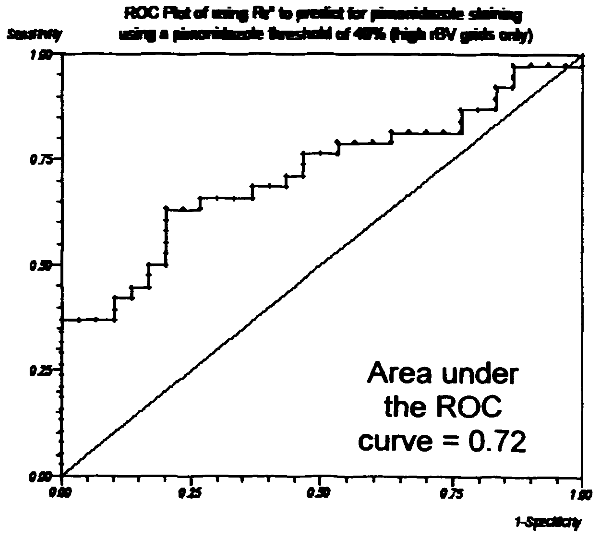

In light of these findings a test for hypoxia in regions of prostate cancer can be proposed:

Test Hypothesis:

Hypoxia in prostate cancer should be diagnosed if:

1) rBV is less than 42 a.u. **OR**,
2) rBV is greater than 42 a.u. **AND** R_2* is greater than $21.3s^{-1}$

In other words: Hypoxia should NOT be diagnosed if:

rBV is greater than 42 a.u. **AND** R_2* is less than $21.3s^{-1}$

Using this test on the data from the above experiment, sensitivity and specificity vales can be produced:

	Pimonidazole Positive	Pimonidazole Negative	Total
MRI Test Positive	52	7	59
MRI Test Negative	13	24	37
Total	65	31	96

Using pimonidazole threshold of 40%

Sensitivity	**80.00% (95% CI 68.23% to 88.9%)**
Specificity	**77.42% (95% CI 58.9% to 90.41%)**
Positive Predictive Value	**88.14% (95% CI 77.07% to 95.09%)**
Negative Predictive Value	**64.86% (95% CI 47.46% to 79.79%)**
Overall Accuracy	**79.17%**

These test statistics vary when using alternate pimonidazole thresholds:

Table 5.9 How pimonidazole labelling threshold affects test statistics

Pimonidazole labelling threshold used to determine whether a tumour was hypoxic	> 10%	> 20%	> 30%	> 40 %	> 50 %
Sensitivity	80.0%	70.2%	74.7%	80.0%	81.7%
Specificity	100.0%	100.0%	85.7%	77.4%	72.2%

5.5.7 Repeatability Analysis

Whole ROI measurements

The distribution of each parameter was not significantly different form normal. The difference between values for the four prostate regions of interest showed no dependence on the mean and therefore no logarithmic transformation was required for these data. A detailed discussion of repeatability can be found in **chapter 3, p110.** Repeatability statistics were as follows:

Table 5.10 The repeatability of R_2^* - regional analysis

Whole Prostate		**Tumour**	
Number of patients	16	Number of patients	13
Repeatability for n=1 (absolute)	2.39	Repeatability for n=1 (absolute)	1.95
Repeatability for n=1 (%)	16.53 %	Repeatability for n=1 (%)	12.92 %
Variance ratio (F)	114.7	Variance ratio (F)	184.1
P-value for F	<0.00001	P-value for F	<0.00001
Interclass correlation coefficient (ICC)	0.98	Interclass correlation coefficient (ICC)	0.99
Coefficient of variation (wCV)	0.060	Coefficient of variation (wCV)	0.047
Benign Peripheral Zone		**Benign Central Zone**	
Number of patients	16	Number of patients	16
Repeatability for n=1 (absolute)	1.78	Repeatability for n=1 (absolute)	5.30
Repeatability for n=1 (%)	11.65	Repeatability for n=1 (%)	42.55
Variance ratio (F)	238.6	Variance ratio (F)	32.3
P-value for F	<0.00001	P-value for F	<0.00001
Interclass correlation coefficient (ICC)	0.99	Interclass correlation coefficient (ICC)	0.94
Coefficient of variation (wCV)	0.042	Coefficient of variation (wCV)	0.154

The susceptibility weighted BOLD technique proved to be extremely repeatable for all four ROIs. For an individual patient's prostate tumour, a change in R_2^* of $1.95s^{-1}$ (or 12.92%) could be considered significant at the 95% confidence level (i.e. not simply a result of test variability). A very high degree of repeatability was also seen for all regions in terms of both ICC (94-99%) and wCV (4.2-15.4%).

Grid based analysis

When the repeatability analysis was performed for each of the grid elements, the difference between values showed a dependence on the mean necessitating logarithmic transformation for these data.

Table 5.11 The repeatability of R_2^* - grid based analysis

All complete grid elements		**Tumour containing grid elements**	
Number of grids	121	Number of grids	637
Repeatability for n=1 relative to mean	4.93-7.25	Repeatability for n=1 relative to mean	-4.49-6.21
Repeatability for n=1 (%)	-31.9-46.9%	Repeatability for n=1 (%)	-27.7-38.4%
Variance ratio (F)	20.96	Variance ratio (F)	31.64
P-value for F	<0.00001	P-value for F	<0.00001
Interclass correlation coefficient (ICC)	0.149	Interclass correlation coefficient (ICC)	0.94
Coefficient of variation (wCV)	0.060	Coefficient of variation (wCV)	0.124

The tumour containing grid elements appeared to be slightly more reproducible than the benign grids, reflecting the results of the ROI based analysis presented above. For an individual tumour containing grid, a fall in R_2^* of $4.49s^{-1}$ (or 27.7%) could be considered significant at the 95% confidence level. The grid-based analysis is less repeatable than the regional analysis.

5.5.8 Carbogen Breathing

The two initial air-breathing R_2^* measurements for each patient were averaged and compared to the R_2^* value taken after 10 minutes of carbogen breathing.

Analysis of tumour regions on an individual patient-by-patient basis showed that nine of the 14 patients had a reduction in tumour R_2^* during carbogen exposure that could be considered statistically significant and distinguishable from test variability at the 95% confidence level **(figure 5.13)**. Analysis of the group as a whole showed a mean reduction in R_2^* of $3.52s^{-1}$ or 21.6% (p = 0.0005) for the prostate tumour ROIs. Results for all four ROIs are given below:

Table 5.12 The response to carbogen breathing – regional assessment

	Tumour	Benign Peripheral Zone	Benign Central Zone	Whole Prostate
Number of patients	14	16	16	16
Mean ΔR_2^* (s^{-1})	-3.52	-0.05	*+0.22* ***(increase)***	-0.36
ΔR_2^* (%)	-21.6	-0.32	*+1.70* ***(increase)***	-2.40
Significance	p = 0.0005	ns	ns	ns
No. of patients with individually significant change (95%CI)	9 of 14	4 of 16	1 of 16	1 of 16

ns Not Significant

Figure 5.13

The change in R_2* during carbogen gas breathing
(red lines indicate individual patients with
changes significant at the 95% confidence level)

Tumour

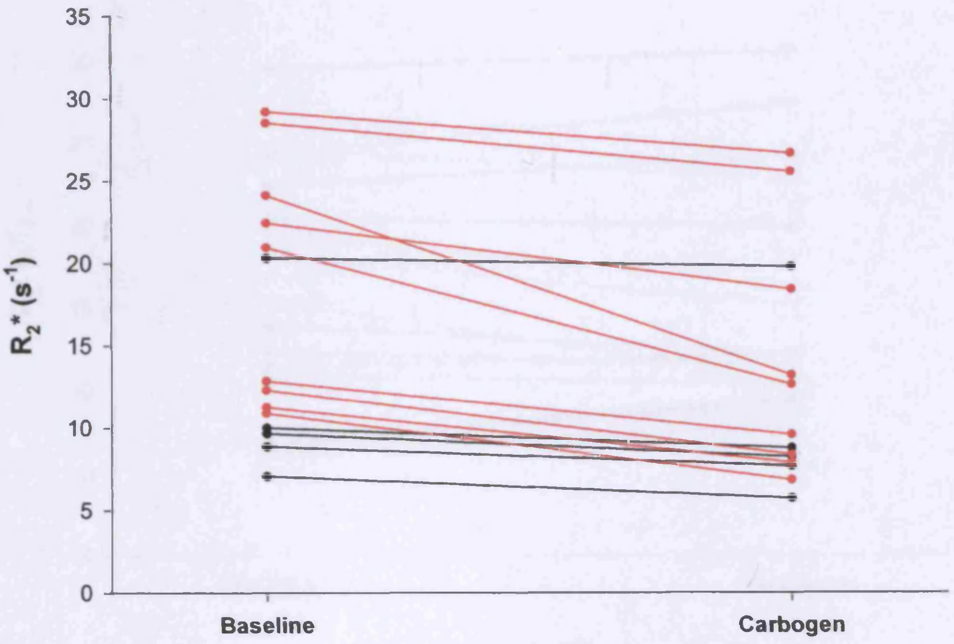

The Change in R_2* during carbogen gas breathing
(red lines indicate individual patients with
changes significant at the 95% confidence level)

Whole Prostate

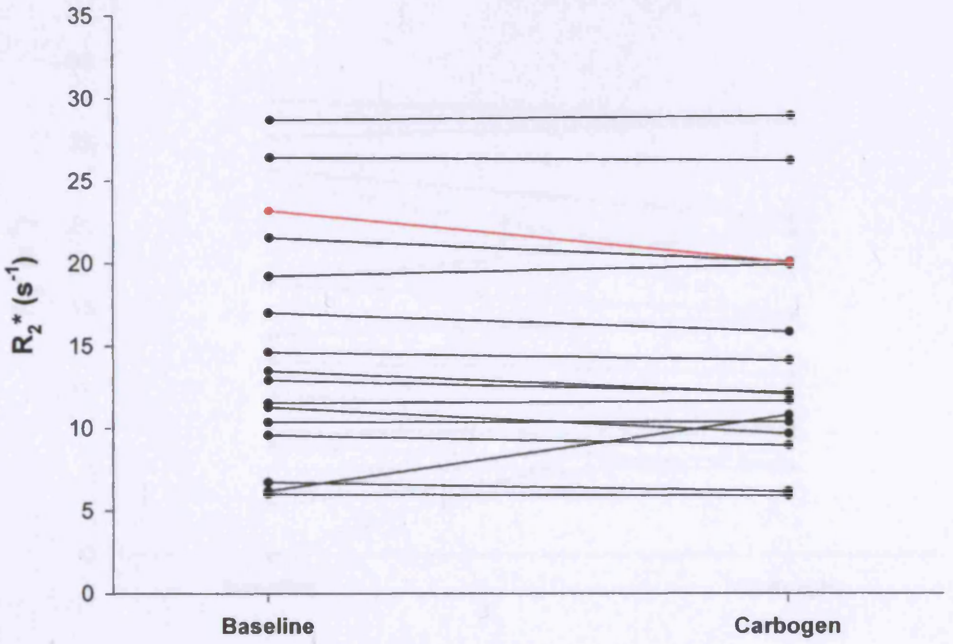

The change in R_2* during carbogen gas breathing
(red lines indicate individual patients with
changes significant at the 95% confidence level)

Peripheral Zone

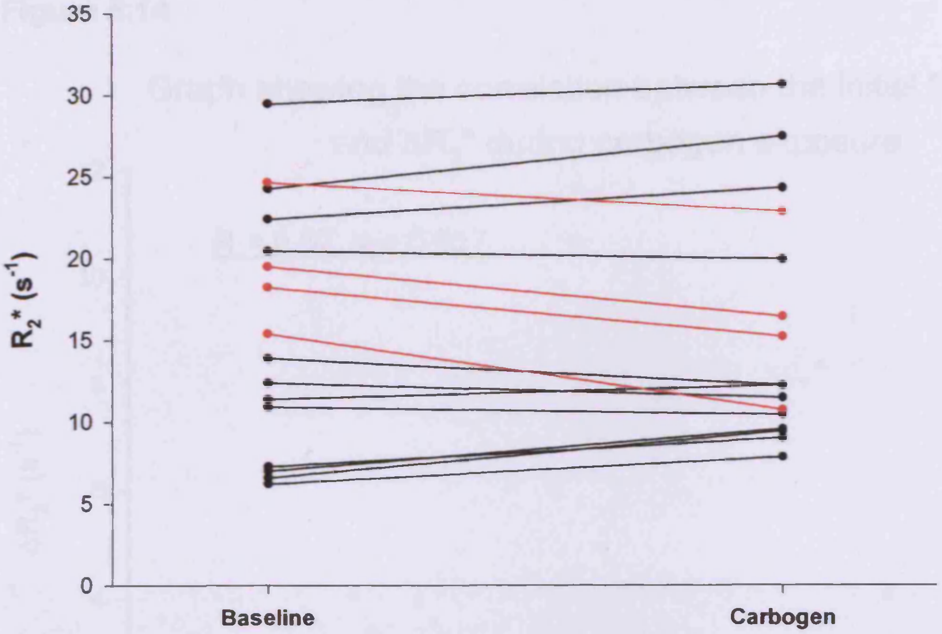

The change in R_2* during carbogen gas breathing
(red lines indicate individual patients with
changes significant at the 95% confidence level)

Central Zone

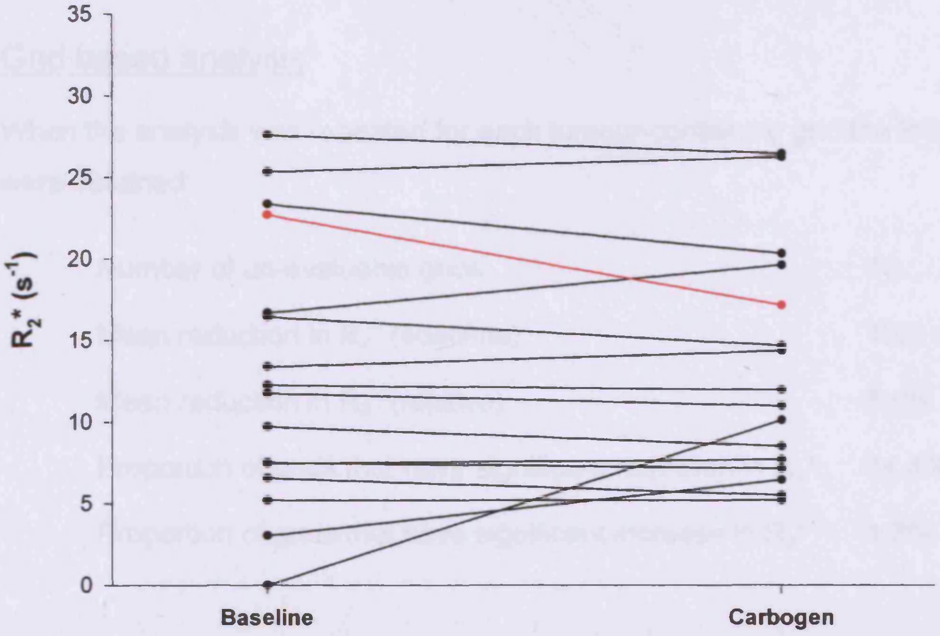

When the low rBV tumours (<40 a.u.) were excluded, there was a statistically significant correlation between the baseline R_2* value and the change in R_2* following carbogen exposure **(figure 5.14)**. The tumour regions that were most hypoxic at baseline responded the most to carbogen breathing.

Figure 5.14

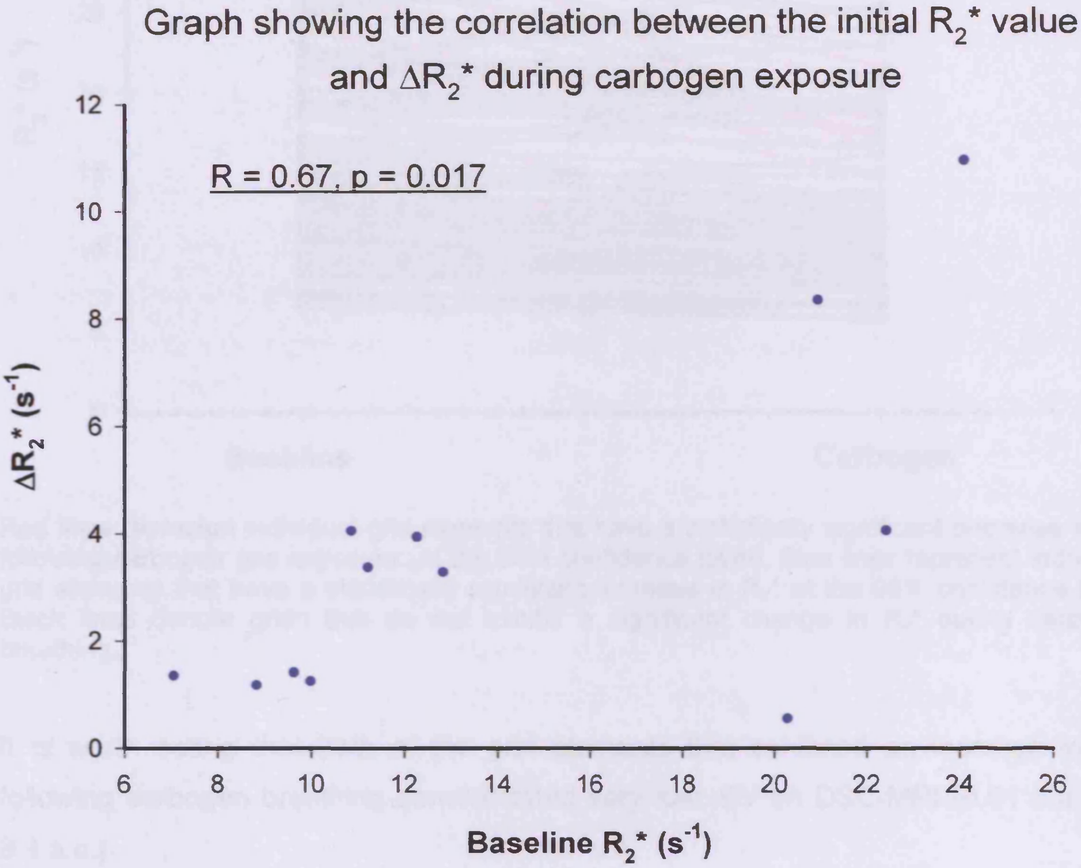

Grid based analysis

When the analysis was repeated for each tumour-containing grid the following results were obtained:

Number of un-evaluable grids	10
Mean reduction in R_2* (absolute)	1.42 s^{-1}
Mean reduction in R_2* (relative)	8.0%
Proportion of grids that have significant reduction in R_2*	14.4% (16 of 111)
Proportion of grids that have significant increase in R_2*	1.8% (2 of 111)

Figure 5.15 The change in R_2* during carbogen gas breathing

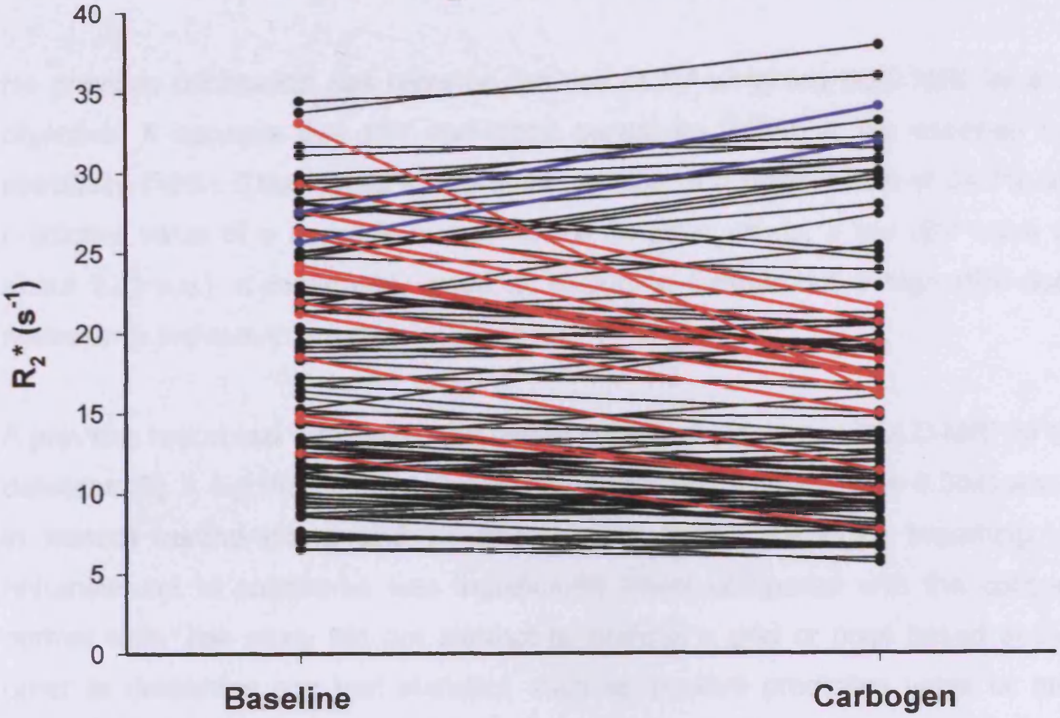

Red lines represent individual grid elements that have a statistically significant decrease in R_2* following carbogen gas exposure (at the 95% confidence level). Blue lines represent individual grid elements that have a statistically significant increase in R_2* at the 95% confidence level. Black lines denote grids that do not exhibit a significant change in R_2* during carbogen breathing.

It is worth noting that both of the grid elements that exhibited an increase in R_2* following carbogen breathing demonstrated very low rBV on DSC-MRI (0.01 a.u. and 8.4 a.u.).

5.6 Discussion

Tumour localisation

It was not the intended purpose of this study to assess the ability of dynamic or susceptibility weighted MR for the purpose of tumour detection. However, given the methodology used, tumour regions had to be defined as part of the hypoxia assessment. Therefore the investigation of how effective each MRI parameter was at locating tumour amongst benign prostatic tissue became an intrinsic part of the analysis process and as a result has been presented here. Numerous studies have reported the diagnostic accuracy of T_1-weighted DCE MRI for this purpose (**Chapter 2, page 65 and table 2.2**), predominately using K^{trans} or AUC as the parameters of choice. The current study confirms K^{trans} as the optimum parameter for tumour localisation (**Table 5.6**) with an area under the ROC curve of 0.71, a sensitivity of 68% and a specificity of 67%.

No previous publication has reported the use of T_2*-weighted DSC MRI for a similar objective. It appears that rBV has good sensitivity (90%) at the expense of poor specificity (18%). This results in a predictive value of a positive test of 34.7% and the predictive value of a negative test of 78.9%. In other words, a low rBV value (below about 220 a.u.) is reasonably good at excluding tumour but a high rBV does not necessarily indicate the presence of cancer.

A previous report has suggested the use of carbogen stimulated BOLD-MRI for tumour detection [7]. A significant T_2*-weighted signal intensity increase ($P = 0.004$) was found in normal central gland and peripheral zone during carbogen breathing. Signal enhancement in carcinoma was significantly lower compared with the contralateral normal side. The study did not attempt to perform a grid or pixel based analysis in order to determine any test statistics such as positive predictive value or negative predictive value for tumour detection, instead choosing to simply highlight the difference in BOLD signal enhancement between benign and malignant tissue. The current study confirms these results with only tumour ROIs showing a significant change in R_2* during carbogen exposure (a change of 21.6%, $p = 0.0005$; **table 5.12**). However, a static R_2* measurement alone is not particularly useful for tumour localisation with a sensitivity of 35% and specificity of 75% and unlikely to improve on the accuracy of the other functional MRI modalities such as DCE, MRS or DWI for this purpose.

Hypoxia Detection

The investigation of tumour hypoxia in human prostate cancer is a greater challenge than the analysis of hypoxia in animals bearing prostate tumour xenografts. This is mainly for two reasons. Firstly, the human prostate is made up of several different tissue types, each with different physiological and vascular characteristics. Secondly, in the modern era where there are a number of forms of treatment for the prostate cancer and more accurate pre-operative staging, radical prostatectomy is generally reserved for patients with low-volume, low-risk disease. As a result only a small proportion of excised tissue is in fact malignant (8.2% in this series). Despite this, if an imaging modality is to be validated as a tool for the detection of tumour hypoxia it must be compared with the current 'gold-standard'. Since the demise of the needle electrode (see chapter 1) immunohistochemical analysis of the excised gland is the only proven method for this purpose. Therefore, notwithstanding the inherent difficulties in the quantitative comparison between a 'thick' radiological image and a 'thin' histological section, this is the only available strategy. The results of such an analysis needs to be interpreted with the understanding that even a 'perfect' imaging technique, that measures exactly the same biological process as the immunohistochemistry, would fail to show 'perfect' correlation because of the issues of anatomical registration and distortion of corresponding imaging and pathological slices.

In spite of these facts, the results of this study corroborate the animal data presented in **chapter 4** and show that it is possible to identify hypoxic regions within human prostate cancer using MRI. For the correlation between pimonidazole staining and R_2^* alone, using the tumour ROI analysis, the Pearson correlation coefficient was 0.64 ($p = 0.0103$) which is of a similar order to the correlation seen for the animal tumours ($r = 0.73$-0.75, $p < 0.0006$). As predicted from the mechanism of the BOLD effect, the inclusion of blood volume information is critical to the interpretation of the parametric R_2^* map **(figure 5.16)**.

Based on the data presented above and by using the optimum thresholds suggested by ROC analysis of the same data, it is possible to achieve a sensitivity of 80% and a specificity of 77% for the detection of hypoxia by combining the R_2^* and rBV measurements. Furthermore, of more relevance to clinical practice, the predictive value of a positive test, i.e. the post-test likelihood of hypoxia, was 88% and the predictive value of a negative test, i.e. the post-test likelihood of no hypoxia, was 65%.

Earlier work using the combination of BOLD and T_2^*-weighted dynamic MRI, reported by Hoskin et. al, demonstrated excellent sensitivity (95%) but low specificity (29%) for hypoxia detection [8]. In that study, regions of prostate cancer were designated as hypoxic depending on whether the R_2^* value was greater or less than that of the obturator internus muscle and whether rBV was greater or less than ischiorectal fat. This binary method does not permit ROC analysis and therefore the optimum thresholds for R_2^* and rBV could not be calculated. The study presented in this chapter has demonstrated an overall accuracy of 79%, using the combined test, by determining these thresholds.

Changing the pimonidazole thresholds used in this analysis can alter the results. In this study pimonidazole is being used as the 'gold-standard' to establish if the MRI determination of whether a grid is hypoxic is in fact 'true' or 'false'. Therefore ascertaining the proportion of brown staining in a grid for it to be considered hypoxic would seem critical.

Figure 5.16 The theoretical change in BOLD MRI signal

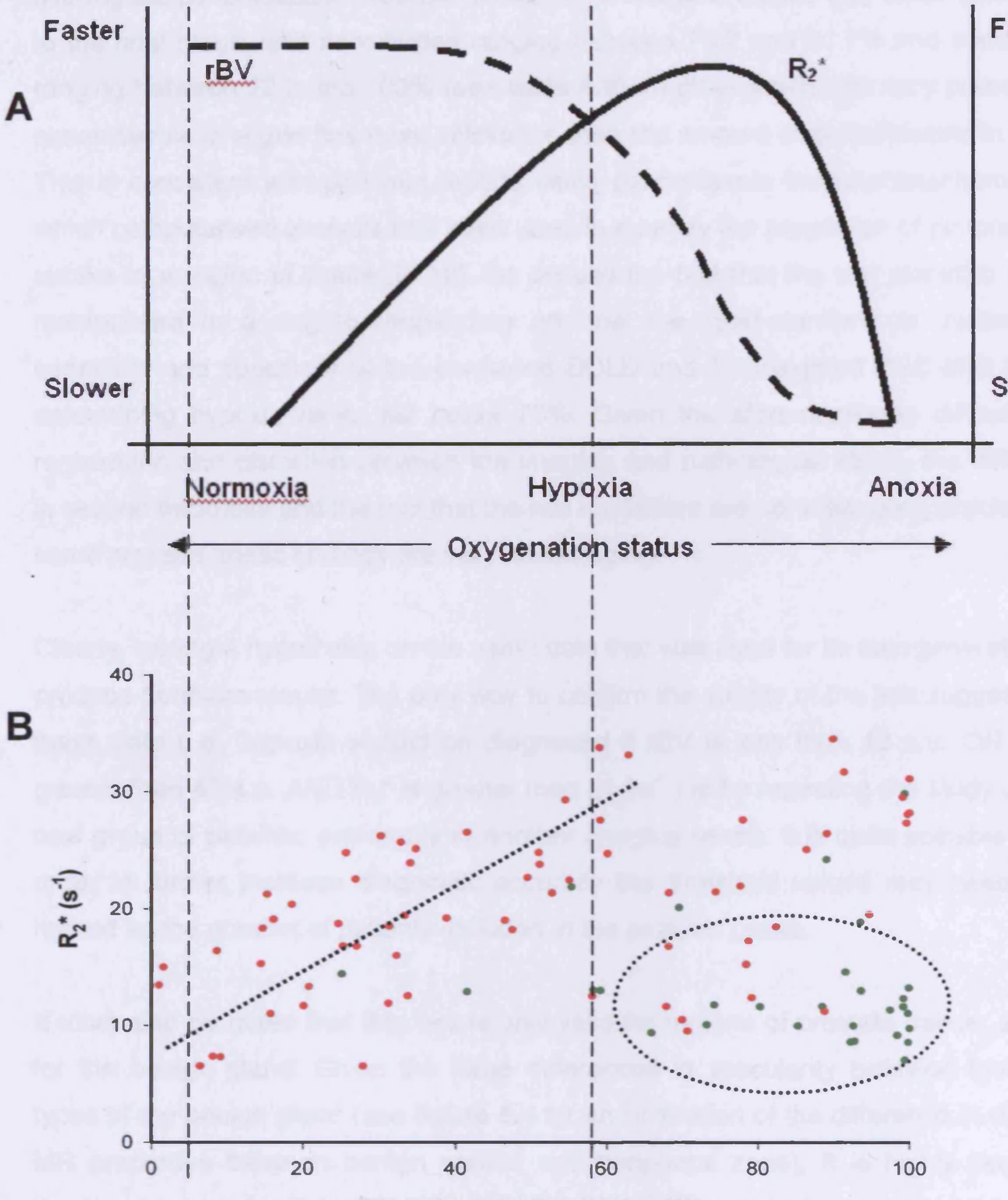

(**A**) Oxygenation status determination with BOLD-MRI images requires blood volume information. This graph depicts the theoretical change in BOLDMRI signal (R_2^*) that would be expected as tissue oxygenation reduces. To correctly interpret R_2^* images to infer oxygenation status, it is necessary to know whether blood is being delivered to the tissues. With the absence of red blood cell delivery, R_2^* levels fall despite the presence of hypoxia. (**B**) Data from the current study confirms that in the presence of high blood volume (red circles), R_2^* correlates with oxygenation. For data points that represent tumour grids with low blood volume (green circles) R_2^* becomes slower and the correlation is lost.

However, as shown in **table 5.8**, although varying the pimonidazole threshold between 20, 30 and 40% causes some change to the sensitivity and specificity of R_2^* (when used without rBV), it does not change the R_2^* threshold, which remains at $21.3s^{-1}$. Reducing the pimonidazole threshold to 10% does alter the R_2^* cut-off to $16.8s^{-1}$.

Calculation of the final test statistics for the combination of R_2* and rBV shows that altering the pimonidazole threshold between 10 and 50% makes only small differences to the final result, with sensitivities ranging between 70.2 and 81.7% and specificities ranging between 72.2 and 100% (see **table 5.9**). In other words, the very presence of pimonidazole in a grid has more relevance than the amount of pimonidazole in a grid. This is consistent with previous reports using pimonidazole immunohistochemistry in which computerised analysis has been used to quantify the proportion of pimonidazole uptake in a region of tissue [9, 10]. So despite the fact that the test statistics can be manipulated to a degree, depending on how the 'gold-standard' is defined, the sensitivity and specificity of the combined BOLD and T_2*-weighted DSC-MRI test for determining hypoxia never fall below 70%. Given the aforementioned difficulties of registration and distortion between the imaging and pathological slices, the difference in section thickness and the fact that the two modalities are not measuring precisely the same process, these findings are very encouraging.

Clearly, testing a hypothesis on the same data that was used for its own generation will produce optimum results. The only way to confirm the validity of the test suggested by these data (i.e. 'hypoxia should be diagnosed if rBV is less than 42 a.u. *OR* rBV is greater than 42 a.u. *AND* R_2* is greater than $21.3s^{-1}$') is by repeating the study using a new group of patients, preferably at another imaging centre. It is quite possible that in order to further increase diagnostic accuracy the threshold values may need to be refined as the number of patients included in the analysis grows.

It must also be noted that this test is only valid for regions of prostate cancer and not for the benign gland. Given the large differences in vascularity between the tissue types of the benign gland (see **figure 5.4** for an illustration of the difference in dynamic MR properties between benign central and peripheral zone), it is highly likely that threshold values for R_2* and rBV would be different for each tissue type. As a result, this method of hypoxia detection can only ever be as good as the ability of MRI to locate tumour. As described in **chapter 2**, with the inclusion of T_1-weighted dynamic MRI, MRS and diffusion weighted imaging, sensitivities and specificities for tumour localisation in excess of 90% have been demonstrated. Future strategies for anatomical and *biological* staging of prostate cancer are therefore likely to include a multi-parameter functional MRI protocol combining several or all of the functional imaging technologies.

Repeatability

The repeatability statistic indicates that for the prostate cancer in an individual patient a change in R_2* of greater or less than 12.9% would be considered statistically significant at the 95% confidence level. In absolute terms a change in R_2* for an individual prostate tumour of $1.95s^{-1}$ in either direction can be considered real and not simply a result of test variability. Considered in conjunction with an ICC of 99% and wCV of 0.047, these results suggest that BOLD MRI is a highly repeatable test for human prostate cancer, reflecting the results of the animal data presented in the previous chapter. It is true to say that the repeatability statistic is only valid in experiments where patient set-up and machine factors are stable. In situations where the patient needs to be moved between measurements or when imaging occurs on different days reproducibility is likely to reduce. Despite this, BOLD-MRI is a technique with sufficient repeatability to be useful in the assessment of changes to the R_2* parameter human prostate cancer over short periods of time.

Carbogen

Chapter 4 described how BOLD-MRI could be used to detect changes in the oxygenation of prostate tumour xenografts as a result of carbogen breathing. In the DU145 animal tumour model an average reduction in R_2* of $3.52s^{-1}$ was demonstrated, representing a 9.8% change from baseline. The human study demonstrated a greater effect, coincidentally also with an average reduction of $3.52s^{-1}$, representing a 21.6% change from baseline in the malignant prostate regions. Nine out of the 14 patients who received carbogen and had detectable tumour at prostatectomy showed a significant decrease in R_2* during carbogen exposure.

There was minimal change in R_2* in the benign central or peripheral prostate zones. For the peripheral zone, four of the 16 patients had a significant reduction in R_2* following carbogen exposure and in the benign central gland only one patient showed a significant response. As shown in the previous chapter, it would appear that the most hypoxic regions respond most to an increase in the inspired oxygen concentration. As depicted in **figures 5.3** the benign prostate tissue is generally less hypoxic than tumour and should therefore demonstrate less of a reduction in R_2*. The failure to demonstrate any response in the benign peripheral gland is most likely to represent a failure of the test itself. **Figure 5.4** shows that the peripheral zone has generally low blood volume compared to benign central zone or prostate tumour. This study has already demonstrated the critical dependence of R_2* on blood volume. Therefore, it may follow that the benign peripheral gland simply has insufficient vascular supply for the BOLD effect to arise.

It should be noted that a previous study by Taylor *et al.* reports more consistent BOLD changes in the benign gland [11]. 13 men with normal prostate glands (four normal volunteers and nine patients with tumours elsewhere in the body) were imaged before and during carbogen gas exposure. Whole prostate measurements were made with no attempt to distinguish between central and peripheral zones. Analysable data were obtained from nine of the patients. There was no significant MR signal intensity change in four patients, and a significant change in five (mean 11.4%, range 8.4–14.0%). Because of the small numbers involved it is not possible to determine whether these results conflict with the current study. Furthermore, since only whole prostate measurements were made, the variation in response between patients may simply reflect the different proportions of benign central gland and benign peripheral gland in each prostate.

Carbogen gas, usually administered with nicotinamide, has radiosensitising properties (see **chapter 1**). It has been used with success in improving the local control rates of radical radiotherapy for squamous cell carcinoma of the head and neck (ARCON) [12]. This study provides *in-vivo* human evidence for an oxygen enhancing effect of carbogen breathing in prostate cancer. The tolerability of carbogen and nicotinamide when given in conjunction with pelvic radiotherapy has already been demonstrated in schedules such as BCON for bladder cancer and in radical radiotherapy for cervix cancer [13]. As a result a pilot study using an ARCON-like radiotherapy schedule is justifiable and supported by the data presented in this thesis.

5.7 Conclusion

The data presented in this chapter demonstrates that real-time non-invasive hypoxia detection in human prostate cancer, using magnetic resonance imaging, is a realistic prospect. The BOLD technique is fast and reproducible adding only a few minutes to a standard diagnostic prostate staging protocol. The experiment has confirmed the importance of combining blood volume information with an R_2^* study. The test proposed by this study requires further validation with at least one new data set using different patients and refinements of R_2^* and rBV thresholds are likely. Once this process is complete, modern MR analysis software could be adapted to combine the BOLD and DSC parametric maps with the relevant thresholds for hypoxia detection and fuse the resulting 'hypoxia map' with sequences devised for tumour localisation.

However, the major limitation that would prevent the immediate clinical implementation of this technique is the limited volume of the prostate that can be imaged with DSC-MRI during each session. With the current limits of technology, T_2^*-weighted dynamic imaging using a gradient echo protocol can image two, eight millimetre thick, slices at the very most. This is not sufficient to visualise an entire prostate gland. Because of the amount of gadolinium contrast required for each examination and the increasing awareness of complications resulting from exposure to high volumes of contrast (such as nephrogenic systemic fibrosis), it is not possible to simply repeat the examination until the whole gland has been imaged. Using echo-planar imaging sequences multiple slices can be generated, although susceptibility artefact can be much worse. Therefore, given these technical constraints, blood volume maps can only be generated for limited portions of each patient's prostate gland.

As previously described, these functional imaging methods are only valid for tumour regions, necessitating accurate tumour localisation in the first place. Therefore, one solution may simply be to image the regions of the prostate that contain tumour. This is not entirely satisfactory given the scattered nature of prostate cancer and the fact that patients may have large volume disease that encases much of their peripheral gland. An alternative approach may be to use other methods to obtain blood volume information. The DCE-MRI parameter K^{trans} is well known to reflect blood flow (and therefore blood volume) information as well as representing vascular permeability and surface area. Further scrutiny of the data presented in this chapter and of other similar studies may confirm whether K^{trans} is a valid substitute for rBV. Other than the fact that multi-slice acquisition is easily obtained with DCE-MRI, there are other advantages. The technique is more reproducible, uses less intravenous contrast and tumour localisation is good (**figure 5.5**). Also, there is a greater experience with DSC-MRI and some commercially available software applications can already generate K^{trans} maps without the need for laborious post-processing.

This experiment has dealt solely with prostate cancer, however there is no reason suggest that the technique would not also apply to other tumour types. In fact many other solid malignancies form larger tumours that are not interspersed with benign tissues making them potentially more suitable for assessment in this way. A similar process of validation would be required, necessitating a comparison between imaging and pathology. This may be difficult for certain tumour types where it is uncommon to remove the tumour in its entirety, such as brain tumours, or in regions that may be difficult to orientate in three dimensions once the tumour has been removed from the body, such as lung or oesophago-gastric malignancies. Despite this, many tumours such as cervix, breast or head and neck, would appear to be ideal candidates for investigation.

References

1 Powell ME, Collingridge DR, Saunders MI, *et al.* Improvement in human tumour oxygenation with carbogen of varying carbon dioxide concentrations. *Radiother Oncol* 1999;50:167-171.

2 Parker C, Milosevic M, Toi A, *et al.* Polarographic electrode study of tumor oxygenation in clinically localized prostate cancer. *Int J Radiat Oncol Biol Phys* 2004;58:750-757.

3 Movsas B, Chapman JD, Horwitz EM, *et al.* Hypoxic regions exist in human prostate carcinoma. *Urology* 1999;53:11-18.

4 Engelbrecht MR, Huisman HJ, Laheij RJ, *et al.* Discrimination of prostate cancer from normal peripheral zone and central gland tissue by using dynamic contrast-enhanced MR imaging. *Radiology* 2003;229:248-254.

5 Futterer JJ, Heijmink SW, Scheenen TW, *et al.* Prostate Cancer Localization with Dynamic Contrast-enhanced MR Imaging and Proton MR Spectroscopic Imaging. *Radiology* 2006.

6 Padhani AR, Harvey CJ, Cosgrove DO. Angiogenesis imaging in the management of prostate cancer. *Nat Clin Pract Urol* 2005;2:596-607.

7 Diergarten T, Martirosian P, Kottke R, *et al.* Functional characterization of prostate cancer by integrated magnetic resonance imaging and oxygenation changes during carbogen breathing. *Invest Radiol* 2005;40:102-109.

8 Hoskin PJ, Carnell DM, Taylor NJ, *et al.* Hypoxia in prostate cancer: correlation of BOLD-MRI with pimonidazole immunohistochemistry-initial observations. *Int J Radiat Oncol Biol Phys* 2007;68:1065-1071.

9 Raleigh JA, Calkins-Adams DP, Rinker LH, *et al.* Hypoxia and vascular endothelial growth factor expression in human squamous cell carcinomas using pimonidazole as a hypoxia marker. *Cancer Res* 1998;58:3765-3768.

10 Varia MA, Calkins-Adams DP, Rinker LH, *et al.* Pimonidazole: a novel hypoxia marker for complementary study of tumor hypoxia and cell proliferation in cervical carcinoma. *Gynecol Oncol* 1998;71:270-277.

11 Taylor NJ, Baddeley H, Goodchild KA, *et al.* BOLD MRI of human tumor oxygenation during carbogen breathing. *J Magn Reson Imaging* 2001;14:156-163.

12 Kaanders JH, Pop LA, Marres HA, *et al.* ARCON: experience in 215 patients with advanced head-and-neck cancer. *Int J Radiat Oncol Biol Phys* 2002;52:769-778.

13 Nordsmark M, Loncaster J, Aquino-Parsons C, *et al.* The prognostic value of pimonidazole and tumour pO2 in human cervix carcinomas after radiation therapy: a prospective international multi-center study. *Radiother Oncol* 2006;80:123-131.

Chapter 6

The effect of androgen deprivation on the volume, vascular kinetics and oxygenation of the prostate gland and prostate tumour, as measured by functional Magnetic Resonance Imaging

6.1 Aims

To assess the changes in vascular permeability, blood flow, blood volume and oxygenation in benign and malignant prostate tissue during a three month period of androgen deprivation, using functional MRI methods.

6.2 Introduction

This chapter contains details of experiments performed to determine whether androgen deprivation causes changes in the vascular kinetics and oxygenation of prostate cancer. DCE-MRI, DSC-MRI, BOLD MRI and Diffusion weighted imaging parameters were used to evaluate patients during a three-month course of androgen deprivation.

6.3 Patients and Methods

6.3.1 Patients, Treatment and Examination Schedule

Between January and October 2005, 20 patients with prostate cancer (age 57-78, Gleason grade 6-9, PSA 3.7-34.0 ng/ml) that were due to be treated with neo-adjuvant androgen deprivation prior to radical radiotherapy were recruited prospectively. The histologic diagnosis of prostate cancer was made by core biopsy in all 20 patients. Patient demographics, tumour pathology, staging and treatment details are shown in **table 6.1**. Inclusion criteria were: (1) Histologically-proven primary prostate carcinoma, (2) Intention to commence at least three months of androgen deprivation therapy (3) Ability to give written informed consent and (4) Age over 18 years. Exclusion criteria were: (1) Contra-indication to MRI, (2) Known allergy to gadopentetate dimeglumine (Gd-DTPA) and (3) Prior exposure to androgen deprivation.

Table 6.1 Androgen Deprivation – MRI Study population

Patient No.	Age	Clinical Stage (TNM)	MRI Stage (TNM)	PSA (ng/ml)	Total Gleason Score	Gleason Grade	Treatment Received
1	78	T1c N0 M0	2c N0 M0	10.9	6	3 + 3	Iodine Seed Brachytherapy
2	73	T1c N0 M0	2c N0 M0	29.8	7	4 + 3	External Beam Radiotherapy
3	67	T2b N0 M0	T3a N0 M0	22.5	7	3 + 4	External Beam Radiotherapy
4	66	T3 N0 M0	3b N0 M0	8.7	6	3 + 3	High Dose Rate Brachytherapy
5	62	T1c N0 M0	3a N0 M0	12.1	7	3 + 4	External Beam Radiotherapy
6	73	T1b N0 M0	1b N0 M0	34	7	4 + 3	External Beam Radiotherapy
7	66	T2c N0 M0	T2c N0 M0	30	8	4 + 4	Androgen Deprivation Alone
8	66	T2c N0 M0	T2c N0 M0	8.4	8	4 + 4	External Beam Radiotherapy
9	72	T2a N0 M0	T2b N0 M0	26	7	3 + 4	External Beam Radiotherapy
10	62	T1c N0 M0	T2c N0 M0	15	7	3 + 4	External Beam Radiotherapy
11	59	T1c N0 M0	T2a N0 M0	13.8	7	3 + 4	External Beam Radiotherapy
12	67	T1c N0 M0	T1c N0 M0	7.7	6	3 + 3	External Beam Radiotherapy
13	68	T1c N0 M0	T3a N0 M0	7.9	6	3 + 3	External Beam Radiotherapy
14	57	T2a N0 M0	T2a N0 M0	5.7	7	3 + 4	External Beam Radiotherapy
15	75	T1c N0 M0	T3a N0 M0	15.2	7	4 + 3	External Beam Radiotherapy
16	61	T2a N0 M0	T3a N0 M0	3.7	7	Not specified	High Dose Rate Brachytherapy
17	78	T2 N0 M0	T3b N0 M0	17.7	6	3 + 3	External Beam Radiotherapy plus HDR Brachytherapy boost
18	70	T2b N0 M0	T3a N0 M0	9.9	9	5 + 4	External Beam Radiotherapy
19	67	T1c N0 M0	T3b N2 M1	6.26	9	5 + 4	Androgen Deprivation Alone
20	65	T1c N0 M0	T3a N0 M0	11.3	7	3 + 4	External Beam Radiotherapy plus HDR Brachytherapy boost

Each patient was examined with five multi-parameter MRI scans. Two prior to the commencement of androgen suppression to define the baseline values and assess reproducibility, one after a month of hormone treatment and two further scans after three months of therapy, to measure the lasting effect of androgen deprivation and to reassess reproducibility whilst on hormones. The examination schedule is depicted in **figure 6.1**.

After completing the two baseline scans, patients were commenced on androgen deprivation therapy. This consisted of two drugs:

1. Bicalutamide (Casodex®, AstraZeneca) 50mg daily for 28 days
2. Goserelin (Zoladex® LA, AstraZeneca) 10.8mg subcutaneous injection given after 14 days of bicalutamide therapy, repeated every 12 weeks until completion of the androgen deprivation treatment period.

Gonadorelin analogues reduce serum testosterone to castrate levels by the depression of lutenising hormone (LH) release from the pituitary gland. However after administration, initial stimulation of LH release occurs, which may produce a theoretical risk of 'tumour flare' caused by the transient rise in testosterone production. In susceptible patients this may cause urinary retention. Bicalutamide, a pure non-steroidal anti-androgen, was administered during the initial stages of gonadorelin analogue therapy to reduce this risk.

Each patient was to receive at least three months of androgen deprivation therapy alone, before proceeding to any further local or systemic treatment for prostate cancer. Androgen deprivation was continued according to the clinical oncologist's discretion. The duration of treatment ranged from six months to lifelong depending on the patient's individual circumstances. In each case, whatever the treatment duration, the study period was the first three months of androgen deprivation. 18 patients subsequently received radical radiotherapy, either in the form of external beam treatment or brachytherapy. Two patients continued on long-term androgen deprivation therapy without radical treatment (one because of personal preference and the other due to the subsequent discovery of iliac and para-aortic lymph node involvement).

This cohort of 20 patients comprised the same group as that studied for the reproducibility analysis. The paired reproducibility scans (1 and 2 for baseline and 4 and 5 for three months) were combined for the purpose of assessment of change

Figure 6.1 MRI schedule for the androgen deprivation study

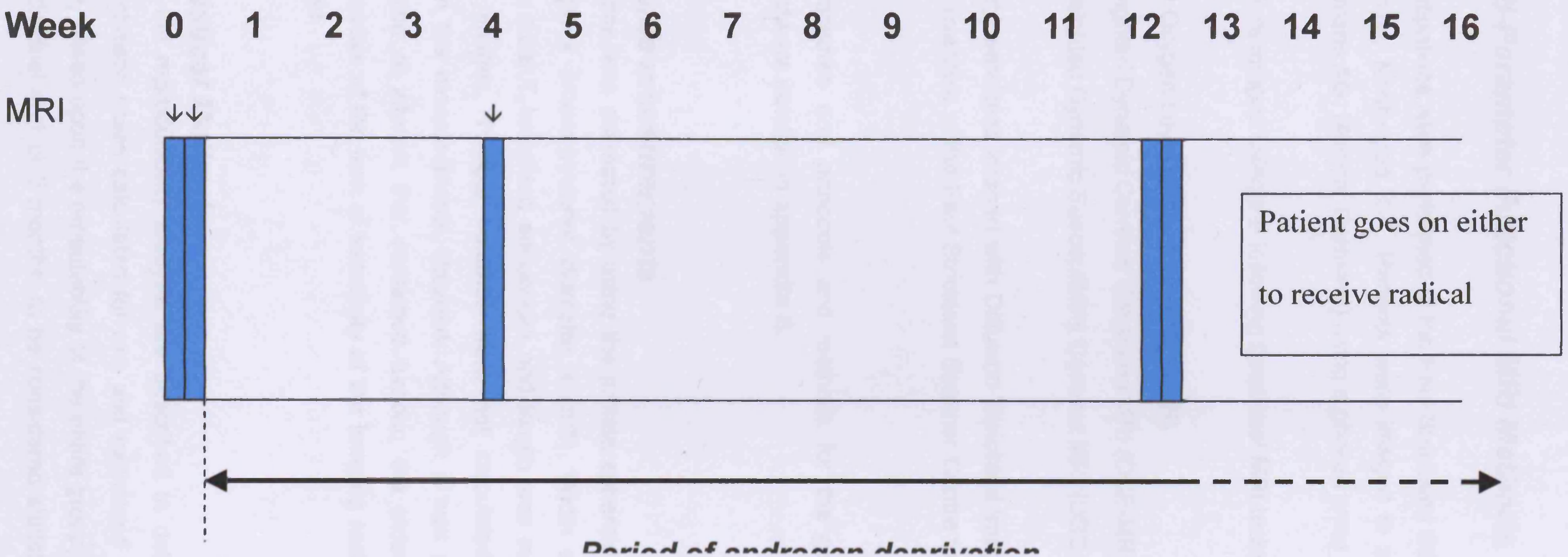

Scans 1 & 2 are performed on consecutive days, prior to the commencement of androgen deprivation therapy
Scan 3 is performed after 4 weeks of androgen deprivation therapy
Scans 4 & 5 are performed on consecutive days, after 12 weeks of androgen deprivation therapy

between baseline, one month and three months following the start of androgen withdrawal.

6.3.2 Multi-Parameter Functional MRI Methods

All MRI investigations were performed at the Paul Strickland Scanner Centre at Mount Vernon Hospital, Northwood, UK. Patients were imaged in a Symphony 1.5T MRI scanner (Siemens AG, Munich, Germany) using a phased array pelvic coil.

All patients were imaged using the following functional MRI techniques:

- Blood Oxygen Level Dependent (BOLD) MRI
- T_1-weighted Dynamic Contrast Enhanced MRI (DCE-MRI)
- T_2^*-weighted Dynamic Susceptibility Contrast MRI (DSC-MRI)

Seven patients were also imaged with Diffusion Weighted Imaging (DWI). This facility only became available at the Paul Strickland Scanner Centre towards the latter stages of this study.

The MRI procedure and protocols and methods for the generation of functional parametric data are detailed in **appendix B**.

6.3.3 Volume measurements

Prostate volume was estimated by using the prolate spheroid formula [1]: volume = width x length x antero-posterior diameter x ($\pi/6$). Width and AP diameter was measured on axial T_2-weighted sequences and length was measured using coronal and sagittal images. Tumour volumes were not calculated because of lack of confidence in the measurements obtained. Although it was possible to confidently define a region of interest that contained tumour, the extent of tumour was not evaluable because of the lack of sensitivity of the imaging methods in the androgen-deprived gland.

6.3.4 Statistical Methods

Methods for the reproducibility analysis are described in detail in **chapter 3**. The repeatability statistic r was calculated for n=1 and expressed as a percentage. This gave a range, based upon the repeatability of the entire group, of change required for any given individual at 1 or 3 months, to be considered statistically significant at the

95% confidence level and not simply be due to the natural variability of that parameter. For the logarithmically transformed data, this range is asymmetrical about the mean by virtue of the fact that logarithmic data are symmetrical around 1 rather than 0 as is the case with standard decimal values. For example, the repeatability statistic for tumour K^{trans} (r) was 0.508 (n=19). Recalculated for n=1 and expressed as a percentage a range of –39.8% to +66.2% was obtained. This means that for an individual patient, a reduction of 39.8% or an increase of 66.2% in tumour K^{trans} following androgen deprivation can be considered to be due to the therapeutic intervention rather than the test variability, at the 95% confidence level.

Significance testing of parameter changes between baseline and 1 month, baseline and 3 months and between 1 and 3 months were performed using a paired student's t-test:

Baseline values were calculated as the mean of the median parameter values for scans 1 and 2 and three month values were calculated as the mean of the median parameter values for scans 4 and 5. This was performed for each parameter for each patient. In the event of missing data for one scan of the reproducibility pair, the median parameter value of the other scan was used.

The difference *d* between each pair of median parameter values was calculated for each patient. The distribution of *d* was tested for normality using the Shapiro-Wilk test. This was repeated for each time period (i.e. baseline to 1 month, baseline to 3 months and 1 to 3 months). The paired students t-test was then performed on the data sets for each parameter, each ROI and each time period. The significance of volume changes following androgen deprivation was calculated in the same way as the MRI parameter changes (see above).

In order to determine whether there was any significant correlation between volume change and change to any of the kinetic parameter values, Spearman's ρ (rho) was calculated. Spearman's ρ (rho) was also used to determine whether there was a correlation between initial parameter value and the magnitude of change of the same parameter.

6.4 Results

6.4.1 General

All 20 patients underwent the five MRI studies according to schedule. All 20 patients were imaged with BOLD and T_1-weighted DCE MRI scans at each of the five study periods (resulting in 100 BOLD and 100 T_1-weighted DCE MRI scans available for analysis). Due to operator error, one patient did not receive a T_2*-weighted imaging sequence during his second scan (leaving 99 T_2*-weighted DSC-MRI images available for analysis). Seven patients were imaged with DWI at each study visit (35 diffusion images available for analysis). No adverse events occurred during the running of the study. The median time between the first two scans and the last two scans was 2 days and 1.5 days respectively. The median time between starting androgen deprivation and the third scan was 29.5 days and was 91.5 days for the fourth scan (scheduling details are given in **table 6.2**).

One patient moved excessively (several centimetres) during the T_1 dynamic experiment of his first scan resulting in no data being available from this study. For this patient the baseline T_1 values are therefore derived from one scan rather than two. Similarly, for the T_2* analysis, no data was acquired during the second scan of one patient because of operator error, therefore the baseline rBV and rBF parameter values are also only derived from one scan for this subject. Due to the variation in the pattern of malignant infiltration between patients, tumour was not visible on every slice for each scan, therefore for some scans 'tumour' values may represent only one or two slices through the prostate. One patient had no tumour visible on any scan, despite positive histology on prostate biopsy, reducing the number of patients evaluable for tumour ROI changes to 19. As expected, with the decrease in peripheral zone signal intensity and the resulting reduction in contrast between benign peripheral zone and tumour on T_2-weighted sequences following androgen deprivation, areas of malignancy became harder to define. In these instances, ROIs were manually copied from the corresponding slice of the pre-treatment scan. Occasionally this was not possible due to poor morphological definition and in these cases only definite areas of tumour were outlined. Out of the 120 scan slices at baseline, 60 slices at one month and 120 slices at three months 112, 55 and 106 tumour ROIs were delineated respectively. For the T_2* parameters, it was not possible to obtain tumour ROI values from scan two of one patient and scan five of another, therefore the baseline data of the first patient and the three month data of the second is calculated from one scan only. As for the T_1 data, one patient had no discernable tumour leaving a total of 19 patients for tumour ROI analysis.

Table 6.2 Schedule information

	Median (Mean) / days	Range / days
Number of days between scan 1 and scan 2	2 (2.75)	1 - 8
Number of days between start of AD and scan 3	29.5 (30.65)	26 - 41
Number of days between start of AD and scan 4	91.5 (92)	82 - 105
Number of days between scan 4 and scan 5	1.5 (2.55)	1 - 14

AD Androgen deprivation

In one instance no normal peripheral zone could be identified because of widespread malignant involvement and one patient had a large homogenous nodular structure occupying much of the central and peripheral gland making delineation of normal peripheral zone and benign central gland impossible. One patient had no normal central zone because of prior trans-urethral resection. This reduced the number of evaluable patients for peripheral and central gland analysis to 18.

6.4.2 Volume Changes (Table 6.3, Figure 6.2)

As expected, androgen deprivation caused shrinkage of the prostate gland. At one month the whole prostate had reduced in volume by an average of 4 mls (9.3%) and by an average of 14.4 mls (34.5%) at 3 months. Volume reduction was statistically significant at each time point. Volume change did not correlate with MRI parameter changes **(table 6.4)** indicating that the functional imaging measurements are likely to be evaluating physiological processes that are independent of volume.

Table 6.3 **Summary of changes in prostate volume caused by androgen deprivation at 1 and 3 months**

Mean Value (ml)	Mean Value (ml)	Mean Value (ml)	Mean Difference (% change) (ml)	Two-sided p-value	Mean Difference (% change) (ml)	Two-sided p-value	Mean Difference (% change) (ml)	Two-sided p-value
baseline	1 month	3 months	baseline – 1 month	baseline – 1 month	baseline – 3 months	baseline – 3 months	1 month – 3 months	1 month – 3 months
42.4	38.3	28.0	4.0 (9.3%)	< 0.0001	14.4 (34.5%)	< 0.0001	10.3 (28.2%)	< 0.0001

p-values in green signify statistically significant results at the 95% confidence level

Figure 6.2 **Prostate Volume Changes**

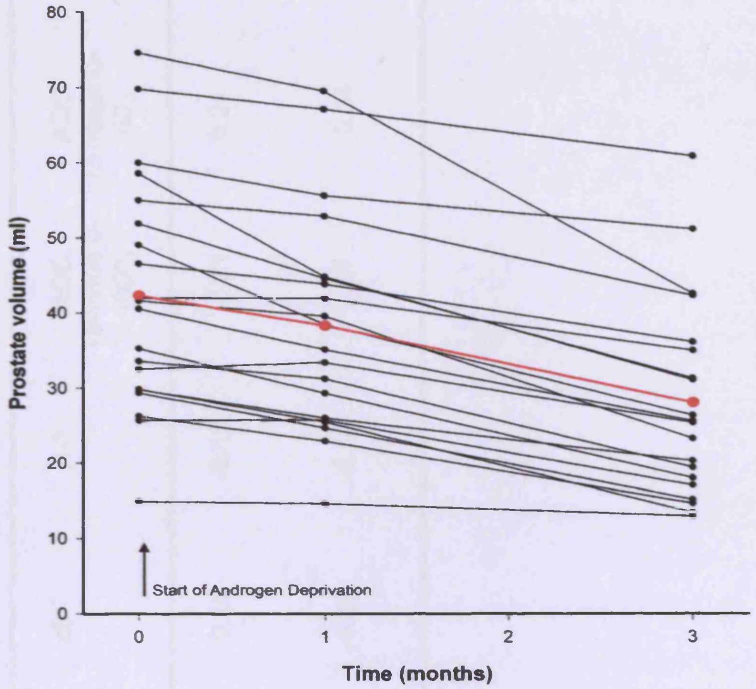

The mean values are shown in red

6.4.3 T_1-weighted DCE MRI analysis
(Table 6.5, Figures 6.3-6.10)

There is a statistically significant reduction in K^{trans}, k_{ep} and AUC_{60} from baseline at both one and three months for the whole prostate, tumour and peripheral zone ROIs. The overall reductions for whole prostate, tumour, peripheral zone and central zones are: K^{trans}, 28.9% ($p = 0.0005$), 52.4% ($p < 0.0001$), 45.3% ($p = 0.0023$) and 18.3% ($p = 0.19$) respectively; k_{ep}, 36.2% ($p < 0.0001$), 54.2% ($p < 0.0001$), 52.9% ($p = 0.0002$) and 38.2% ($p = 0.0002$) respectively; AUC_{60}, 31.2% ($p = 0.0003$), 48.8% ($p < 0.0001$), 34.0% ($p = 0.0102$) and 7.7% ($p = 0.55$) respectively. For V_e the overall increases were 13.7% ($p = 0.0752$), 10.0% ($p = 0.26$), 20.6% ($p = 0.106$) and 30.0% ($p = 0.0233$) respectively. The rate of change is greatest during the first month, as illustrated in **figure 6.4**, although for whole prostate and tumour K^{trans} and AUC, the change that occurs between one and three months continues to be significant.

Based on the reproducibility statistics described in the **chapter 3 (table 3.1)**, the proportion of individual patients that achieved a significant change in parameter values after three months of androgen deprivation for whole prostate and tumour measurements respectively was: 50% and 68% for K^{trans}, 50% and 53% for V_e, 75% and 84% for k_{ep}, and 35% and 56% for AUC.

Table 6.4 Correlation between volume changes and MRI parameter changes

All values quoted are the Spearman's Rank Correlation Coefficient ρ (rho)

Time-point	ROI	K^{trans}	V_e	k_{ep}	AUC_{60}	rBV	rBF	R_2^*	ADC (b-value 0-1000)	ADC (b-value 0-50)	ADC (b-value 150-1000)
Baseline – 1 month	Whole Prostate	0.17	-0.26	0.36	0.25	-0.13	-0.16	-0.15	-0.21	0.21	-0.25
Baseline – 3 months	Whole Prostate	0.06	-0.16	0.39	0.11	-0.22	-0.25	-0.12	0.07	-0.54	-0.14

All values for ρ (rho) were not statistically significant results at the 95% confidence level

6.4.4 T_2-weighted DSC-MRI analysis*

(Table 6.6, Figures 6.11-6.14)

Blood volume and flow parameter changes proved to be even more striking, with tumour values decreasing by 83% and 79% respectively in the first month **(figures 6.11 and 6.13)**. Reductions in both rBV and rBF for whole prostate, tumour and peripheral gland were complete by one month, with no significant reduction occurring between one and three months. Only central gland volume and flow parameter changes occurred more slowly, with no significant change in either parameter by one month but a reduction of 56% and 57% respectively by three months ($p = 0.007$ and $p = 0.0024$ respectively). 14 out of the 19 evaluable patients demonstrated an individually significant change in tumour rBV at one month.

6.4.5 BOLD MRI analysis

(Table 6.7, Figures 6.15-6.17)

By three months significant increases in R_2^* had occurred for all ROIs, most notably for tumour, with a rise of 41.1% ($p < 0.0001$). The tumour ROI was the only region to demonstrate a significant change by one month (15.8%, $p = 0.0064$), with the other areas changing more slowly. Due to the relatively high variability in the R_2^* measurement compared to the degree of change in R_2^* caused by androgen deprivation, the highly significant changes seen for the group did not translate into high proportions of individual patients with confirmed significant R_2^* increase, at the 95% confidence level (1 out of 20 for whole prostate and 4 out of 19 for tumour).

6.4.6 DWI analysis

(Table 6.8, Figures 6.18-6.23)

Due to small patient numbers, changes in diffusion ADC values were generally non-significant. The only exceptions to this were a 14% reduction in whole prostate overall ADC at three months ($p = 0.0288$) and a 29% reduction in peripheral zone ADC between one and three months ($p = 0.0358$). The trend for overall ADC (b-values of 0 - 1000 s/mm^2) was for an increase between baseline and one month and then a decrease between one and three months, with the final ADC measurement being lower than the starting value. The trend pattern for 'late' ADC values (b-values of 150 - 1000 s/mm^2) was similar. The 'early', flow-dependent, ADC measurment (b-values of 0 - 50 s/mm^2), showed a mixed trend with initial decreases for whole prostate and tumour and initial increases for peripheral and central gland ROIs. By three months only the tumour values remained higher than their value at baseline.

Table 6.5 **Summary of changes in MRI parameters caused by androgen deprivation at 1 and 3 months – T1-weighted DCE MRI Parameters**

Para-meter	ROI	Mean Value baseline	Mean Value 1 month	Mean Value 3 months	Mean Difference (% change) baseline – 1 month	Two-sided p-value baseline–1 month	Mean Difference (% change) baseline – 3 months	Two-sided p-value baseline–3 months	Mean Difference (% change) 1 month – 3 months	Two-sided p-value 1 month – 3 months	Proportion of patients with individually significant change at 1 month	Proportion of patients with individually significant change at 3 months
K^{trans} min^{-1}	Whole Prostate	0.206	0.170	0.146	-0.035 (-17.1)	0.0138	-0.059 (-28.9)	0.0005	-0.024 (-14.2)	0.0265	7 out of 20	10 out of 20
	Tumour	0.273	0.164	0.130	-0.109 (-39.8)	0.0011	-0.143 (-52.4)	< 0.0001	-0.034 (-20.9)	0.0056	9 out of 19	13 out of 19
	Peripheral Zone	0.126	0.082	0.069	-0.044 (-35.0)	0.0042	-0.057 (-45.3)	0.0023	-0.013 (-15.8)	0.1024	3 out of 18	4 out of 18
	Central Zone	0.253	0.200	0.206	-0.052 (-20.7)	0.0655	-0.046 (-18.3)	0.1938	0.006 (3.0)	0.7956	3 out of 18	8 out of 18
Ve x100%	Whole Prostate	0.416	0.494	0.473	0.078 (18.8)	0.0014	0.057 (13.7)	0.0752	-0.021 (-4.3)	0.3815	7 out of 20	10 out of 20
	Tumour	0.412	0.461	0.453	0.050 (12.1)	0.1185	0.041 (10.0)	0.2554	-0.009 (-1.9)	0.7215	6 out of 19	10 out of 19
	Peripheral Zone	0.292	0.349	0.352	0.056 (19.3)	0.0396	0.060 (20.6)	0.1055	0.004 (1.1)	0.9184	5 out of 18	10 out of 18
	Central Zone	0.326	0.388	0.422	0.063 (19.4)	0.0039	0.097 (30.0)	0.0233	0.034 (8.9)	0.3069	6 out of 18	10 out of 18
Kep min^{-1}	Whole Prostate	0.513	0.360	0.327	-0.153 (-29.8)	< 0.0001	-0.186 (-36.2)	< 0.0001	-0.033 (-9.1)	0.0786	10 out of 20	15 out of 20
	Tumour	0.680	0.368	0.311	-0.312 (-45.9)	< 0.0001	-0.369 (-54.2)	< 0.0001	-0.057 (-15.4)	0.0719	9 out of 19	16 out of 19
	Peripheral Zone	0.461	0.252	0.217	-0.209 (-45.3)	0.0001	-0.244 (-52.9)	0.0002	-0.035 (-13.9)	0.0726	2 out of 18	5 out of 18
	Central Zone	0.808	0.548	0.500	-0.260 (-32.2)	0.0015	-0.309 (-38.2)	0.0002	-0.049 (-8.8)	0.3819	8 out of 18	10 out of 18
AUC mmol.s	Whole Prostate	10.84	8.88	7.46	-1.96 (-18.1)	0.0141	-3.38 (-31.2)	0.0003	-1.43 (-16.1)	0.0173	8 out of 20	7 out of 20
	Tumour	14.23	9.09	7.28	-5.14 (-36.1)	0.0019	-6.95 (-48.8)	< 0.0001	-1.81 (-19.9)	0.007	9 out of 19	12 out of 19
	Peripheral Zone	7.32	5.50	4.84	-1.82 (-24.8)	0.0177	-2.49 (-34.0)	0.0102	-0.67 (-12.1)	0.144	3 out of 18	4 out of 18
	Central Zone	13.02	11.17	12.01	-1.84 (-14.1)	0.1528	-1.00 (-7.7)	0.5575	0.84 (7.5)	0.4938	5 out of 18	10 out of 18

p-values in green signify statistically significant results at the 95% confidence level
p-values in red signify statistically non-significant results at the 95% confidence level

Figure 6.3 Changes in K^{trans} during androgen deprivation

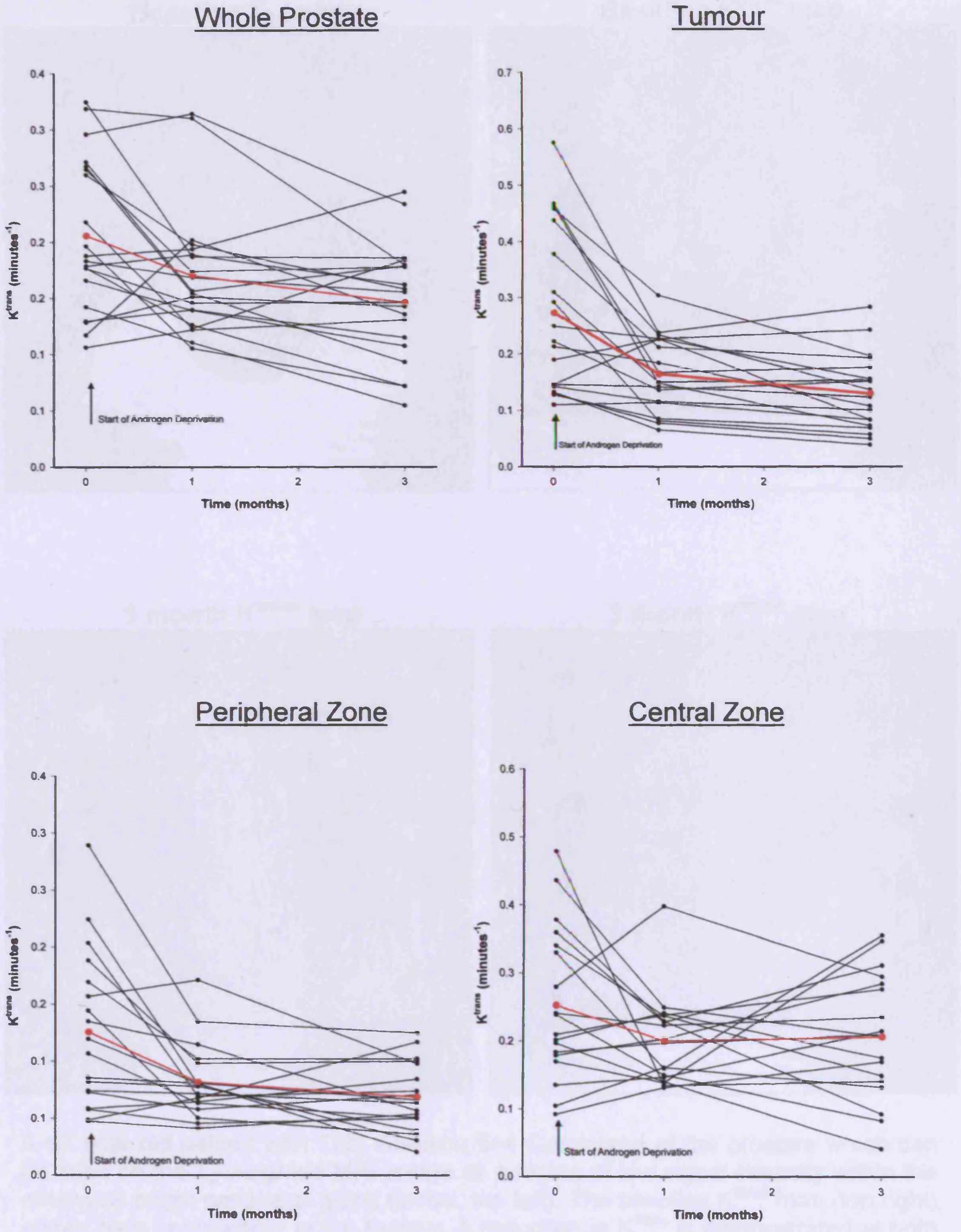

Figure 6.4 Illustration of the change in K^{trans} during 3 months of Androgen deprivation.

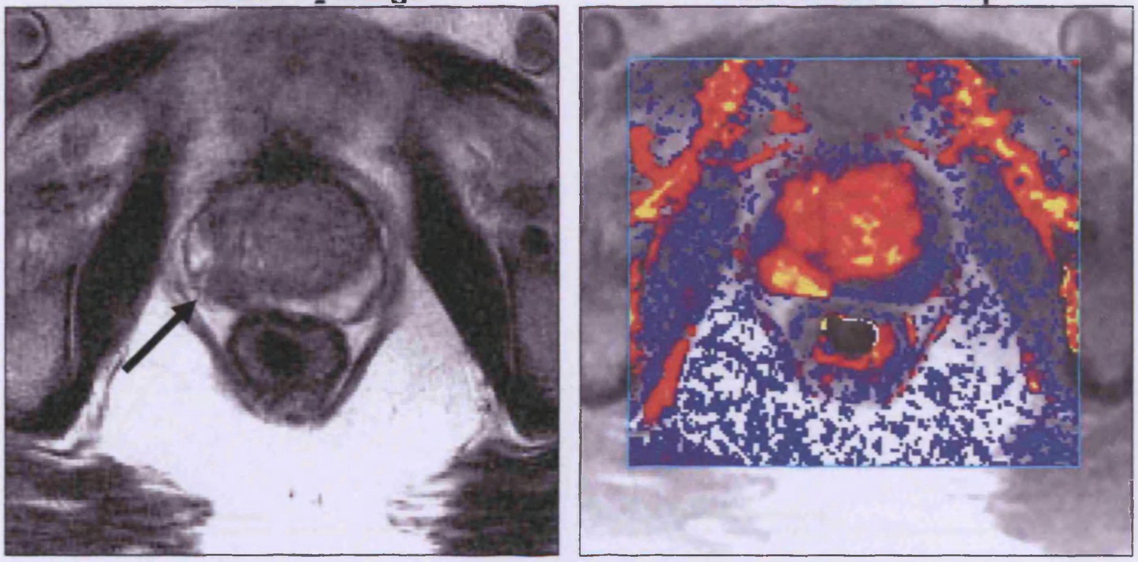
Baseline T_2 image

Baseline K^{trans} map

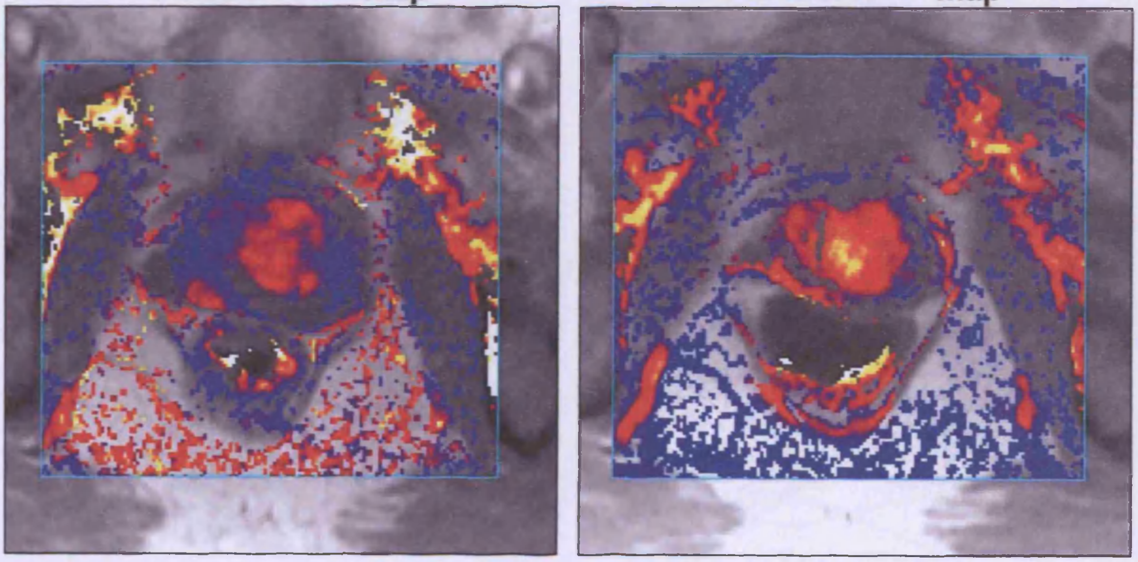
1 month K^{trans} map

3 month K^{trans} map

A 67 year old patient with T3b, Gleason 5+4 Carcinoma of the prostate which can be seen on the T_2-weighted MRI image as a region of low signal intensity within the otherwise bright peripheral gland (arrow, top left). The baseline K^{trans} map (top right) shows high permeability in the tumour. A reduction in K^{trans} is demonstrated at both one and three month following androgen deprivation (bottom images).

Figure 6.5 Changes in V_e during androgen deprivation

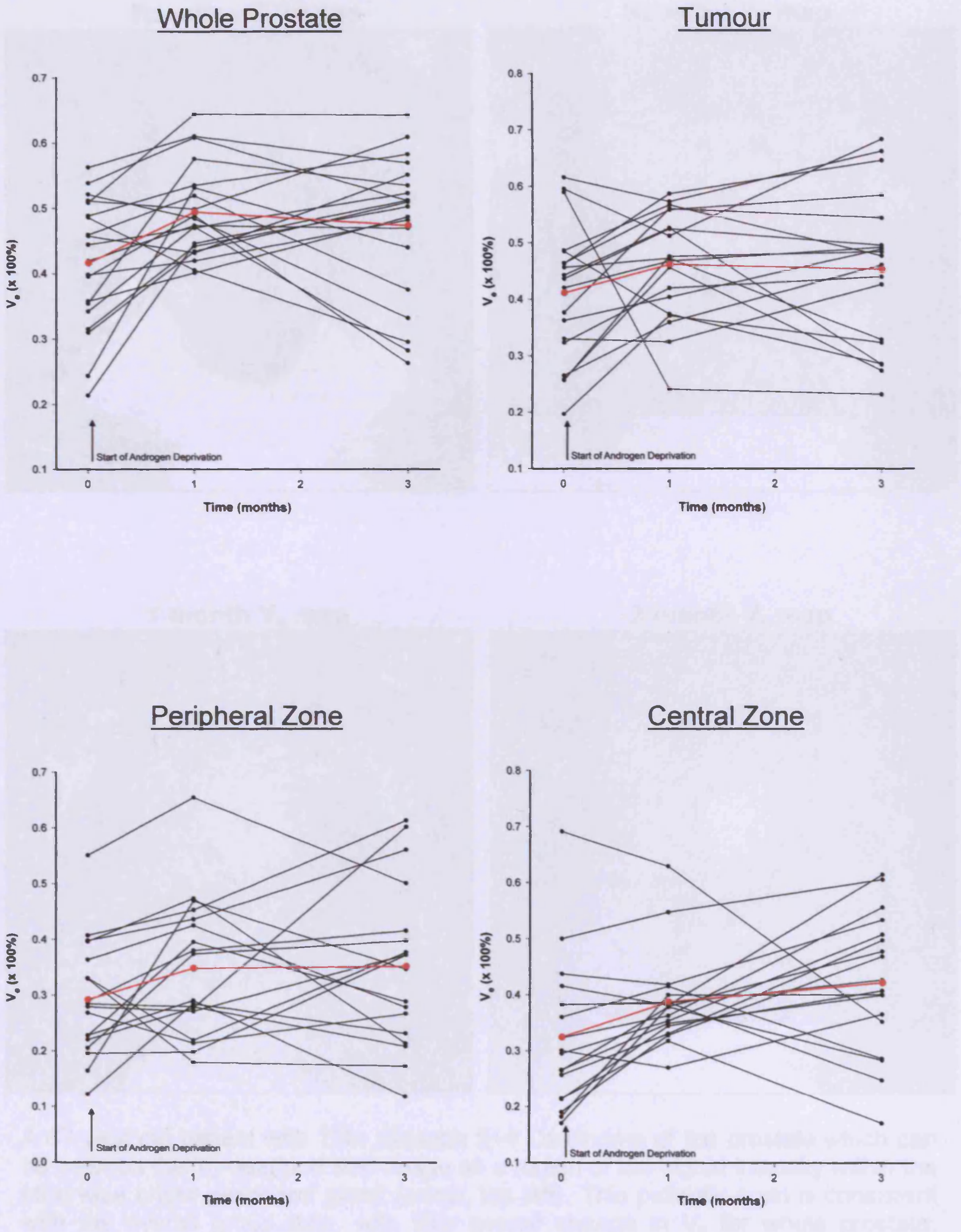

Figure 6.6 Illustration of the change in V_e during 3 months of Androgen deprivation.

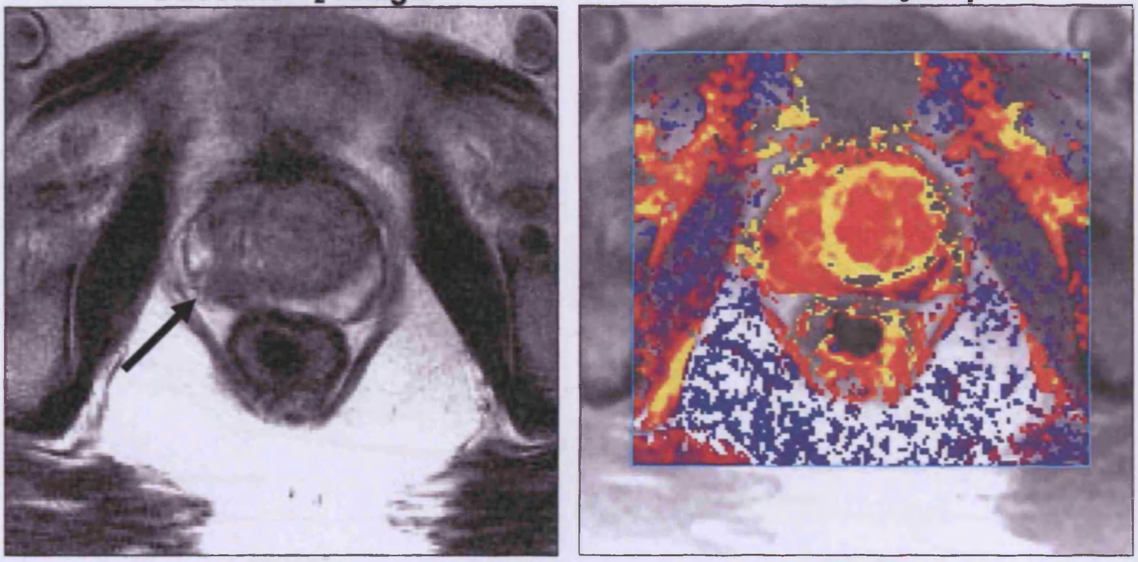

Baseline T_2 image **Baseline V_e map**

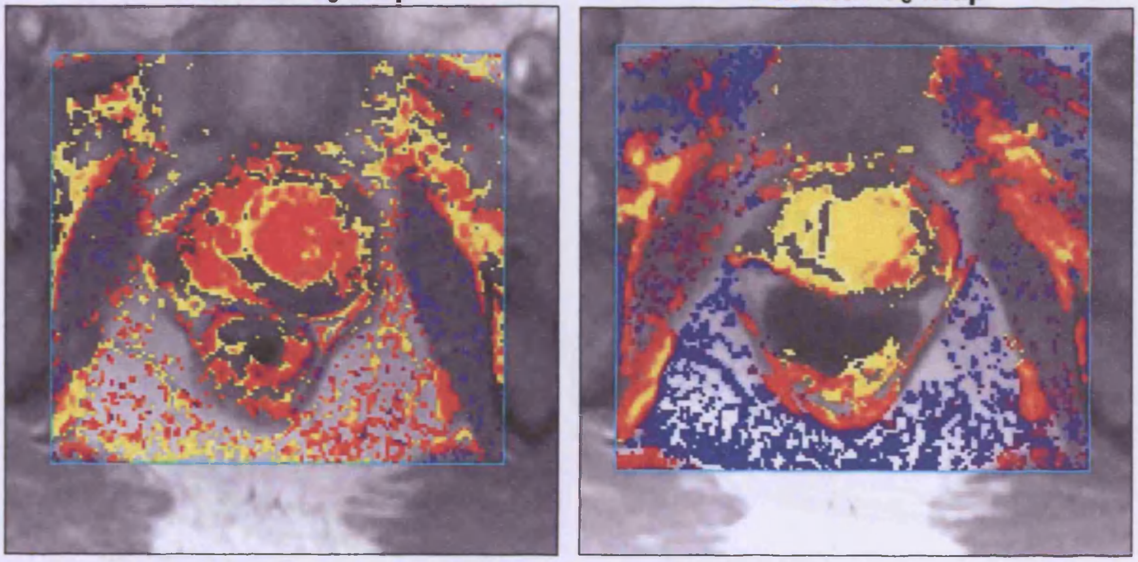

1 month V_e map **3 month V_e map**

A 67 year old patient with T3b, Gleason 5+4 Carcinoma of the prostate which can be seen on the T_2-weighted MRI image as a region of low signal intensity within the otherwise bright peripheral gland (arrow, top left). This patient's scan is consistent with the overall group data, with little overall change in V_e for whole prostate, tumour or peripheral zone but a noticeable change in central gland values after 3 months of androgen deprivation (bottom left).

Figure 6.7 Changes in K_{ep} during androgen deprivation

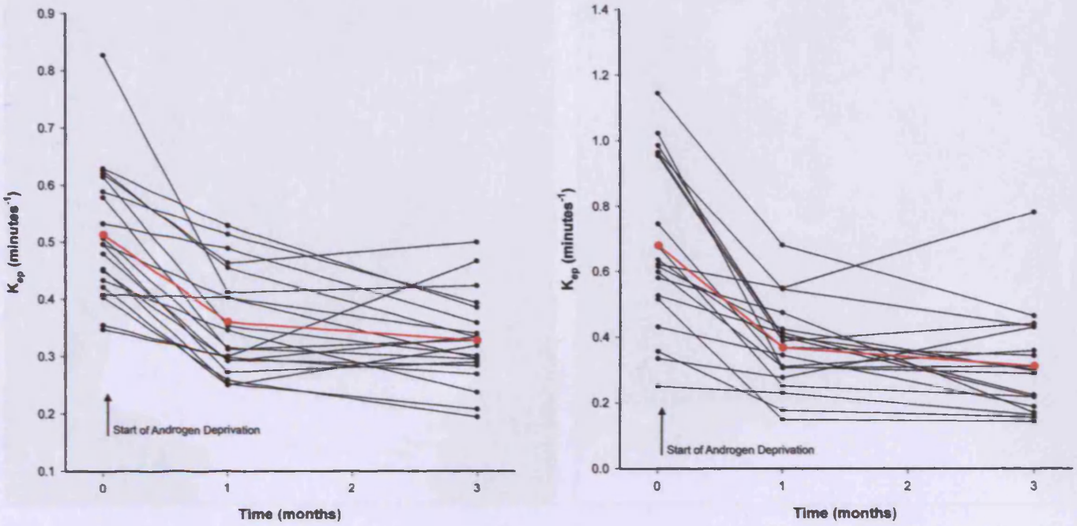

Whole Prostate

Tumour

Peripheral Zone

Central Zone

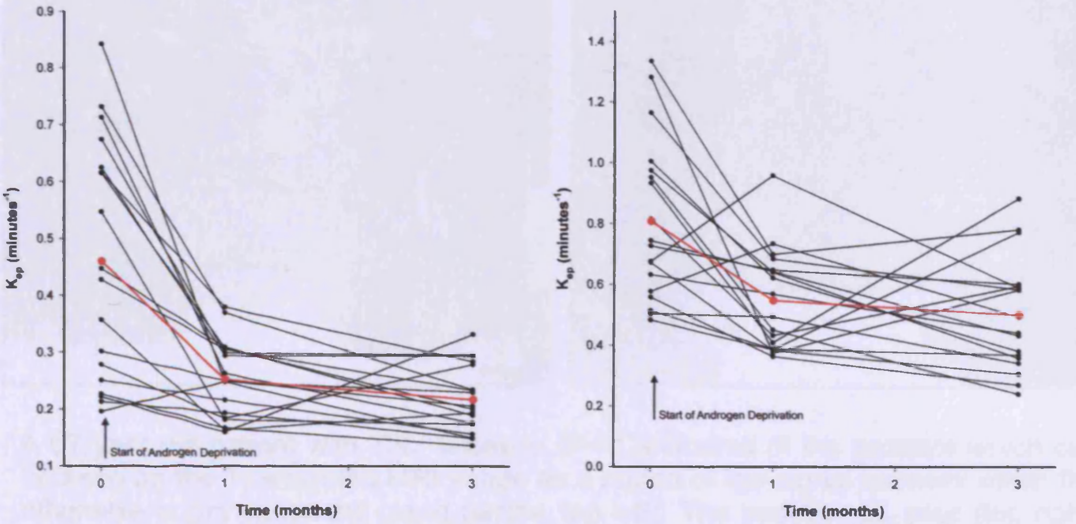

Figure 6.8 Illustration of the change in k_{ep} during 3 months of Androgen deprivation.

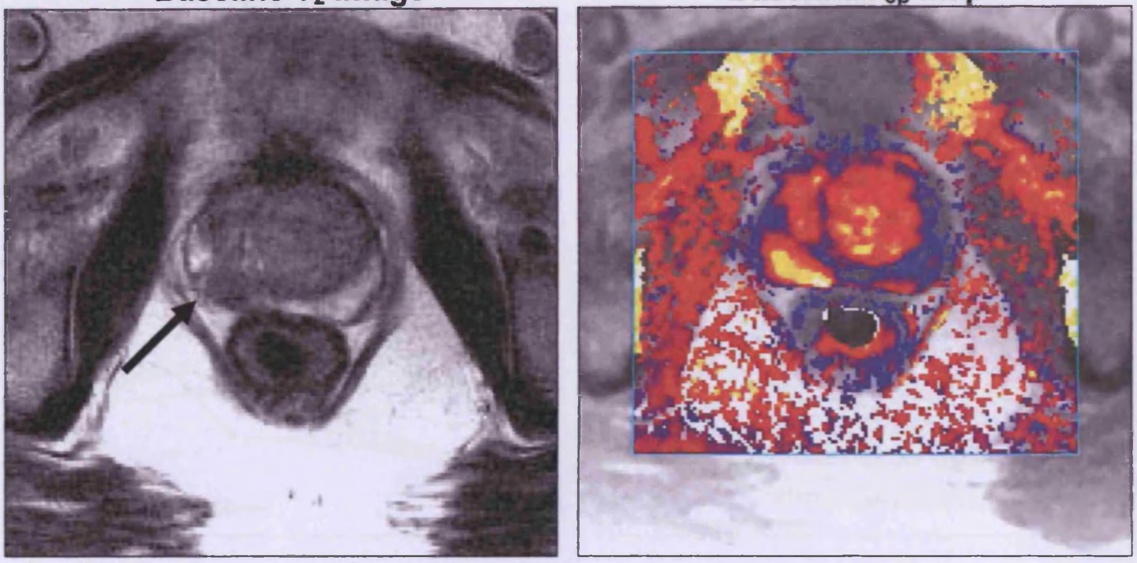

Baseline T_2 image **Baseline k_{ep} map**

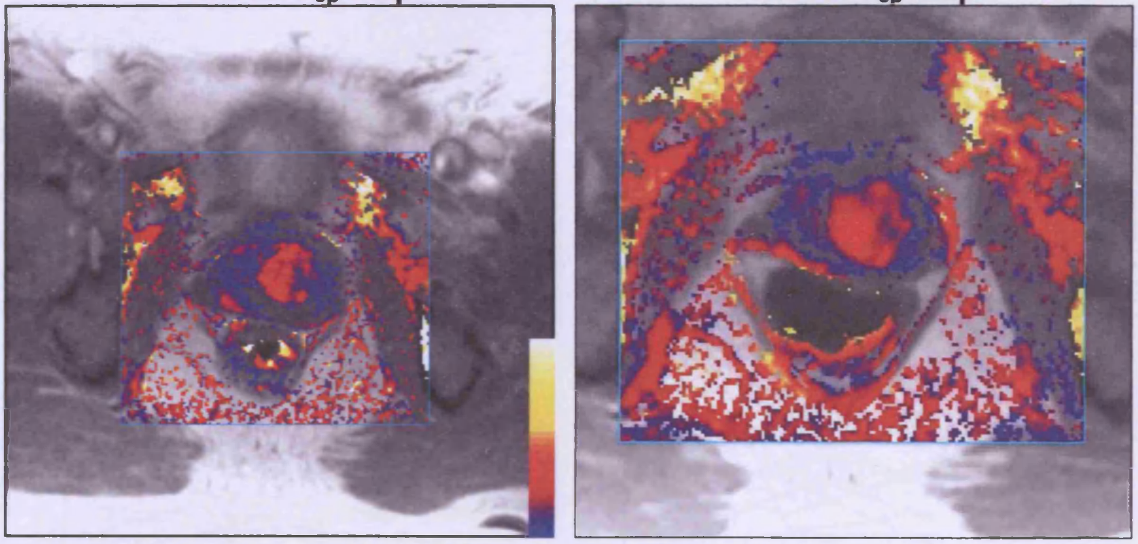

1 month k_{ep} map **3 month k_{ep} map**

A 67 year old patient with T3b, Gleason 5+4 Carcinoma of the prostate which can be seen on the T_2-weighted MRI image as a region of low signal intensity within the otherwise bright peripheral gland (arrow, top left). The baseline k_{ep} map (top right) shows high membrane permeability in the tumour. A reduction in k_{ep} is demonstrated at both one and three month following androgen deprivation (bottom images).

Figure 6.9 Changes in AUC during androgen deprivation

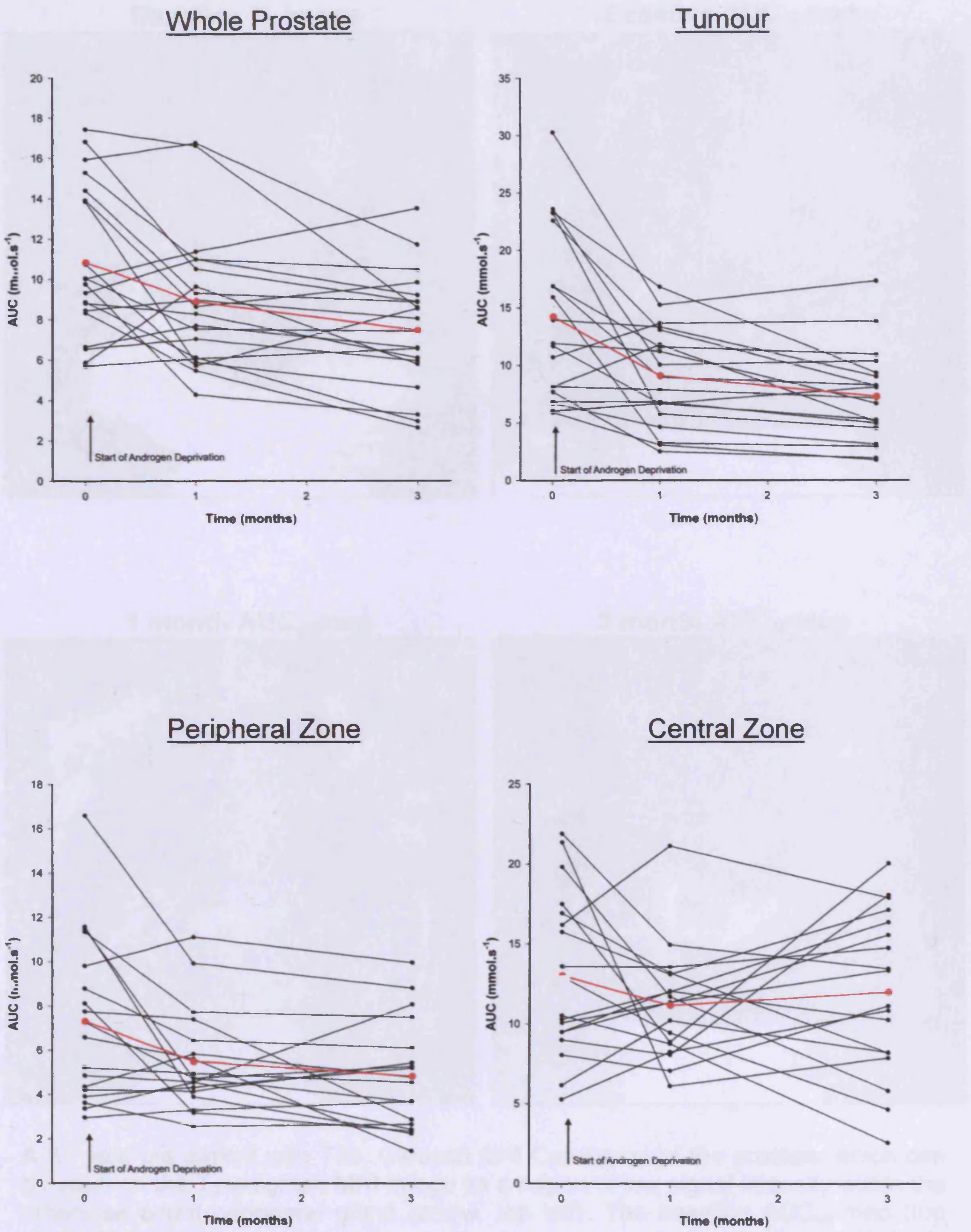

Figure 6.10 Illustration of the change in AUC_{60} during 3 months of Androgen deprivation.

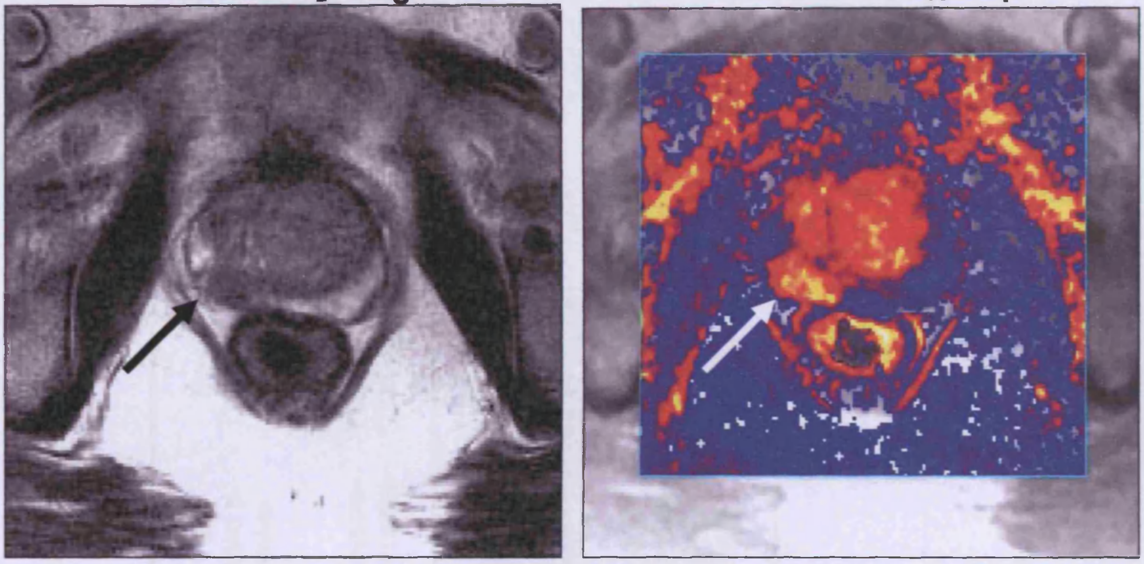

Baseline T_2 image

Baseline AUC_{60} map

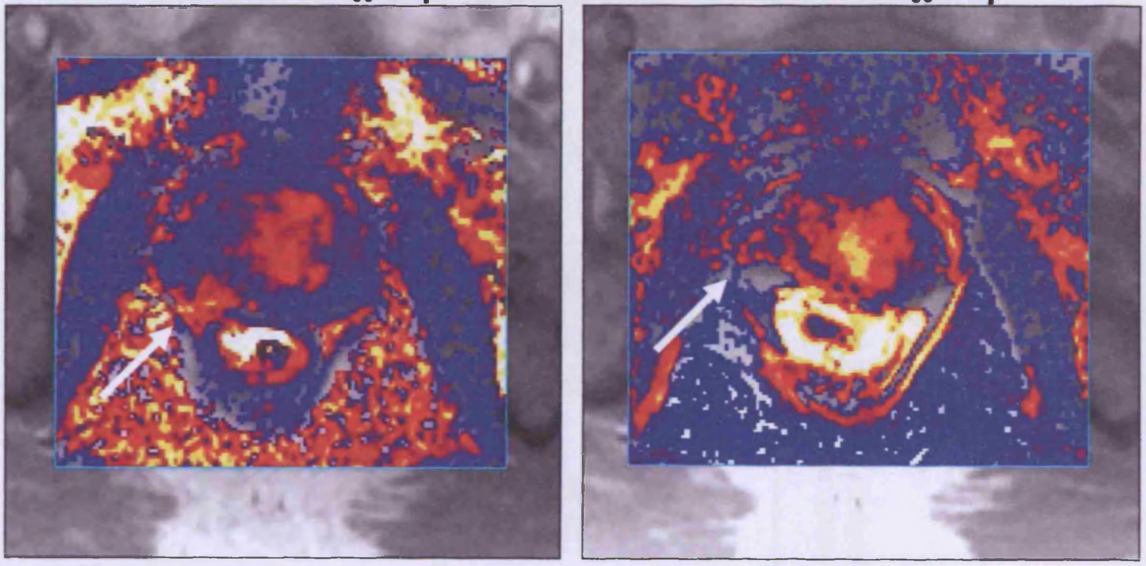

1 month AUC_{60}map

3 month AUC_{60} map

A 67 year old patient with T3b, Gleason 5+4 Carcinoma of the prostate which can be seen on the T_2-weighted MRI image as a region of low signal intensity within the otherwise bright peripheral gland (arrow, top left). The baseline AUC_{60} map (top right) shows high parameter values in the tumour (arrow). A reduction in AUC_{60} is demonstrated at both one and three month following androgen deprivation (arrow, bottom images).

Table 6.6 Summary of changes in MRI parameters caused by androgen deprivation at 1 and 3 months – T_2*-weighted DSC MRI Parameters

Para-meter	ROI	Mean Value	Mean Value	Mean Value	Mean Difference (% change)	Two-sided p-value	Mean Difference (% change)	Two-sided p-value	Mean Difference (% change)	Two-sided p-value	Proportion of patients with individually significant change	Proportion of patients with individually significant change
		baseline	1 month	3 months	baseline – 1 month	baseline– 1 month	baseline – 3 months	baseline– 3 months	1 month – 3 months	1 month – 3 months	at 1 month	at 3 months
rBV	Whole Prostate	141.42	55.71	47.94	-85.71 (-60.6)	0.0002	-93.48 (-66.1)	0.0002	-7.77 (-13.9)	0.4803	9 out of 20	11 out of 20
	Tumour	251.77	42.17	34.18	-209.6 (-83.3)	< 0.0001	-217.6 (-86.4)	0.0001	-7.99 (-18.9)	0.447	14 out of 19	12 out of 19
	Peripheral Zone	86.97	35.39	23.69	-51.57 (-59.3)	0.050	-63.28 (-72.8)	0.015	-11.7 (-33.1)	0.1251	2 out of 18	2 out of 18
	Central Zone	164.80	130.97	72.60	-33.82 (-20.5)	0.3588	-92.19 (-55.9)	0.007	-58.37 (-44.6)	0.0831	2 out of 18	6 out of 18
rBF	Whole Prostate	2.368	1.033	0.979	-1.336 (-56.4)	< 0.0001	-1.390 (-58.6)	0.0003	-0.054 (-5.2)	0.7585	9 out of 20	7 out of 20
	Tumour	4.198	0.878	0.783	-3.319 (-79.1)	< 0.0001	-3.415 (-81.3)	< 0.0001	-0.095 (-10.9)	0.6064	11 out of 19	12 out of 19
	Peripheral Zone	1.536	0.689	0.515	-0.847 (-55.1)	0.0307	-1.021 (-66.5)	0.0055	-0.174 (-25.3)	0.1569	2 out of 18	1 out of 18
	Central Zone	2.817	2.146	1.220	-0.671 (-23.8)	0.2578	-1.597 (-56.7)	0.0024	-0.926 (-43.2)	0.0641	4 out of 18	8 out of 18

p-values in green signify statistically significant results at the 95% confidence level
p-values in red signify statistically non-significant results at the 95% confidence level

Figure 6.11 Changes in relative Blood Volume during androgen deprivation

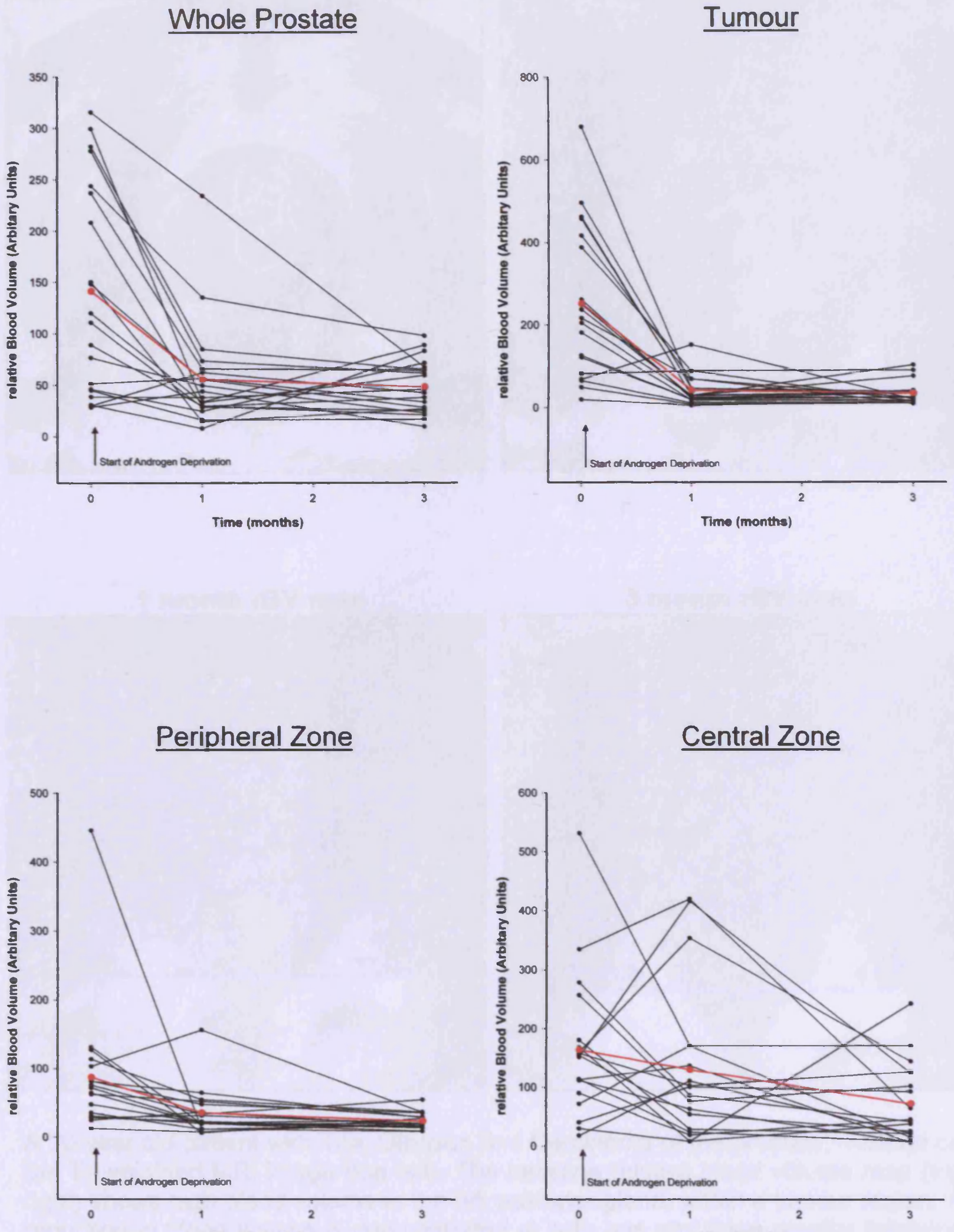

Figure 6.12 Illustration of the change in rBV during 3 months of Androgen deprivation.

Baseline T_2 image **Baseline rBV map**

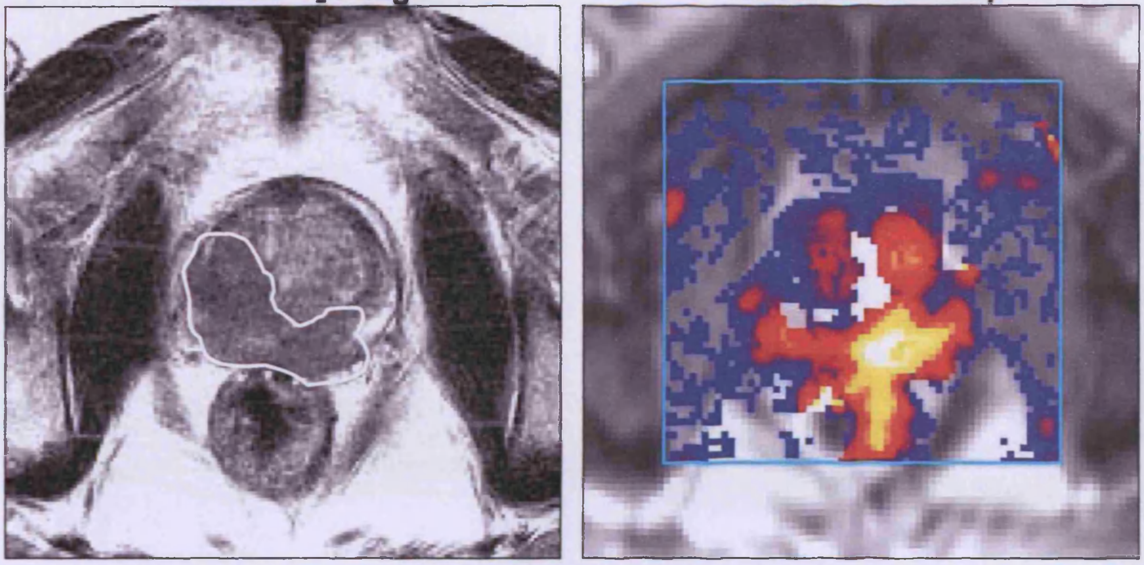

1 month rBV map **3 month rBV map**

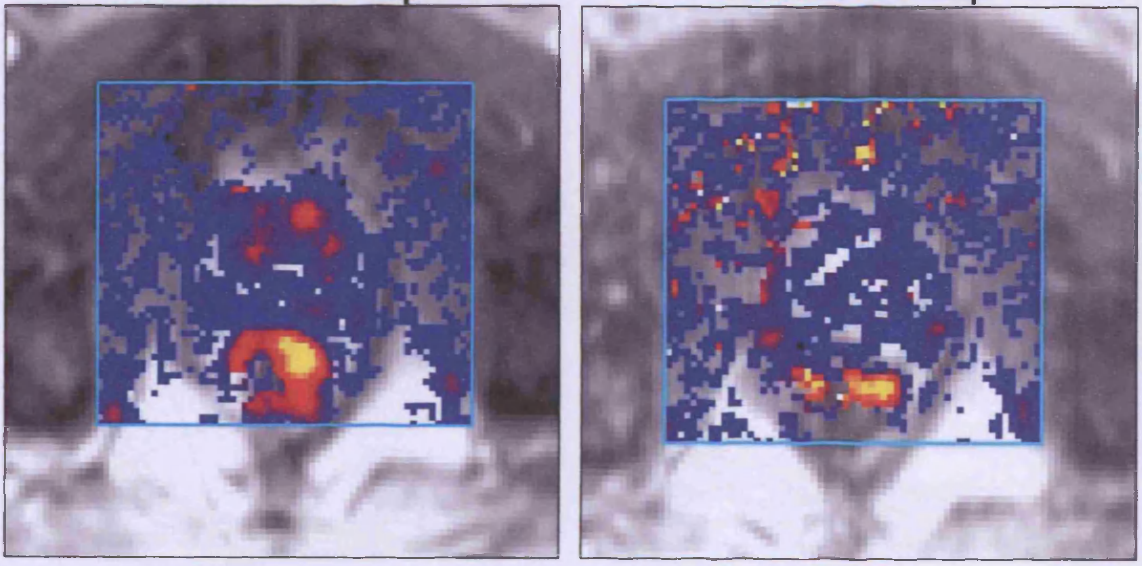

A 70 year old patient with T3a, Gleason 5+4 Carcinoma of the prostate, outlined on the T_2-weighted MRI image (top left). The baseline relative blood volume map (top right) shows high blood volume in the left posterior gland, within a tumour region. A reduction in blood volume is demonstrated at both one and three months following androgen deprivation (bottom images). A reduction in blood volume within the non-malignant regions of the prostate can also be seen. High blood volume is seen within the well vascularised normal rectum throughout the experiment.

Figure 6.13 Changes in relative Blood Flow during androgen deprivation

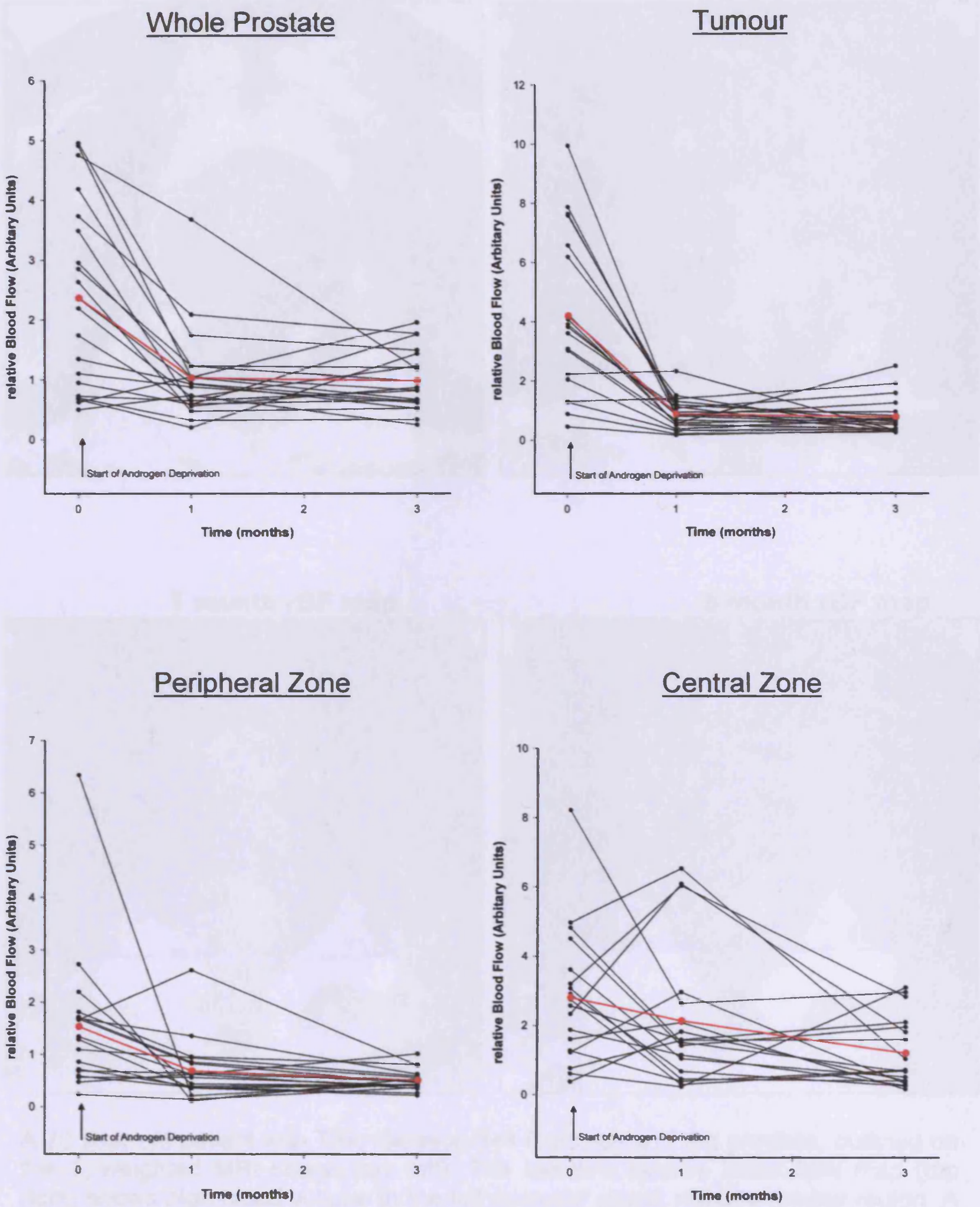
Whole Prostate

Tumour

Peripheral Zone

Central Zone

Figure 6.14 Illustration of the change in rBF during 3 months of Androgen deprivation.

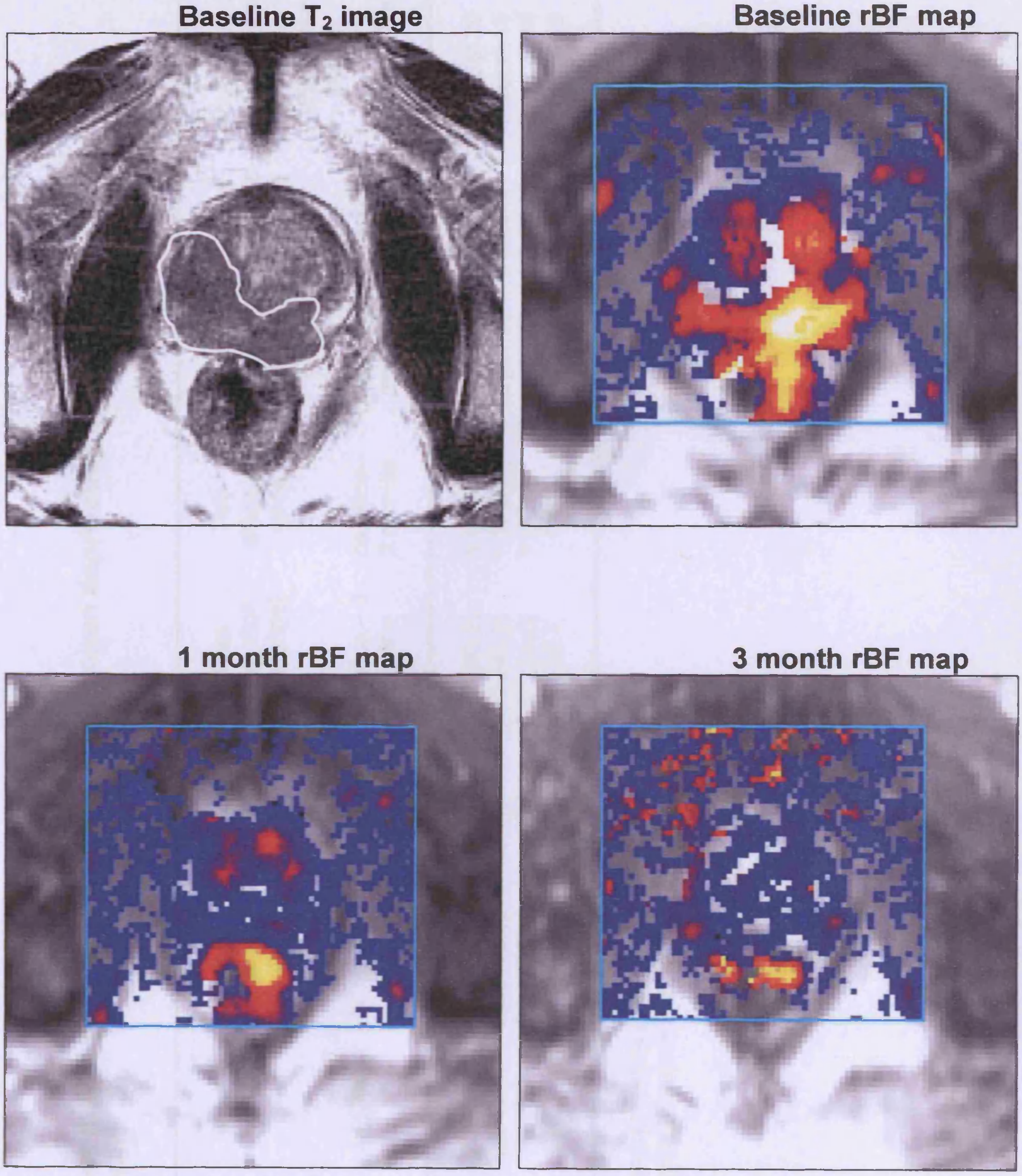

Baseline T_2 image

Baseline rBF map

1 month rBF map

3 month rBF map

A 70 year old patient with T3a, Gleason 5+4 Carcinoma of the prostate, outlined on the T_2-weighted MRI image (top left). The baseline relative blood flow map (top right) shows high blood volume in the left posterior gland, within a tumour region. A reduction in blood flow is demonstrated at both one and three months following androgen deprivation (bottom images). A reduction in blood flow within the non-malignant regions of the prostate can also be seen. High blood volume is seen within the well vascularised normal rectum throughout the experiment.

Table 6.7 Summary of changes in MRI parameters caused by androgen deprivation at 1 and 3 months – R_2* (BOLD MRI)

Parameter	ROI	Mean Value	Mean Value	Mean Value	Mean Difference (% change)	Two-sided p-value	Mean Difference (% change)	Two-sided p-value	Mean Difference (% change)	Two-sided p-value	Proportion of patients with individually significant change	Proportion of patients with individually significant change
		baseline	1 month	3 months	baseline – 1 month	baseline–1 month	baseline – 3 months	baseline–3 months	1 month – 3 months	1 month – 3 months	at 1 month	at 3 months
R_2* (s^{-1})	Whole Prostate	17.24	17.45	20.73	0.21 (1.2)	0.7716	3.50 (20.3)	< 0.0001	3.28 (18.8)	0.0002	0 out of 20	1 out of 20
	Tumour	16.59	19.21	23.41	2.62 (15.8)	0.0064	6.82 (41.1)	< 0.0001	4.20 (21.9)	0.0006	2 out of 19	4 out of 19
	Peripheral Zone	14.09	14.47	19.66	0.38 (2.7)	0.7562	5.57 (39.5)	< 0.0001	5.19 (35.9)	0.0014	2 out of 18	2 out of 18
	Central Zone	10.35	9.72	13.73	-0.63 (-6.1)	0.6016	3.38 (32.7)	0.0197	4.01 (41.3)	0.0207	1 out of 18	1 out of 18

p-values in green signify statistically significant results at the 95% confidence level
p-values in red signify statistically non-significant results at the 95% confidence level

Figure 6.15 Changes in R_2^* during androgen deprivation

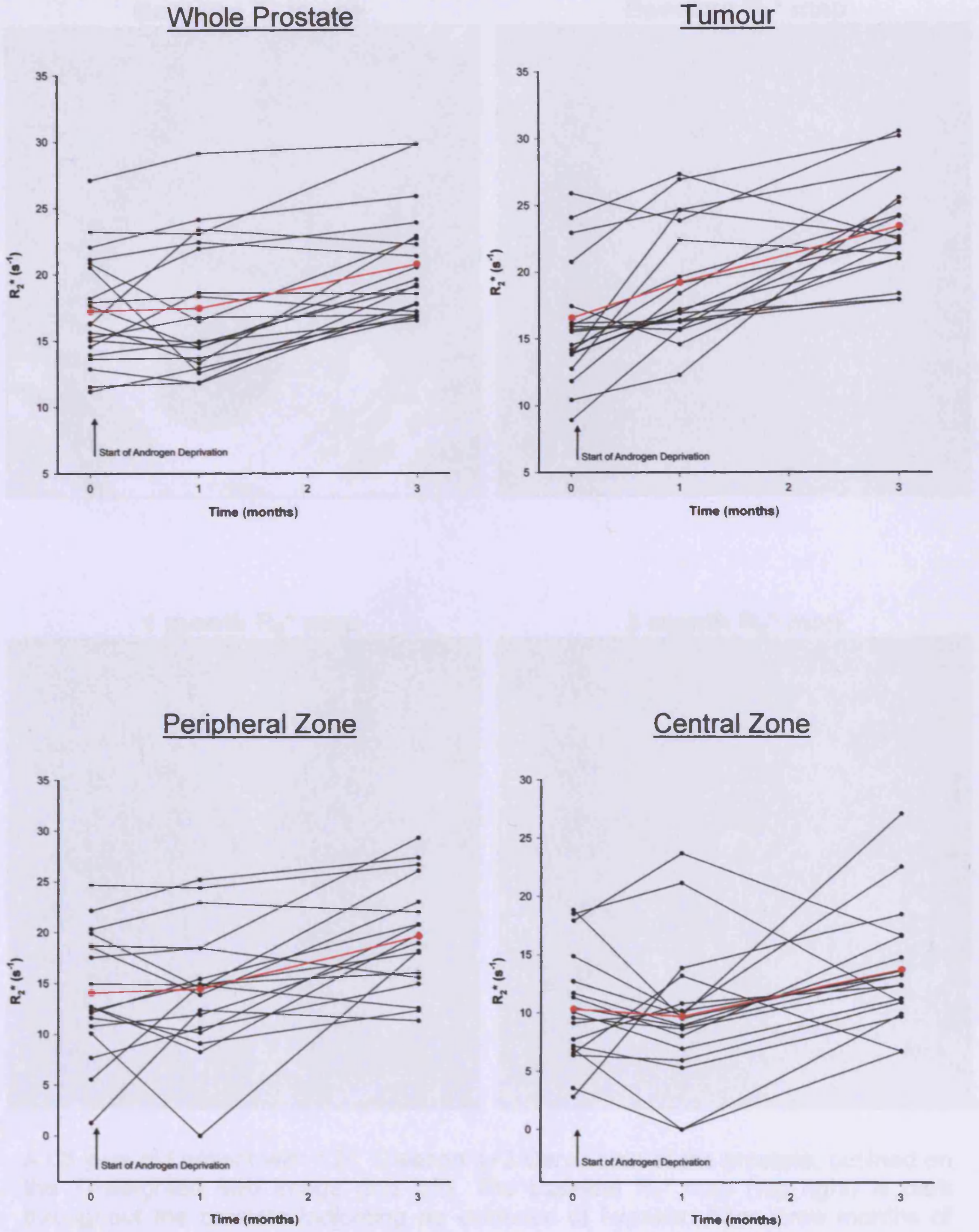

Figure 6.16 Illustration of the change in R_2* during 3 months of Androgen deprivation.

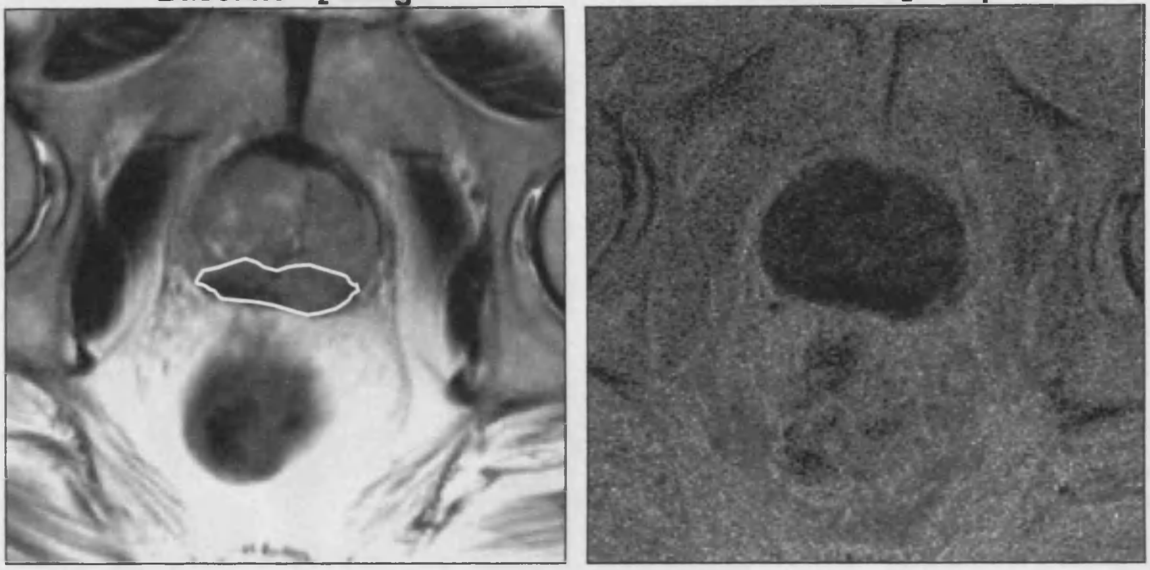

Baseline T_2 image

Baseline R_2* map

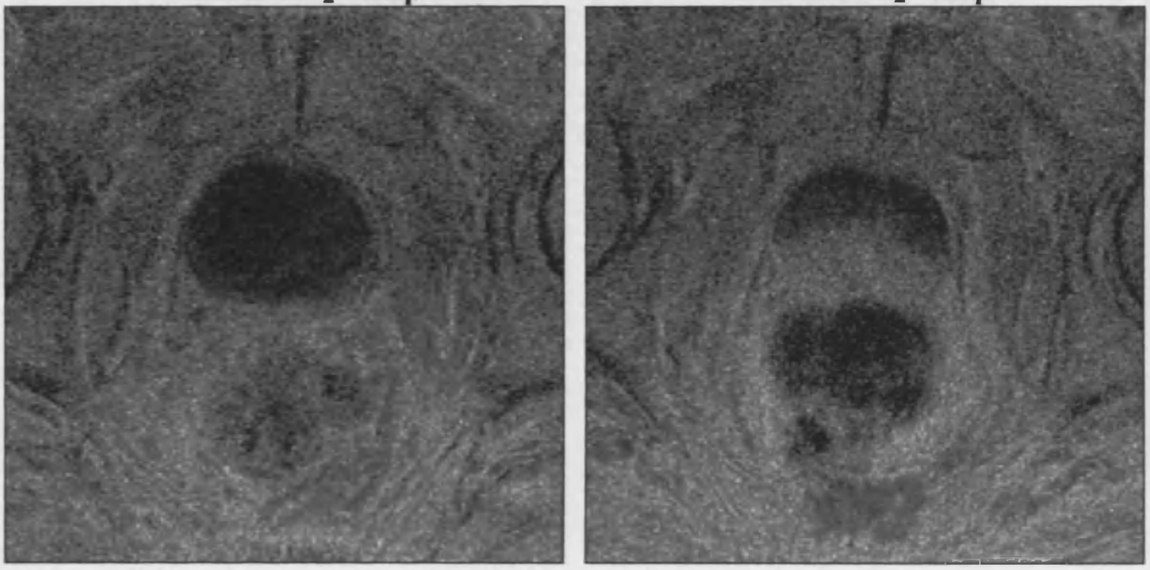

1 month R_2* map

3 month R_2* map

A 68 year old patient with T2c, Gleason 4+3 Carcinoma of the prostate, outlined on the T_2-weighted MRI image (top left). The baseline R_2* map (top right) is dark throughout the prostate indicating no evidence of hypoxia. After three months of androgen deprivation there appears to be an increase in deoxyhaemoglobin level across the posterior gland.

Figure 6.17 Illustration of the change in R_2* during 3 months of Androgen deprivation.

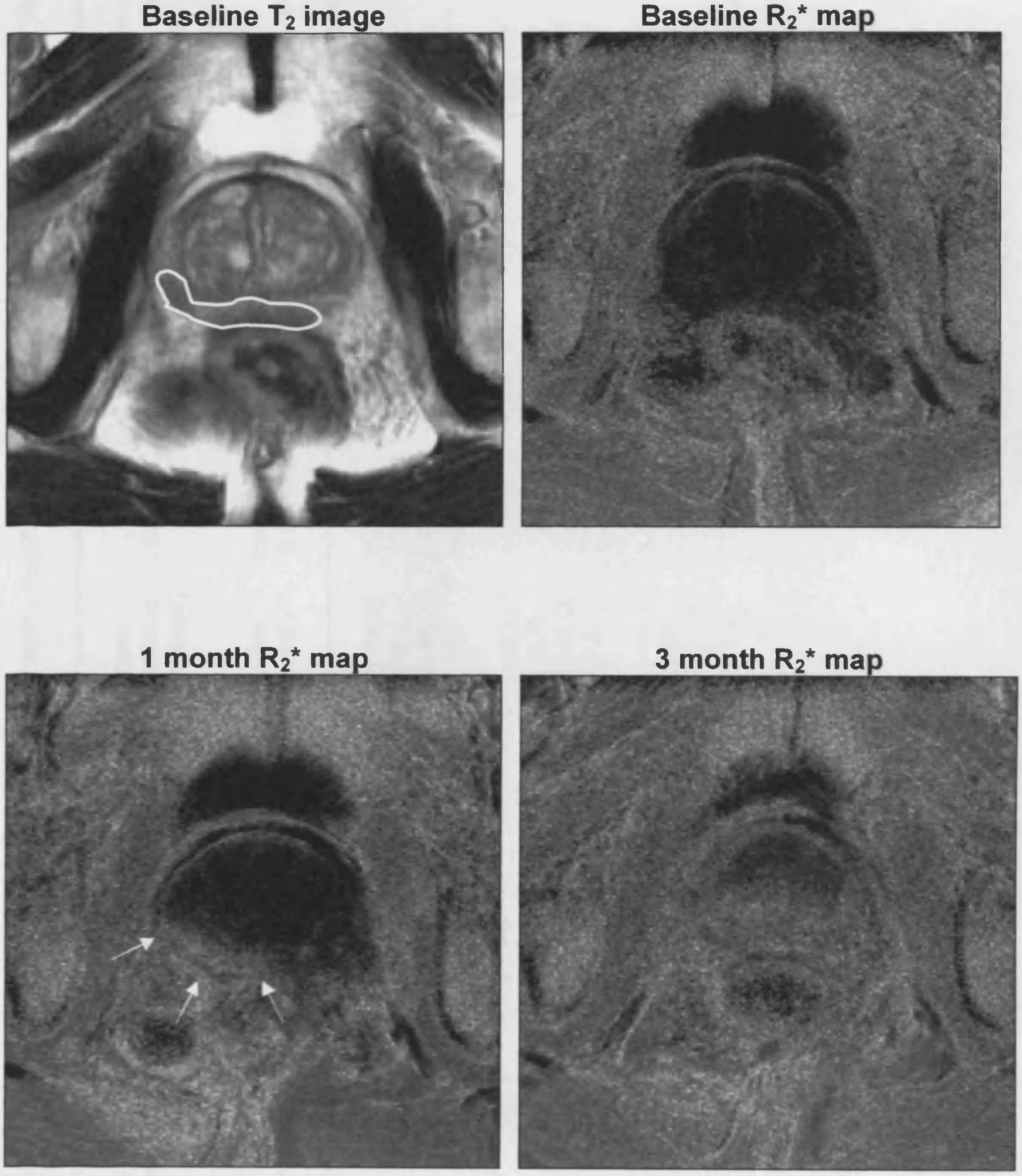

Baseline T_2 image

Baseline R_2* map

1 month R_2* map

3 month R_2* map

Table 6.8 Summary of changes in MRI parameters caused by androgen deprivation at 1 and 3 months – Diffusion Weighted ADC values

Para-meter	ROI	Mean Value	Mean Value	Mean Value	Mean Difference (% change)	Two-sided p-value	Mean Difference (% change)	Two-sided p-value	Mean Difference (% change)	Two-sided p-value	Proportion of patients with individually significant change	Proportion of patients with individually significant change
		Base-line	1 month	3 months	baseline – 1 month	baseline– 1 month	baseline – 3 months	baseline– 3 months	1 month – 3 months	1 month – 3 months	at 1 month	at 3 months
ADC (b-value 0-1000)	Whole Prostate	130.4	131.0	112.1	0.6 (0.4)	0.924	-18.3 (-14.0)	0.0288	-18.9 (-14.4)	0.0837	0 out of 7	1 out of 7
	Tumour	62.7	62.9	53.8	0.1 (0.2)	0.9933	-9.0 (-14.3)	0.4435	-9.1 (-14.5)	0.4239	0 out of 7	0 out of 7
	Peripheral Zone	149.4	168.5	119.2	19.1 (12.8)	0.3403	-30.3 (-20.3)	0.0881	-49.4 (-29.3)	0.0358	3 out of 7	2 out of 7
	Central Zone	152.0	184.9	142.1	32.9 (21.6)	0.1358	-9.9 (-6.5)	0.399	-42.8 (-23.2)	0.0847	4 out of 7	3 out of 7
ADC (b-value 0-50)	Whole Prostate	414.9	380.1	381.4	-34.8 (-8.4)	0.1637	-33.5 (-8.1)	0.1039	1.3 (0.3)	0.9578	0 out of 7	0 out of 7
	Tumour	385.5	351.2	434.8	-34.3 (-8.9)	0.8004	49.3 (12.8)	0.6656	83.6 (23.8)	0.1679	3 out of 7	2 out of 7
	Peripheral Zone	405.8	467.4	357.2	61.6 (15.2)	0.3863	-48.6 (-12.0)	0.288	-110.2 (-23.6)	0.1431	0 out of 7	0 out of 7
	Central Zone	366.1	380.2	361.1	14.1 (3.8)	0.8036	-5.0 (-1.4)	0.9309	-19.1 (-5.0)	0.6997	0 out of 7	0 out of 7
ADC (b-value 150 - 1000)	Whole Prostate	104.0	107.9	87.3	3.9 (3.7)	0.5988	-16.7 (-16.1)	0.0533	-20.6 (-19.1)	0.0953	0 out of 7	1 out of 7
	Tumour	42.3	47.2	38.6	4.9 (11.6)	0.7763	-3.7 (-8.8)	0.5109	-8.6 (-18.3)	0.5974	1 out of 7	0 out of 7
	Peripheral Zone	126.8	140.2	91.7	13.4 (10.6)	0.6379	-35.1 (-27.7)	0.0685	-48.5 (-34.6)	0.0943	3 out of 7	2 out of 7
	Central Zone	134.4	170.3	121.7	35.9 (26.7)	0.1037	-12.7 (-9.4)	0.2024	-48.6 (-28.5)	0.0671	3 out of 7	1 out of 7

p-values in green signify statistically significant results at the 95% confidence level
p-values in red signify statistically non-significant results at the 95% confidence level

Figure 6.18 Changes in Apparent Diffusion Coefficient during androgen deprivation

(b-values 0 – 1000 s/mm^2)

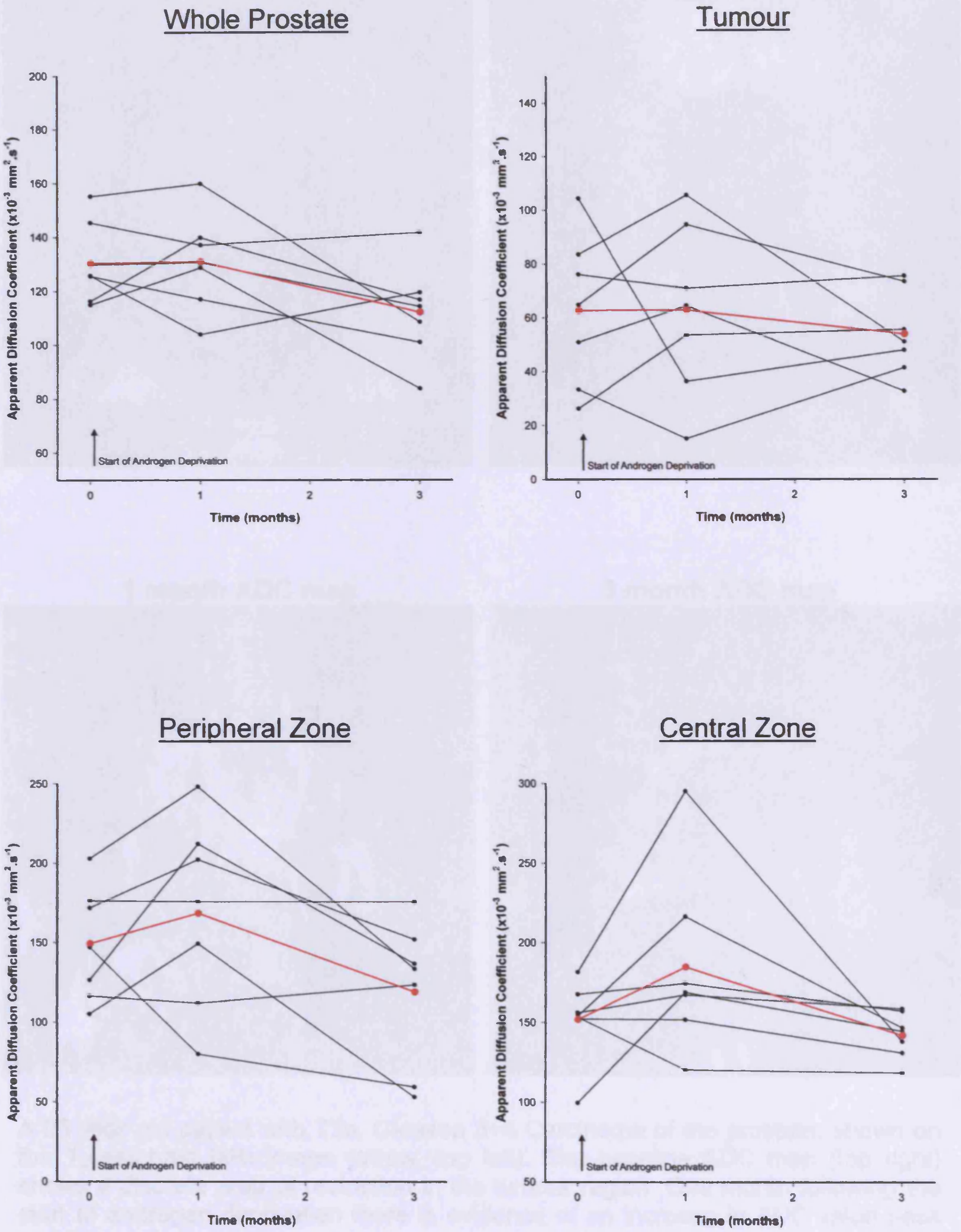

Figure 6.19 **Illustration of the change in ADC during 3 months of Androgen deprivation (b-values 0 – 1000 s/mm^2).**

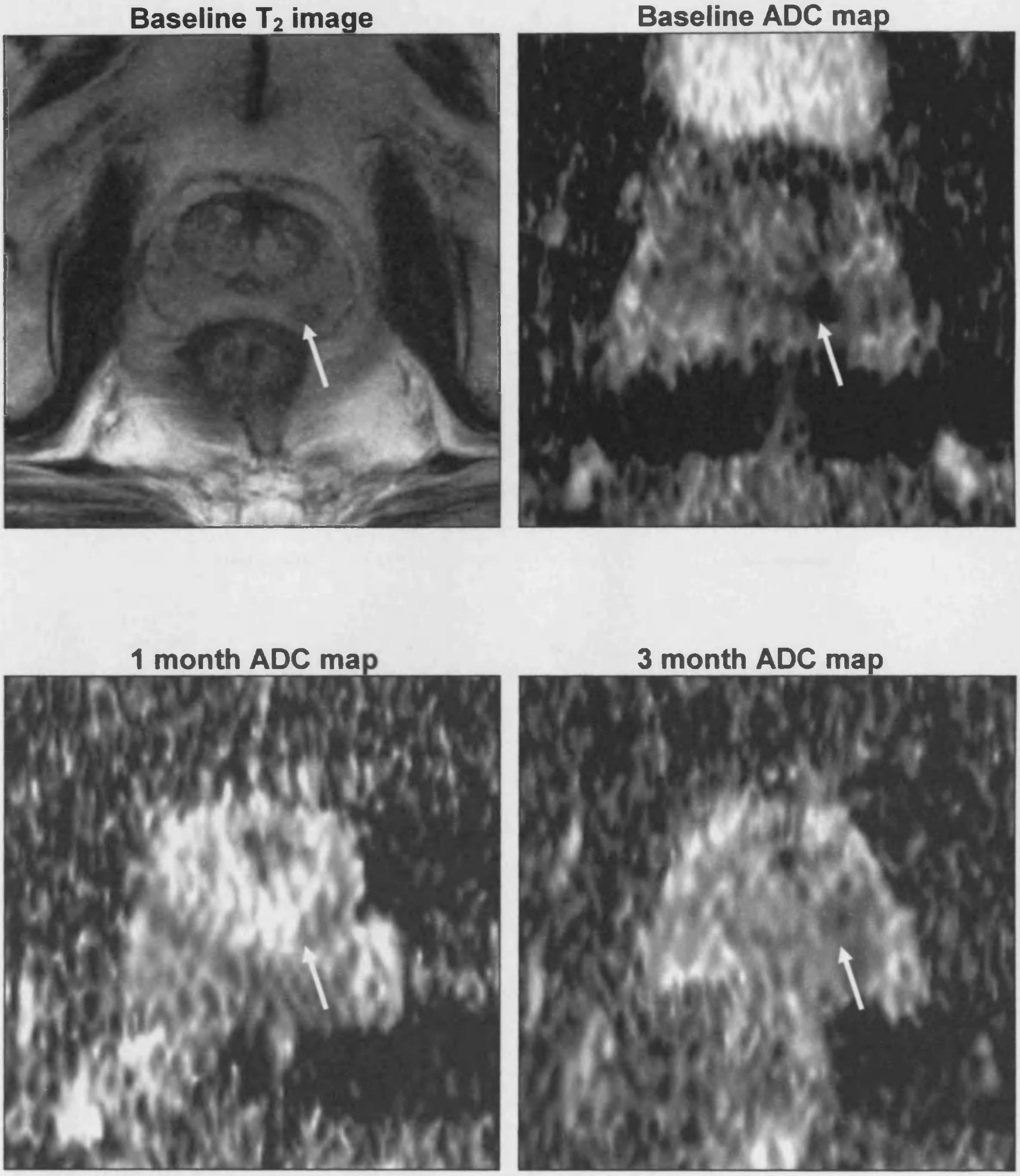

Baseline T_2 image

Baseline ADC map

1 month ADC map

3 month ADC map

A 65 year old patient with T3a, Gleason 3+4 Carcinoma of the prostate, shown on the T_2-weighted MRI image (arrow, top left). The baseline ADC map (top right) shows a discrete area of restriction in the tumour region. One month following the start of androgen deprivation there is evidence of an increase in ADC value (less restriction) in the tumour. After three months there appears to be some further restriction in the tumour region but not significantly different to that seen at 1 month.

Figure 6.20 **Changes in Apparent Diffusion Coefficient during androgen deprivation (b-values 0 – 50 s/mm^2)**

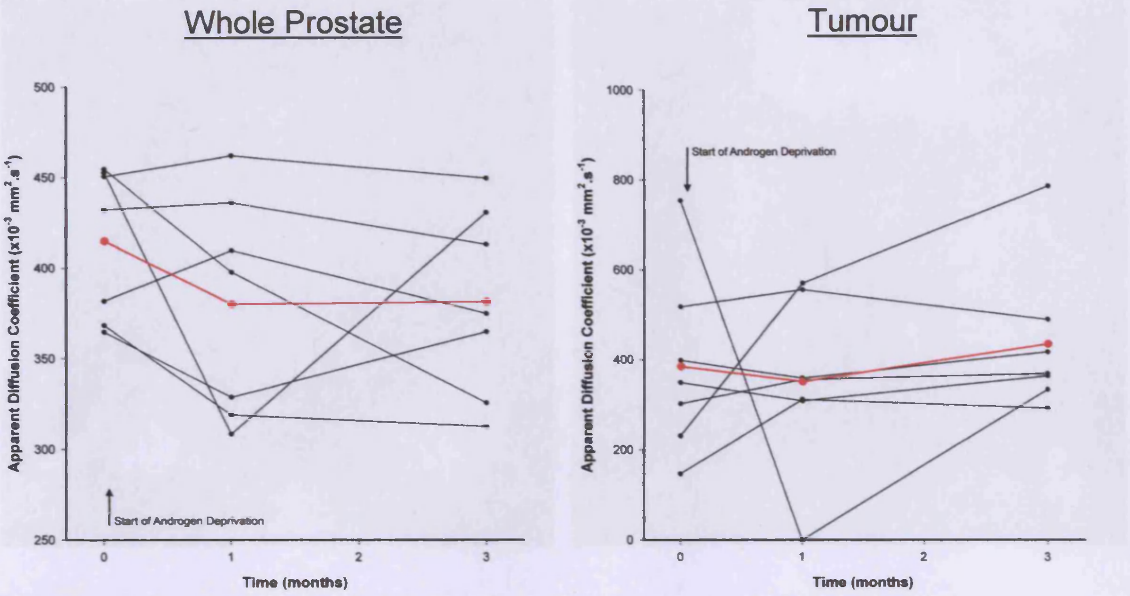
Whole Prostate

Tumour

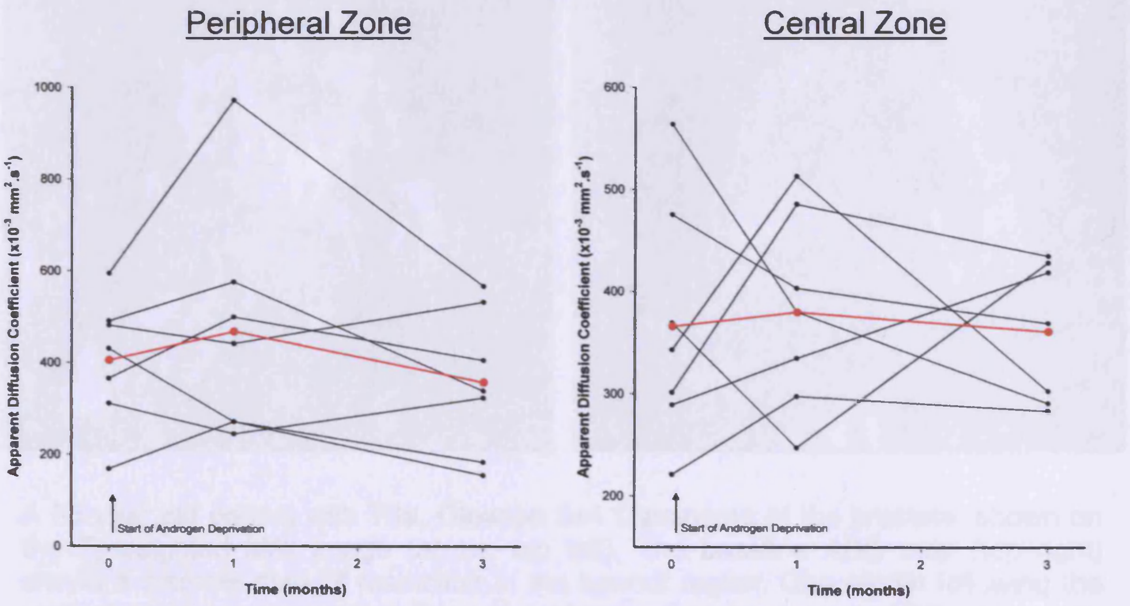
Peripheral Zone

Central Zone

Figure 6.21 **Illustration of the change in ADC during 3 months of Androgen deprivation (b-values 0 – 1000 s/mm^2).**

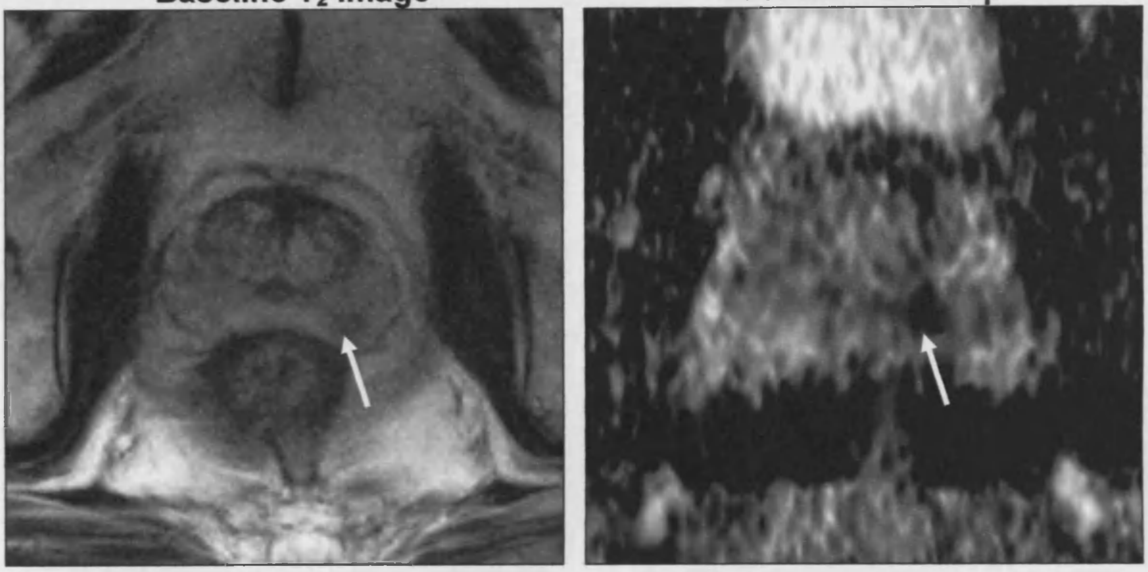

Baseline T$_2$ image **Baseline ADC map**

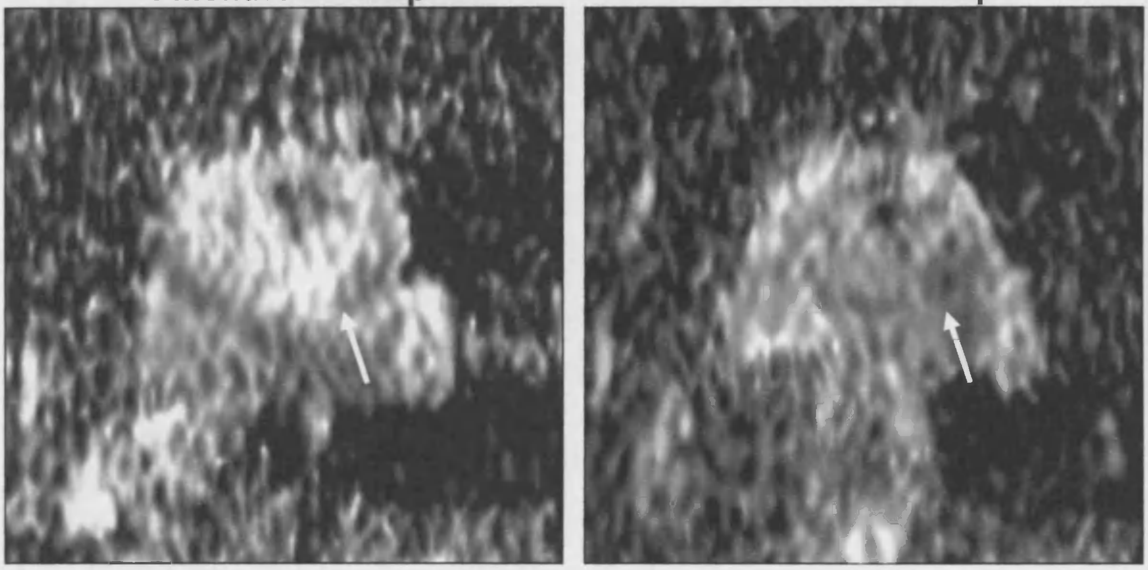

1 month ADC map **3 month ADC map**

A 65 year old patient with T3a, Gleason 3+4 Carcinoma of the prostate, shown on the T$_2$-weighted MRI image (arrow, top left). The baseline ADC map (top right) shows a discrete area of restriction in the tumour region. One month following the start of androgen deprivation there is evidence of an increase in ADC value (less restriction) in the tumour. After three months there appears to be some further restriction in the tumour region but not significantly different to that seen at 1 month.

Figure 6.22 **Changes in Apparent Diffusion Coefficient during androgen deprivation (b-values 150 – 1000 s/mm^2)**

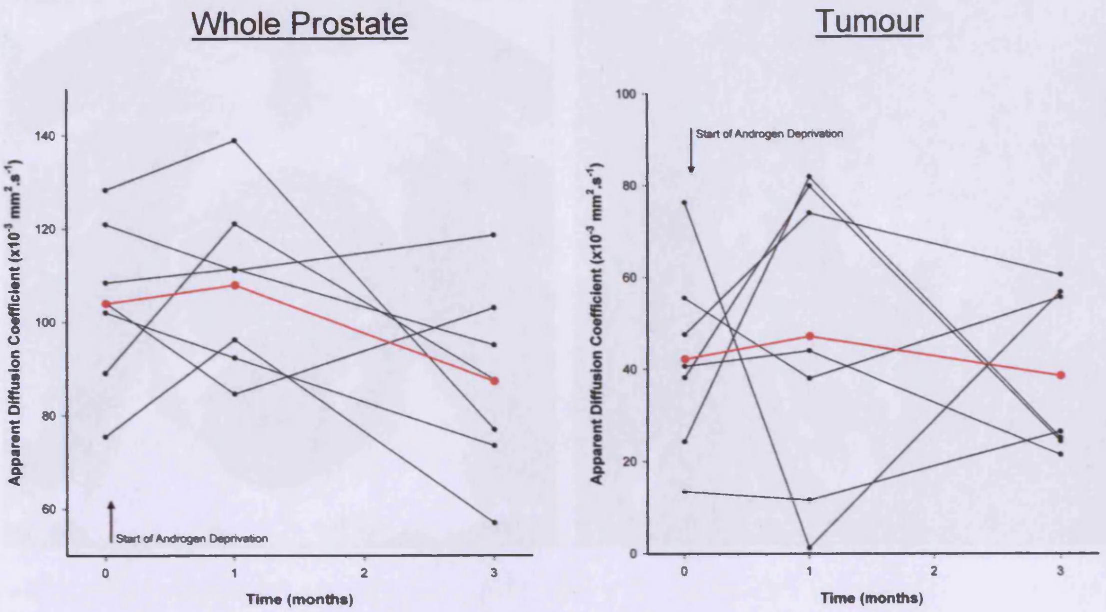

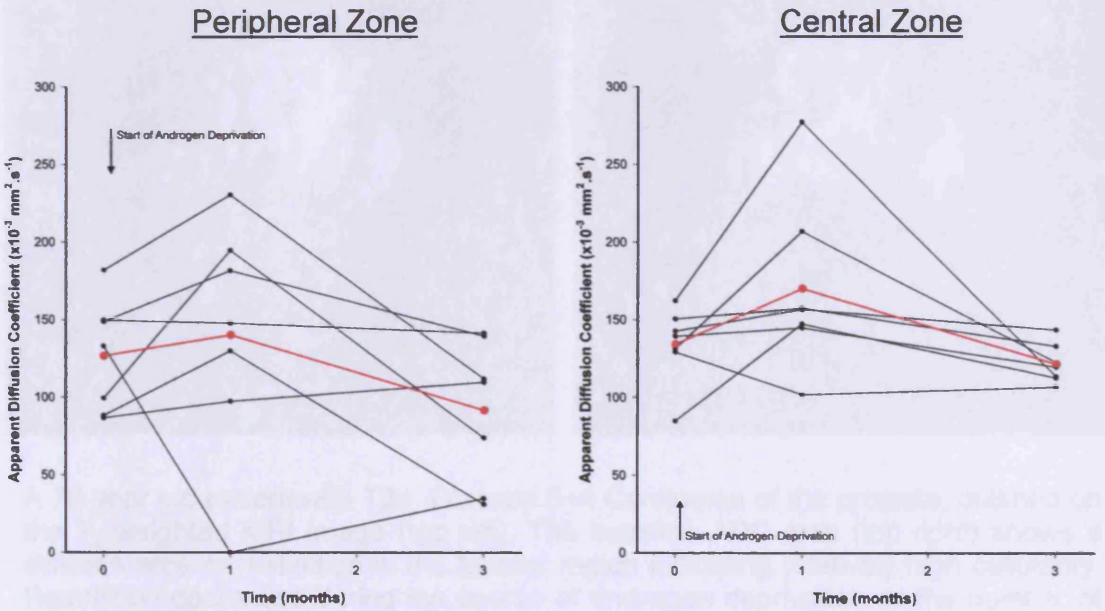

Figure 6.23 Illustration of the change in ADC during 3 months of Androgen deprivation (b-values 150 – 1000 s/mm^2).

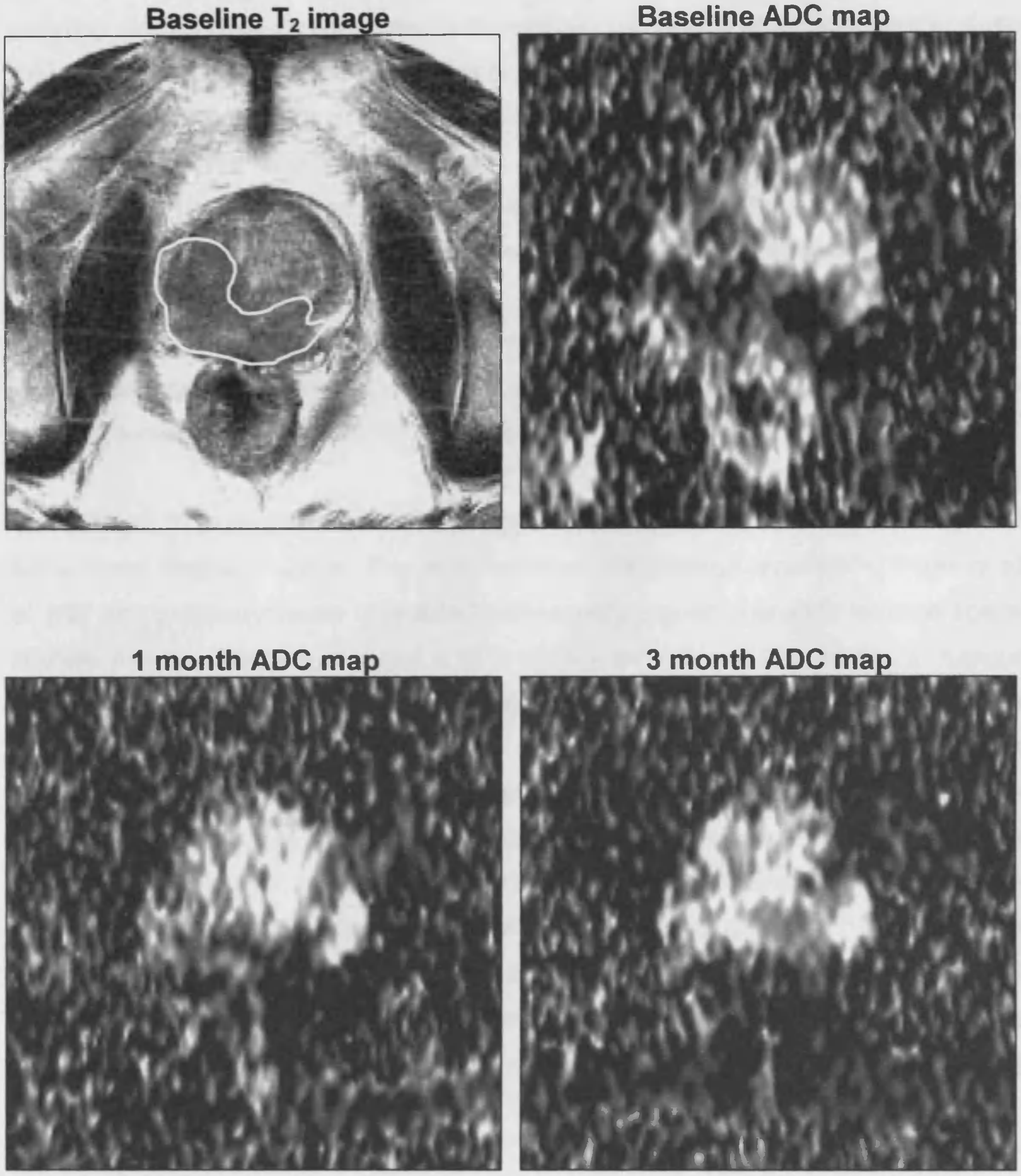

Baseline T_2 image

Baseline ADC map

1 month ADC map

3 month ADC map

A 70 year old patient with T3a, Gleason 5+4 Carcinoma of the prostate, outlined on the T_2-weighted MRI image (top left). The baseline ADC map (top right) shows a discrete area of restriction in the tumour region indicating relatively high cellularity. Restriction decreases during the course of androgen deprivation as the number of cells per unit volume decreases (bottom images).

6.5 Discussion

One of the initial reasons that investigation into androgen deprivation therapy prior to radiotherapy began was the assumption that a reduction in whole prostate volume would lead to a smaller target and therefore smaller radiation field sizes. Radiotherapy planning studies have demonstrated a theoretical reduction in rectal and bladder dose if radiation were to be deferred until after hormonal gland reduction, with the promise of an improvement in acute and late radiation toxicity to these organs [2, 3]. Many studies have confirmed that androgen withdrawal reduces prostate gland volume [4-7], with reductions of 10 – 52% reported in the literature. This study offers no surprises, with whole prostate volumes reducing by an average of 9.3% at one month and by 34.5% at three months. However, the hope that volume reduction induced by androgen withdrawal would lead to an increased therapeutic ratio has not been realised, with most studies demonstrating no toxicity improvement or even worsening of side effects following radiotherapy, particularly in regard to sexual function [8-11].

The dynamic T_1 experiments reflect changes in capillary permeability and the volume of extracellular 'leakage' space. This study confirms the findings reported by Padhani *et al.* [12] with a demonstration of reduced permeability and no change in leakage space at three months. Padhani reported a 56% (42% - 64%, $p = 0.1$) reduction in tumour K^{trans} at 3 months. This study shows remarkably similar results with a corresponding reduction in tumour K^{trans} of 52.4% (31.3% - 73.5%, $p < 0.0001$). A comparison between this study and the study of Padhani *et al*, which are the only two studies to have investigated the change in dynamic T_1 parameters following androgen deprivation in human prostate cancer, is shown in **table 6.9**. The only real differences between the results of the two studies is a significant reduction in central gland K^{trans} demonstrated by Padhani, with only a trend for this ROI in the current study. Similarly, Padhani *et al* showed a significant rise in peripheral gland v_e, with this study again showing only a trend. These differences are likely to be due to greater patient numbers (38 evaluable) in their study.

The current study reveals a number of outcomes that have not been reported previously. Most notably, that the change in vascular permeability predominately occurs during the first month after the start of androgen deprivation. For every parameter measured in all four ROIs, the percentage change between baseline and one month exceeded the change between one and three months. In fact for k_{ep}, changes in parameter values appear to be complete by one month, with no further significant changes occurring during the remainder of the study period. These findings do not lend weight to previous supposition that the reduction in capillary permeability

Table 6.9 Comparison of changes in K^{trans} and V_e, induced by three months of androgen deprivation between Padhani *et al.* and the current study.

	Padhani *et al.*			Current Study		
	Peripheral Zone	Central Gland	Tumour	Peripheral Zone	Central Gland	Tumour
Percentage reduction in K^{trans} (95% Confidence Interval)	31 (10–50)	41 (4-59	56 (42-64)	45.3 (18.8-71.8)	18.3 (-10.3-46.9)	52.4 (31.3-73.5)
P-value	< 0.001	< 0.009	0.01	0.0023	0.19	< 0.0001
Percentage increase in V_e (95% Confidence Interval)	46 (10–100)	20 (10-44)	0 (-9-22)	20.6 (-4.8-46.0)	30.0 (4.7-55.3)	10.0 (-7.8-27.8)
P-value	0.02	< 0.001	> 0.05	0.11	0.0233	0.26

may be, at least in part, due to the development of interstitial fibrosis, which is known to occur as a result of androgen withdrawal [13, 14]. Mature collagen deposition is a recognised cause of a decrease in permeability to low molecular weight contrast media but is unlikely to develop within four weeks of starting treatment.

The reduction in vascular endothelial growth factor, VEGF (also know as vascular permeability factor) is likely to be the predominant initiator for permeability change following androgen deprivation. Studies in normal male rats and in mice bearing human prostate carcinomas have shown that castration results in a rapid decrease in VEGF expression within 24 hours and a marked reduction in neovascularization by three days [15, 16]. Similarly, biopsy of the human prostate, before and after ablative endocrine therapy, demonstrates a significant reduction in VEGF levels post-treatment [17, 18]. These changes in VEGF result in physiological and architectural changes to the vasculature within days and are therefore likely to be apparent when imaged at one month.

Relative blood volume and blood flow changes during androgen deprivation in the human prostate have never been reported before. The results are unequivocal, with five-fold reductions of both parameters compared to the pre-treatment values in the regions of prostate carcinoma ($p < 0.0001$). These vascular changes appear to have concluded by the end of the first treatment month, with no further significant alterations occurring during the remainder of the study period. Once again, the reduction in VEGF is the most likely factor causing the induction and maintenance of these changes. In both tumour xenografts and primary human tumours, the neo-vasculature contains a substantial proportion of immature blood vessels, characterized by a lack of periendothelial cells. These cells undergo selective apoptosis in the absence of VEGF [19]. In the Shionogi tumour model, endothelial cells begin to undergo apoptosis before neoplastic cells, and degeneration of tumour vessels precedes the decrease in tumour size. The regressing vessels begin to exhibit normal phenotype, i.e., lower diameter, tortuosity, vascular permeability, and leukocyte adhesion [20]. Two weeks after castration, a second wave of angiogenesis and tumour growth begins with a concomitant increase in VEGF expression as both vascular endothelium and tumour cells become hormone refractory. This pattern of capillary architecture change has also been demonstrated by the examination of whole-mount prostatectomy specimens from untreated and androgen-ablated patients [17].

These anti-vascular and anti-angiogenic effects, exhibited in both prostate cancer as well as benign prostatic tissue as a result of androgen withdrawal, are confirmed by the

T_2* experiments in this study. **Figures 6.11 and 6.13** depict the extent of change in blood volume and flow within the first month of therapy in both the benign but especially the malignant gland. The maintenance of vascular function in the non-androgen dependent rectal mucosa is also demonstrated.

Hypoxic tumours are more radioresistant that well oxygenated ones [21]. Hypoxia can inhibit the action of some chemotherapeutic agents and there is evidence that hypoxic tumours are more likely to invade and metastasise. There is increasing published data that hypoxia is a poor prognostic indicator in prostate cancer [22-26]. Mathematical modelling studies strongly suggest that severe hypoxia in the prostates of certain patients may limit the overall cancer cure rate by conventional radiation therapy [27]. The finding that androgen deprivation may induce or worsen existing hypoxia therefore has serious implications regarding the timing of androgen withdrawal with radiotherapy.

The reproducibility of the R_2* parameter itself has been confirmed by repeatability measurements in normal tissue (obturator internus muscle) **(table 3.4, chapter 3)**. The variability in prostate cancer is greater, reflecting the heterogeneity and instability of the tumour blood supply, resulting in changes to individual patients being harder to confirm with statistical significance. Nevertheless, for the group of twenty patients as a whole, there is a significant increase in R_2* for every prostate region, with a 41% rise in tumour R_2* ($p < 0.0001$) at three months. Increases in R_2* are consistent with increased presence of paramagnetic species. As previously mentioned, interstitial fibrosis is known to gradually develop following months of androgen withdrawal. Collagen contains paramagnetic species and as a result causes inhomogeneity in the microscopic magnetic field gradients in fibrotic regions, which is reflected by high R_2*. However, in this experiment the change in R_2* was too rapid to be explicable by the development of fibrosis (an increase at one month of 15.8%, $p=0.0064$), making the development of tumour hypoxia a more likely explanation.

R_2* measurements taken in isolation neither reflect tissue pO_2 nor do they reflect O_2 consumption by tumour cells. R_2* reflects the number of deoxyhaemoglobin molecules per unit volume imaged, thereby being dependent of blood flow and volume. For example, a hypoxic tumour region with low blood volume may contain fewer deoxyhaemoglobin molecules than a similar region that is well oxygenated with a greater blood volume, despite the ratio of deoxygenated haemoglobin to oxygenated haemoglobin being greater, simply because there is more blood, and therefore more haem, in the latter.

In this study blood volume and blood flow was measured in conjunction with R_2*. The increases seen in R_2* occurred *despite* a reduction of flow and volume. Tumour R_2* values increased in 84% of the patients. It follows that three months of androgen deprivation therapy may well be causing, or at least exacerbating existing hypoxia within the prostate and in regions of prostate cancer.

In previous studies, the R_2* value of obturator internus has been used as a benchmark to determine whether clinically relevant hypoxia is present [28]. Using this method of analysis for the current study, 5% of prostate tumours would be considered hypoxic at baseline compared with 32% following three months of hormonal treatment. It is likely that the use of obturator internus as an internal standard results in a conservative assessment of the prevalence of hypoxia. The BOLD effect in skeletal muscle is at least as complex as the effect seen in tumours, complicated by the presence of myoglobin, which has an identical haem structure as haemoglobin but a dramatically different volume of distribution [29, 30]. Muscle contraction also has a significant effect, with higher R_2* values obtained when the muscle is at rest, as would be the case when lying supine during an MRI examination [31]. In this experiment obturator internus gave an R_2* value of $25.0s^{-1}$ ($24.04s^{-1} - 25.95s^{-1}$).

A method more appropriate for the assessment of tumour hypoxia that may be of clinical significance, as suggested by the validation experiments in **chapter 5** would be to use a combined test, diagnosing hypoxia if rBV is less than 42 a.u. or if rBV is greater than 42 a.u. *and* R_2* is greater than $21.3s^{-1}$. Using this as the hypoxia cut-off value for the current study, 25% of the regions of prostate tumour would be considered hypoxic at baseline (five of the 20 patients) compared with 90% following three months of hormonal therapy (18 of the 20 patients). This was calculated as follows:

	Baseline	3 months
Number of patients with rBV < 42 au	4	17
Number of patients with rBV > 42 au AND R_2* >$21.3s^{-1}$	1	1
Number of patients with hypoxic tumours	**5**	**18**

The under-powered diffusion data is difficult to interpret with any degree of confidence. However, some of the trends observed warrant further study. The overall apparent diffusion coefficient (ADC) encompasses both the diffusion of water molecules within tissue as well as contributions from the flow of water molecules within vessels. It is possible to distinguish between these two components of measured water diffusion by altering the degree of diffusion weighting. Lower b-values (0 – 50 s/mm^2) reflecting perfusion and higher b-values (150 – 1000 s/mm^2) giving an indication of tumour cellularity. As previously demonstrated, androgen deprivation causes a considerable and persistent reduction in blood flow. It also reduces prostate cellularity, most notably in the regions of tumour. As a result, one would expect a decrease in the restriction to the movement of water molecules and therefore an increase in ADC measurements.

Indeed the early, perfusion weighted, ADC values for tumour rise over the three-month study period (not significant) but the dramatic changes in blood flow seen after only one month with the T_2*-weighted dynamic imaging, are not apparent. The trend for changes induced by androgen deprivation as measured by the late, cellularity weighted ADC values, follows a similar pattern for each of the prostate regions. An initial rise during the first month is followed by a fall between one and three months, to a value similar to or slightly lower than baseline. The explanation for this may be due to the balance of two competing factors. The decrease in cellularity, caused by androgen withdrawal causes an initial rise in ADC. The subsequent development of interstitial fibrosis, which may be established by three months [13, 14], causes further restriction to the diffusion of water molecules and results in a fall of ADC, countering the effect of reduced cellularity. This initial rise followed by a fall in ADC may limit the potential of cellularity-weighted diffusion MRI to evaluate early response to endocrine therapy, however these results need to be viewed with caution given the patient numbers involved.

6.6 Conclusion

Considering the results of the T_1, T_2* and BOLD experiments together, androgen deprivation not only causes substantial morphological changes to the prostate gland but also induces profound vascular collapse and a reduction in capillary membrane permeability. Increased R_2* in regions of prostate cancer and a reduction in blood volume, suggest the induction of tumour hypoxia.

These findings have considerable implications regarding the timing of androgen deprivation and radiotherapy. In pre-clinical models, the fact that an increase in radiation-induced post-mitotic apoptosis as a result of androgen withdrawal is not associated with an overall increase in tumour cell death [32], suggests that the supra-additivity in one tumour cell population is offset by sub-additivity in another. The induction of tumour hypoxia as a result of substantial vascular shutdown may be the mechanism for this apparent induction of radio-resistance in a susceptible group of tumour cells.

Clinical data is largely supportive of the use of androgen deprivation with radiotherapy, although as previously described; none of the clinical studies can differentiate between additive and synergistic effects for the combination. Neo-adjuvant studies have generally assessed androgen deprivation prior to and during radiotherapy versus no hormonal therapy at all. The resulting relapse-free survival benefits suggest that the tumour cell-killing effects of androgen withdrawal outweigh any inhibition to cell death caused by radio-resistance. However, if the benefits of combined therapy are indeed additive rather than synergistic, then deferring hormonal therapy until after radiotherapy is complete may offer an even greater advantage, with similar cytotoxicity without the negative effects of radio-resistance. This may be why in contrast to the neo-adjuvant trials, the adjuvant studies have been able to show a true survival advantage.

This study has demonstrated that non-invasive MR imaging at multiple-time points during androgen deprivation therapy, is a valuable clinical technique. It has demonstrated the potent effects of hormonal treatment on the prostate and tumour vasculature and provided evidence that the resulting environment may support tumour hypoxia. Given the lack of convincing clinical evidence for the superiority of neoadjuvant androgen withdrawal over the use of androgen deprivation in the adjuvant setting, these findings raise questions regarding the indiscriminate use of hormonal therapy prior to radical radiotherapy.

References

1 Wolff JM, Boeckmann W, Mattelaer P, Handt S, Adam G, Jakse G. Determination of prostate gland volume by transrectal ultrasound: correlation with radical prostatectomy specimens. *Eur Urol.* 1995;28:10-12.

2 Samper PM, Lopez Carrizosa MC, Perez Casas A, *et al.* Impact of neoadjuvant hormonal therapy on dose-volume histograms in patients with localized prostate cancer under radical radiation therapy. *Clin Transl Oncol.* 2006;8:599-605.

3 Zelefsky MJ, Harrison A. Neoadjuvant androgen ablation prior to radiotherapy for prostate cancer: reducing the potential morbidity of therapy. *Urology.* 1997;49:38-45.

4 Chen M, Hricak H, Kalbhen CL, *et al.* Hormonal ablation of prostatic cancer: effects on prostate morphology, tumor detection, and staging by endorectal coil MR imaging. *AJR Am J Roentgenol.* 1996;166:1157-1163.

5 Nakashima J, Imai Y, Tachibana M, Baba S, Hiramatsu K, Murai M. Effects of endocrine therapy on the primary lesion in patients with prostate carcinoma as evaluated by endorectal magnetic resonance imaging. *Cancer.* 1997;80:237-241.

6 Pinault S, Tetu B, Gagnon J, Monfette G, Dupont A, Labrie F. Transrectal ultrasound evaluation of local prostate cancer in patients treated with LHRH agonist and in combination with flutamide. *Urology.* 1992;39:254-261.

7 Shearer RJ, Davies JH, Gelister JS, Dearnaley DP. Hormonal cytoreduction and radiotherapy for carcinoma of the prostate. *Br J Urol.* 1992;69:521-524.

8 Hollenbeck BK, Wei JT, Sanda MG, Dunn RL, Sandler HM. Neoadjuvant hormonal therapy impairs sexual outcome among younger men who undergo external beam radiotherapy for localized prostate cancer. *Urology.* 2004;63:946-950.

9 Liu M, Pickles T, Agranovich A, *et al.* Impact of neoadjuvant androgen ablation and other factors on late toxicity after external beam prostate radiotherapy. *Int J Radiat Oncol Biol Phys.* 2004;58:59-67.

10 Peeters ST, Hoogeman MS, Heemsbergen WD, *et al.* Volume and hormonal effects for acute side effects of rectum and bladder during conformal radiotherapy for prostate cancer. *Int J Radiat Oncol Biol Phys.* 2005;63:1142-1152.

11 Wahlgren T, Nilsson S, Ryberg M, Lennernas B, Brandberg Y. Combined curative radiotherapy including HDR brachytherapy and androgen deprivation in localized prostate cancer: a prospective assessment of acute and late treatment toxicity. *Acta Oncol.* 2005;44:633-643.

12 Padhani AR, MacVicar AD, Gapinski CJ, *et al.* Effects of androgen deprivation on prostatic morphology and vascular permeability evaluated with MR imaging. *Radiology.* 2001;218:365-374.

13 Guinan P, Didomenico D, Brown J, *et al.* The effect of androgen deprivation on malignant and benign prostate tissue. *Med Oncol.* 1997;14:145-152.

14 Polito M, Muzzonigro G, Minardi D, Montironi R. Effects of neoadjuvant androgen deprivation therapy on prostatic cancer. *Eur Urol.* 1996;30 Suppl 1:26-31; discussion 38-29.

15 Stewart RJ, Panigrahy D, Flynn E, Folkman J. Vascular endothelial growth factor expression and tumor angiogenesis are regulated by androgens in hormone responsive human prostate carcinoma: evidence for androgen dependent destabilization of vascular endothelial growth factor transcripts. *J Urol.* 2001;165:688-693.

16 Burchardt M, Burchardt T, Chen MW, *et al.* Vascular endothelial growth factor-A expression in the rat ventral prostate gland and the early effects of castration. *Prostate.* 2000;43:184-194.

17 Mazzucchelli R, Montironi R, Santinelli A, Lucarini G, Pugnaloni A, Biagini G. Vascular endothelial growth factor expression and capillary architecture in high-grade PIN and prostate cancer in untreated and androgen-ablated patients. *Prostate.* 2000;45:72-79.

18 Quinn DI, Henshall SM, Sutherland RL. Molecular markers of prostate cancer outcome. *Eur J Cancer.* 2005;41:858-887.

19 Benjamin LE, Golijanin D, Itin A, Pode D, Keshet E. Selective ablation of immature blood vessels in established human tumors follows vascular endothelial growth factor withdrawal. *J Clin Invest.* 1999;103:159-165.

20 Jain RK, Safabakhsh N, Sckell A, *et al.* Endothelial cell death, angiogenesis, and microvascular function after castration in an androgen-dependent tumor: role of vascular endothelial growth factor. *Proc Natl Acad Sci U S A.* 1998;95:10820-10825.

21 Gray LH, Conger AD, Ebert M, Hornsey S, Scott OC. The concentration of oxygen dissolved in tissues at the time of irradiation as a factor in radiotherapy. *Br J Radiol.* 1953;26:638-648.

22 Carnell DM, Smith RE, Daley FM, Saunders MI, Bentzen SM, Hoskin PJ. An immunohistochemical assessment of hypoxia in prostate carcinoma using pimonidazole: implications for radioresistance. *Int J Radiat Oncol Biol Phys.* 2006;65:91-99.

23 Milosevic M, Bristow R, chung p, Panzarella T, Toi A, Hill RP. Prostate Cancer Hypoxia Correlates with Poor Patient Outcome Following Treatment with Radiotherapy. *Int J Radiat Oncol Biol Phys.* 2004;60:s236-s237.

24 Movsas B, Chapman JD, Greenberg RE, *et al.* Increasing levels of hypoxia in prostate carcinoma correlate significantly with increasing clinical stage and patient age: an Eppendorf pO(2) study. *Cancer.* 2000;89:2018-2024.

25 Tatum JL, Kelloff GJ, Gillies RJ, *et al.* Hypoxia: importance in tumor biology, noninvasive measurement by imaging, and value of its measurement in the management of cancer therapy. *Int J Radiat Biol.* 2006;82:699-757.

26 Zhao D, Constantinescu A, Chang CH, Hahn EW, Mason RP. Correlation of tumor oxygen dynamics with radiation response of the dunning prostate R3327-HI tumor. *Radiat Res.* 2003;159:621-631.

27 Nahum AE, Movsas B, Horwitz EM, Stobbe CC, Chapman JD. Incorporating clinical measurements of hypoxia into tumor local control modeling of prostate cancer: implications for the alpha/beta ratio. *Int J Radiat Oncol Biol Phys.* 2003;57:391-401.

28 Hoskin P, Carnell D, Taylor N, *et al.* Hypoxia in prostate cancer: correlation of BOLD-MRI with pimonidazole immunohistochemistry. *Int J Radiat Oncol Biol Phys.*In Press.

29 Carlier PG, Bertoldi D, Baligand C, Wary C, Fromes Y. Muscle blood flow and oxygenation measured by NMR imaging and spectroscopy. *NMR Biomed.* 2006;19:954-967.

30 Donahue KM, Van Kylen J, Guven S, *et al.* Simultaneous gradient-echo/spin-echo EPI of graded ischemia in human skeletal muscle. *J Magn Reson Imaging.* 1998;8:1106-1113.

31 Meyer RA, Towse TF, Reid RW, Jayaraman RC, Wiseman RW, McCully KK. BOLD MRI mapping of transient hyperemia in skeletal muscle after single contractions. *NMR Biomed.* 2004;17:392-398.

32 Pollack A, Salem N, Ashoori F, *et al.* Lack of prostate cancer radiosensitization by androgen deprivation. *Int J Radiat Oncol Biol Phys.* 2001;51:1002-1007.

Chapter 7

Concluding Discussion

The experiments described in this thesis have demonstrated that functional magnetic resonance imaging techniques are capable of mapping hypoxia within prostate cancer with a sensitivity of 70 - 82% and a specificity of 72 - 100%, depending on the thresholds used for the test. Accounting for the intrinsic difficulties with the methodology required to prove the accuracy of such a test, requiring the correlation between a pathological section and an MRI image, these results are very promising. The functional MR examination process itself is fast and minimally invasive, making it readily incorporable within existing diagnostic MR schedules.

The parametric maps produced using BOLD and T_1-weighted dynamic sequences are highly repeatable and reproducible, suggesting that they are potentially robust clinical tools. The T_2*-weighted dynamic scans proved to be much less reproducible, largely resulting from the susceptibility artefacts generated by rectal gas. Strategies to combat rectal gas formation and faster imaging at increased magnetic field strength may improve this matter. This study is the first to document the variability and repeatability of T_1- and T_2*-weighted dynamic MRI and ISW-MRI for the various regions of the human prostate gland. Reproducibility statistics for each kinetic parameter in every prostate region have been documented and will provide a valuable source of reference for any group that plans to use these measures as a method for assessing treatment response in the benign or malignant prostate. Awareness of the intrinsic variability of any biomarker is vital for accurate study design. In particular, knowledge of the degree a particular parameter has to change, on an individual patient basis, for the change to be considered statistically significant, will facilitate accurate power calculations. T_1 derived kinetic parameters exhibit a high degree of reproducibility compared to the T_2* weighted measures. Both sets of parameters become more variable following androgen deprivation. In contrast, the reproducibility of R_2* improves with androgen ablation therapy reflecting the antiangiogenic effects of this treatment.

Another important conclusion of the studies reported in this work is that the oxygenation of prostate cancer improves during carbogen gas breathing. There is an average R_2* decrease of 9.8 -10% in prostate cancer xenografts and 21.6% in human tumours. Carbogen, in conjunction with nicotinamide (ARCON), has radiosensitizing properties. Over the past 15 years a number of early phase human studies have been conducted using ARCON in a variety of tumour sites. A study of 215 patients with locally advanced head and neck cancer indicated very favourable rates of locoregional tumour control and overall survival. The actuarial 3-year local control rates were 80% for larynx, 69% for hypopharynx, 88% for oropharynx, and 37% for oral cavity tumors. Regional control rates were 100% for N0, 93% for N1, and 74% for N2 disease. Following this promising early data, the ARCON schedule has also been tested in bladder cancer. A multi-centre phase III trial (BCON) comparing 55Gy in 20 fractions of external beam with or without carbogen and nicotinamide has recently completed accrual. No study has ever investigated carbogen in the clinical setting for prostate cancer. The results presented here suggest that a study of similar design to BCON is justified.

Despite recent advances, many patients treated for prostate cancer with curative intent do not remain disease free in the long term, with disease-free 5-year survival rates for T1-T2 disease of 63-96% for external beam radiotherapy and 83-92% in equivalent risk patients treated with external-beam plus a brachytherapy boost. For T3 disease the corresponding 5-year disease-free survival rates are 32-87% and 31-56% respectively. The two principle causes for this failure remain inadequate initial staging leading to the incorrect assumption that the disease is localized at presentation and biological resistance which may reflect varying degrees of hypoxia and intrinsic resistance.

Part of this problem may be due to the fact that many aspects of prostate cancer therapy have traditionally been anatomically based. Staging procedures assess the pattern and depth of invasion and the number and distribution of metastases. Therapeutic strategies are defined by the primary tumour stage and radiation treatments and dosing constraints are subject to anatomical boundaries. Functional magnetic resonance imaging techniques have the ability to look beyond anatomy to identify specific cellular characteristics. Maps of intrinsic radio-resistance within the prostate can potentially be produced for every patient.

In-vivo hypoxia and vascular imaging techniques may serve several roles in clinical oncology. At the time of initial diagnosis and staging, an estimation of the extent of tumour hypoxia and angiogenesis would provide additional information for risk-stratification and assessment of prognosis. The functional information gained in the treatment planning stages may lead to the optimal choice of treatment modality, or combination of treatment modalities. For example, if the tumour is found to be very hypoxic, radiotherapy could be combined with hypoxic sensitizers or the breathing of high oxygen containing gas mixtures. Highly proliferating cancers may be more appropriately treated with combined chemo-radiotherapy or in conjunction with other biological agents. Tumours with extensive evidence of neo-vascularization or expression of vascular growth factors may benefit from treatment with anti-angiogenic or anti-vascular drugs.

Currently, radiotherapy is planned using physical tumour volumes. However, tumours are heterogeneous with areas of varying radiosensitivity based on biological characteristics. The ability to incorporate biological information into the radiotherapy planning process and to increase the dose administered to relatively resistant regions could achieve better local tumour control and overall survival.

In order to test the hypothesis that biologically targeted radiotherapy offers an advantage over anatomically based radiotherapy planning, three processes require integration: (1) Quantitative imaging of the biological characteristics of tumours. (2) The generation of radiotherapy dose-distributions that optimise dose to biological sub-volumes within the target and (3) Precise radiation delivery. This thesis has begun to address the first of these issues with regard to prostate cancer. With the phenomenal technological advances in radiotherapy over the past few years there has been considerable progress in the remaining two areas.

Modelling studies have demonstrated theoretical advantages for biological conformality. However the translation of these ideas into clinical studies has been limited for two major reasons: Most groups have concentrated on external-beam Intensity-Modulated Radiotherapy (IMRT) for treatment delivery. There are a number of technical limitations of IMRT that need to be overcome before efficacy studies of biological conformality can be undertaken. IMRT requires a motionless target if precise doses are to be administered to small regions within tumours. Immobilisation devices, respiratory gating and image guidance technology are becoming highly advanced and have already reached the levels of accuracy required for biological 'dose-painting'. However most centres are still gaining technical and clinical experience with IMRT, making the prospect of delivering biological conformal radiotherapy using this method some years away.

Brachytherapy is a technique in which radiation sources are placed within the tumour itself, bypassing the need for immobilisation and image guidance during treatment delivery. High dose gradients are achieved providing the most conformal dose distributions of all radiotherapy techniques. High dose-rate (HDR) brachytherapy is delivered over a period of minutes rather than weeks. This eliminates the effects of tumour cell repopulation and the difficulties that may be encountered when attempting to deliver radiation to a biologically relevant tumour sub-volume that may change over a prolonged treatment course. This technology is available for use today and fulfils every physical requirement for biological dose painting. It is for these reasons that HDR brachytherapy may be the ideal treatment strategy with which to explore the principle of biologically based treatment planning in the clinic.

In the future, as our familiarity with image guidance grows, external beam IMRT will become a realistic option for the delivery of biologically optimised dose distributions and may be used in combination with HDR brachytherapy for prostate cancer, or as sole modality therapy for tumour sites that are not suitable for implantation.
As exemplified by the experiments detailed in chapter 6, biological imaging also provides new endpoints for response assessment. This thesis has established the value of vascular imaging for the demonstration of blood flow changes induced by therapeutic strategies such as androgen deprivation. With the proliferation of second line treatment strategies such as cryotherapy or high frequency ultrasound and the development of new targeted agents including antibodies and vaccines, the importance of early response assessment after, or even during, the primary treatment has increased considerably. The conflicting results of clinical studies that have tried to assess the role of androgen deprivation in conjunction with radical radiotherapy (as outlined in the introduction to chapter 6) suggests that not all patients benefit from treatment with hormones prior to radiation. It would be interesting to correlate the degree and nature of the response to neo-adjuvant androgen deprivation, in terms of changes to blood flow, vascular permeability and oxygenation, with response to radiotherapy and final outcome. This approach could lead to individualised treatments based on the intrinsic biology of each tumour.

Further work has already begun using identical MR sequences to examine the vascular and oxygenation changes that occur during a course of radical external beam radiotherapy to the prostate. Similar to what is seen with androgen deprivation, changes in vascular and oxygenation parameters may inform on a tumour's individual radiobiology. Furthermore, the parametric maps generated by this process will determine the feasibility of specific targeting of sub-volumes within the prostate and how these regions change throughout a course of treatment.

In coming years, as novel PET tracers become validated and the signal to noise ratio of PET imaging improves, it will be possible to integrate these techniques into the biological targeting process. As for MR, PET imaging of hypoxia is still in an experimental phase. The two most promising radiotracers for this purpose, ^{18}F-misonidazole and Cu-ATSM, both have significant difficulties that are yet to be overcome. With ^{18}F-misonidazole there is a low tumour to background ratio and a slow washout time for normoxic cells. Cu-ATSM appears to have a critical dependence on blood flow and would necessitate concomitant blood flow estimation. Furthermore the radiopharmaceuticals are difficult and expensive to make and require the presence of a nearby cyclotron facility that is willing to temporarily suspend FDG production for the time it takes to produce these investigational tracers.

Even with highly validated PET tracers, such as FDG, incorporating the biological information it produces into radiotherapy planning protocols is fraught with difficulty. On a PET image tumour boundaries are generally defined as a percentage of the maximum standardised uptake value (SUV). However many factors affect SUV measurements and therefore it is hard enough to delineate the tumour borders let alone devise a way to determine the margins of biological targets within tumours. There are also considerable issues regarding registration when dealing with images of low signal-to-noise ratio. Furthermore, PET is also at a disadvantage in terms of response assessment, with a limitation in the number of examinations that can be performed as a result of the radiation exposure to each patient.

In summary, this research has demonstrated the feasibility of hypoxia imaging in prostate cancer. Although there is, as yet, no imaging modality that can precisely map tissue pO_2, the combination of BOLD-MRI and dynamic susceptibility contrast MRI provides a valuable surrogate and predicts the pattern of hypoxia, as determined by pimonidazole immunohistochemistry, with reasonable accuracy. The research has also shown that prostate cancer responds to carbogen gas breathing and that androgen deprivation causes profound vascular collapse within one month of starting therapy. These findings should help in the rational design of future studies that aim to target tumour vasculature and combat tumour hypoxia in prostate cancer.

Appendix A

Methods for Histological Analysis

A1 Tumour removal and cutting

A1. Tumour xenografts in mice (figure A1)

1) The dead mouse is positioned in the same orientation as in the MRI scanner.
2) The right side of the tumour is painted with Indian ink to facilitate orientation during analysis.
3) The tumour is cut in the transverse plane at the same level as the MRI scan. The front portion is placed directly in formalin (40% w/v formaldehyde in water) and the rear portion is placed in zinc fixative.
4) Samples were protected from light.
5) The samples were then paraffin embedded, and cut into 4μm sections using a microtome and mounted on to glass slides for staining.

A1.2 Human prostate specimens (figure A2)

1) The prostate was removed from the patient during a radical prostatectomy procedure.
2) The prostate was immediately placed in formalin.
3) 24 - 48 hours later the specimen was ready to be cut.
4) The MRI image was used to orientate the specimen prior to cutting.
5) The prostate was sliced in one action through the same plane that was used to obtain the MRI images. A 5 mm thick section was cut and replaced in formalin for transportation from the hospital to the laboratory.
6) The whole 5mm thick axial section of prostate was then paraffin embedded, and cut into 4μm sections using a microtome and mounted on to glass slides for staining.

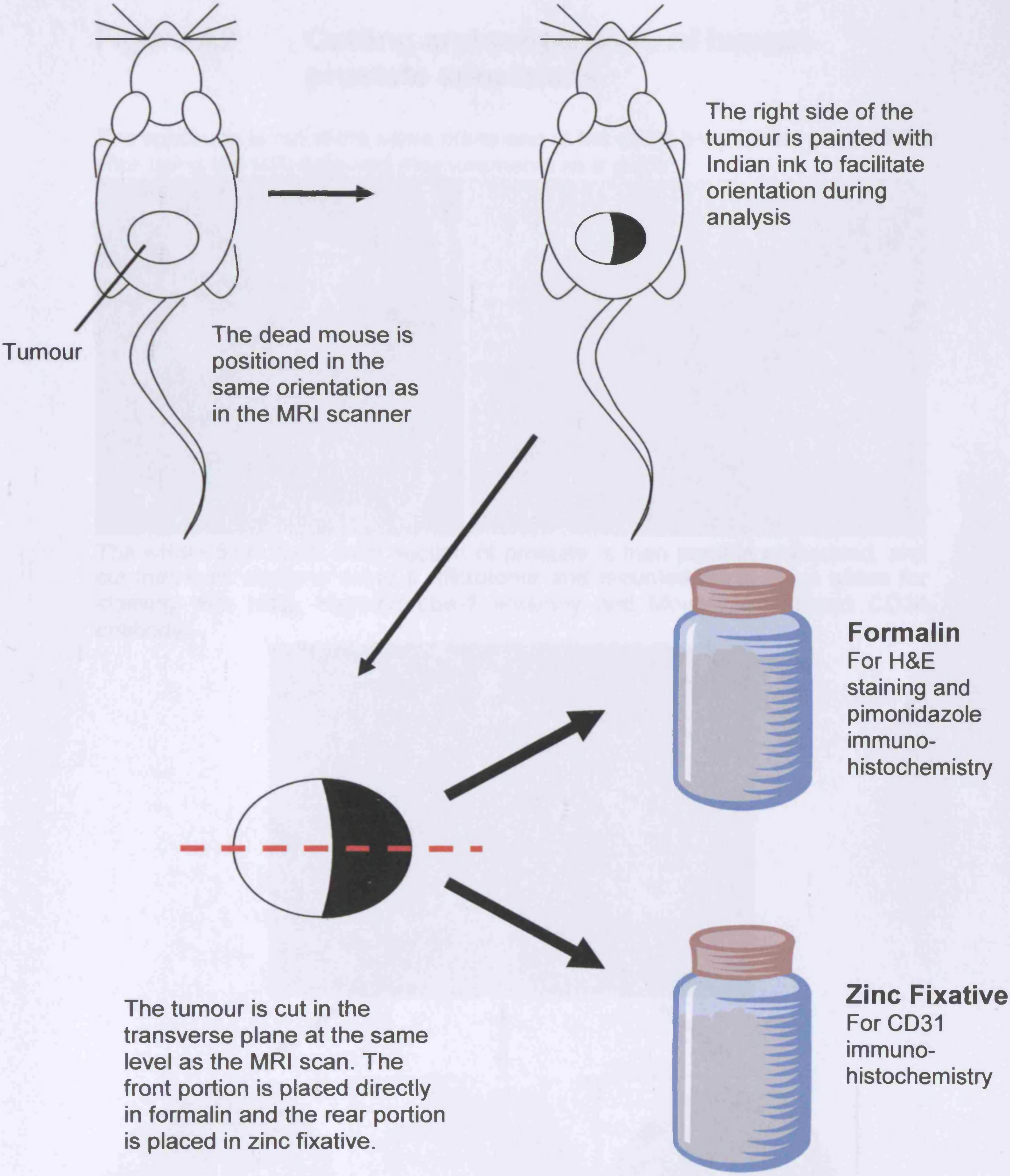

The dead mouse is positioned in the same orientation as in the MRI scanner

The right side of the tumour is painted with Indian ink to facilitate orientation during analysis

Formalin
For H&E staining and pimonidazole immunohistochemistry

Zinc Fixative
For CD31 immunohistochemistry

The tumour is cut in the transverse plane at the same level as the MRI scan. The front portion is placed directly in formalin and the rear portion is placed in zinc fixative.

Figure A1 **Cutting and preparation of murine xenografts**

Figure A2 Cutting and preparation of human prostate specimens

The specimen is cut in the same plane and at the same level as the central MRI slice using the MRI data and measurements as a guide:

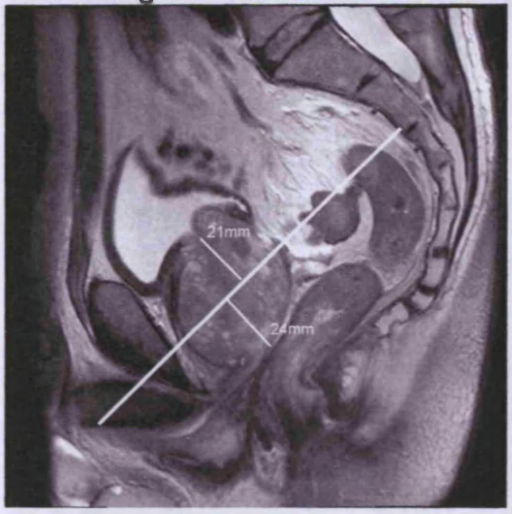

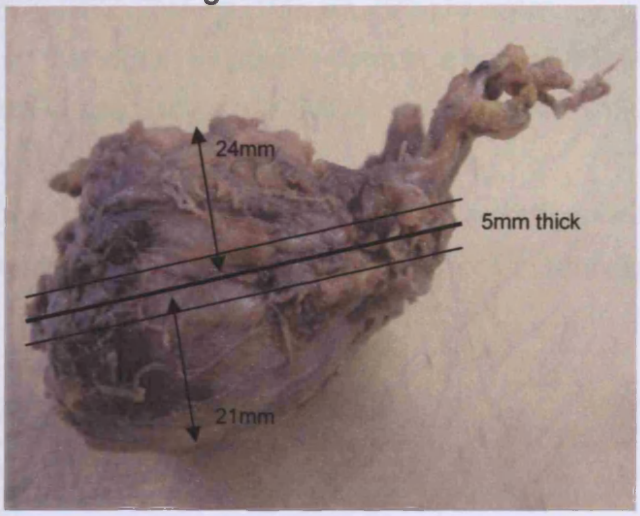

The whole 5mm thick axial section of prostate is then paraffin embedded, and cut into 4μm sections using a microtome and mounted on to glass slides for staining with H&E, Hypoxyprobe-1 antibody and Mouse anti-Human CD34 antibody:

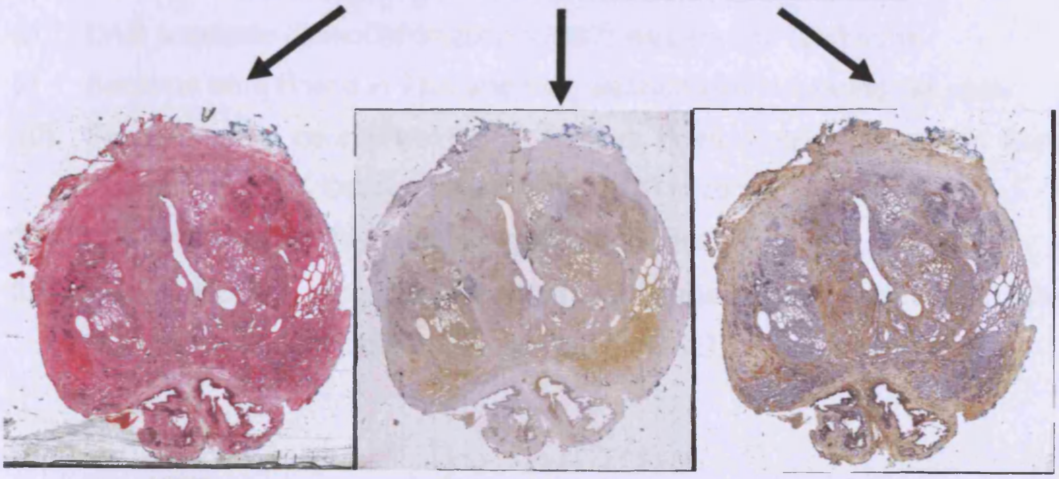

H&E Pimonidazole CD34

A2 Slide preparation for pimonidazole staining

1) The 4µm thick formalin fixed paraffin embedded sections were dewaxed in xylene for five minutes.
2) Sections were rehydrated through graded alcohols (100, 90, 70%) to water.
3) Antigen retrieval was performed on the slides by placing them in a bath of 10mM citric acid (pH6) and boiling for 8 minutes using an 800W microwave oven (2450 MHz Panasonic NN-6453BBPQ).
4) The volume of fluid was topped up to its original level and the slides were then left to stand for 20 minutes at room temperature before being washed well in running tap water.

A3 Pimonidazole Staining

A3.1 For tumour xenografts in mice

1) Sections were rinsed in Tris Buffer Saline (TBS).
2) Dako Protein Block (DakoCytomation Ely Cambs X0909) was applied for 5 minutes.
3) Excess was tipped off.
4) Hypoxyprobe-1 antibody (Chemicon Europe Ltd Hamps HP2-100) diluted 1/100 in antibody diluent (DakoCytomation S2022) was applied for 60 minutes.
5) Sections were washed in TBS (3mins).
6) Anti-FITC monoclonal antibody (Chemicon Europe Ltd) diluted 1.100 in Dako antibody diluent was applied for 30 minutes.
7) Sections were washed three times in TBS (3mins).
8) DAB substrate (DakoCytomation K3467) was applied for 5 mins.
9) Sections were rinsed in TBS and then washed well in running tap water.
10) Sections were counterstained in Mayers haematoxylin (Surgipath Europe Ltd Peterborough UK Cat No 01582E) for 10-60 seconds.
11) Sections were washed well in running tap water.
12) Finally, sections were dehydrated through graded alcohols, cleared in xylene and mounted in DPX (Surgipath Europe Ltd 08600E).

A3.2 For Human Prostates

1. Endogenous peroxidase was blocked using Dako peroxidase block (DakoCytomation S2023)) for 5 mins
2. Sections were washed in running tap water
3. Dako Protein Block (X0909) was applied for 5 minutes.
4. Excess was tipped off.
5. Anti-Pimonidazole IGg1 antibody (Chemicon Europe Cat no HP1) diluted 1/100 in TBS for 30mins was applied.
6. Specimens were washed three times in TBS (3mins).
7. Envision HRP polymer (DakoCytomation K5007) was applied for 30 minutes.
8. Wash three times in TBS (3mins)
9. DAB substrate (DakoCytomation,part of K5007 kit) was applied for 5 minutes.
10. Specimens were rinsed in TBS and then washed well in running tap water.
11. Specimens were counterstained with Mayers Haematoxylin (Surgipath Europe Ltd, 01522E) for 10-60 seconds.
12. Specimens were washed again in running tap water.
13. Specimens were then dehydrated through graded alcohols, cleared in xylene and mounted in DPX (Surgipath Europe Ltd 08600E).

A4 Slide preparation for vascular endothelial staining (CD31 / CD34)

1) 4um paraffin sections were dewaxed in xylene and rehydrated through grade alcohols (100,90 and 70%) to water.
2) Sections were transferred to a slide tray and rinsed with TBS (Tris Buffered Saline). Sections were dried and circled with a resin pen.

A4.1 CD31 staining for tumour xenografts in mice

1) Dako Peroxidase blocking reagent (S2023) was applied for five minutes.
2) Sections were rinsed in distilled water.
3) Sections were rinsed in TBS.
4) Dako serum free protein block (X0909) was applied for five minutes.
5) Excess solution was discarded and rat anti-mouse CD31 (pecam-1) antibody was applied (Pharmingen Int., 01951A) diluted 1/500 in TBS for one hour at room temperature.
6) Sections were washed three times in TBS, over three minutes.

7) Biotinylated rabbit anti-rat IqG (DAKO, EO468) diluted 1/400 in TBS was applied for one hour at room temperature.
8) Sections were washed three times in TBS (three minutes).
9) Dako StreptABComplex DakoCytomation K0377 was applied for one hour room temperature.
10) Sections were washed three times in TBS (three minutes).
11) Excess fluid was drained off and DAB solution was applied for five minutes (Vector SK-4100).
12) Sections were rinsed in distilled water and then washed well in tap water.
13) Mayers Haematoxylin counter stain was applied for 5-60 seconds.
14) Sections were washed in running tap water.
15) Sections were dehydrated through graded alcohols, cleared in xylene and mounted in DPX. (surgipath 08600E).

A4.2 CD34 staining for human prostates

1) Slides were pre-treated for 5 minutes in an enzyme bath containing 0.1% trypsin and 1% calcium chloride at 37°C.
2) Slides were washed well in water.
3) Endogenous peroxidase was blocked with DakoCytomation peroxidase block (Dako Cytomation S2023) for 5 minutes.
4) Slides were washed well in water.
5) Slides were rinsed in TBS
6) Protein Block (Dako Cytomation X0909) was applied for 5 minutes.
7) Excess was tipped off.
8) Mouse anti-Human CD34 antibody (Novacastra Labs Ltd Peterborough UK, NCL-L-END) diluted 1/75 in antibody diluent (DakoCytomation UK, S2023).) was applied for 1 hour at room temperature.
9) Slides were washed three times in TBS (3minutes).
10) Dako Envision HRP Mouse polymer ((K5007) was applied for 30 minutes.
11) Slides were washed in TBS.
12) DAB substrate (20ul DAB/1ml) was applied.
13) Slides were rinsed in TBS and then washed well in running tap water.
14) Slides were counterstained in Mayers haematoxylin for 10-60 seconds.
15) Slides were washed well in running tap water.
16) Slides were dehydrate through graded alcohols, cleared in xylene and mounted in DPX.

A5 Digitisation of histology slides [1] (figure A3)

1) The prepared glass slide with a cover slip was cleaned to remove dust and debris and mounted on a Nikon eclipse TE2000-E microscope.
2) Microscopy was performed at x40 (x4 objective lens and x10 eyepiece).
3) Background corrections were performed to compensate for any artefact caused by particles on the lens or due to discolouration of the slide. The 'white average' was created using a clean area of the slide adjacent to the specimen. The 'black average' was determined by blocking the light source.
4) The region of interest was defined on the computer screen using x and y co-ordinates.
5) The focal plane was defined by focusing on three co-ordinates in a triangular pattern within the region of interest (chosen by the computer). The computer then calculated and compensated for any variations in the thickness of the specimen, which may have caused parts of the image to be out of focus. This was particularly important for the large prostate whole-mount specimens.
6) Multiple images were acquired using the computer controlled motorised microscope stage. In order that no part of the specimen was omitted, a 10% overlap between each image was specified.
7) The separate images were then 'stitched' together using an in-house program ('Image Stitching' – Gray Cancer Institute, Northwood, Middlesex, UK). The program used pixel data that allowed alignment at a cellular level. The 10% overlap was removed at this stage.
8) The resulting image was saved as a .tif file.
9) Every pixel of the image contained information in an 8-bit format with a value between 0 and 255 for each of the colours red, green and blue. 0 indicating a total absence of that colour and 255 indicating complete saturation. This provided quantification of colour and allowed subsequent analysis of each histology image on the basis of colour intensity.

Figure A3 Digitisation of histology slides

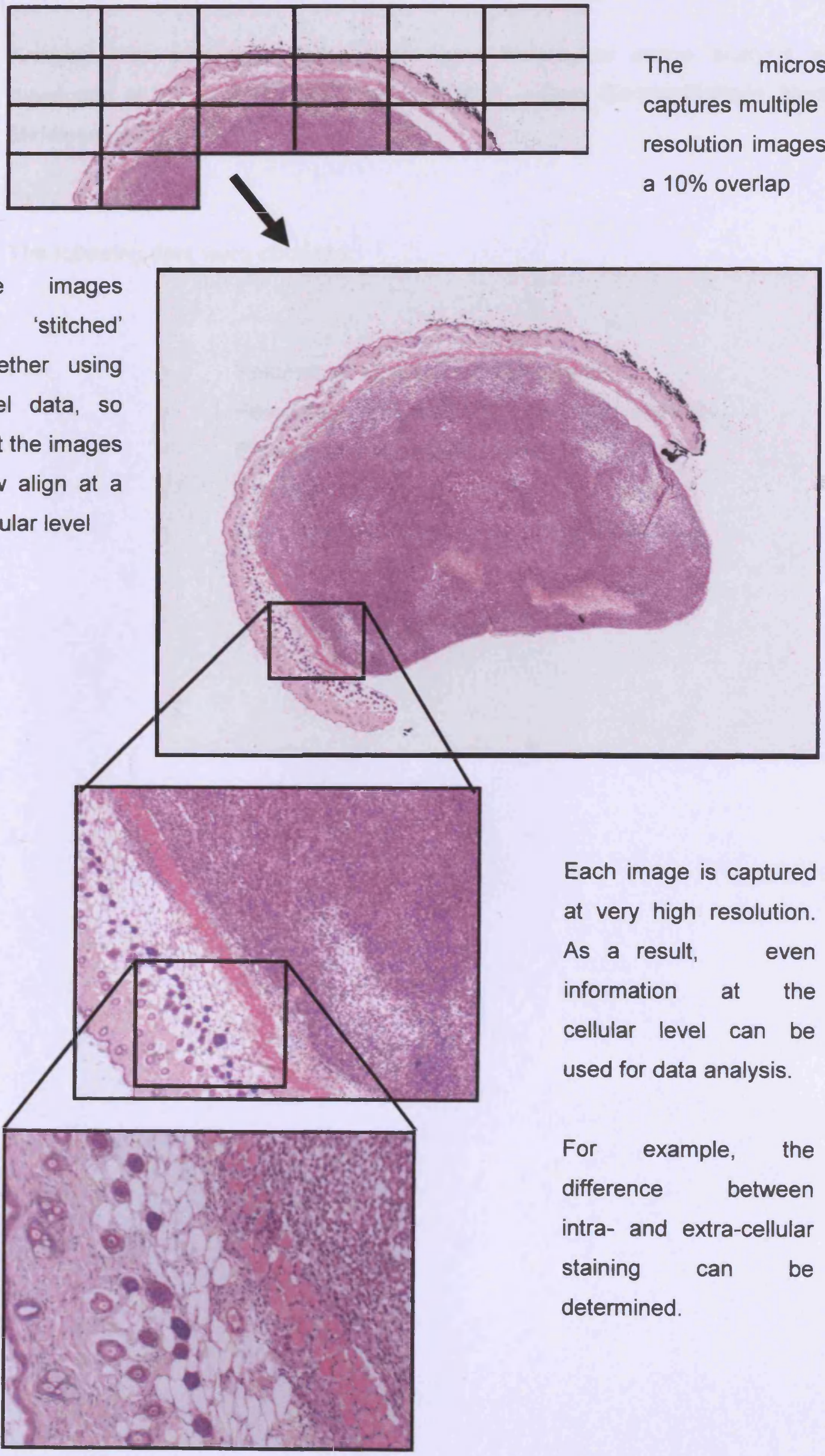

The microscope captures multiple high-resolution images with a 10% overlap

The images are 'stitched' together using pixel data, so that the images now align at a cellular level

Each image is captured at very high resolution. As a result, even information at the cellular level can be used for data analysis.

For example, the difference between intra- and extra-cellular staining can be determined.

A6 Histological Analysis (figure A4)

Analysis was performed using customised histological image analysis software developed at the Gray Cancer Institute ('TRI2' – Gray Cancer Institute, Northwood, Middlesex, UK).

The following data were obtained:

- Percentage area stained for whole ROI
- Percentage area stained for each grid element
- Staining Intensity for whole ROI
- Staining Intensity for each grid element
- Summary statistics for each of the above

Figure A4 Histological Analysis

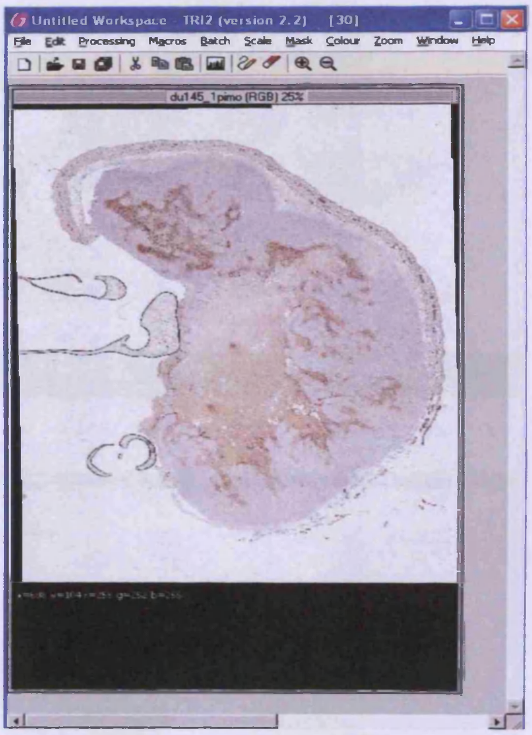

The .tif image was loaded into the TRI2 software.

The image was re-scaled using a standard binning method

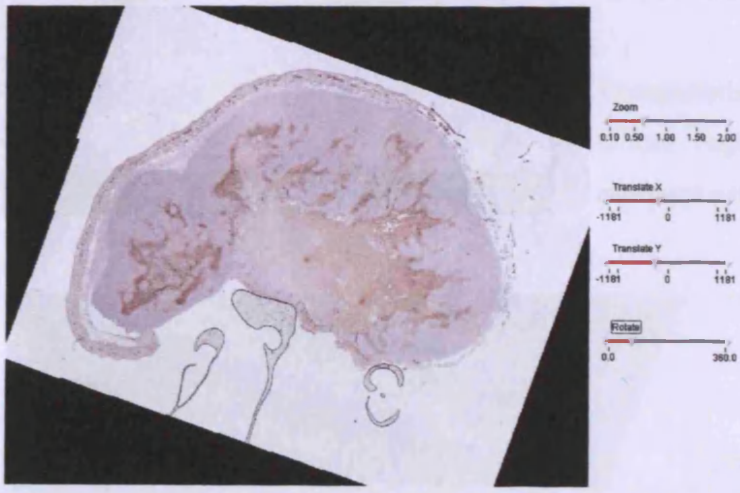

The image was then rotated to match the orientation of the MRI scan.

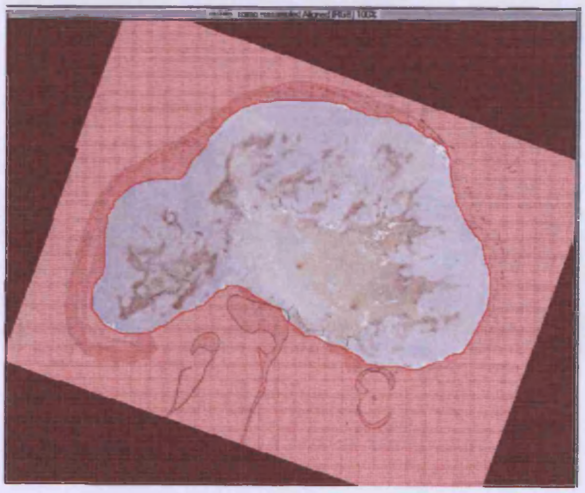

The region of interest (ROI) was drawn.

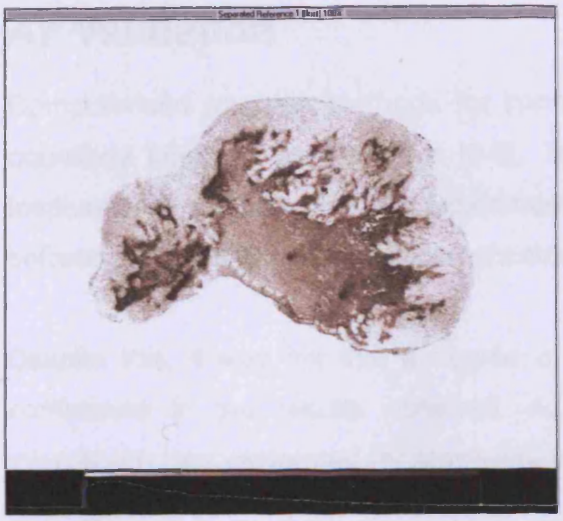

Linear unmixing was performed on the image. This process picked out the brown pixels from the non-brown pixels. The range of saturation and hue for the brown colour was pre-chosen to match the colour range of the immunohistochemical staining.

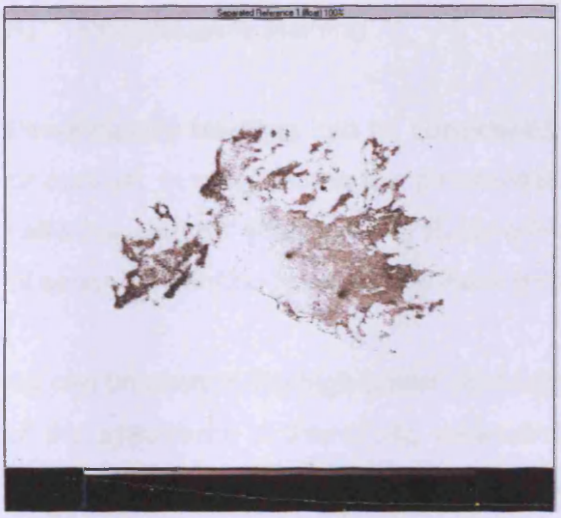

Pre-determined intensity thresholds were set to exclude background staining. These thresholds varied between tumour type and between immunohistochemical stains.

The resulting image was converted to 8-bit format to facilitate data processing.

Grids were applied.

Computerised calculation provided data for the whole region of interest and for each grid element within it.

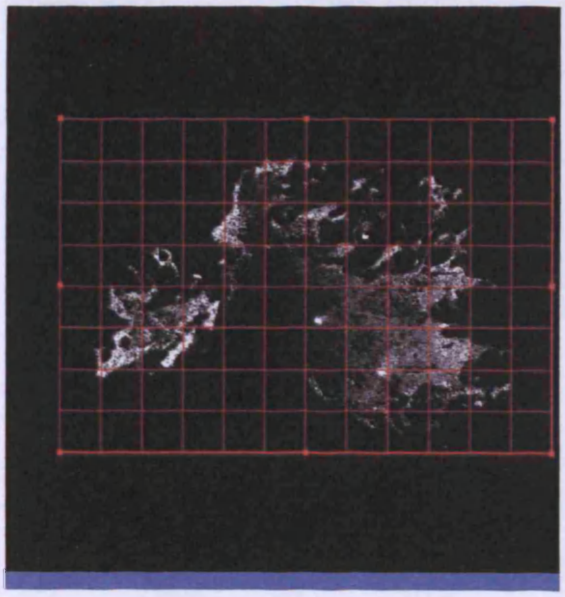

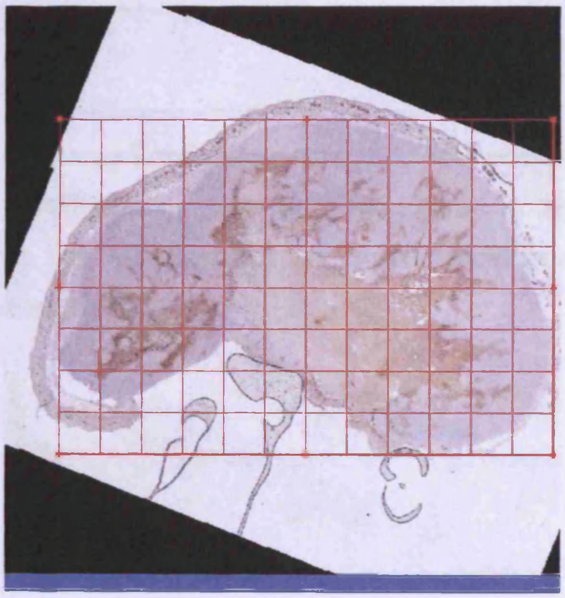

A7 Validation

Computerised analysis methods for immunohistochemical analysis have been used countless times in the literature [2-6]. The 'in-house' software at the Gray Cancer Institute that was used in these experiments is the latest version of continually evolving software that has been in development since 2003.

Despite this, it was felt that a degree of internal validation was required to provide confidence in the results obtained. As a result, manual verification using light microscopy was performed for approximately 10% of the grid elements for each stain in each tumour:

A) Pimonidazole staining

Pimonidazole labelling can be considered 'positive' if the brown staining is cytoplasmic or nuclear, in other words the pimonidazole is bound within the cell as a result of the cell's low oxygen environment. Extracellular staining is artefactual and usually a result of secondary antibody binding to extracellular protein elements within the tissue.

As can be seen in the high power light microscopy images in **figure A5**, taken from one of the specimens in this study, intracellular pimonidazole labelling predominates with virtually no background staining. There is sharp demarcation between labelled and unlabelled cells. It is therefore likely that brown pixels on the computerised analysis image correspond accurately to intracellular pimonidazole staining.

The manual verification has confirmed this:
10% of grid squares were manually scored using light microscopy at x400 power. Estimates of the percentage area of pimonidazole staining per grid were made to the nearest 10%. These were compared with the results obtained by computerised analysis. A high degree of correlation was seen ($r^2 = 0.95$).

Figure A5 A high power light microscopy image showing the cytoplasmic and nuclear pimonidazole staining in a section of human prostate carcinoma.

Note that there is virtually no background brown staining.

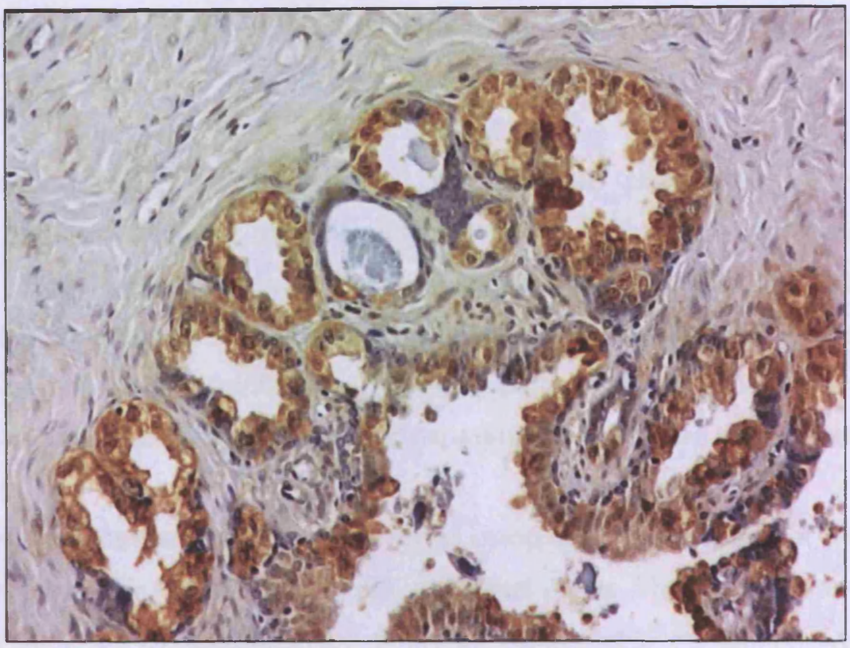

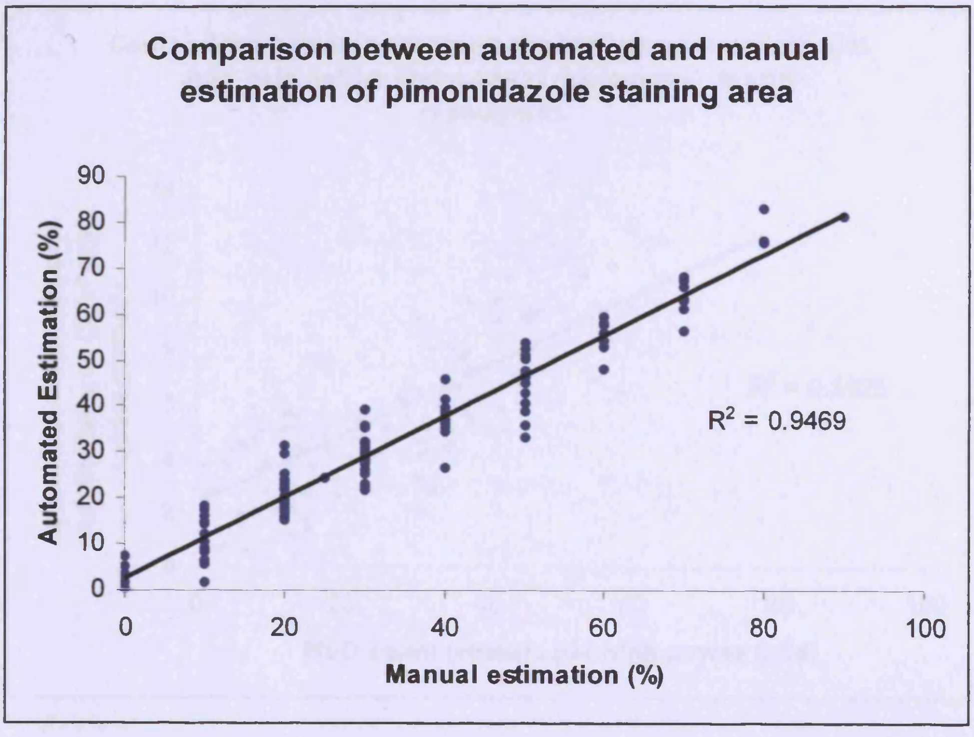

B) CD31 / CD34 staining

This situation with CD31/CD34 is more complex than for pimonidazole labelling because of two factors:

1) There is a higher degree of background staining, especially for fibrotic tumours.
2) Computerised analysis calculates the proportion of brown stain within any given region and can therefore only reflect the total vascular endothelial cross sectional area, NOT the microvessel density.

Despite these factors, the critical point that requires clarification is whether the proportion of brown staining, as determined by computer analysis, correlates with the number of blood vessels within any given region of interest. Correlations between MVD counts and total vascular endothelial area counts have already been reported in the literature [7, 8]. A manual verification analysis was performed for both the animal and human immunohistochemistry used in the experiments presented in this thesis:

10% of grid squares were manually scored using light microscopy at x400 power. Estimates of the microvessel density per grid were made. These were compared with the results obtained by computerised analysis. Reasonable correlation was seen for the animal tumours ($r^2 = 0.59$), less correlation was observed in the human prostates reflecting the high degree of fibrosis in areas of benign hyperplasia ($r^2 = 0.28$):

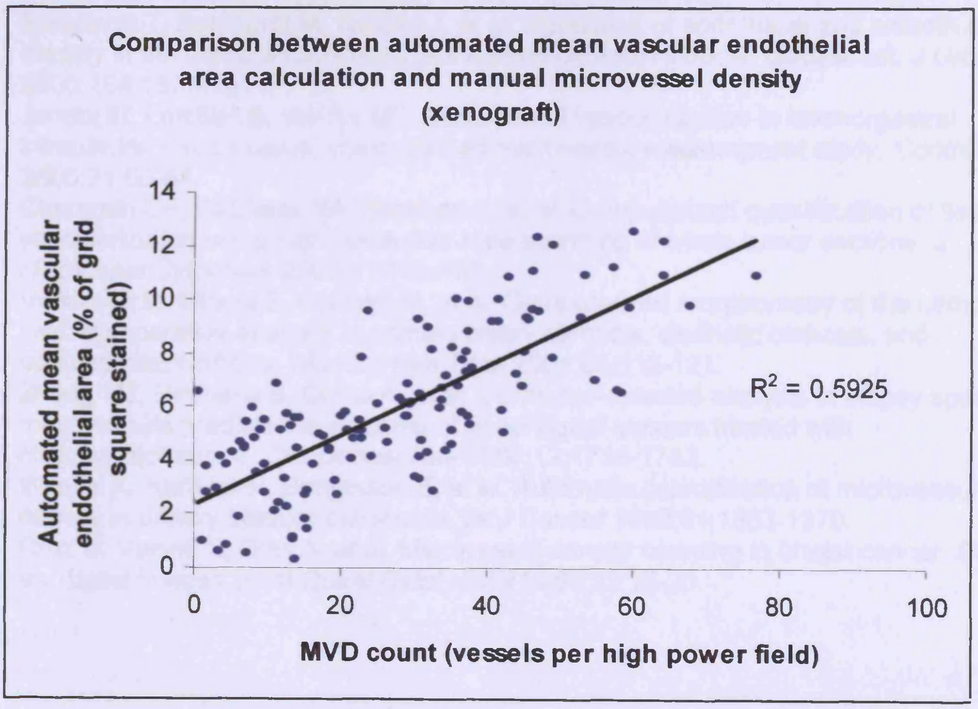

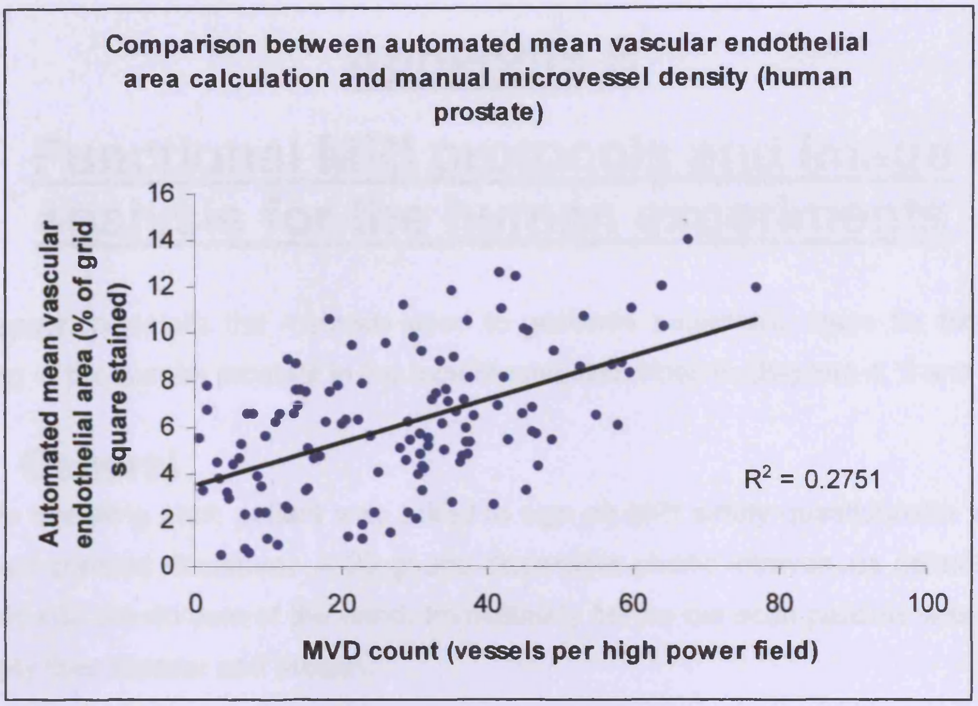

References

1 Barber PR, Vojnovic B, Atkin G, *et al.* Applications of cost-effective spectral imaging microscopy in cancer research. *J. Phys. D: Appl. Phys.* 2003;36:1729–1738.

2 Burchardt T, Burchardt M, Karden J, *et al.* Reduction of endothelial and smooth muscle density in the corpora cavernosa of the streptozotocin induced diabetic rat. *J Urol* 2000;164:1807-1811.

3 Jondet M, Letellier B, Verdys MT. Endometrial vascularization in levonorgestrel intrauterine device users; computerized microvessel measurement study. *Contraception* 2005;71:60-64.

4 Chantrain CF, DeClerck YA, Groshen S, *et al.* Computerized quantification of tissue vascularization using high-resolution slide scanning of whole tumor sections. *J Histochem Cytochem* 2003;51:151-158.

5 Vertemati M, Minola E, Goffredi M, *et al.* Computerized morphometry of the cirrhotic liver: comparative analysis in primary biliary cirrhosis, alcoholic cirrhosis, and posthepatitic cirrhosis. *Microsc Res Tech* 2004;65:113-121.

6 Zhang SC, Hironaka S, Ohtsu A, *et al.* Computer-assisted analysis of biopsy specimen microvessels predicts the outcome of esophageal cancers treated with chemoradiotherapy. *Clin Cancer Res* 2006;12:1735-1742.

7 Wester K, Ranefall P, Bengtsson E, *et al.* Automatic quantification of microvessel density in urinary bladder carcinoma. *Br J Cancer* 1999;81:1363-1370.

8 Cruz D, Valenti C, Dias A, *et al.* Microvessel density counting in breast cancer. Slides vs. digital images. *Anal Quant Cytol Histol* 2001;23:15-20.

Appendix B

Functional MRI protocols and image analysis for the human experiments

This appendix details the methods used to generate parametric maps for biological imaging of the human prostate in the experiments described in chapters 4, 5 and 6.

B1 General

Prior to scanning each patient was asked to sign an MRI safety questionnaire and an informed consent document. A 20 gauge disposable plastic intravenous cannula was inserted into the dorsum of the hand. Immediately before the scan patients was asked to empty their bladder and rectum.

B2 Anatomical Scanning

Small field-of-view T_1 and T_2-weighted anatomical scans perpendicular to the urethra were used to stage tumours and to identify tumour slice locations. Images were inspected for the presence of a peripheral zone abnormality consistent with cancer. The central slice for functional imaging was chosen to contain a satisfactory tumour region for data analysis.

B3 Functional Imaging

1. BOLD-MRI: Five spoiled gradient-echo images were acquired for three slices through the prostate with varying TE (5-60ms), TR=100ms, flip angle=40°, FOV=200mm, 256^2 matrix, from which R_2* maps were calculated.

2. DCE-MRI: Proton density weighted (PDW) images were acquired for three slices to facilitate the calculation of kinetic parameters (TE 10ms, TR 350ms, flip angle=10°, three slices of eight millimetre thickness). T_1-weighted spoiled gradient recall echo [FLASH] sequences (TE 5ms, TR 74ms, flip angle = 70°, 3 slices) were acquired with a time resolution of 12 seconds (40 time points over 8 minutes) for three slices through the prostate. A bolus of 0.1 mmol/kg b.w. of gadopentetate dimeglumine contrast agent was administered at 4 millilitres per second during the fifth image acquisition (i.e. beginning after 48 seconds) using a power injector.

3. DSC-MRI: A T_2*-weighted sequence was used to acquire data every 2 seconds over 2 minutes (TE 20ms, TR 30ms, flip angle = 40 °, one slice of eight millimetre thickness). A bolus of 0.2 mmol/kg b.w. of Gd-DTPA was administered at 4ml/s after 20 seconds.

4. Diffusion Imaging: Five images were obtained for three slices through the prostate (TE 137ms, TR 3600ms, flip angle = 90 °) with b-values of 0, 50, 150, 500 and 1000 from which ADC maps were calculated.

B4 MRI data Analysis

Voxel based calculations were performed using two customised analysis software packages developed at the Institute of Cancer Research, Royal Marsden Hospital, London, UK. For the T_1 and T_2* weighted dynamic imaging, Magnetic Resonance Imaging Workbench© (MRIW) version 4.2.1 was used. For the BOLD-MRI and diffusion weighted imaging analysis, DiffusionView© version 2.1.3 was used.

R_2* maps were calculated using in-house software written in IDL (Research Systems; Boulder, CO). A straight line was fitted to a plot of $\ln S_t$ against TE for each pixel using a least-squares approach, of which the gradient is -R_2* (units s^{-1}) **(figure B1)**. Pixels with either negative or zero values were excluded from analysis. The dynamic MRI images were analyzed using custom analysis software (MRIW). R_2* values were calculated for each time point of the T_2*- weighted DCE-MRI data set and fitted using a γ-variate function:

$$C(t) \alpha \Delta R_2 * (t) = -\frac{1}{TE} \ln\left(\frac{S(t)}{S_0}\right)$$

Where C(t) is contrast agent concentration in blood at time t, S_0 and S(t) are the signal intensities at the baseline and at time t, respectively and TE is the echo time of the MR sequence used. The relative blood volume (rBV; arbitrary units) is then the integral of the ΔR_2*-time curve (using the γ-variate fit).

$$rBV = \int \Delta R_2 *(t) dt$$

The relative mean transit time (MTT) was approximated by measuring the width of the ΔR_2*-time curve at half its maximum value. Relative blood flow (rBF) was then obtained by substituting in the transit time equation:

$$MTT = rBV/rBF$$

Figure B1

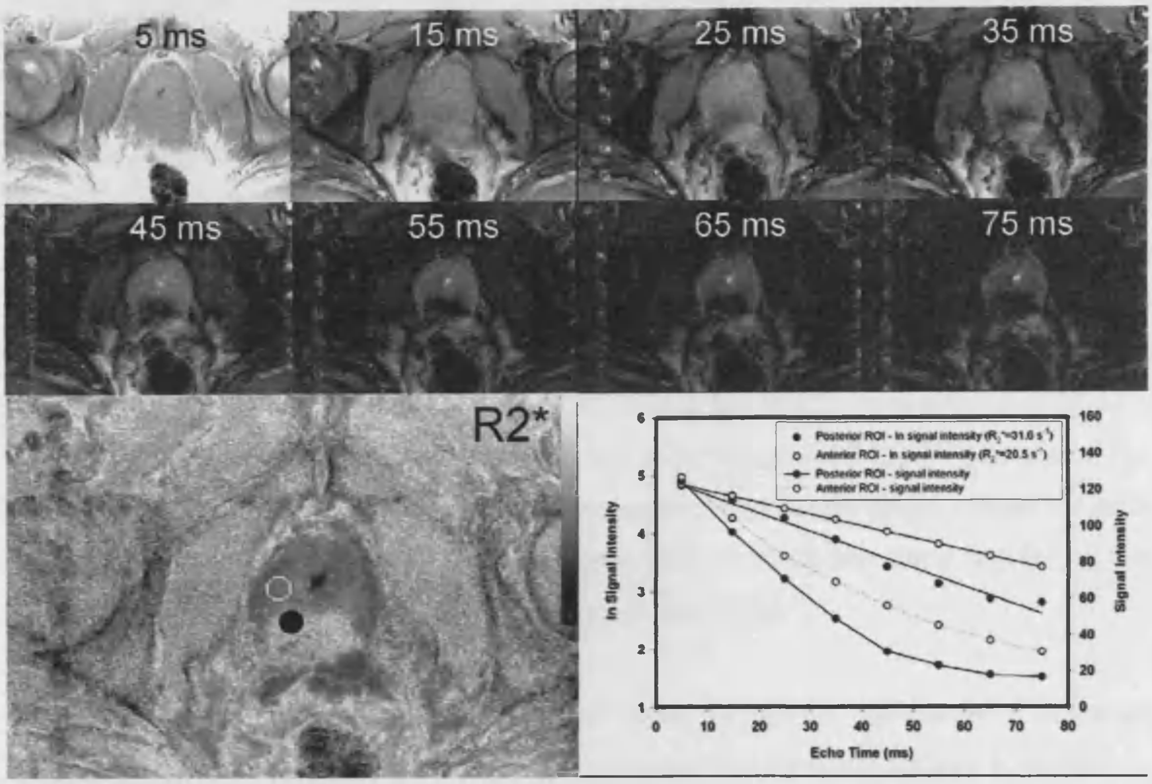

Blood oxygenation level dependent (BOLD)-MRI data collection and analysis. The top two rows show the native BOLD-MRI images acquired with lengthening echo time values raging from 5 to 75 ms. It can be seen that the back of the gland darkens faster than the front of the gland. Signal intensity and ln signal intensity changes are shown in the graph, as well as the linear regression of the ln signal intensity data. The gradient of the linear regression is the R_2* value in s^{-1}. This process is repeated for every pixel to yield the R_2* map (bottom row, left). The positions of the two regions of interest (ROIs) shown in the graph are indicated on the R_2* map.

B5 Region of interest (ROI) definition

Initially, four regions of interest were outlined for each prostate (whole prostate, tumour, peripheral zone and central zone). **(figure B2)**

ROIs were defined using information from several acquisition sequences. The whole prostate ROIs were defined on T_2-weighted images. Tumour ROIs were defined using combinations of T_2-weighted, contrast enhanced T_1-weighted and diffusion ADC maps. In general, an irregular mass of low signal intensity in the peripheral zone seen on the T_2-weighted images was considered to represent tumour. When an obvious malignant peripheral zone tumour was contiguous with homogeneous low signal intensity in the central gland, the finding was interpreted as probable central glandular involvement. A consultant radiologist with a specialist interest in prostate cancer independently verified these regions (ARP). Normal peripheral zone was determined on the basis of homogeneous high signal intensity on non-contrast enhanced T_2-weighted sequences. Benign prostatic hyperplasia, which arises from the transitional zone, was considered part of the central gland of the prostate (central and transitional zones). The MR imaging features of benign prostatic hyperplasia were uniform areas of low signal intensity (glandular benign prostatic hyperplasia) or areas of nodular whorls with low signal intensity. Central zone ROIs were also outlined on non-contrast enhanced T_2-weighted sequences, based on anatomical detail.

For the androgen deprivation / reproducibility experiments this was performed for each of the five scans per patient and for all three slices per MRI examination (apart from the T_2*-weighted DSC-MRI scan for which only one slice through the prostate was acquired – see above). Giving a total of 60 ROIs per patient for BOLD, T_1-weighted DCE-MRI and DWI analysis and 20 ROIs per patient for the T_2*-weighted DSC-MRI analysis. For each scan, data from the three slices were combined to produce single values for each of the four prostate regions. ROI definition was performed on the same day for all five scans for each patient to minimise intra-observer variability.

For the immunohistochemical analysis in chapter 5, 5x5mm grid-based ROIs were defined using the DiffusionView© software package and then transposed to MRIW for the dynamic analysis **(figure B3)**. The DiffusionView© software was able to analyse all grid elements simoultaneously, whereas in MRIW each grid element had to be analysed separately. The following parameters were measured / calculated:

BOLD MRI	R_2*
T_1-weighted DCE MRI (semi-quantitative)	AUC
T_1-weighted DCE MRI (quantitative)	Ktrans
	Kep
	Ve
T_2-weighted DSC MRI	rBV
	rBF
Diffusion Weighted Imaging	Overall ADC, b-values 0–1000
	Early ADC, b-values 0–150
	Late ADC, b-values 500–1000

B6 Arterial Input Function

The methods and models used to calculate each parameter are described in detail in chapter 2. For quantitative perfusion measurements it is necessary to measure the exact delivery of a tracer, the arterial input function, to the organ in question. In all of the perfusion experiments presented in this thesis, the modified Fritz-Hansen method was used [1-3]. This technique has been validated against arterial blood samples.

Figure B2 Illustration of the method for ROI definition

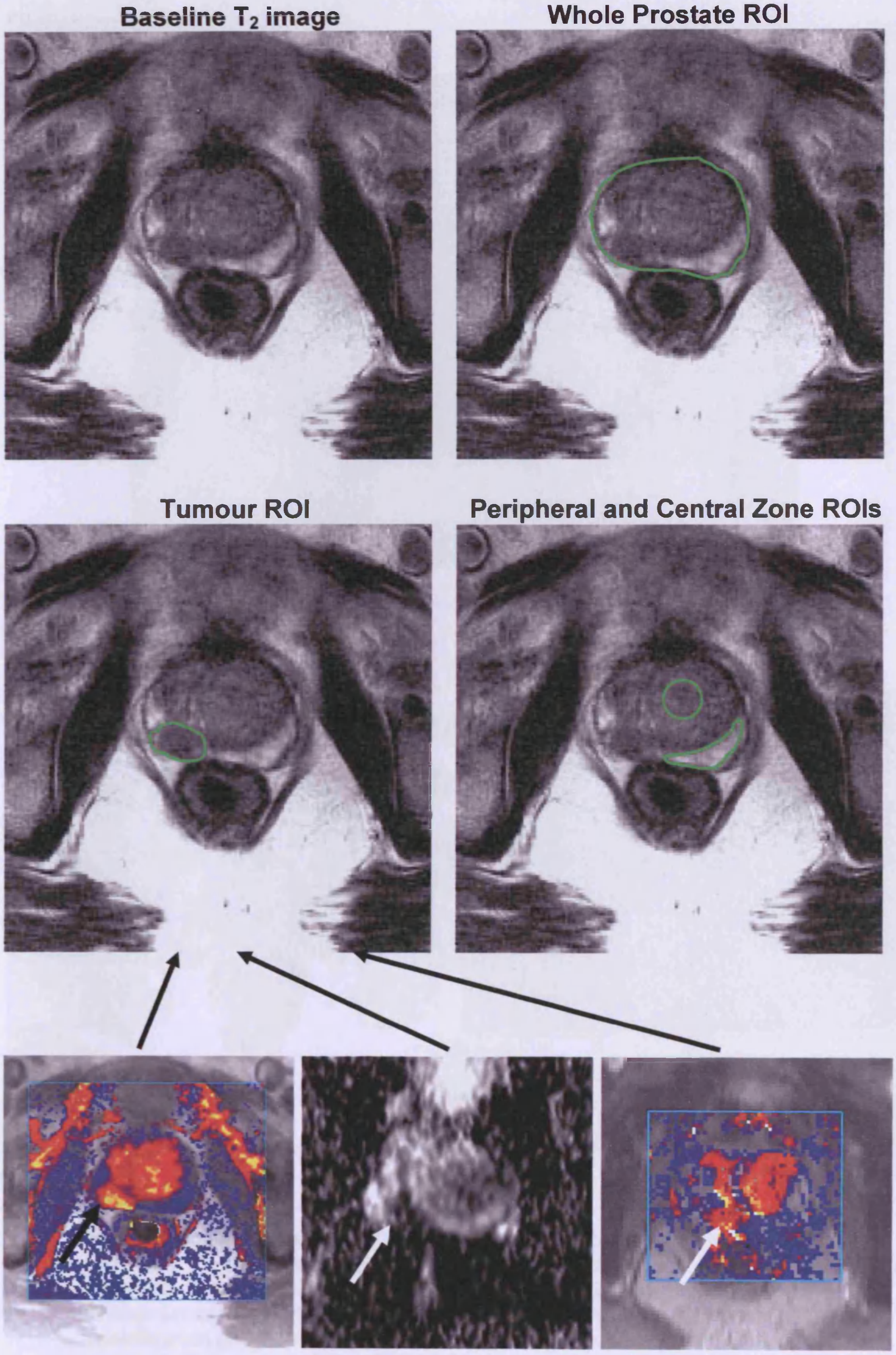
Baseline T_2 image

Whole Prostate ROI

Tumour ROI

Peripheral and Central Zone ROIs

ROIs were defined on T_2-weighted MRI sequences. For tumour regions, information from dynamic and diffusion images were also used to aid localisation and discriminate tumour from benign peripheral zone.

Figure B3 Grid-based ROI definition

DiffusionView©

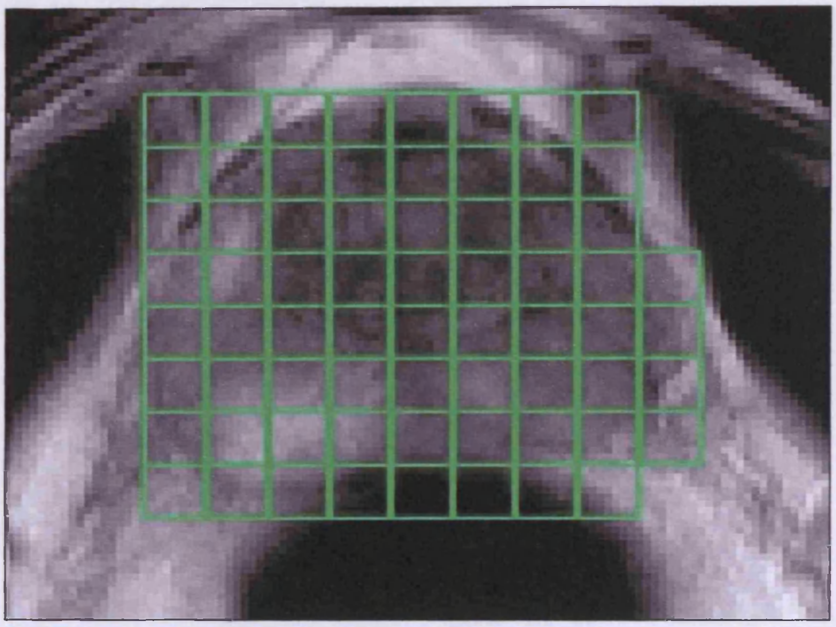

MRIW

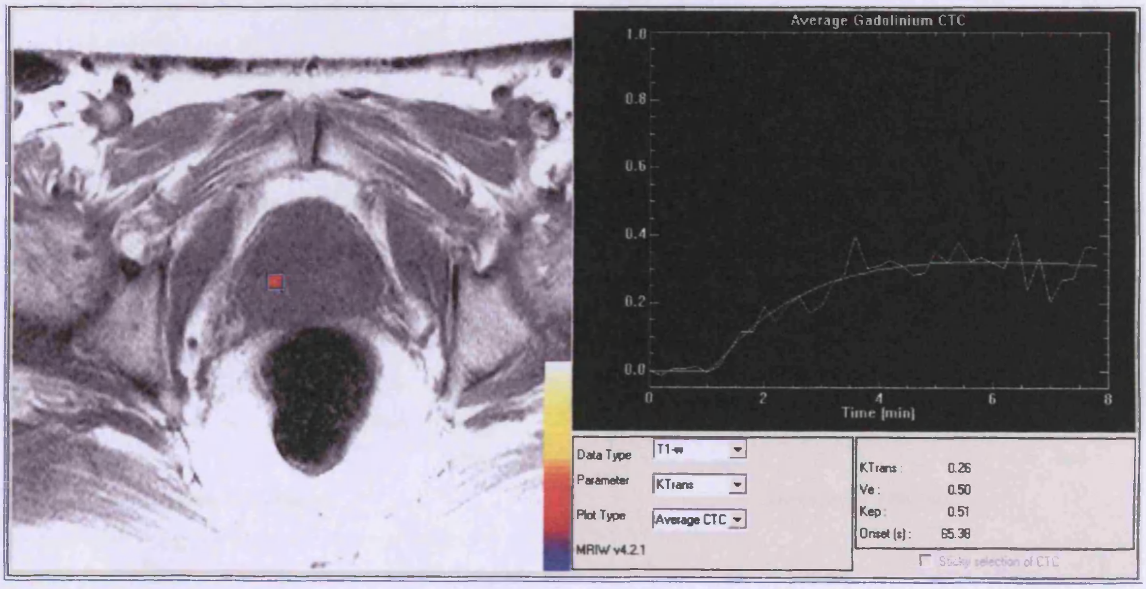

Data Type: T1-w
Parameter: KTrans
Plot Type: Average CTC
MRIW v4.2.1

KTrans : 0.26
Ve : 0.50
Kep : 0.51
Onset (s) : 65.38

☐ Sticky selection of CTC

References

1 Walker-Samuel S, Leach MO, Collins DJ. Evaluation of response to treatment using DCE-MRI: the relationship between initial area under the gadolinium curve (IAUGC) and quantitative pharmacokinetic analysis. *phys med biol* 2006;51:3593–3602.

2 Walker-Samuel S, Parker C, Leach MO, *et al.* Reproducibility of reference tissue quantification of dynamic contrast-enhanced data: comparison with a fixed vascular input function. *phys med biol* 2007;52:75–89.

3 Fritz-Hansen T, Rostrup E, Larsson HBW, *et al.* Measurement of the Arterial Concentration of Gd-DTPA Using MRI: A Step Toward Quantitative Perfusion Imaging. *Magn Reson Med* 1996;36:225-231.

Appendix C

Difference between median parameter values plotted against mean of median parameter values. Mean difference is shown with 95% confidence interval.

T$_1$-weighted Parameters

K^{trans}

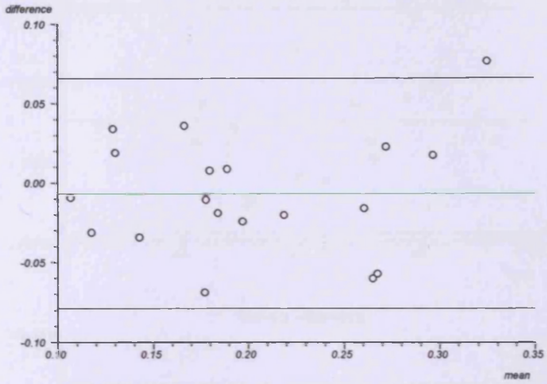
Whole Prostate - Baseline

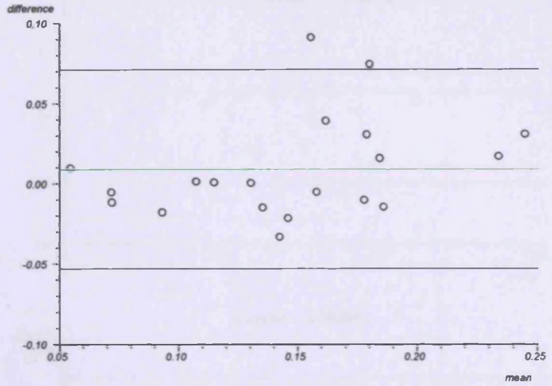
Whole Prostate – 3 Months

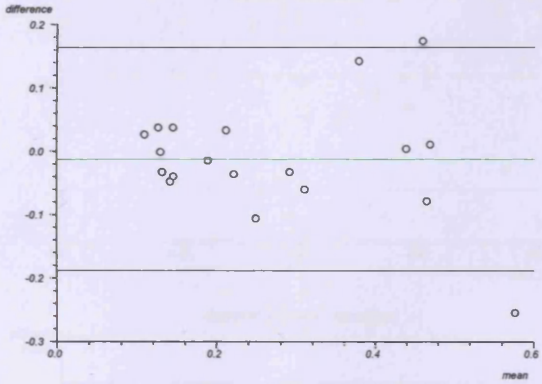
Tumour - Baseline

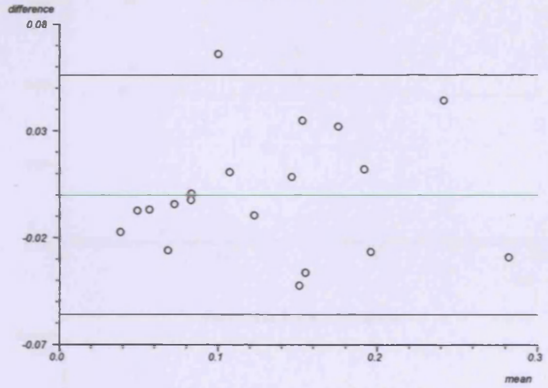
Tumour – 3 Months

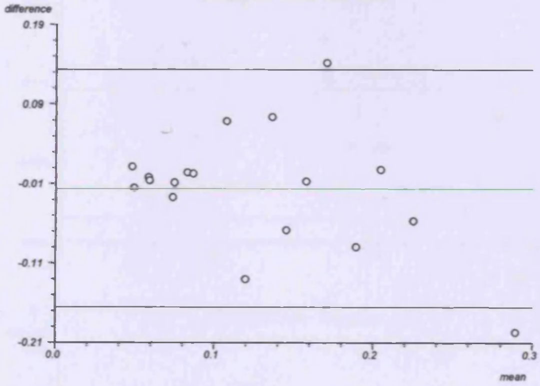
Peripheral Zone - Baseline

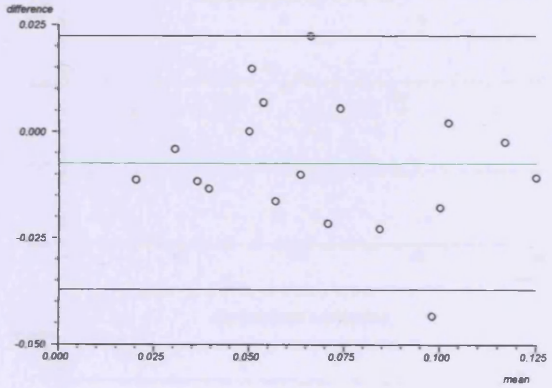
Peripheral Zone – 3 Montls

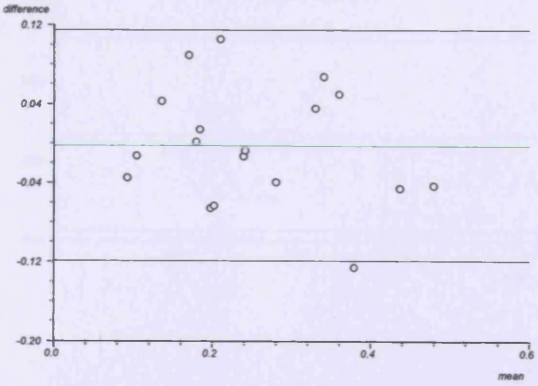
Central Zone - Baseline

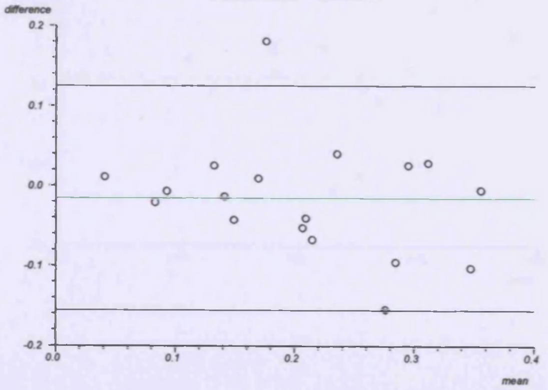
Central Zone – 3 Months

v_e

Whole prostate - Baseline

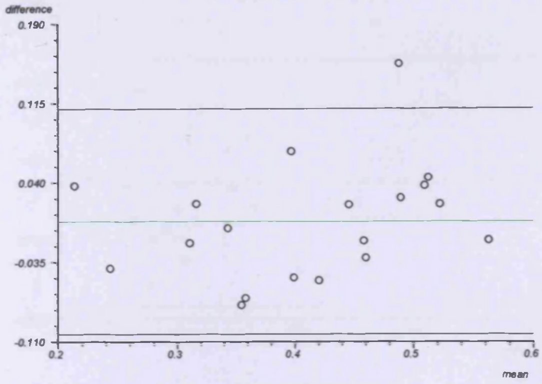

Whole Prostate – 3 Months

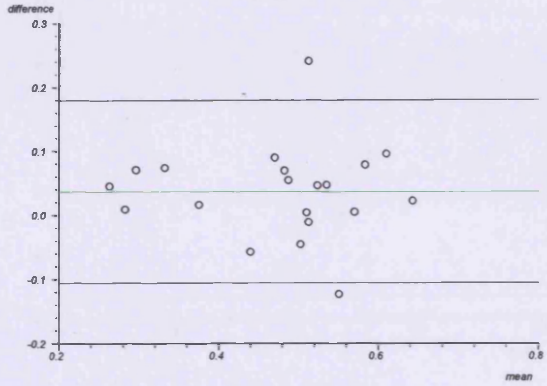

Tumour - Baseline

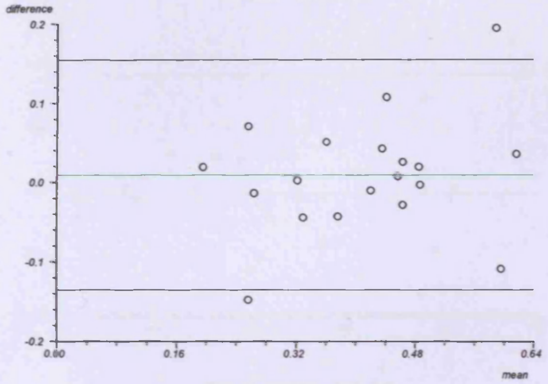

Tumour – 3 Months

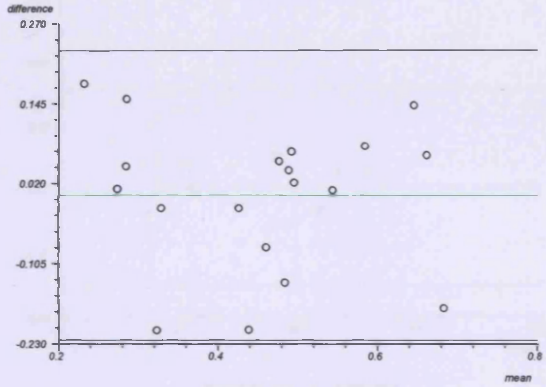

Peripheral Zone - Baseline

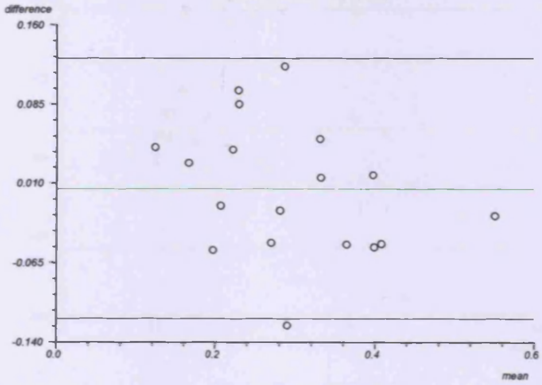

Peripheral Zone – 3 Months

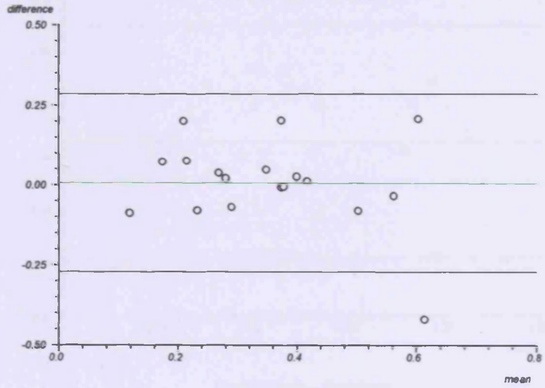

Central Zone - Baseline

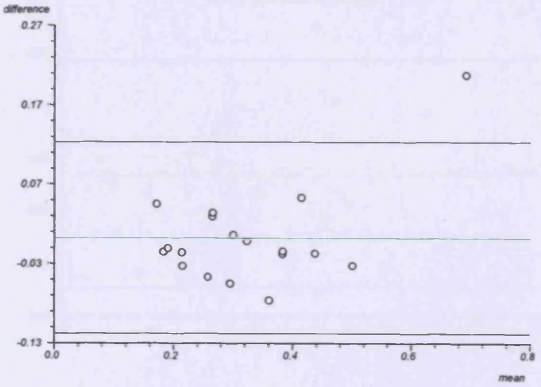

Central Zone – 3 Months

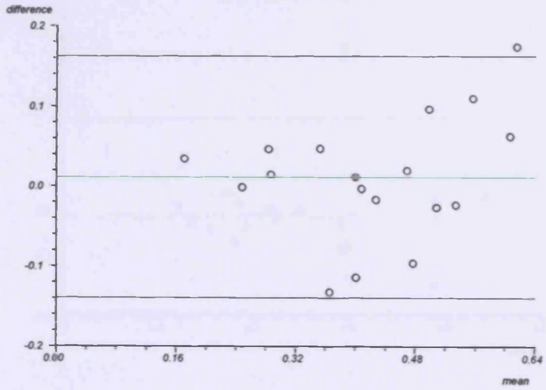

k_{ep}

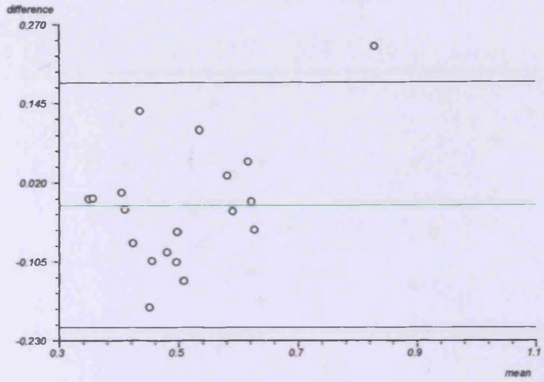
Whole Prostate - Baseline

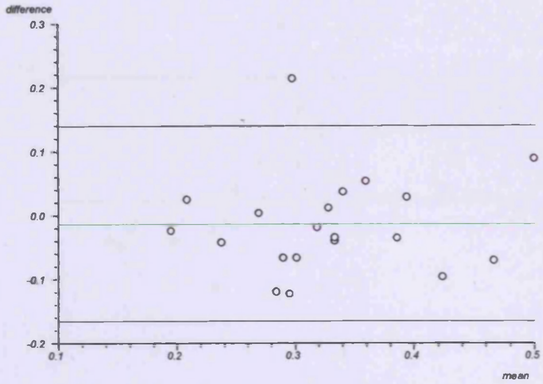
Whole Prostate – 3 Months

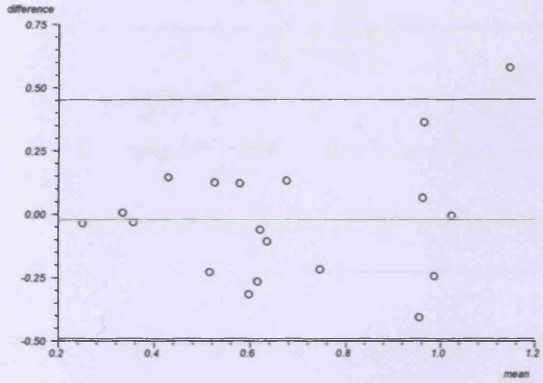
Tumour - Baseline

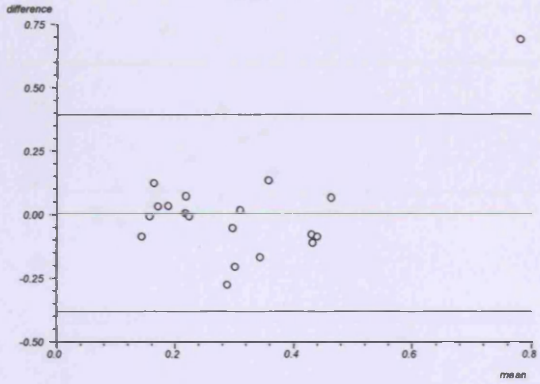
Tumour – 3 Months

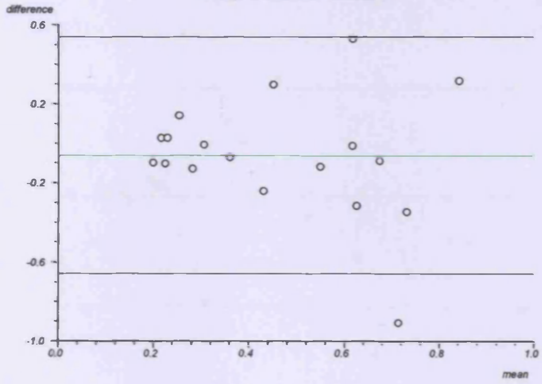
Peripheral Zone - Baseline

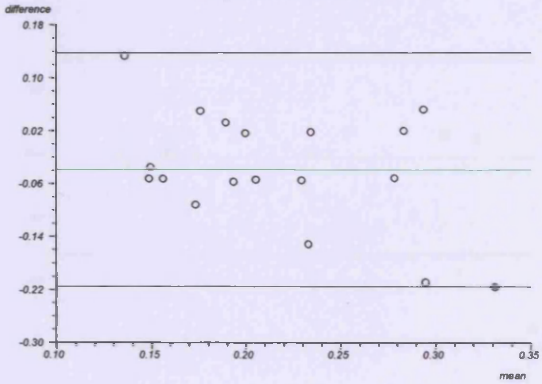
Peripheral zone – 3 Months

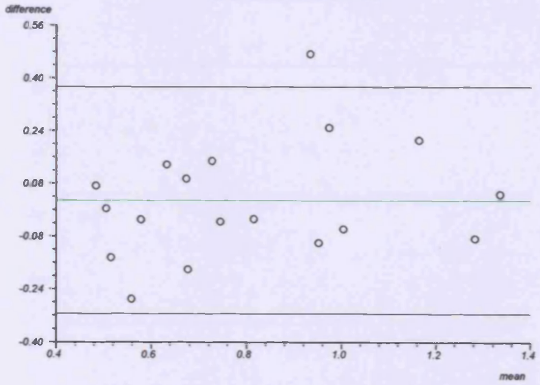
Central Zone - Baseline

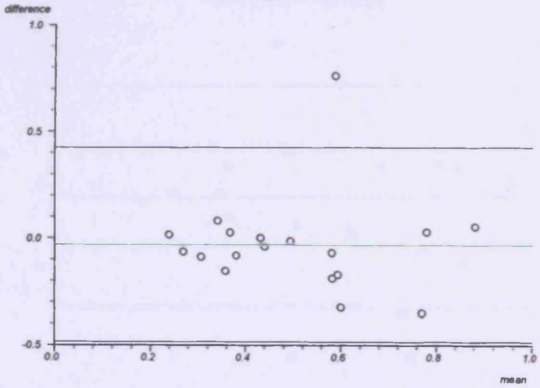
Central Zone – 3 Months

AUC$_{60}$

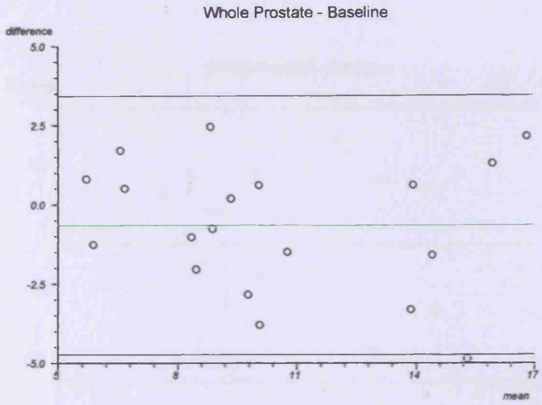
Whole Prostate - Baseline

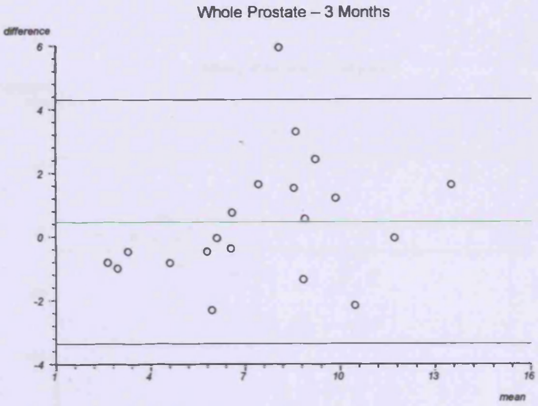
Whole Prostate – 3 Months

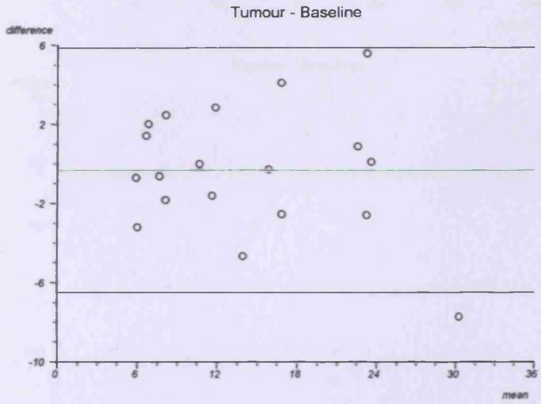
Tumour - Baseline

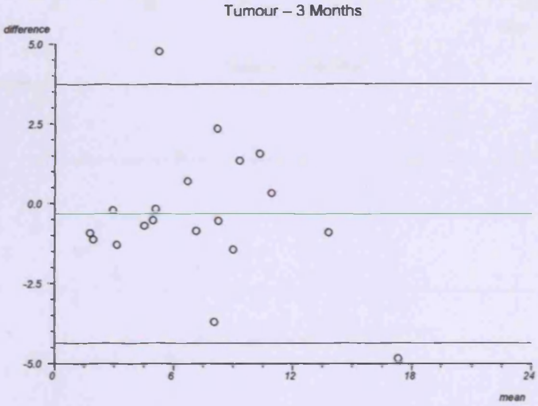
Tumour – 3 Months

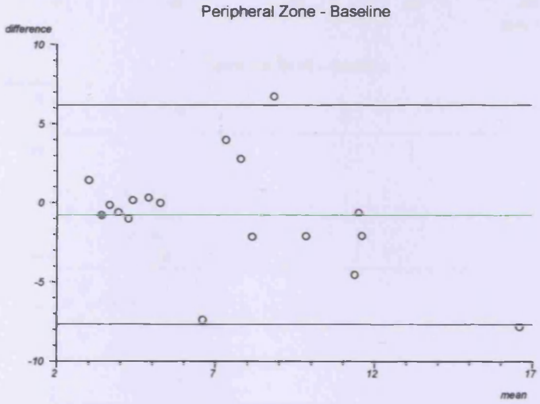
Peripheral Zone - Baseline

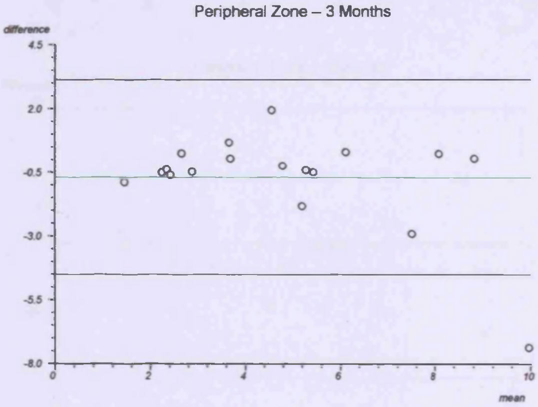
Peripheral Zone – 3 Months

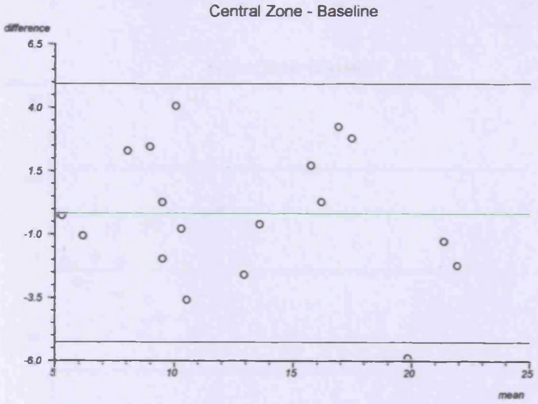
Central Zone - Baseline

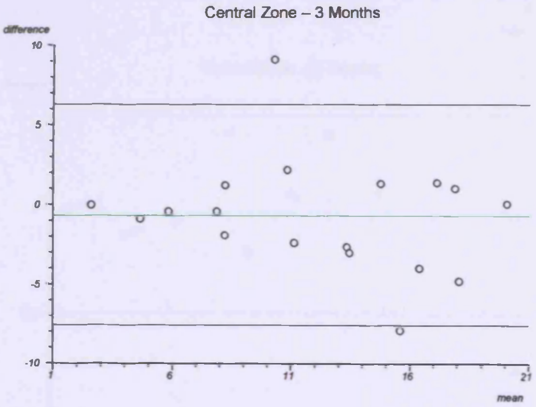
Central Zone – 3 Months

T_2*-weighted Parameters

rBV

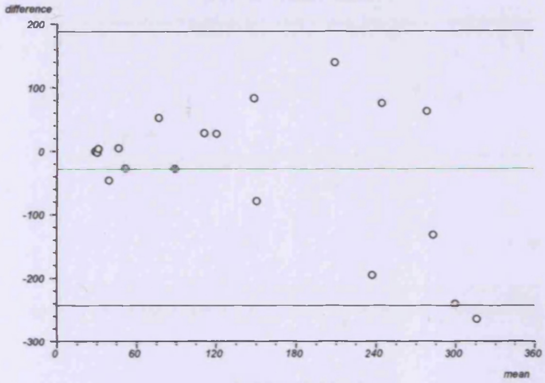
Whole Prostate - Baseline

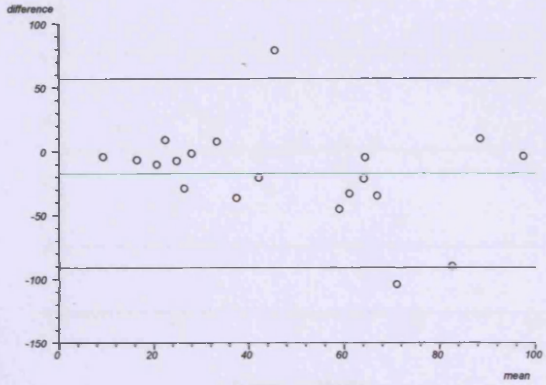
Whole Prostate – 3 Months

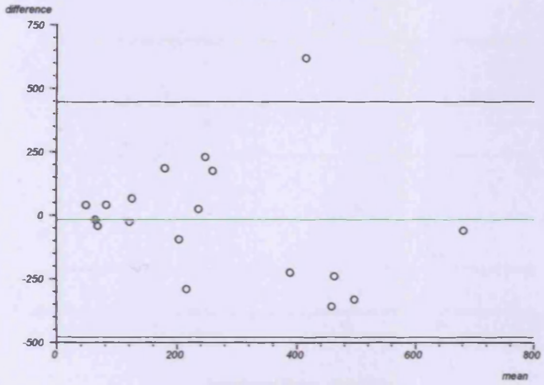
Tumour - Baseline

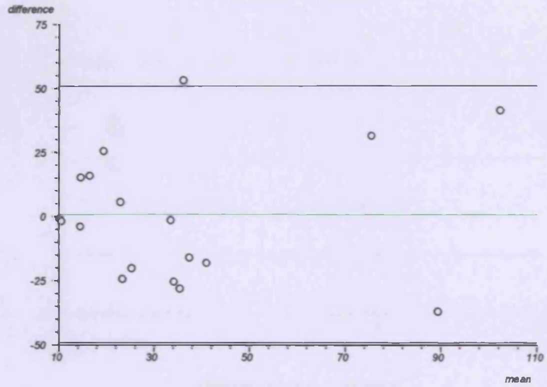
Tumour – 3 Months

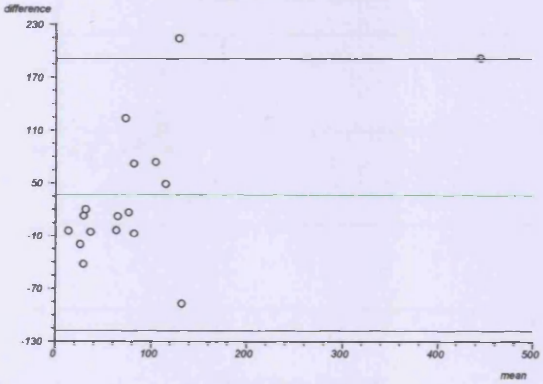
Peripheral Zone - Baseline

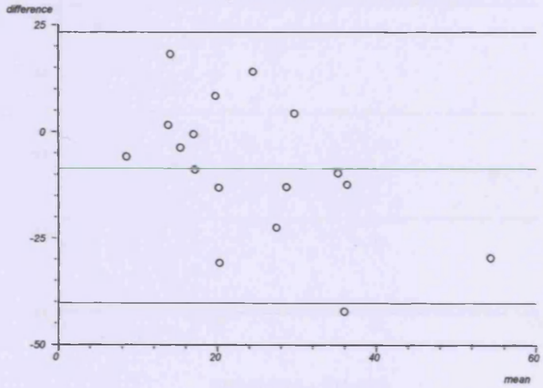
Peripheral Zone – 3 Months

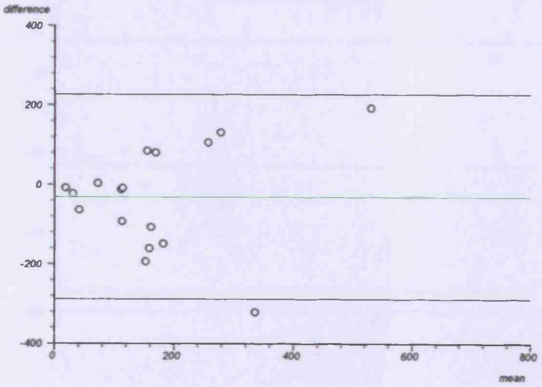
Central Zone - Baseline

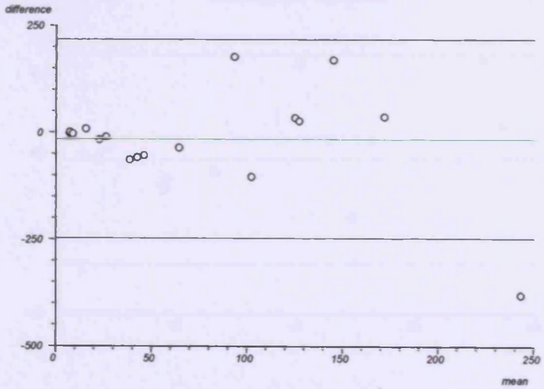
Central Zone – 3 Months

rBF

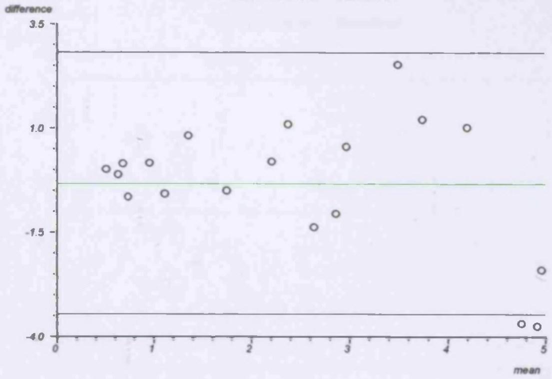
Whole Prostate - Baseline

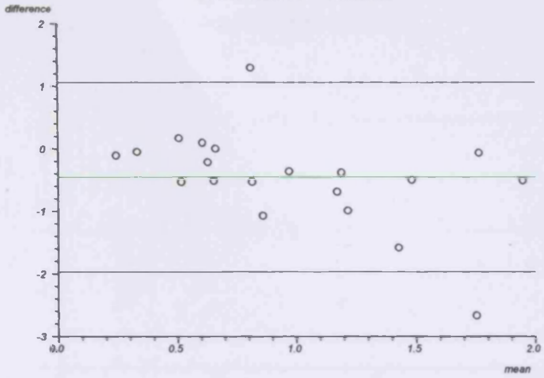
Whole Prostate – 3 Months

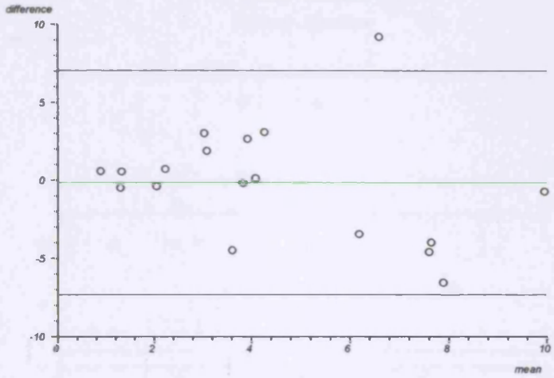
Tumour - Baseline

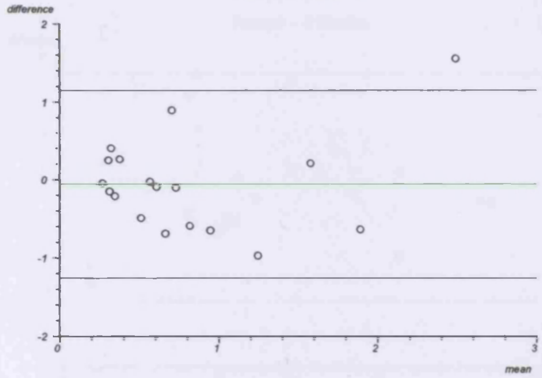
Tumour – 3 Months

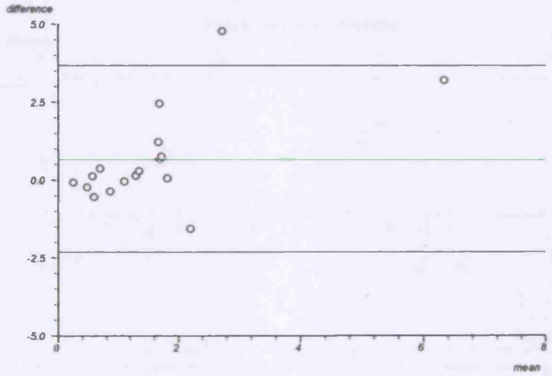
Peripheral Zone - Baseline

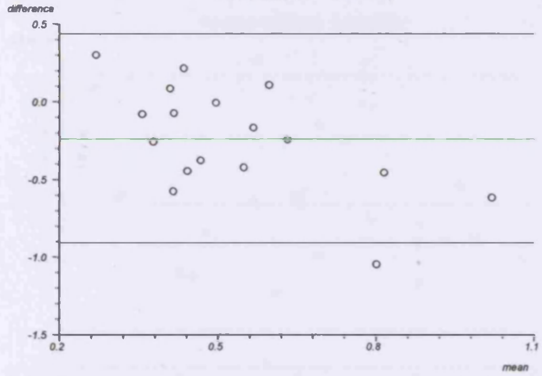
Peripheral Zone – 3 Months

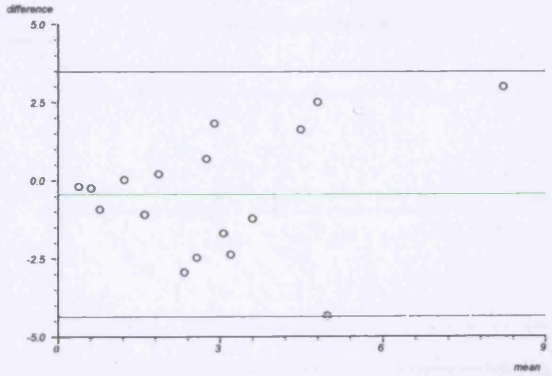
Central Zone - Baseline

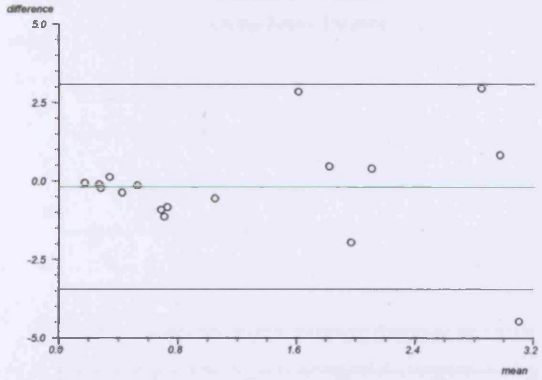
Central Zone – 3 Months

BOLD-MRI

R_2*

Whole Prostate - Baseline

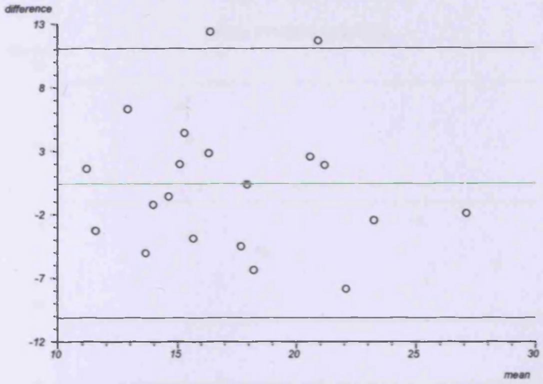

Whole Prostate – 3 Months

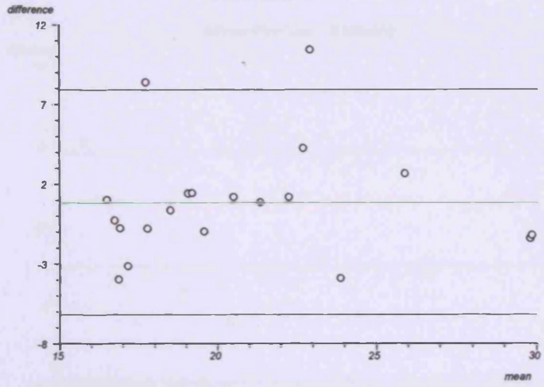

Tumour - Baseline

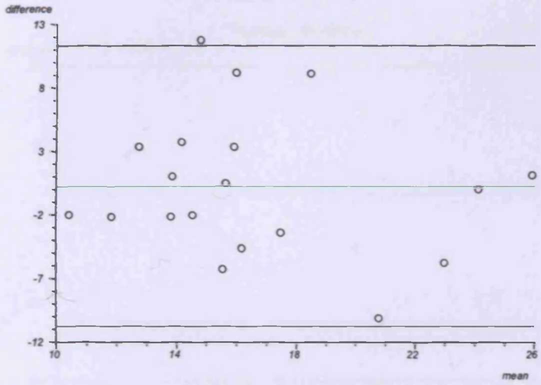

Tumour – 3 Months

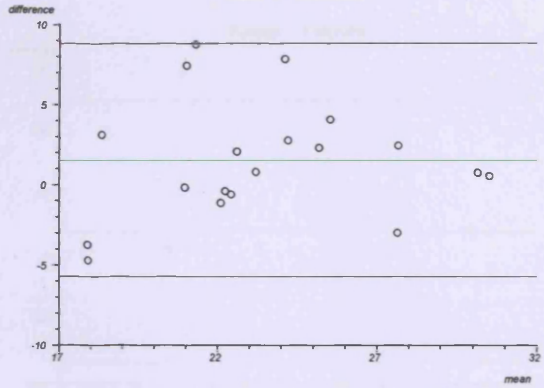

Peripheral Zone - Baseline

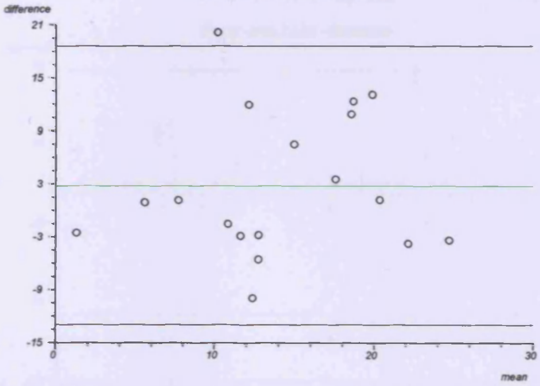

Peripheral Zone – 3 Months

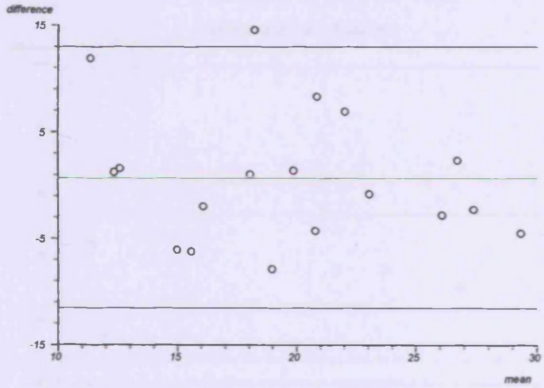

Central Zone - Baseline

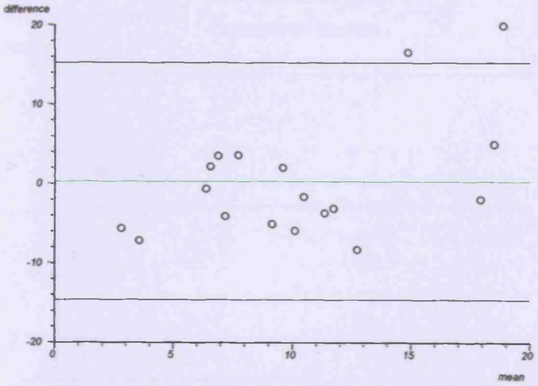

Central Zone – 3 Months

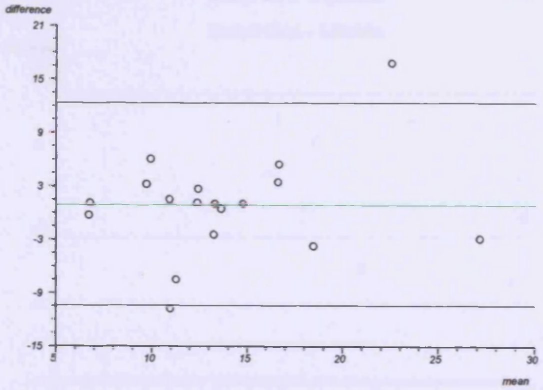

Diffusion weighted ADC parameters

ADC (b-values 0-1000 s/mm^2)

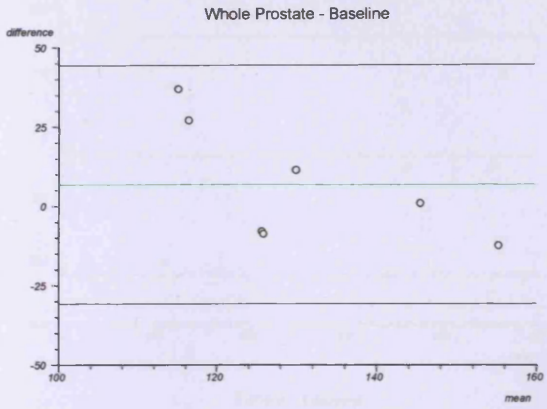
Whole Prostate - Baseline

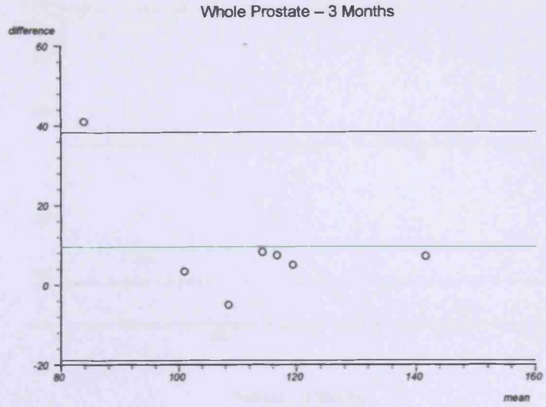
Whole Prostate – 3 Months

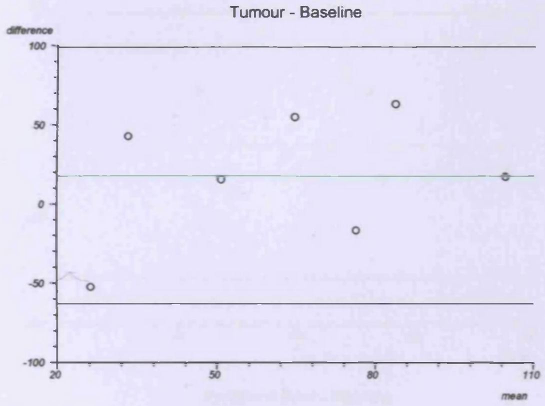
Tumour - Baseline

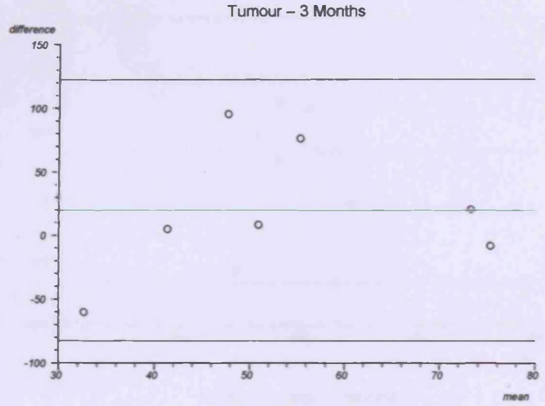
Tumour – 3 Months

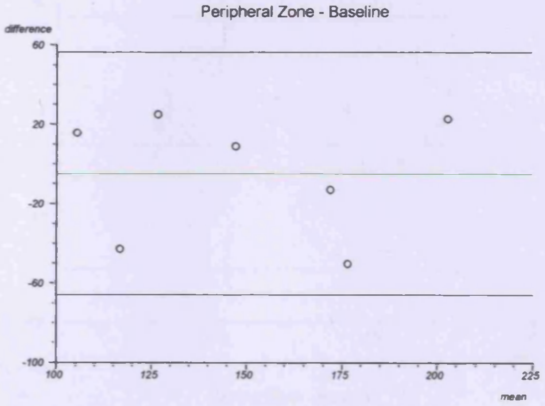
Peripheral Zone - Baseline

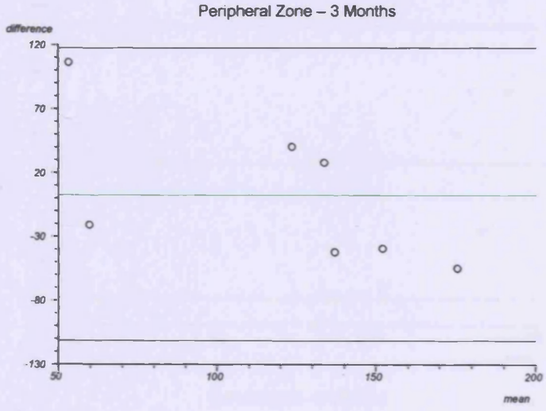
Peripheral Zone – 3 Months

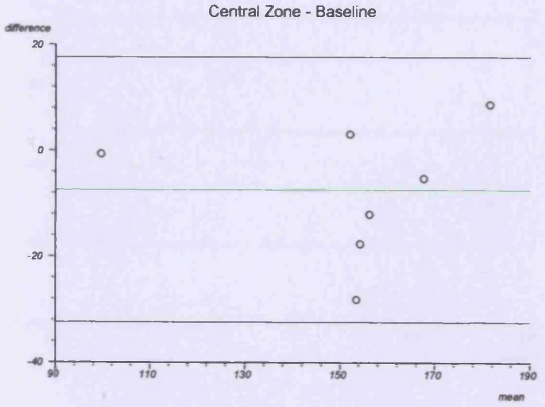
Central Zone - Baseline

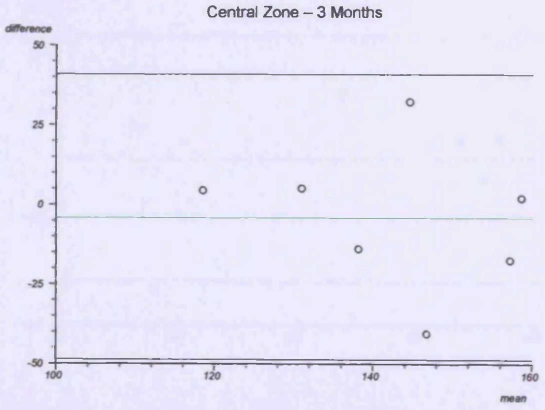
Central Zone – 3 Months

ADC (b-values 0-50 s/mm^2)

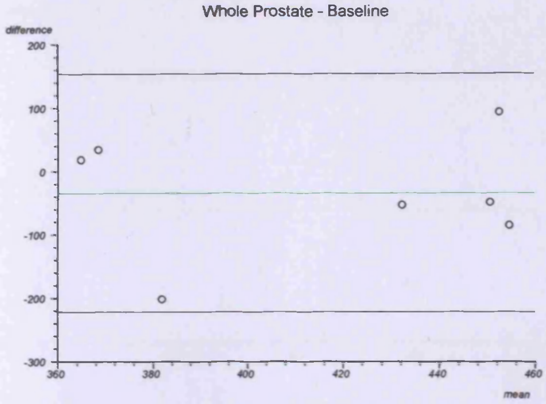
Whole Prostate - Baseline

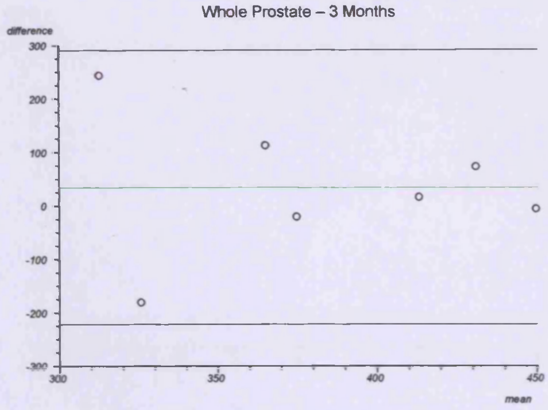
Whole Prostate – 3 Months

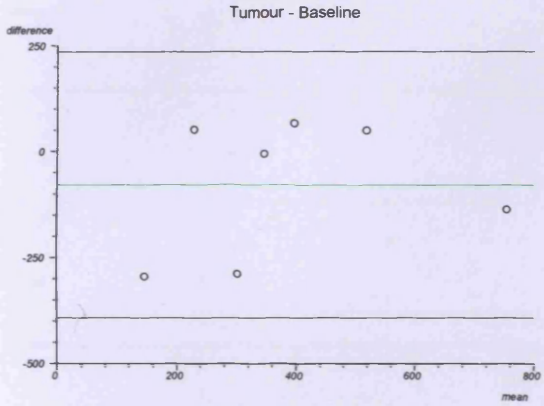
Tumour - Baseline

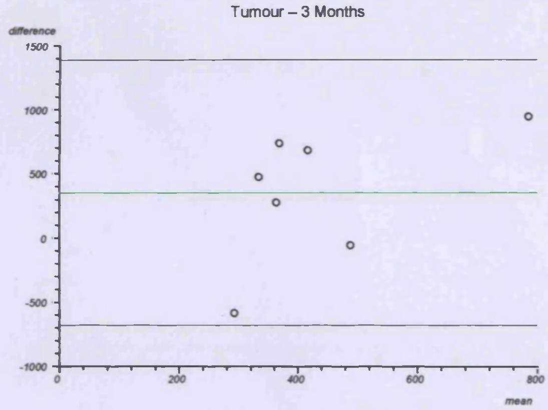
Tumour – 3 Months

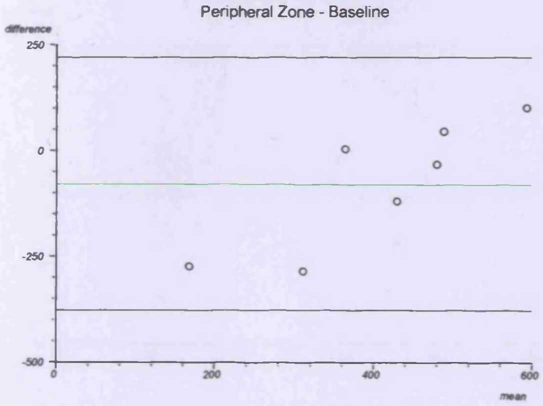
Peripheral Zone - Baseline

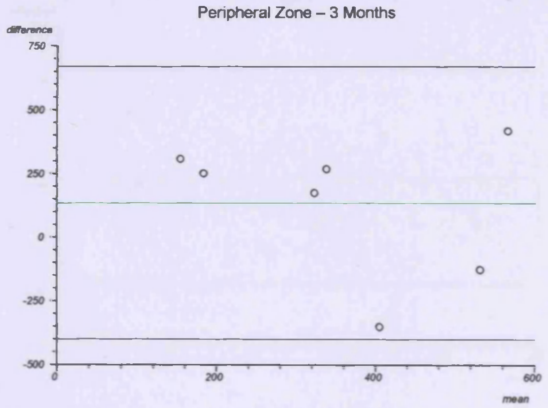
Peripheral Zone – 3 Months

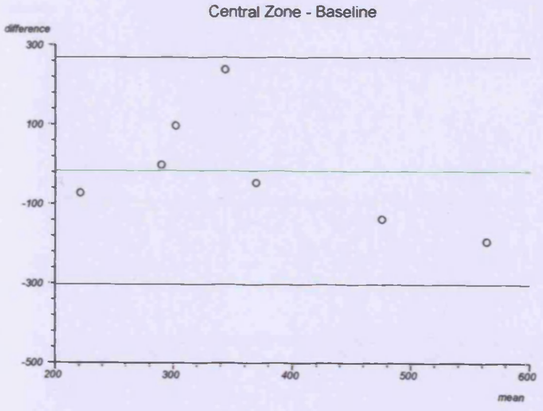
Central Zone - Baseline

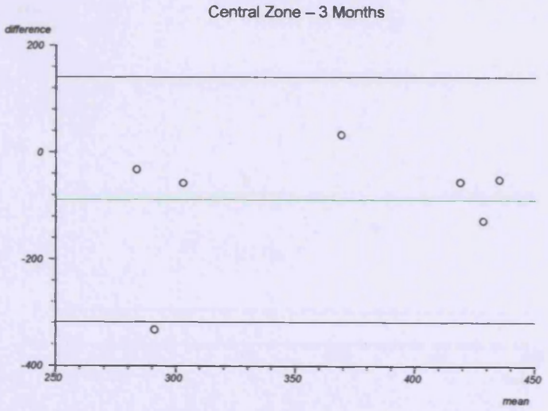
Central Zone – 3 Months

ADC (b-values 150-1000 s/mm^2)

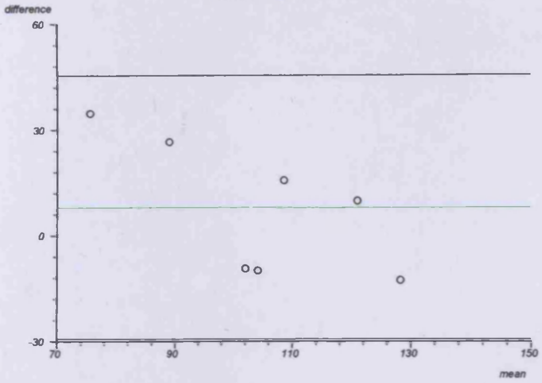
Whole Prostate - Baseline

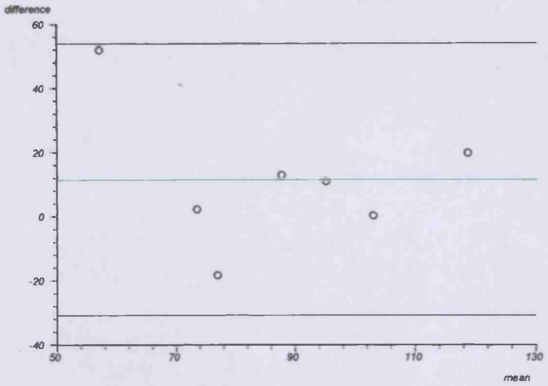
Whole Prostate – 3 Months

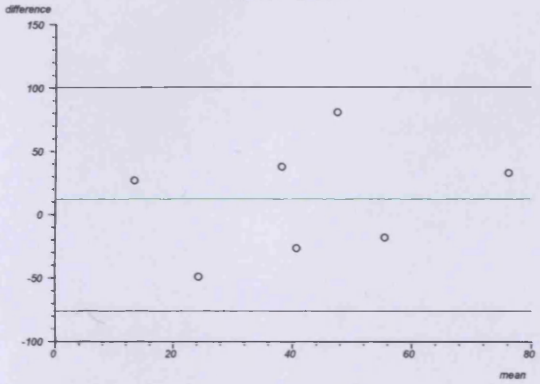
Tumour - Baseline

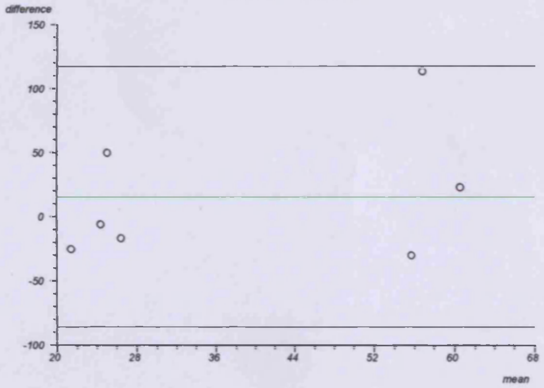
Tumour – 3 Months

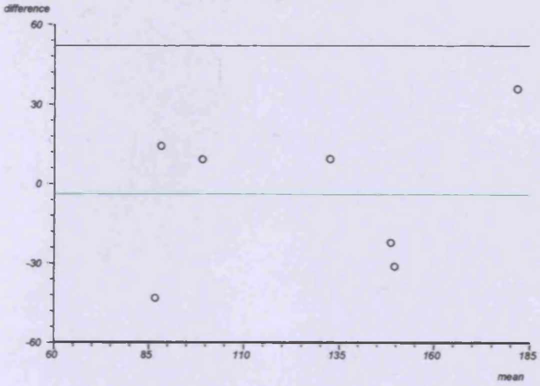
Peripheral Zone - Baseline

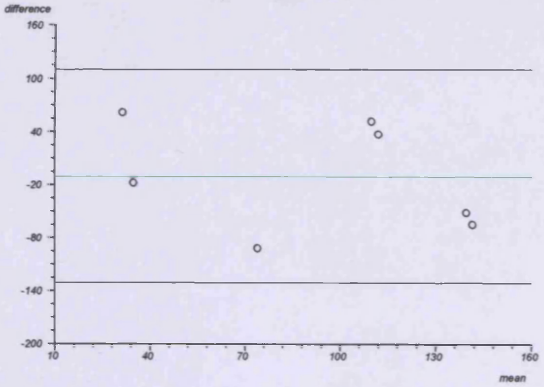
Peripheral Zone – 3 Months

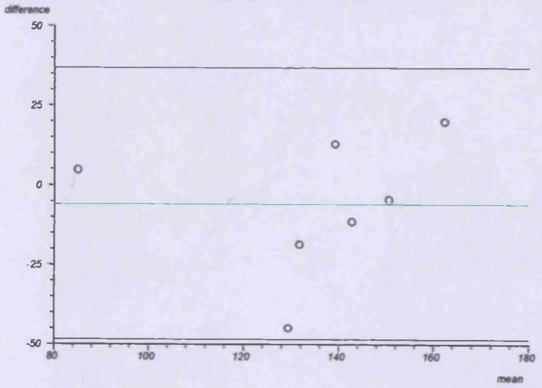
Central Zone - Baseline

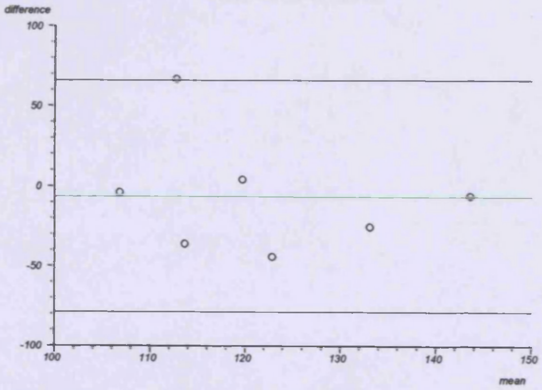
Central Zone – 3 Months